6-12-2020 2:00 PM

A Novel System and Image Processing for Improving 3D Ultrasound-guided Interventional Cancer Procedures

Derek J. Gillies, *The University of Western Ontario*

Supervisor: Fenster, Aaron, *The University of Western Ontario*

A thesis submitted in partial fulfillment of the requirements for the Doctor of Philosophy degree in Medical Biophysics

Abstract

Image-guided medical interventions are diagnostic and therapeutic procedures that focus on minimizing surgical incisions for improving disease management and reducing patient burden relative to conventional techniques. Interventional approaches, such as biopsy, brachytherapy, and ablation procedures, have been used in the management of cancer for many anatomical regions, including the prostate and liver. Needles and needle-like tools are often used for achieving planned clinical outcomes, but the increased dependency on accurate targeting, guidance, and verification can limit the widespread adoption and clinical scope of these procedures. Image-guided interventions that incorporate 3D information intraoperatively have been shown to improve the accuracy and feasibility of these procedures, but clinical needs still exist for improving workflow and reducing physician variability with widely applicable cost-conscience approaches. The objective of this thesis was to incorporate 3D ultrasound (US) imaging and image processing methods during image-guided cancer interventions in the prostate and liver to provide accessible, fast, and accurate approaches for clinical improvements.

An automatic 2D-3D transrectal ultrasound (TRUS) registration algorithm was optimized and implemented in a 3D TRUS-guided system to provide continuous prostate motion corrections with sub-millimeter and sub-degree error in 36 ± 4 ms. An automatic and generalizable 3D TRUS prostate segmentation method was developed on a diverse clinical dataset of patient images from biopsy and brachytherapy procedures, resulting in errors at gold standard accuracy with a computation time of 0.62 s. After validation of mechanical and image reconstruction accuracy, a novel 3D US system for focal liver tumor therapy was developed to guide therapy applicators with 4.27 ± 2.47 mm error. The verification of applicators post-insertion motivated the development of a 3D US applicator segmentation approach, which was demonstrated to provide clinically feasible assessments in 0.246 ± 0.007 s. Lastly, a general needle and applicator tool segmentation algorithm was developed to provide accurate intraoperative and real-time insertion feedback for multiple anatomical locations during a variety of clinical interventional procedures. Clinical translation of these developed approaches has the potential to extend the overall patient quality of life and

outcomes by improving detection rates and reducing local cancer recurrence in patients with prostate and liver cancer.

Keywords

Image-guided interventions, prostate cancer, liver cancer, three-dimensional ultrasound, 2D-3D image registration, 2D image segmentation, 3D image segmentation, real-time image processing

Summary for Lay Audience

Medical procedures that use imaging are useful for diagnosis or treatment of patients as open surgery is often avoided, reducing the side-effects and time needed for healing. Needle-like tools are often used for managing diseases, like prostate and liver cancer, by taking samples for testing, bringing radiation directly into a tumor for treatment or heating small regions in the body to kill the cancer cells. Although the small tool sizes are helpful, higher physician skills are needed to read 2D images for understanding the 3D body while guiding these tools, which can lead to missed cancer diagnoses and treatments that have cancer recurrence. 3D information has been shown to reduce the occurrence of these poor procedure outcomes, but systems that generate 3D information are often expensive and make procedures longer. The goal of this work was to use 3D ultrasound (US) imaging with the software during image-guided prostate and liver cancer procedures.

One software approach was created to correct for prostate motion and performed with small errors at more than 15 times per second when installed in our 3D US system. Another software approach was made to automatically recognize the prostate in 3D US images. This method performed in less than one second and had the same error as humans when tested on images from different procedures, demonstrating the multi-purpose potential of the software. A new 3D US system was made for guiding liver cancer therapy by controlling three motors to create new types of images and a clinical navigation procedure that guided therapy needles to targets identified in the images. The software was made for this system to recognize needles in 3D US images in less than one second, improving the speed that needle placements could be checked. Lastly, the software was made to automatically recognize needles in 2D US images from a large range of clinical procedures and areas in the body. We believe that this research will increase the use of image-guided needle procedures to help patients with cancer while taking advantage of the reduced side-effects and time for healing.

Co-authorship Statements

This thesis is an integration of five articles, each constituting a chapter, and are either published or under peer-review. As the first author of these manuscripts, I was a significant contributor to all aspects of the studies including study design, data analysis, drafting, and revising the manuscripts. All authors contributed editorial feedback during the manuscript review. Listed below are the specific contributions for all co-authors for each manuscript in this thesis.

Chapter 2 is an original research article entitled "*Real-time Registration of 2D to 3D Ultrasound Images for Image-guided Prostate Biopsy*" and was published in the journal *Medical Physics* in 2017. This manuscript was co-authored by Derek J. Gillies, Lori Gardi, Tharindu De Silva, Shuang-ren Zhao, and Aaron Fenster. My contributions to the chapter included manual identification of fiducials for validation, developing software for evaluation using MATLAB and Excel, parameter optimization, experimental design, all phantom fabrication and testing, data analysis and interpretation, and manuscript preparation. Lori Gardi was responsible for software development in C++ including clinical integration of the algorithm to the biopsy system, recording of data, and image visualization. Tharindu De Silva was responsible for the registration algorithm conception, implementation on a central processing unit (CPU), and clinical data selection and preparation. Shuang-ren Zhao was responsible for the graphics processing unit (GPU) implementation of the code. Aaron Fenster was the Principal Investigator and provided supervision on experimental design, data interpretation, and manuscript writing.

Chapter 3 is an original research article entitled "*Automatic prostate segmentation using deep-learning on clinically diverse 3D transrectal ultrasound images*". This manuscript was published in the journal *Medical Physics* in 2020. This manuscript was co-first authored by Nathan Orlando and Derek J. Gillies with co-authorship from Igor Gyacskov, Cesare Romagnoli, David D'Souza, and Aaron Fenster. Nathan Orlando and I equally split contributions for study design, data collection, image formatting conversion, developing software for evaluation using MATLAB and Excel, 3D CNN implementations (including model training, validation, and testing), data analysis, interpretation, and

manuscript preparation. Igor Gyacskov was responsible for all manual segmentations, 2D U-Net development (including model training, validation, and testing), and 3D segmentation reconstruction. Cesare Romagnoli and David D'Souza were physicians who helped with 3D TRUS data acquisition and clinical perspective. Aaron Fenster was the Principal Investigator and provided supervision on experimental design, data interpretation, and manuscript writing.

Chapter 4 is an original research article entitled "*Geometrically Variable Three-Dimensional Ultrasound for Mechanically Assisted Image-Guided Therapy of Focal Liver Cancer Tumors*" and was accepted for publication in *Medical Physics* on June 28, 2020. This manuscript was co-authored by Derek J. Gillies, Jeffrey Bax, Kevin Barker, Lori Gardi, Nirmal Kakani, and Aaron Fenster. My contributions to the chapter included experimental design, all phantom fabrication and testing, optical tracking evaluations, developing software for evaluation using MATLAB, Excel, and 3D Slicer, navigation workflow conception, manual identification of fiducials and needles for evaluation, data analysis and interpretation, and manuscript preparation. Jeffrey Bax designed the 3D US counterbalance and tracking system, manufactured the system, and developed forward joint kinematics. Kevin Barker performed the design and manufacturing of the three-motor scanner, all 3D-printing designs, fabrication, and developed all scanning driving tables. Lori Gardi was responsible for software development in C++ including system implementation of scanning, tracking, and navigation workflows, recording of ultrasound data, and image visualization. Nirmal Kakani was the physician responsible for clinical perspective and volunteer image assessment. Aaron Fenster was the Principal Investigator and provided supervision on experimental design, data interpretation, and manuscript writing.

Chapter 5 is an original research article entitled "*Three-dimensional Therapy Needle Applicator Segmentation for Ultrasound-guided Focal Liver Ablation*" and was published in the journal *Medical Physics* in 2019. This manuscript was co-authored by Derek J. Gillies, Joseph Awad, Jessica R. Rodgers, Chandima Edirisinghe, Derek W. Cool, Nirmal Kakani, and Aaron Fenster. My contributions to the chapter included experimental design, phantom fabrication, image acquisition, developing software for evaluation using

MATLAB, Excel, and 3D Slicer, C++ algorithm CPU parallelization, parameter optimization, coordination of manual needle tip and shaft data collection, data analysis and interpretation, and manuscript preparation. Joseph Awad was responsible for algorithm conception and initial C++ implementation. Jessica R. Rodgers was responsible for 3D Slicer software development and manual identification of needles for evaluation. Chandima Edirisinghe was responsible for the C++ algorithm workflow and test bench adaptation. Derek W. Cool was a clinical perspective physician and helped to coordinate manual tip and shaft data collection for the multi-user trial. Nirmal Kakani was the physician responsible for clinical perspective and clinical 3D US patient image acquisition. Aaron Fenster was the Principal Investigator and provided supervision on experimental design, data interpretation, and manuscript writing.

Chapter 6 is an original research article entitled "*A Deep Learning Method for General Needle and Applicator Segmentation in Two-dimensional Ultrasound Images from Multiple Applications and Anatomical Regions*" and was submitted to *Medical Physics* on April 15, 2020, and is currently under peer-review. This manuscript was co-first authored by Derek J. Gillies and Jessica R. Rodgers with co-authorship from Igor Gyacskov, Priyanka Roy, Nirmal Kakani, Derek W. Cool, and Aaron Fenster. Jessica R. Rodgers and I equally split contributions for study design, data analysis and interpretation, and manuscript preparation. I was responsible for phantom, liver, and kidney image organization and conversion, manual segmentation 3D Slicer software development, coordinating the multi-user data collection, identification of some tip and shaft locations, developing the largest island with linear fit post-processing, and MATLAB software for pixel map metrics. Jessica R. Rodgers was responsible for developing RANSAC post-processing, identification of most tip and shaft locations, gynecologic image collection and conversion, and MATLAB software for tip and trajectory metrics. Igor Gyacskov was responsible for 2D U-Net development (including model training, validation, and testing). Priyanka Roy was responsible for prostate image collection and manual segmentations. Nirmal Kakani was a physician responsible for clinical perspective. Derek W. Cool was a physician responsible for the clinical perspective and collection of image sequences from liver and kidney procedures. Aaron Fenster was the Principal Investigator and provided supervision on experimental design, data interpretation, and manuscript writing.

Acknowledgments

The work completed in this thesis is the result of many individuals who have guided and supported me over the past five years.

Thank you to my supervisor, Dr. Aaron Fenster, for the numerous opportunities to improve myself and for pushing me to strive to be my best. I am grateful for the time, freedom, and happiness you have given me, as well as your patience to develop me into the person I am today. Your dedication to my success has made my graduate experience truly exceptional and your open door has always welcomed me with positivity. I have greatly appreciated your understanding, direction, and ability to make me laugh while overcoming challenges. Your leadership has provided me with clear advice and guidance when needed, while also leaving me with subtle lessons I often reflect upon; I still question how to define an imaginary number after all these years. Thank you for your wisdom, life-advice, and many "Fenster-isms," such as "try not to be so predictable," "the future is now," and "who cares about starting, it's about finishing."

Thank you to my advisory committee, Dr. Terry Peters, Dr. Ting-Yim Lee, and Dr. Ali Khan. I will always cherish your willingness to listen, question, teach, and support me. You have all been great mentors. Thank you to all the willing volunteers and patients who have made research translation possible and the physicians for their efforts with data collection and clinical perspective, especially Dr. Nirmal Kakani and Dr. Derek Cool.

Thank you to the past and present members of the Fenster lab and other individuals at Robarts who have contributed to the work in this thesis, making my experience easier, thought provoking, and enjoyable. In addition to their technical skills and support, specific thanks to David Tessier, Kevin Barker, and Ivailo Petrov for their thoughtful, open-minded, generous, and caring attitudes. Thank you to Jessica Rodgers for joining me through basically every milestone of graduate school, while helping me navigate numerous research challenges and life events with your positivity. I've gotten more comfortable when speaking at conferences, but I'll never forget the immense support you gave me early-on. Thank you to Nathan Orlando for your kindness, deep conversations, and motivation. It's been fantastic sharing many accomplishments with you – hopefully we made Pingge proud.

Thank you to Sam Papernick for sharing jokes, music suggestions, and personal experiences. It's hilarious how similar we are and I look forward to seeing your future achievements. Thank you to the many other people who have supported and taught me lessons including, but not limited to, Igor Gyacskov, Jeffrey Bax, Lori Gardi, Jacques Montreuil, Chandima Edirisinghe, Justin Michael, Eric Knull, Claire Park, Tom Hrinivich, Priyanka Roy, Andrew Harris, Andrew McCann, Imrie Pentz, Tharindu De Silva, Ren Zhao, Daniel Lorusso, Chris Norley, Hristo Nikolov, and Steven Pollman.

Thank you to the many friends who have encouraged me to finish and helped make some of my happiest memories along the way. Thank you to Dante Capaldi for your humor, honesty, and mentorship. You have helped me through some of my toughest times and you continue to be such a great role model. Thank you to Tomi Nano for your ingenious perspectives, unending motivation, and receptive nature for any topic of conversation. Thank you to Eric Lessard for your generosity, confidence, and being able to match my sarcasm with even more sarcasm than I thought possible. Thank you to Amy Schranz for bringing people together and initiating many coffee time, lunch time, and neighborly evenings to get through the stresses of graduate school. Thank you to the many other friendships developed in London, including Megan Fennema, Amanda Kuti, Jordan Cornwall, Olivia Stanley, Terenz Escartin, Raanan Marants, Rachel Eddy, Golafsoun Ameri, Amanda Hamilton, Heather Young, and Dickson Wong. Thank you to the friends who put up with me after the many years together and continually make efforts to improve my life: Joshua, Justin, Julian, Dakota, Eric, Natalie, Travis, Melissa, Anmol, Shana, Jenell, Davis, Russell, and Tina.

Thank you to my family for the constant love and support. Thank you, Mom and Dad, for always being there for me and providing me with ongoing guidance to better myself. Thank you to my brother, Chad, for being dependable and always looking for ways to help make life easier. Thank you to Zoie for your generosity and efforts to brighten my day.

Thank you to the extremely supportive other ($p<0.001$) in my life, Allie. You have been an amazing friend and possess an incredible ability to make me smile under any circumstances. I am so glad you could help me get through graduate school and I can't

express enough the joy you have brought to my life. Your pursuit for doing things you love is inspirational and I am eager to explore many more adventures together.

Thank you to my examiners, Dr. Elvis Chen, Dr. Douglas Hoover, Dr. Jagath Samarabandu, and Dr. Tim Salcudean. I appreciate your time and effort to examine my thesis and participate in my defense.

Finally, I would like to thank the following sources of funding for supporting this work: the Cancer Research and Technology Transfer strategic training program, the National Sciences and Engineering Research Council, the Ontario Institute for Cancer Research Imaging Translation Program, and the Canadian Institutes of Health Research.

Table of Contents

List of Tables

List of Figures

List of Abbreviations

2D	Two-dimensional
3D	Three-dimensional
A/VPD	Area/Volume Percent Difference
ALA	Axis Localization Accuracy
ANOVA	Analysis of Variance
AOI	Area-of-interest
ATE	Applicator Tip Error
BT	Brachytherapy
CBCT	Cone-beam X-ray Computed Tomography
CI	Confidence Interval
CNN	Convolutional Neural Network
CPU	Central Processing Unit
CT	Computed Tomography
DiceXEnt	Dice Plus Cross-entropy
DoF	Degrees-of-freedom
DRE	Digital Rectal Exam
DSC	Dice-similarity Coefficient
FLE	Fiducial Localization Error
FRE	Fiducial Registration Error
GPU	Graphics Processing Unit
GSS	Golden Section Search
HCC	Hepatocellular Carcinoma
HD	Hausdorff Distance
HDR	High-dose-rate
IQR	Interquartile Range
IR	Interventional Radiologist
IRE	Irreversible Electroporation
LDR	Low-dose-rate
MSD	Mean Surface Distance
MR	Magnetic Resonance
MRI	Magnetic Resonance Imaging
MWA	Microwave Ablation
NCC	Normalized Cross-correlation
PIP	Parallel Integral Projection
PSA	Prostate-specific Antigen
Q1	First Quartile (25%)
Q3	Third Quartile (75%)
RANSAC	Random Sample Consensus
RFA	Radiofrequency Ablation
RMS	Root-mean-square
RMSD	Residual Mean Surface Distance
rmU-Net	Reconstructed Modified U-Net
ROI	Region-of-interest
sA/VPD	Signed Area/Volume Percent Difference

SBR	Signal-to-background Ratio
SD	Standard Deviation
sHD	Signed Hausdorff Distance
sMSD	Signed Mean Surface Distance
SNR	Signal-to-noise Ratio
SR	Sagittally Reconstructed
TRE	Target Registration Error
TRUS	Transrectal Ultrasound
TU	Trained User
U	User
US	Ultrasound

Chapter 1

1 Introduction

Image-guided medical interventions is a growing field that has many clinical applications from neurosurgery to cancer diagnosis and therapy.[1] Recent advancements in hardware and software have benefitted this field from intra-operative tools in the form of tracking, visualization, and advanced image processing technologies, which provide easier and enhanced image guidance. Utilities such as image segmentation and registration are becoming necessities for physicians as they "potentially lead to shortened operation time, reduced radiation dose, minimized contrast medium, and most importantly, increased accuracy."[2] As the interest in minimally invasive procedures continues to rise, increasing image guidance accuracy will lead to increased dissemination and success of current approaches.

Diagnosis and therapy of prostate and liver cancer can be pursued with image-guided interventional approaches, but currently suffer from undesirable limitations, such as high false-negative rates[3] and local cancer recurrence.[4] Accordingly, the focus of this thesis is to improve the accuracy and reduce user variability of image-guided interventions using lower-cost solutions that incorporate three-dimensional (3D) ultrasound (US) and advanced image processing techniques. This thesis is mainly focused on applications in prostate and liver cancer diagnoses and therapies, but applications to other relevant anatomies, such as gynecologic and kidney cancer, are provided to demonstrate the potential widespread impact of the investigated solutions. This work has the potential to detect clinically significant tumors earlier, result in fewer diagnostic and therapeutic sessions, determine appropriate treatment selection, reduce the local cancer recurrence after focal tumor ablation, and treat more complex tumor locations. The remainder of this chapter describes the current status of prostate and liver cancer prevalence (1.1), therapeutic options for patients with these disease sites (1.2), image-guided interventions (1.3) with selected image processing techniques (0) as alternatives to conventional therapy, and the unmet needs, hypothesis, and specific objectives of the thesis (1.5).

1.1 Motivation

1.1.1 Prostate cancer

Prostate cancer is the most commonly diagnosed non-skin cancer in Canadian men with 1 in 9 males expected to be diagnosed with the disease in their lifetimes.[5] This disease site accounted for 20.3% (22,900) of all new cancer cases, with 99% of cases occurring in men over the age of 50. Prostate cancer was projected to be the third most common cause of cancer deaths in Canadian males in 2019, but the mortality rate has been declining by 2.8% per year since 1994 and has the third-highest five-year net survival rate (93%) in most recent predictions.[5] Although the disease is most often highly treatable, prostate cancer has a wide range of clinical presentation from slow-growing to fatally aggressive, which is characterized by a standardized numerical scoring system (i.e., Gleason score).[6]

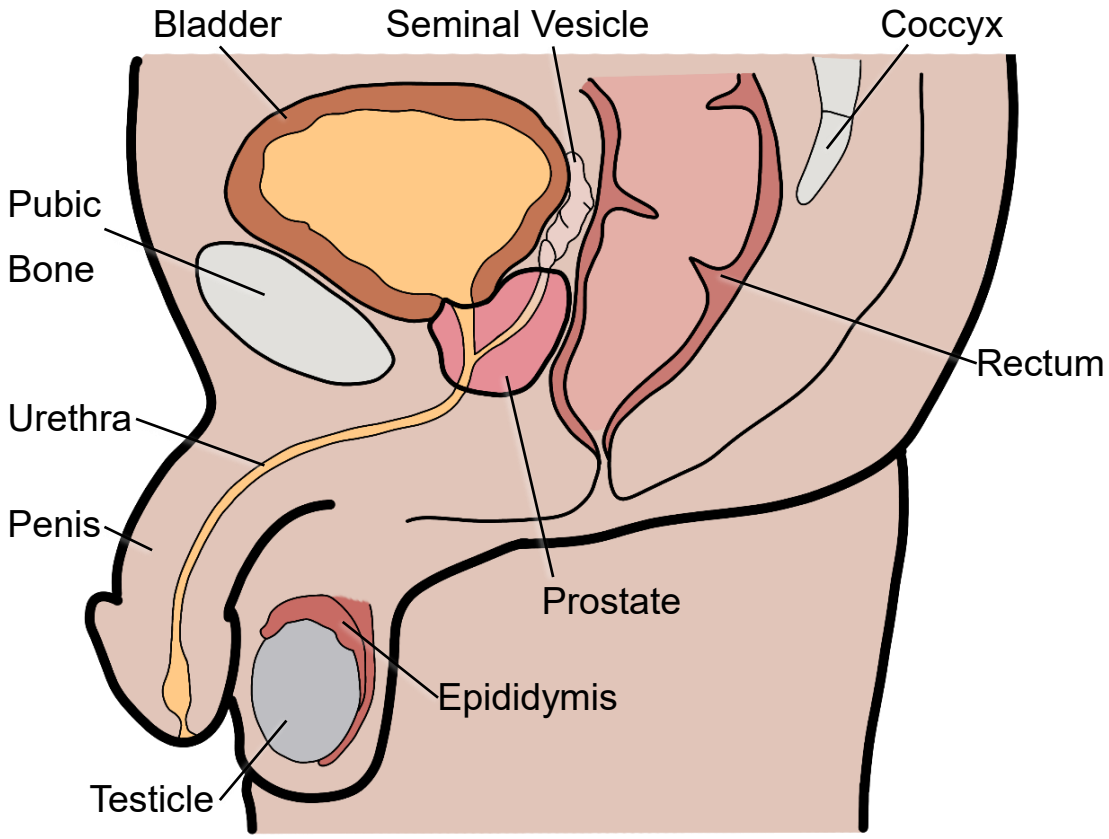

Figure 1.1 Local anatomy in the male pelvis surrounding the prostate.

The prostate is a gland of the male reproductive system located in the pelvis inferiorly to the bladder, posterior to the pubic symphysis, and anterior to the rectum (Fig. 1).[7] This non-vital gland surrounds the urethra and contributes secretions in the formation of semen. The presence of disease can lead to symptoms such as frequent urination, blood in the urine and semen, as well as discomfort from an enlarged prostate.[8] Although these symptoms can be difficult and sometimes intolerable, metastatic disease that spreads through the body is the primary concern as five-year survival rates are approximately 30% relative to almost 100% for local or regional prostate cancer.[9] This variability in survival correlating with disease aggressiveness stresses the need for earlier cancer detection before late-stage disease development and more aggressive treatments for high-risk disease.

1.1.2 Liver cancer

Liver cancer is one of the fastest rising cancers in Canada. While it only represents less than 2% of all new cancer cases, liver cancer incidence in Canada has been increasing in males (3.3%) and females (2.7%), second only to thyroid cancer, based on the average annual percent change between 1984 and 2015.[5] More concerning are the annual changes in mortality rates since 1984, which shows that liver cancer is the highest statistically significant ($p < 0.001$) increasing change in males (3.1%) and females (2.2%).[5] Once diagnosed with the disease, the prognosis is poor as liver cancer has the fourth-lowest five-year net survival rate (19%). This rate is also an underestimate relative to other sources as it does not consider cancers of the intrahepatic bile duct or the large number of unspecified cases based on primary or metastatic classifications, which would increase the number of cases by 45.9%.[5]

These statistics get worse on a global scale as liver cancer accounts for the fifth and ninth-highest incidence rates for cancer and the second and sixth-highest mortality rates, for men and women respectively.[10] One major cause for the high mortality rate is the asymptomatic nature of most primary liver cancers with very few to nonexistent traditional cancer markers, like bleeding and palpable lesions. This leads to large and late-stage tumor diagnoses that are less treatable with curative intent. However, improvements in early detection of liver cancer have been observed more recently, partially attributed to the widespread use of ultrasound screening for individuals at risk for liver cancer.[11]

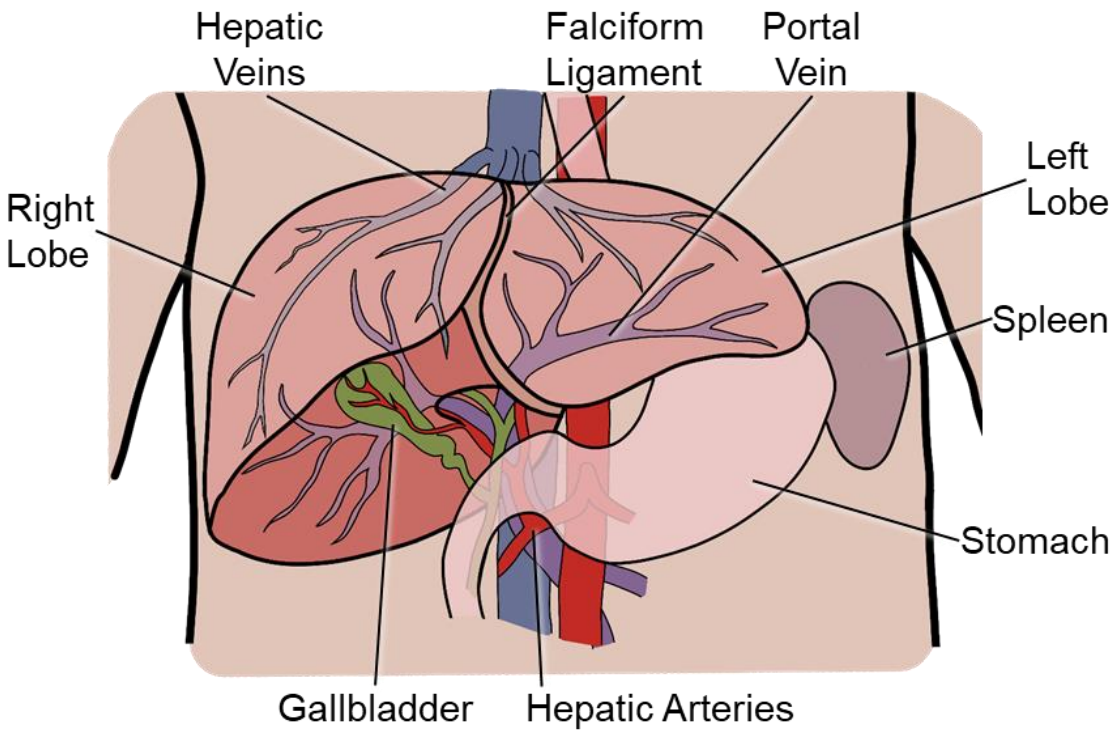

Figure 1.2 Local anatomy in the abdomen surrounding the liver.

The liver is the largest solid organ in the body located inferiorly to the diaphragm and normally resting against the lateral and anterior abdominal walls. It is predominantly divided into two lobes (i.e., right and left) by the falciform ligament, but it is often more finely divided into eight segments unequally distributed between the two lobes and in relation to the hepatic arterial, portal, and biliary drainage.[7] The primary functions of the liver are to produce bile for digestion, process nutrients and drugs, and filter blood from the stomach and intestines.

The most common subtype of liver cancer is hepatocellular carcinoma (HCC) and is highly prevalent in low-income and developing countries.[11] Liver cancer is predominantly due to the incidence of hepatitis B and C viruses[12,13] and is often preceded by cirrhosis (scarring), but includes other risk factors like excessive alcohol consumption, smoking, fatty liver disease, diabetes, obesity, and aflatoxin (produced by some fungi on crops, like corn and peanuts[14]) exposure.[5,12] Although increases in mortality rates have been mostly attributed to hepatitis and alcohol consumption,[12] universal vaccinations against hepatitis B have been shown to reduce the incidence of HCC with statistical significance.[15] The liver is also

a frequent site for metastatic cancer originating from other parts of the body, such as the lung, breast, pancreas, gastrointestinal tract and lymphatic system.[12]

1.2 Conventional therapeutic options

1.2.1 Prostate cancer

Over-diagnoses of prostate cancer has been a concern with the increased use of prostate-specific antigen (PSA) for screening as many prostate cancers would not affect quality or quantity of life if left undetected.[16] Recent Canadian guidelines in 2014 have mirrored the decisions from the United States Preventive Services Task Force to decrease PSA screening in men over 75 and asymptomatic men, which has resulted in a 9% decrease in the annual percent change for prostate cancer incidence since 2011.[17] Although surgery, radiation, and drug-based therapies are effective in the management of prostate cancer, recent motivation has been focused towards conservative management techniques and focal methods of treatment.[18]

1.2.1.1 Active surveillance

Active surveillance refers to deferring treatment and observing patients with serial PSA assessments, repeated biopsies, and other recurring diagnostic exams to wait until low-risk disease shows signs of higher-risk and likely well within the window of opportunity for cure.[19] Concerns with overtreatment of low-risk prostate cancer have led to increases in the number of patients recommended for active surveillance; for example, the percentage of patients with low-risk disease in the United States on active surveillance increased from 15% to 42% in 2015,[20] with the majority of increases in patients over age 75.[9]

1.2.1.2 Radical prostatectomy

Radical prostatectomy is a surgical procedure that completely removes the prostate gland and its attachments around the base of the bladder.[7] This procedure is considered an excellent treatment option for patients with early prostate cancer;[21] however, side effects include incontinence, impotence, and altered bowel habits with approximately 35% of patients experiencing biochemical recurrence within ten years.[22] Following recent

guidelines to reduce overtreatment of low-risk disease, prostatectomies have declined from 47% to 31% as of 2015.[20]

1.2.1.3 Systemic treatments

Advanced prostate cancer that has metastasized beyond the prostate is most often treated using androgen deprivation or chemotherapy.[9] Androgens like testosterone and dihydrotestosterone are essential for the prostate and overexpression of the androgen signaling pathways are often observed in proliferating prostate tumor cells.[23] Suppressing these hormones in the body is a foundational and mainstay treatment for advanced prostate cancer; however, not all prostate cancers respond to this form of therapy and many can develop into castration-resistant prostate cancer.[24] The remaining treatment option is often chemotherapy with palliative intent,[25] but the utility of involving chemotherapy at different stages of disease progression have been investigated.[26]

1.2.1.4 External beam radiation therapy

External beam radiation is a well-established form of therapy for low to intermediate-risk prostate cancer, with application to high-risk in some cases, and is often treated alone or in combination with androgen deprivation therapy.[27] Radiation therapy is associated with improved long-term sexual function and urinary continence relative to prostatectomy, but patients have been observed to have worse bowel function and treatments are often long, typically requiring multiple weeks of treatment sessions.[28] Recent evidence suggests that there is an increased risk of overall and prostate cancer-specific mortality compared to surgery for clinically-localized prostate cancer,[29] but new techniques incorporating accurate imaging such as intensity-modulated and stereotactic radiation therapy have focused on increasing the dose-per-fraction to the prostate (reducing the overall physical dose), improving coverage of tumor volumes, and reducing adverse side effects through the use of smaller and more conformal fields.[27,30]

1.2.1.5 Prostate brachytherapy

Prostate brachytherapy refers to procedures where radioactive sources are implanted or brought within the prostate using needles, typically guided by a rigid template with

regularly spaced holes every 5 mm in a grid-like system. Prostate brachytherapy is most often used as a monotherapy to treat early, localized prostate cancer tumors[31] and in combination with external beam therapy for intermediate and high-risk patients. This procedure involves either permanently implanting low-dose-rate (LDR) radioactive seeds or temporarily holding a high-dose-rate (HDR) radioactive source at specified positions in hollow needles based on calculated dwell time durations. Since the radioactive sources are implanted or temporarily held within the prostate, highly conformal dose distributions can be achieved with improved healthy tissue sparing of organs-at-risk, such as the bladder, urethra, and rectum, compared to external beam radiation.[32] For intermediate and high-risk prostate cancer, brachytherapy can also be used to boost radiation dose to the tumor following external beam radiation therapy for a statistically significant benefit in 5-year biochemical-progression-free survival, but a complete understanding of long-term toxicities is still unknown.[31]

1.2.2 Liver cancer

Liver cancer is typically diagnosed using a combination of health history, physical and imaging examination, blood tests, and biopsy.[33] Since the liver rests on the lateral and anterior abdominal walls, the liver is easily accessible and can be treated using open surgery or percutaneous (through the skin) approaches. Although it is generally understood that early detection of cancer can lead to improved survival outcomes, early-stage HCC is currently difficult to diagnose because it is usually a single, asymptomatic lesion measuring less than two centimeters in diameter, with no vascular or distant metastases.[34]

1.2.2.1 Transplantation or resection

Resection and transplantation have conventionally been the curative surgical options of choice for treating patients with HCC.[35] This is either the removal of some of the liver segments or the entire organ, depending on the number, location, and spread of the disease.[36] Surgical resection is usually considered for early-stage HCC with a single lesion less than three centimeters,[35] sometimes with up to three lesions,[12] as sufficient remaining liver function is necessary for survival.[36] The presence of comorbidities, such as cirrhosis,

can increase the risk of HCC recurrence after liver resection and typically motivates the need for other treatment options, like transplantation.

Transplantation is a desirable method for curing liver cancer as it has the potential to remove localized tumors and underlying cirrhosis, which presents as complications in other forms for therapy. Although transplantation is the preferred treatment modality for patients with solitary HCC, poor liver function, or multifocal HCC, patient eligibility is low, complications can be frequent and severe, and the lack of consistent donors leads to long waiting times.[37] Both resection and transplantation are limited to approximately 10% to 20% of patients[36] and even if the patient is eligible for this type of procedure, complications rates have been observed to be approximately 26% in resection and 33% in transplantation.[38] Also, conventional techniques to treat and manage individuals with liver cancer have been typically associated with high costs, both clinically and financially, with the scarcity of liver donors often leading to a preferential selection of other alternatives, such as liver ablation.[12]

1.2.2.2 Chemotherapy

Advanced-stage liver cancer that has spread beyond the organ to local nodes and distant sites or has invaded the portal or hepatic veins typically have very few options for therapy. Standard chemotherapy is not tolerated well and has not been shown to be effective in treating advanced HCC.[12] The most recognized treatment option for advanced-stage liver cancer with well-preserved liver function is chemotherapy treatment with a molecular target agent, sorafenib, to slow tumor proliferation and angiogenesis, but overall survival is usually only extended by two to seven months.[39,40]

1.2.2.3 External beam radiation therapy

External beam radiation has been used increasingly in the treatment of liver cancer due to advances in planning and delivery that have improved sparing of the radiosensitive healthy tissue.[12] Radiation therapy is most often ideal for early to intermediate-stage liver cancer and is most often recommended when other techniques are not possible or as a bridge to transplantation.[41] Breathing motion and liver position changes can make it difficult for

radiation therapy, but advances in imaging and liver motion tracking have led to more investigation into conformal radiation delivery, dose-escalation, and fewer fractions of therapy.[42]

1.2.2.4 Embolization

Intermediate stage liver cancer typically refers to a multinodular disease that has either more than three lesions or two to three lesions with at least one greater than five centimeters.[37] Patients showing signs of this stage are often treated with embolization,[43] with the most common form being transarterial chemoembolization (TACE), which focuses on inducing tumor necrosis by acute arterial occlusion with the addition of chemotherapeutic drugs.[36] These are typically salvage or bridge therapies for patients with preserved liver function and do not usually have curative intent as complete necrosis is not typically achieved for larger tumors due to incomplete embolization and tumor angiogenesis.[35] Approaches that combine TACE with other procedures have been investigated for tumors larger than three centimeters to make patients eligible for other curative approaches,[44] with the use of TACE post-resection showing benefits compared to other anti-recurrence therapies.[45] Embolization can also be performed using radiation sources, such as Yttrium-90, with evidence suggesting potential benefits for patients with advanced tumor stages and few treatment options.[46]

1.2.2.5 Ablation

Ablation techniques are considered the best treatment alternatives for HCC patients who are not eligible for surgical techniques.[36] Tumor ablation is defined as the direct application of therapies to eradicate or substantially destroy focal tumors, either using chemicals or energy-based (i.e., thermal or non-thermal) approaches.[47] These ablation approaches can include the use of ethanol, radiofrequency, microwave, freezing (cryo), laser, high-frequency ultrasound, and irreversible electroporation.[48] Therapy is applied through the use of applicators, such as electrodes in radiofrequency ablation (RFA), antennas in microwave ablation, or fibres in laser ablation, to provide a focal region of therapy. These procedures can be used in a palliative setting for pain management, but also has the potential for curative intent on early-stage or small tumors. For example, RFA is considered a first-line

treatment option for HCC in the liver[49] and has been shown to have similar survival as a resection for solitary lesions less than five centimeters with well-preserved liver function.[50] Since these procedures have small incision sites, these minimally or less-invasive procedures have been observed to result in procedures with a rate of complications of less than 2%.[51] In addition, these procedures are often associated with lower costs as treatment times, hospital stays, and the need for blood transfusions are reduced.[34]

The most common treatment approaches for tumor ablation in the abdomen are either RFA or microwave ablation (MWA). These thermal methods both focus on the production of heat for tissue ablation but have different mechanisms of heat production that require different equipment and application techniques. RFA techniques use applicators that are needle-like and typically use a single monopolar active applicator, occasionally separating at the tip into multiple tines for a larger ablation volume, with a 375-500 kHz alternating current dissipating at one or more grounding pads to produce resistive heat.[47,52] MWA uses needle-like applicators without the need for grounding pads and generates microwaves with a frequency between 915 MHz and 2.45 GHz to produce frictional heat from oscillating water molecules.[52] Both techniques allow for multiple applicators to be placed, depending on the size and geometry of the lesion being targeted for therapy, but MWA can also allow for simultaneous activation of applicators to exploit electromagnetic field overlap. Aside from the current size of the MWA applicators, this method has the potential to offer improved performance over RFA.[52] Although both methods have numerous benefits, one limitation is the proximity of lesions to large vessels as sufficient heating cannot be achieved due to the heat sink effect, which requires other forms of therapy. The placement accuracy of the therapeutic applicators is also critical for procedure success due to the percutaneous nature of these procedures and the focal volume of therapy. Unfortunately, current approaches have been observed to show a range of local cancer recurrence rates between 6-39% of patients treated for HCC or colorectal liver metastases.[4,41,50,53]

1.3 3D Image-guided interventions

Medical imaging can have an impact on nearly every aspect of interventions to achieve successful diagnostic or therapeutic outcomes. Classification for the use of medical images

throughout a procedure is most often separated based on five separate categories: planning, targeting, monitoring, modification, and assessment.[54] With the wide use of digital images, recent advancements have focused on merging or fusing 3D images in different combinations from these categories, alongside image processing for clinical workflow improvements, for improving patient side-effects and outcomes in various image-guided interventions related to prostate and liver cancer.

1.3.1 MR-TRUS fusion biopsy

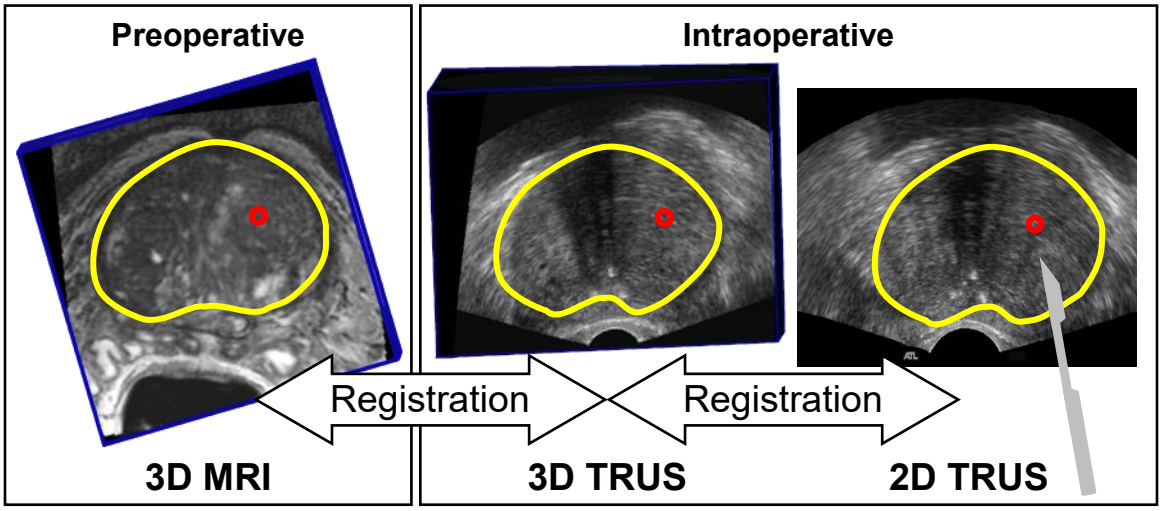

Figure 1.3 Image-guidance pipeline for MR-TRUS fusion-guided prostate biopsy. The prostate (yellow) and regions suspicious of cancer (red) identified in MRI can be targeted using real-time 2D US guidance for biopsy sampling after two image registration steps.

Concerns of prostate cancer over-diagnosis with over-treatment and missed diagnoses using conventional biopsy techniques have led to the development of a targeted magnetic resonance (MR)-transrectal ultrasound (TRUS) fusion biopsy approach.[55] The conventional technique for definitive diagnosis of prostate cancer is a template biopsy method that typically samples six to twelve tissue regions using biopsy cores guided by 2D US, which are processed and examined histologically for prostate cancer.[56] In contrast, fusion biopsy uses preoperative multi-parametric MR images, including T1-weighted, T2-weighted, diffusion-weighted, and dynamic contrast-enhanced imaging,[57] fused with intraoperative US images to perform sampling of suspicious cancer regions determined using both image modalities. This forms an imaging pipeline where the preoperative MR

image is registered to an intraoperative 3D TRUS image, followed by a subsequent registration between the 3D TRUS image and live 2D TRUS images.[58] Although MR-guided systems without TRUS have been developed,[59] this combination of imaging modalities allows for an outpatient procedure without costly interventional suites. The combination of US with multiple MR imaging sequences enables the physician to perform targeted biopsies based on the superior soft-tissue contrast and functional information from MR images, while still using real-time and lower cost image guidance provided from US imaging.

One of the main factors contributing to the success of an MR-TRUS guided procedure is the detection of clinically significant prostate cancer. Clinically significant prostate cancer has been defined[60] as a tumor with a volume greater than 0.5 cm^3, which is comparable to a sphere with a radius of 5 mm. When using an MR-TRUS fusion approach, evidence has been shown that clinically significant prostate cancer is sampled more frequently and with fewer biopsy cores, leading to less detection of clinically insignificant cancer.[61] Results from the Prostate MR Imaging Study (PROMIS) showed that primary biopsy can also be avoided in approximately 27% of patients and MR images can also be used to direct TRUS biopsy to detect 18% more cases with clinically significant prostate cancer,[62] potentially reducing the misdiagnosis and overtreatment of prostate cancer.

1.3.2 3D US-guided brachytherapy

Brachytherapy approaches rely on the accurate guidance of needles to place radiation sources at planned locations to achieve sufficient therapy while sparing healthy organs at risk. Prostate cancer applications typically use 2D US as the standard of care for guiding approximately 10-20 needles to planned locations as it is portable, inexpensive, real-time, and does not use ionizing radiation.[63] Based on an accurate volume and shape of the prostate relative to the inserted needles, radiation plans can be computed and optimized to produce 3D patient-specific therapies.[64] Methods have been investigated to incorporate CT[65] or MR[66] images for planning, but the widespread use of US has many practical advantages as the entire procedure can be completed without moving the patient, which saves time, resources, and clinical costs.[67] However, 2D US images rely on the subjectivity of the physician to mentally form an impression of the 3D anatomical space, which can

introduce variability when determining needle positions relative to their intended targets for therapy and away from organs at risk, such as the rectum and urethra.[68] These images also do not inherently allow for the required accurate 3D prostate volume and shape for gland dose calculation, requiring interpolation and approximations based on limited fields-of-view.

Generating 3D US images for prostate brachytherapy can provide a solution for the limitations of conventional 2D US techniques and can be acquired using different geometries depending on the transducers available and structures of interest. End-fire transrectal ultrasound (TRUS) probes are often used for biopsy procedures as they can allow for improved sampling in the sagittal and transverse sections of the prostate,[69] but are often difficult to use during brachytherapy when inserting multiple needles at a time and correlating the US images relative to the guidance template. Side-fire TRUS probes can take advantage of sagittal transducer elements, which generate submillimeter spatial resolution in the needle insertion directions that can lead to <1 mm tip localization uncertainty during prostate brachytherapy.[70] Side-fire probes can also be combined with transverse US elements to form biplane probes for accurately identifying the central cross-section of the needles for determining 3D needle trajectories and offer simple pull-back 3D US image reconstruction with the use of commercial steppers (Civco Medical Instruments, Iowa, United States).

Motorized 3D US systems have been developed for prostate brachytherapy applications to provide consistent and repeatable image reconstructions while enabling approaches to return the US probe to implants at later time points.[71,72] 3D US systems have also been developed for brachytherapy applications treating breast[73] and gynecologic cancers,[74] which similarly requires the precise placement and identification of needles for sufficient therapy and avoiding organs-at-risk. Regardless of the anatomical location being treated with 3D US-guided brachytherapy or the chosen dose-rate approach, localizing needle tips and trajectories accurately is necessary for correct computation of dose plans.

1.3.3 Image-guided ablation

The use of CT, MR, and 2D US imaging for the five main categories of image-guided interventions have been investigated for increasing the feasibility and scope of focal ablation procedures in the liver. CT images provide a versatile utility for ablation procedures as they are used preoperatively to identify the presence of cancer (typically using intravenous contrast material),[54] intraoperatively for intermittent images with partial access during applicator insertions and verification of placement,[75] and postoperatively for follow-up.[76] CT fluoroscopy can be used for near real-time intraoperative imaging, but radiation exposure to the patient and personnel is a major consideration.[77]

MR images have also been used as they offer advantages such as improved soft-tissue contrast, nonionizing radiation, and the potential for real-time treatment monitoring,[78] but intraoperative access to the patient is often limited and the need for real-time images typically reduces the achievable image resolution and contrast,[79] all with higher associated costs. The use of 2D US for real-time image feedback is beneficial when placing therapeutic ablation applicators intraoperatively in the treatment of liver cancer and also does not use ionizing radiation. However, similar to issues experienced in biopsy and brachytherapy, these images can increase the burden on the physician as they need to mentally reconstruct the complex anatomy, which can introduce subjective image guidance variability. These 2D US-guided insertions also require extensive training to interpret the US images, perform image and applicator alignment for real-time tracking of the applicator insertion, and verification of the final placement to assess expected therapeutic margins. CT, MR, and 2D US images all have aspects that make them advantageous for image-guided ablation procedures, but variability in therapy applicator image-guidance still remains, which leads to the insufficient placement of therapeutic applicators, contributing to the local cancer recurrence rates as discussed in Sec. 1.2.2.5.

1.4 Image processing in image-guided interventions

1.4.1 Image-based registration

Image registration is an image processing technique that spatially aligns two or more images of the same scene taken from different times, viewpoints, and/or image modalities.[80] Use of the image signal intensity information to perform spatial alignment refers to image-based registration techniques, which can be performed in multiple ways and is dependent on the choices made on four main components: image similarity metric, optimization approach, transformation degrees-of-freedom (DoF), and interpolator.[81] In general, the image similarity metric provides the quantitative measure for comparing different transformations sampled using an optimization approach, with voxel interpolation to resample the image in the new coordinate system. Transformations can be performed simply using image translations and rotations, as in a rigid approach, up to complex operations like pixel-wise deformations, as in a non-rigid deformable approach.[82] These choices not only influence the accuracy of an image-based registration approach but also the computer computation time required to perform the operations, which can be an important factor for practical implementation during procedures with intraoperative image-guidance.

1.4.2 Image-based segmentation

Image segmentation, labeling, or contouring refers to the process of classifying image pixels or identifying boundaries corresponding to image regions that share relevant characteristics, like an organ or an interventional tool.[83] This can be done manually by drawing regions in the image or identifying points that are later joined using defined assumptions, which is often the gold-standard method for an image segmentation task. However, due to the user-required effort, this is often a time-consuming process that can be a limiting factor for clinical workflow, as is the case for some intraoperative interventions like MR-TRUS fusion biopsy. Since this limitation can occasionally prevent the clinical adoption of image-guided interventions, the frequent investigation into semi-automated and fully automated methods are performed to ease the burden on the user.[84]

Artificial intelligence is a broad umbrella term that is defined as any device that perceives its environment and takes actions that maximize its chance of success at some goal.[85] Recent efforts into fully automated segmentation methods have focused on data-driven approaches, such as convolutional neural networks (CNNs), which reduce the amount of user selection when determining relevant image features for discriminating image regions, referred to as hand-crafted features in traditional machine learning.[86] Data-driven approaches are performed by supplying an algorithm with previously acquired data and allowing optimization methods to determine the relevant image characteristics through training of model parameters. This approach is often referred to as deep learning, which can be either performed using a supervised approach, where images with previously identified regions are provided for training, or an unsupervised approach, where only the images are given and the algorithm tries to automatically determine inferences without training labels. The development of graphics processing units (GPUs) has made deep learning approaches more feasible as they allow for highly parallel and simultaneous computational processing, unlike more traditional central processing units.[87] While supervised learning requires more effort to produce a large enough dataset with required annotations, typically performed manually, unsupervised learning is more challenging and often requires larger datasets to determine reliable inferences. However, providing annotations for supervised deep learning tasks is often performed manually, which can incorporate errors and biases into the trained deep learning network.[88]

1.5 Challenges in image-guided interventions

1.5.1 Previous work and unmet needs

1.5.1.1 Motion compensation during MR-TRUS fusion biopsy

Performing image-based registration during MR-TRUS guided biopsy has been investigated previously to correct for intraoperative patient and prostate motion for accurate needle delivery. Accurate needle sampling during fusion biopsy is typically achieved when errors from four main sources throughout the workflow are minimal, namely (1) the mechanical guidance system,[55] (2) MR-3D TRUS multi-modal registration,[89] (3) 3D-3D TRUS preprocedural initialization and intraoperative

correction,[90] and (4) 2D-3D TRUS motion compensation.[58] In the last form of correction, real-time image guidance is performed using live 2D TRUS images, typically on a US system with an image refresh rate of approximately 15 frames-per-second, providing the information needed for an image-based registration.

Since the patient is awake and not constrained or intubated during the MR-TRUS fusion biopsy, prostate motion arises due to sources including the respiratory cycle, the cardiac cycle, and general patient motion from discomfort and response to audible feedback from the spring-driven biopsy gun. TRUS transducer pressure caused by the physician can also change throughout the image-guided procedure, potentially leading to prostate deformations. These sources of motion can cause target misalignment,[90] which increases needle targeting errors and the chance of missing cancer suspicious regions based on the registered MR image. To accurately sample a target, recent work has shown that a needle delivery system, including hardware and image-guidance software, requires an overall delivery error of 1.6 mm to sample a tumor of 1 cm^3 with 95% probability.[91]

2D-3D TRUS registration has been performed with promising results using a normalized cross-correlation (NCC) similarity metric and a Powell optimization to determine rigid registration corrections.[58] The choice to use an NCC similarity metric is beneficial for single modality registration problems as it does not rely on the computation of derivatives, which can be time-intensive and often unknown, while also inherently being suitable for computational parallelization on simultaneous threads provided by GPU hardware. These advantages allow for faster processing and lower overall computation times, with the potential to be performed throughout the course of a fusion biopsy. However, computation times must be less than or equal to the displayed images to provide a seamless appearance without lag, which is often necessary for usability. In addition to physician usability, a continuous and automatic approach has the potential to compound errors throughout the procedure based on previous misalignments and has not been investigated.

1.5.1.2 Prostate segmentation in 3D TRUS

3D image-guided procedures in the prostate, such as MR-TRUS fusion biopsy and brachytherapy, rely on the identification of the pixels and boundary of the prostate gland

in 3D TRUS images for performing necessary workflow tasks like accurate needle guidance, gland volume computation, and dose calculations. Conventional workflows typically rely on the gold standard manual identification of the prostate in these images, but this process is time-consuming and can be variable due to physician subjectivity, which can increase the risk to patients during procedures that use anesthesia.[92] Therefore, the investigation into automatic approaches for prostate segmentation in 3D TRUS images potentially provides an effective solution for providing a fast and objective method to improve clinical workflow during 3D US-guided prostate procedures.

3D TRUS prostate segmentation that is partial or fully automatic has been previously investigated and has been shown to be feasible in numerous publications.[93–96] Unfortunately, 3D TRUS prostate segmentation still remains a clinically unmet need as investigated methods have lacked clinical translation due to computation complexity and time. Most recently, the data-driven approach of CNNs have been investigated to address these issues,[97,98] but minimal evidence of robustness to variable clinical datasets has been shown as these methods have been applied to specific and limited dataset sizes. 3D TRUS images previously investigated are typically from a single US machine and one acquisition geometry with matched voxel dimensions and sizes, which can limit understanding of performance, especially when pursuing cross-validation approaches. Additionally, comparison between previous publications can be challenging when not assessed on the same dataset and when reported evaluation metrics are not consistent.

1.5.1.3 Image-guidance during focal liver tumor therapies

Focal liver tumor therapies rely on the accurate guidance of ablation applicators to provide sufficient cancer therapy. Procedures that incorporate 3D information, such as CT imaging,[99] MR imaging,[78] and electromagnetic tool tracking,[100] have been shown to improve targeting accuracy that leads to higher clinical success rates on first ablation attempts and fewer sessions overall when compared to conventional techniques.[101,102] However, these methods can be limited in widespread adoption as factors like increased procedure times, patient radiation dose, sophisticated and costly interventional suites, and environmental limitations can make these approaches less feasible. Therefore, a clinical

need exists for a cost-effective intraoperative approach that can help physicians improve the image guidance to lesions for sufficient cancer therapy without local recurrence.

3D US is an alternative method for image guidance that can provide real-time intraoperative imaging that is portable and able to provide multiplanar images for visualizing complex anatomy and focal therapy ablation applicators.[103,104] Similar to a prostate fusion biopsy or brachytherapy workflow, a mechanical 3D US system has been previously developed that has the potential to provide a lower-cost guidance system for accurately targeting lesions based on targets derived in 3D US or other image modalities if registered.[105] While this system provided sufficient proof-of-concept information on clinical feasibility and validation of needle positions within 3D US images, clinical usability was limited due to factors like manual locking components, scanner bulkiness, and a lack of tracking information for guidance, and was never investigated for performing active navigation to prospective targets.

1.5.1.4 Segmentation of therapy applicators in 3D US liver images

3D US imaging and systems like the one described in Sec. 1.5.1.3 have the potential to improve focal liver tumor therapies by increasing visualization of anatomy, reducing the mental burden and complexity for physicians, and enabling accurate localization of therapy needle-like applicators. Although 3D US has the potential to provide benefits to these procedures, increasing the visual information presented to the physician could add time to the procedure and visibility of the needle applicators can change depending on factors such as insertion angle, depth, applicator diameter, and choice of US transducer.[106] Providing automation to applicator identification based on image information may provide a low-cost solution to reduce the time required for verifying applicator positions, especially during multi-applicator insertions, increasing the feasibility of incorporating 3D US into focal liver tumor ablation therapies.

Existing methods for image-based 3D US applicator segmentation have primarily focused on other needle applications for the prostate,[107] breast,[108] heart,[109] and anesthetic administration,[110] where factors affecting needle visibility are drastically different. Deep applicator insertions up to 30 cm and steep insertion angles relative to the US transducer

result in challenging images for determining tip and trajectory information necessary for assessing the expected therapeutic volumes in focal liver ablation therapies. A clinical dataset on liver patients has also not been investigated and could present unexpected issues relative to current work on other applications and benchtop experiments.

1.5.1.5 Segmentation of tools during 2D US interventions

Identifying and localizing needle-like tools intraoperatively is a common need in image-guided interventions that conventionally use 2D US imaging, such as biopsy, brachytherapy, and ablation, for guiding these tools to perform accurate diagnoses and therapies. Although technology like 3D US imaging has the potential to improve tool localization and verification, as described in Sec. 1.5.1.4, 2D US is still the clinical standard at most institutions for image-guided interventions. Thus, clinical needs for improving guidance still exist for providing optimal therapy while minimizing risks to healthy tissue and to avoid adverse events like local cancer recurrence.[111] By using technology like image-based segmentation for automatic tool segmentation, a low-cost solution with the potential for widespread accessibility could be provided in these situations without the need for additional equipment, signal processing, and operating room set-up. Once tools are accurately identified, additional information can also be displayed, such as providing ablation volumes relative to the tip location in focal liver ablation therapies to predict therapeutic margins during applicator insertion, which could potentially improve clinical workflow and reduce the need for repeated adjustments and reinsertions.

Recent efforts focusing on automatic image-based tool segmentation in 2D US images have investigated the use of data-driven approaches, like CNNs, to provide robust methods with fast computation times for image-guided interventions.[112,113] Using annotated datasets for training deep learning networks, applications in procedures with steep needles[112] and kidney biopsy[113] have shown promising results for using CNN approaches. Although tools in many interventional procedures have similar needle-like appearances, most approaches for image-based tool segmentation in 2D US images are application-specific and lack evidence for generalizability, such as evaluation on other anatomical applications, US systems and acquisition settings, and variable tool visibility.

1.5.2 Hypothesis

The central hypothesis of this thesis is that the incorporation of 3D US and advanced image processing techniques will increase the accuracy and reduce the user variability of image-guided interventions in the management of prostate and liver cancer.

1.5.3 Objectives

The objectives of this thesis are to:

1. Develop an automatic motion correction algorithm approaching the frame rate of an US system to be used in fusion-based 3D TRUS prostate biopsy systems.

2. Develop a pre-insertion automatic deep learning-based approach to segment the prostate for biopsy and brachytherapy applications in 3D TRUS images.

3. Develop a geometrically variable 3D US mechanically assisted system to guide and verify the placement of therapy needle applicators in focal liver tumor therapy.

4. Develop a semi-automatic approach for identifying therapy needle applicators in 3D US images from focal liver tumor therapies.

5. Develop a general and automatic deep learning-based approach for identifying needle-like tools in 2D US images from various image-guided interventional procedures.

1.6 Thesis outline

The overarching goal of this thesis is to address the specific thesis objectives in five manuscripts (Chapters 2 to 6).

Chapter 2: Real-time registration of 3D to 2D ultrasound images for image-guided prostate biopsy

Patient motion can be continuous or intermittent throughout MR-TRUS prostate biopsy procedures and causes misalignment of the MR-derived targets during targeted biopsy workflows. This chapter describes our work to develop a real-time and continuous motion

compensation algorithm for automatic registration of 2D and 3D TRUS images. Retrospective patient images were used for adapting, developing, and optimizing the real-time capabilities of a previously published approach[58] through the use of a GPU, image downsampling, 2D area-of-interest cropping, and optimization search space direction initialization. The optimized algorithm was implemented on a 3D TRUS-guided system and evaluated on a tissue-mimicking prostate phantom with embedded spheres. This phantom was mounted on a translation and rotation stage to compare the real-time registration method against a single user-initiated correction for known displacements.

The optimized continuous registration method was shown to significantly reduce registration times compared to a user-initiated method and resulted in sub-millimeter and sub-degree registration errors for both approaches. By continually registering images, optimization search spaces are often small between subsequent image frames and led to reduced iterations for convergence. This work was novel as it developed the first approach to achieve 2D to 3D TRUS image registrations that resulted in computation times approximately at the frame rate of an US system. This provided an approach to improve clinical workflow during image-guided prostate biopsy procedures.

Chapter 3: Automatic prostate segmentation using deep-learning on clinically diverse 3D transrectal ultrasound images

3D TRUS imaging has been shown to benefit needle-based procedures for diagnosing and treating prostate cancer (i.e., biopsy and brachytherapy); however, these images require the physician to manually or semi-automatically segment the prostate, which is time-consuming and difficult, often occurring while the patient is under sedation or anesthesia. This novelty and literature contributions of this chapter focuses on the development of a new deep learning-based approach to automatically segment the prostate in a clinically diverse 3D TRUS dataset. Modifications were made to a previously published deep learning U-Net architecture[114] and 3D TRUS images were acquired from different procedures (biopsy and brachytherapy), acquisition geometries (end-fire and side-fire), and ultrasound systems. We developed a 3D segmentation method involving deep-learning predictions on 2D radial slices, followed by reconstruction into a 3D surface, to exploit the utility of the 3D TRUS dataset and take advantage of the approximately spherical nature

of the prostate. This method was compared to fully 3D approaches and evaluations were performed on an extensive variety of metrics to provide a comparison to other published methods and a baseline for future comparisons.

The automatic prostate segmentation method performed with significant improvement over fully 3D approaches and other recently published methods. The automatic prostate segmentation method on 3D TRUS images was shown to be fast, accurate, and generalizable, providing promising results for clinical translation and application to other 3D TRUS geometries (i.e., pull-back 3D TRUS images). This method has the potential to decrease overall clinical procedure times and anesthesia risks during prostate biopsy and brachytherapy.

Chapter 4: Geometrically variable three-dimensional ultrasound for mechanically assisted image-guided therapy of focal liver cancer tumors

Image-guided focal liver ablation procedures provide numerous benefits compared to other liver cancer therapeutic techniques, such as reduced recovery times and complication rates; however, insufficient targeting and coverage of ablation volumes have been shown to limit these procedures and the scope of eligible patients. This chapter is on the development and evaluation of a novel geometrically variable 3D ultrasound scanner, mechanically assisted system, and 3D-printed therapy applicator guide to provide methods for imaging and guiding focal ablations to the diverse anatomical locations and presentations of liver tumors. The system was evaluated for image reconstruction with a grid phantom, tracking system accuracy when compared to optical tracking, image-guidance using three different navigation approaches in end-to-end mock ablation phantom procedures, and clinical feasibility through healthy volunteer imaging.

The system resulted in ≤3% mean geometric reconstruction errors, <7% volumetric reconstruction errors, and <2 mm mean tracking system errors. A combined navigation approach that used the scanner motors and tracking system for in-plane image corrections resulted in the best performing mean needle targeting errors with <4.3 mm based on external cone-beam CT imaging. Healthy volunteer imaging resulting in good qualitative images and evidence for sufficient clinical feasibility. Our system provides approaches for

improving liver tumor therapy targeting and has the potential for application to other abdominal interventions and widespread accessibility to developing countries.

Chapter 5: Three-dimensional therapy needle applicator segmentation for ultrasound-guided focal liver ablation

The 3D US system described in Chapter 4 can benefit from the addition of software tools to improve clinical workflow and improve localization of applicators in focal liver tumor ablation therapies. Local cancer recurrence remains high in these procedures and current limitations still exist for verifying applicator positions in 3D US liver images. This arises since localization accuracy is impacted by factors including the applicator insertion angle, depth, and size, in addition to the choice of the transducer and local anatomic acoustic reflections. This chapter focuses on the development and evaluation of a new 3D US semi-automated therapy applicator segmentation algorithm for *in-vivo* 3D US clinically imaged applicators used in focal liver tumor ablations. While general needle-like segmentation algorithms for 3D US have been discussed in the literature and tested on tissue mimicking models, such as agar, chicken breast, bovine, and porcine tissues, this work is novel as it provides evaluation on in-vivo clinically acquired 3D US images, which has not been reported for the unique imaging characteristics of needle applicators used in percutaneous liver tumor ablations.

The segmentation method aims to provide an intraoperative tool using a single point to reduce the complexity of the segmentation problem. Optimization was performed on homogeneous tissue-mimicking phantoms prior to a user study on clinical 3D US images. Trajectory, axis localization, and tip localization errors were evaluated and suggested the approach could be useful in a clinical environment when paired with a 3D US system.

Chapter 6: A deep learning method for general needle and applicator segmentation in two-dimensional ultrasound images from multiple applications and anatomical regions

Many image-guided interventions rely on the temporal resolution of 2D US to perform optimal needle-like tool insertions for achieving sufficient diagnoses and treatments of cancer. Accurate identification of tools in these images can be challenging with previously investigated software methods developing application-specific approaches for automatic

tool segmentation. This chapter is on the development of a new general deep learning-based approach with post-processing to automatically segment tools in 2D US images for a wide range of clinical procedures. This can be paired with other interventional tools, such as those described in Chapters 4 and 5, to further improve the clinical workflow and targeting of needle-like tools. Unlike any other approach, this method was evaluated on a clinically diverse dataset from prostate and gynecologic brachytherapy, liver ablation, and kidney biopsy and ablation procedures, where tool appearance drastically varies.

Segmentation performed the best when using a random sample consensus post-processing technique, but at the cost of increased segmentation time. Image-guided interventions with tools parallel to the US probe surface (i.e., prostate and gynecologic regions) performed the best due to tool contrast and decreased performance was observed as tool angulation increased (i.e., in liver and kidney regions). Our method was able to perform predictions of these tools in near real-time and provides the potential for improving image guidance during a broad range of cancer interventions.

Chapter 7: Conclusions and future work

This chapter focuses on the overall conclusions of the previous chapters and will discuss future work that could potentially address remaining unmet needs from this thesis.

1.7 References

1. Cleary K, Peters TM. Image-Guided Interventions: Technology Review and Clinical Applications. *Annu Rev Biomed Eng*. 2010;12(1):119-142. doi:10.1146/annurev-bioeng-070909-105249

2. Liao R, Zhang L, Sun Y, Miao S, Chefd'Hotel C. A Review of Recent Advances in Registration Techniques Applied to Minimally Invasive Therapy. *IEEE Trans Multimed*. 2013;15(5):983-1000. doi:10.1109/TMM.2013.2244869

3. Rabbani F, Stroumbakis N, Kava BR, Cookson MS, Fair WR. Incidence and Clinical Significance of False-Negative Sextant Prostate Biopsies. *J Urol*. 1998;159(4):1247-1250. doi:10.1016/s0022-5347(01)63574-2.

4. Tanis E, Nordlinger B, Mauer M, et al. Local recurrence rates after radiofrequency ablation or resection of colorectal liver metastases. Analysis of the European Organisation for Research and Treatment of Cancer #40004 and #40983. *Eur J Cancer*. 2014;50(5):912-919. doi:10.1016/j.ejca.2013.12.008

5. Canadian Cancer Statistics Advisory Committee. *Canadian Cancer Statistics 2019*. Toronto, ON: Canadian Cancer Society; 2019. cancer.ca/Canadian-Cancer-Statistics-2019-EN . Accessed March 18, 2020.

6. Gleason DF. Classification of prostatic carcinomas. *Cancer Chemother Reports*. 1966;50(3):125-128.

7. Drake RL, Vogl AW, Mitchell AW. *Gray's Anatomy for Students*. 3rd ed. Churchhill Livingstone; 2015.

8. Jønler M, Nielsen OS, Wolf H. Urinary symptoms, potency, and quality of life in patients with localized prostate cancer followed up with deferred treatment. *Urology*. 1998;52(6):1055-1062. doi:10.1016/S0090-4295(98)00449-X

9. Miller KD, Nogueira L, Mariotto AB, et al. Cancer treatment and survivorship statistics, 2019. *CA Cancer J Clin*. 2019;69(5):363-385. doi:10.3322/caac.21565

10. Stewart BW, Wild C. *World Cancer Report 2014*. Lyon; 2014.

11. Chuang S-C, Vecchia C La, Boffetta P. Liver cancer: Descriptive epidemiology and risk factors other than HBV and HCV infection. *Cancer Lett*. 2009;286(1):9-14. doi:10.1016/j.canlet.2008.10.040

12. Canadian Cancer Society's Advisory Committee on Cancer Statistics. *Canadian Cancer Statistics 2013*. Toronto, ON: Canadian Cancer Society; 2013. http://www.cancer.ca/~/media/cancer.ca/CW/cancer information/ cancer 101/Canadian cancer statistics/canadian-cancer-statistics-2013-EN. pdf?la=en. Accessed March 18, 2020.

13. El–Serag HB, Rudolph KL. Hepatocellular Carcinoma: Epidemiology and Molecular Carcinogenesis. *Gastroenterology*. 2007;132(7):2557-2576. doi:10.1053/j.gastro.2007.04.061

14. Hesseltine CW, Shotwell OL, Ellis JJ, Stubblefield RD. Aflatoxin formation by Aspergillus flavus. *Bacteriol Rev*. 1966;30(4):795-805. http://www.ncbi.nlm.nih.gov/pubmed/5342522.

15. Chang M-H, You S-L, Chen C-J, et al. Decreased Incidence of Hepatocellular Carcinoma in Hepatitis B Vaccinees: A 20-Year Follow-up Study. *JNCI J Natl Cancer Inst*. 2009;101(19):1348-1355. doi:10.1093/jnci/djp288

16. Lu-Yao GL, Albertsen PC, Moore DF, et al. Outcomes of localized prostate cancer following conservative management. *JAMA*. 2009;302(11):1202-1209. doi:10.1001/jama.2009.1348

17. Bell N, Gorber SC, Shane A, et al. Recommendations on screening for prostate cancer with the prostate-specific antigen test. *Can Med Assoc J*. 2014;186(16):1225-1234. doi:10.1503/cmaj.140703

18. Kasivisvanathan V, Emberton M, Ahmed HU. Focal Therapy for Prostate Cancer: Rationale and Treatment Opportunities. *Clin Oncol*. 2013;25(8):461-473. doi:10.1016/j.clon.2013.05.002

19. Cooperberg MR, Carroll PR, Klotz L. Active surveillance for prostate cancer: progress and promise. *J Clin Oncol*. 2011;29(27):3669-3676. doi:10.1200/JCO.2011.34.9738

20. Mahal BA, Butler S, Franco I, et al. Use of Active Surveillance or Watchful Waiting for Low-Risk Prostate Cancer and Management Trends Across Risk Groups in the United States, 2010-2015. *JAMA*. 2019;321(7):704. doi:10.1001/jama.2018.19941

21. Peschel RE, Colberg JW. Surgery, brachytherapy, and external-beam radiotherapy for early prostate cancer. *Lancet Oncol*. 2003;4(4):233-241. doi:10.1016/S1470-2045(03)01035-0

22. Freedland SJ, Humphreys EB, Mangold L a, et al. Risk of Prostate Cancer–Specific Mortality Following Biochemical Recurrence After Radical Prostatectomy. *JAMA*. 2005;294(4):433. doi:10.1001/jama.294.4.433

23. Crawford ED, Heidenreich A, Lawrentschuk N, et al. Androgen-targeted therapy in men with prostate cancer: evolving practice and future considerations. *Prostate Cancer Prostatic Dis*. 2019;22(1):24-38. doi:10.1038/s41391-018-0079-0

24. Saad F, Hotte SJ. Guidelines for the management of castrate-resistant prostate cancer. *Can Urol Assoc J*. 2010;4(6):380-384. doi:10.5489/cuaj.10167

25. Gilligan T, Kantoff PW. Chemotherapy for prostate cancer. *Urology*. 2002;60(3):94-100. doi:10.1016/S0090-4295(02)01583-2

26. Hankinson SJ, Fam M, Patel NN. A review for clinicians: Prostate cancer and the antineoplastic properties of metformin. *Urol Oncol Semin Orig Investig*. 2017;35(1):21-29. doi:10.1016/j.urolonc.2016.10.009

27. Pollack A, Walker G, Horwitz EM, et al. Randomized Trial of Hypofractionated External-Beam Radiotherapy for Prostate Cancer. *J Clin Oncol*. 2013;31(31):3860-3868. doi:10.1200/JCO.2013.51.1972

28. Donovan JL, Hamdy FC, Lane JA, et al. Patient-Reported Outcomes after Monitoring, Surgery, or Radiotherapy for Prostate Cancer. *N Engl J Med*. 2016;375(15):1425-1437. doi:10.1056/NEJMoa1606221

29. Wallis CJD, Saskin R, Choo R, et al. Surgery Versus Radiotherapy for Clinically-localized Prostate Cancer: A Systematic Review and Meta-analysis. *Eur Urol*. 2016;70(1):21-30. doi:10.1016/j.eururo.2015.11.010

30. Kamran SC, D'Amico A V. Radiation Therapy for Prostate Cancer. *Hematol Oncol Clin North Am*. 2020;34(1):45-69. doi:10.1016/j.hoc.2019.08.017

31. Kee DLC, Gal J, Falk AT, et al. Brachytherapy versus external beam radiotherapy boost for prostate cancer: Systematic review with meta-analysis of randomized trials. *Cancer Treat Rev*. 2018;70(Oct):265-271. doi:10.1016/j.ctrv.2018.10.004

32. Martin T, Baltas D, Kurek R, et al. 3-D Conformal HDR Brachytherapy as Monotherapy for Localized Prostate Cancer. *Strahlentherapie und Onkol*. 2004;180(4):225-232. doi:10.1007/s00066-004-1215-4

33. Thumanu K, Sangrajrang S, Khuhaprema T, et al. Diagnosis of liver cancer from blood sera using FTIR microspectroscopy: a preliminary study. *J Biophotonics*. 2014;7(3-4):222-231. doi:10.1002/jbio.201300183

34. Livraghi T, Meloni F, Di Stasi M, et al. Sustained complete response and complications rates after radiofrequency ablation of very early hepatocellular carcinoma in cirrhosis: Is resection still the treatment of choice? *Hepatology*. 2007;47(1):82-89. doi:10.1002/hep.21933

35. Bruix J, Sherman M. Management of hepatocellular carcinoma. *Hepatology*. 2005;42(5):1208-1236. doi:10.1002/hep.20933

36. El-Serag HB, Marrero JA, Rudolph L, Reddy KR. Diagnosis and Treatment of Hepatocellular Carcinoma. *Gastroenterology*. 2008;134(6):1752-1763. doi:10.1053/j.gastro.2008.02.090

37. El-Serag HB. Hepatocellular Carcinoma. *N Engl J Med*. 2011;365(12):1118-1127. doi:10.1056/NEJMra1001683

38. Schoenberg MB, Bucher JN, Vater A, et al. Resection or Transplant in Early Hepatocellular Carcinoma: A Systematic Review and Meta-analysis. *Dtsch Aerzteblatt Online*. 2017;114(31-32):519-526. doi:10.3238/arztebl.2017.0519

39. Estfan B, Byrne M, Kim R. Sorafenib in Advanced Hepatocellular Carcinoma. *Am J Clin Oncol*. 2013;36(4):319-324. doi:10.1097/COC.0b013e3182468039

40. Cheng A-L, Guan Z, Chen Z, et al. Efficacy and safety of sorafenib in patients with advanced hepatocellular carcinoma according to baseline status: Subset analyses of the phase III Sorafenib Asia–Pacific trial. *Eur J Cancer*. 2012;48(10):1452-1465. doi:10.1016/j.ejca.2011.12.006

41. Dawson LA. Overview: Where Does Radiation Therapy Fit in the Spectrum of Liver Cancer Local-Regional Therapies? *Semin Radiat Oncol*. 2011;21(4):241-246. doi:10.1016/j.semradonc.2011.05.009

42. Brock KK. Imaging and Image-Guided Radiation Therapy in Liver Cancer. *Semin Radiat Oncol*. 2011;21(4):247-255. doi:10.1016/j.semradonc.2011.05.001

43. Llovet JM, Real MI, Montaña X, et al. Arterial embolisation or chemoembolisation versus symptomatic treatment in patients with unresectable hepatocellular carcinoma: a randomised controlled trial. *Lancet*. 2002;359(9319):1734-1739. doi:10.1016/S0140-6736(02)08649-X

44. Wang X, Hu Y, Ren M, Lu X, Lu G, He S. Efficacy and Safety of Radiofrequency Ablation Combined with Transcatheter Arterial Chemoembolization for Hepatocellular Carcinomas Compared with Radiofrequency Ablation Alone: A Time-to-Event Meta-Analysis. *Korean J Radiol*. 2016;17(1):93. doi:10.3348/kjr.2016.17.1.93

45. Zhong C, Guo R, Li J, et al. A randomized controlled trial of hepatectomy with adjuvant transcatheter arterial chemoembolization versus hepatectomy alone for Stage III A hepatocellular carcinoma. *J Cancer Res Clin Oncol*. 2009;135(10):1437-1445. doi:10.1007/s00432-009-0588-2

46. Sangro B, Carpanese L, Cianni R, et al. Survival after yttrium-90 resin microsphere radioembolization of hepatocellular carcinoma across Barcelona clinic liver cancer stages: A European evaluation. *Hepatology*. 2011;54(3):868-878. doi:10.1002/hep.24451

47. Ahmed M, Solbiati L, Brace CL, et al. Image-guided Tumor Ablation: Standardization of Terminology and Reporting Criteria—A 10-Year Update. *Radiology*. 2014;273(1):241-260. doi:10.1148/radiol.14132958

48. Wells SA, Hinshaw JL, Lubner MG, Ziemlewicz TJ, Brace CL, Lee FT. Liver Ablation: Best Practices. *Radiol Clin North Am*. 2015;53(5):933-971. doi:10.1016/j.rcl.2015.05.012

49. Lee DH, Lee JM, Lee JY, et al. Radiofrequency Ablation of Hepatocellular Carcinoma as First-Line Treatment: Long-term Results and Prognostic Factors in 162 Patients with Cirrhosis. *Radiology*. 2014;270(3):900-909. doi:10.1148/radiol.13130940

50. Hong SN, Lee S-Y, Choi MS, et al. Comparing the outcomes of radiofrequency ablation and surgery in patients with a single small hepatocellular carcinoma and well-preserved hepatic function. *J Clin Gastroenterol*. 2005;39(3):247-252. doi:10.1097/01.mcg.0000152746.72149.31

51. Yang W, Yan K, Goldberg SN, et al. Ten-year survival of hepatocellular carcinoma patients undergoing radiofrequency ablation as a first-line treatment. *World J Gastroenterol*. 2016;22(10):2993. doi:10.3748/wjg.v22.i10.2993

52. Brace CL. Radiofrequency and Microwave Ablation of the Liver, Lung, Kidney, and Bone: What Are the Differences? *Curr Probl Diagn Radiol*. 2009;38(3):135-143. doi:10.1067/j.cpradiol.2007.10.001

53. Siperstein AE, Berber E, Ballem N, Parikh RT. Survival After Radiofrequency Ablation of Colorectal Liver Metastases. *Ann Surg*. 2007;246(4):559-567. doi:10.1097/SLA.0b013e318155a7b6

54. Solomon SB, Silverman SG. Imaging in interventional oncology. *Radiology*. 2010;257(3):624-640. doi:10.1148/radiol.10081490

55. Bax J, Cool D, Gardi L, et al. Mechanically assisted 3D ultrasound guided prostate biopsy system. *Med Phys*. 2008;35(12):5397. doi:10.1118/1.3002415

56. Presti JC. Prostate biopsy: current status and limitations. *Rev Urol*. 2007;9(3):93-98. http://www.pubmedcentral.nih.gov/articlerender.fcgi?artid=PMC2002498.

57. Stabile A, Giganti F, Rosenkrantz AB, et al. Multiparametric MRI for prostate cancer diagnosis: current status and future directions. *Nat Rev Urol*. 2020;17(1):41-61. doi:10.1038/s41585-019-0212-4

58. De Silva T, Fenster A, Cool DW, et al. 2D-3D rigid registration to compensate for prostate motion during 3D TRUS-guided biopsy. *Med Phys*. 2013;40(2):022904. doi:10.1118/1.4773873

59. Pondman KM, Fütterer JJ, ten Haken B, et al. MR-Guided Biopsy of the Prostate: An Overview of Techniques and a Systematic Review. *Eur Urol*. 2008;54(3):517-527. doi:10.1016/j.eururo.2008.06.001

60. Ploussard G, Epstein JI, Montironi R, et al. The Contemporary Concept of Significant Versus Insignificant Prostate Cancer. *Eur Urol*. 2011;60(2):291-303. doi:10.1016/j.eururo.2011.05.006

61. Kasivisvanathan V, Rannikko AS, Borghi M, et al. MRI-Targeted or Standard

Biopsy for Prostate-Cancer Diagnosis. *N Engl J Med*. 2018;378(19):1767-1777. doi:10.1056/NEJMoa1801993

62. Ahmed HU, El-Shater Bosaily A, Brown LC, et al. Diagnostic accuracy of multi-parametric MRI and TRUS biopsy in prostate cancer (PROMIS): a paired validating confirmatory study. *Lancet*. 2017;389(10071):815-822. doi:10.1016/S0140-6736(16)32401-1

63. Banerjee S, Kataria T, Gupta D, et al. Use of ultrasound in image-guided high-dose-rate brachytherapy: enumerations and arguments. *J Contemp Brachytherapy*. 2017;2(2):146-150. doi:10.5114/jcb.2017.67456

64. Carey B. The current role of imaging for prostate brachytherapy. *Cancer Imaging*. 2007;7(1):27-33. doi:10.1102/1470-7330.2007.0003

65. Zelefsky MJ, Hollister T, Raben A, Matthews S, Wallner KE. Five-year biochemical outcome and toxicity with transperineal CT-planned permanent I-125 prostate implantation for patients with localized prostate cancer. *Int J Radiat Oncol*. 2000;47(5):1261-1266. doi:10.1016/S0360-3016(00)00550-2

66. Hanania AN, Kudchadker RJ, Bruno TL, Tang C, Anscher MS, Frank SJ. MRI-assisted radiosurgery: A quality assurance nomogram for palladium-103 and iodine-125 prostate brachytherapy. *Brachytherapy*. 2020;19(1):38-42. doi:10.1016/j.brachy.2019.10.002

67. Lauche O, Delouya G, Taussky D, et al. Single-fraction high-dose-rate brachytherapy using real-time transrectal ultrasound based planning in combination with external beam radiotherapy for prostate cancer: dosimetrics and early clinical results. *J Contemp Brachytherapy*. 2016;2(2):104-109. doi:10.5114/jcb.2016.59216

68. Crook JM, Potters L, Stock RG, Zelefsky MJ. Critical organ dosimetry in permanent seed prostate brachytherapy: Defining the organs at risk. *Brachytherapy*. 2005;4(3):186-194. doi:10.1016/j.brachy.2005.01.002

69. Paul R, Korzinek C, Necknig U, et al. Influence of transrectal ultrasound probe on prostate cancer detection in transrectal ultrasound-guided sextant biopsy of prostate. *Urology*. 2004;64(3):532-536. doi:10.1016/j.urology.2004.04.005

70. Siebert F-A, Hirt M, Niehoff P, Kovács G. Imaging of implant needles for real-time HDR-brachytherapy prostate treatment using biplane ultrasound transducers. *Med Phys*. 2009;36(8):3406-3412. doi:10.1118/1.3157107

71. Bax J, Smith D, Bartha L, et al. A compact mechatronic system for 3D ultrasound guided prostate interventions. *Med Phys*. 2011;38(2):1055-1069. doi:10.1118/1.3531540

72. Hrinivich WT, Hoover DA, Surry K, et al. Accuracy and variability of high-dose-rate prostate brachytherapy needle tip localization using live two-dimensional and

sagittally reconstructed three-dimensional ultrasound. *Brachytherapy*. 2017;16(5):1035-1043. doi:10.1016/j.brachy.2017.06.008

73. Michael J, Morton D, Batchelar D, Hilts M, Crook J, Fenster A. Development of a 3D ultrasound guidance system for permanent breast seed implantation. *Med Phys*. 2018;45(8):3481-3495. doi:10.1002/mp.12990

74. Rodgers JR, Surry K, Leung E, D'Souza D, Fenster A. Toward a 3D transrectal ultrasound system for verification of needle placement during high-dose-rate interstitial gynecologic brachytherapy. *Med Phys*. 2017;44(5):1899-1911. doi:10.1002/mp.12221

75. Leng S, Christner JA, Carlson SK, et al. Radiation Dose Levels for Interventional CT Procedures. *Am J Roentgenol*. 2011;197(1):W97-W103. doi:10.2214/AJR.10.5057

76. Sainani NI, Gervais DA, Mueller PR, Arellano RS. Imaging After Percutaneous Radiofrequency Ablation of Hepatic Tumors: Part 1, Normal Findings. *Am J Roentgenol*. 2013;200(1):184-193. doi:10.2214/AJR.12.8478

77. Nawfel RD, Judy PF, Silverman SG, Hooton S, Tuncali K, Adams DF. Patient and Personnel Exposure during CT Fluoroscopy-guided Interventional Procedures. *Radiology*. 2000;216(1):180-184. doi:10.1148/radiology.216.1.r00jl39180

78. Clasen S, Pereira PL. Magnetic resonance guidance for radiofrequency ablation of liver tumors. *J Magn Reson Imaging*. 2008;27(2):421-433. doi:10.1002/jmri.21264

79. Yutzy SR, Duerk JL. Pulse sequences and system interfaces for interventional and real-time MRI. *J Magn Reson Imaging*. 2008;27(2):267-275. doi:10.1002/jmri.21268

80. Zitová B, Flusser J. Image registration methods: a survey. *Image Vis Comput*. 2003;21(11):977-1000. doi:10.1016/S0262-8856(03)00137-9

81. Oliveira FPM, Tavares JMRS. Medical image registration: a review. *Comput Methods Biomech Biomed Engin*. 2014;17(2):73-93. doi:10.1080/10255842.2012.670855

82. Fitzpatrick JM, Hill DLG, Maurer CR. Image Registration. In: *Handbook of Medical Image Processing and Analysis, Volume 2:*. Bellingham, WA: SPIE Press; 2000:447-514.

83. Smistad E, Falch TL, Bozorgi M, Elster AC, Lindseth F. Medical image segmentation on GPUs – A comprehensive review. *Med Image Anal*. 2015;20(1):1-18. doi:10.1016/j.media.2014.10.012

84. Hesamian MH, Jia W, He X, Kennedy P. Deep Learning Techniques for Medical Image Segmentation: Achievements and Challenges. *J Digit Imaging*. 2019;32(4):582-596. doi:10.1007/s10278-019-00227-x

85. Russell SJ, Norvig P. *Artificial Intelligence: A Modern Approach*. Englewood Cliffs, New Jersey: Prentice-Hall, Inc; 2003.

86. Nanni L, Ghidoni S, Brahnam S. Handcrafted vs. non-handcrafted features for computer vision classification. *Pattern Recognit*. 2017;71:158-172. doi:10.1016/j.patcog.2017.05.025

87. Ongsulee P. Artificial intelligence, machine learning and deep learning. In: *2017 15th International Conference on ICT and Knowledge Engineering (ICT&KE)*. IEEE; 2017:1-6. doi:10.1109/ICTKE.2017.8259629

88. Aeffner F, Wilson K, Martin NT, et al. The Gold Standard Paradox in Digital Image Analysis: Manual Versus Automated Scoring as Ground Truth. *Arch Pathol Lab Med*. 2017;141(9):1267-1275. doi:10.5858/arpa.2016-0386-RA

89. Sun Y, Yuan J, Qiu W, Rajchl M, Romagnoli C, Fenster A. Three-Dimensional Nonrigid MR-TRUS Registration Using Dual Optimization. *IEEE Trans Med Imaging*. 2015;34(5):1085-1095. doi:10.1109/TMI.2014.2375207

90. Karnik V V., Fenster A, Bax J, Romagnoli C, Ward AD. Evaluation of intersession 3D-TRUS to 3D-TRUS image registration for repeat prostate biopsies. *Med Phys*. 2011;38(4):1832. doi:10.1118/1.3560883

91. Martin PR, Cool DW, Romagnoli C, Fenster A, Ward AD. Magnetic resonance imaging-targeted, 3D transrectal ultrasound-guided fusion biopsy for prostate cancer: Quantifying the impact of needle delivery error on diagnosis. *Med Phys*. 2014;41(7):073504. doi:10.1118/1.4883838

92. Reich DL, Hossain S, Krol M, et al. Predictors of Hypotension After Induction of General Anesthesia. *Anesth Analg*. 2005;101(3):622-628. doi:10.1213/01.ANE.0000175214.38450.91

93. Qiu W, Yuan J, Ukwatta E, Sun Y, Rajchl M, Fenster A. Prostate Segmentation: An Efficient Convex Optimization Approach With Axial Symmetry Using 3-D TRUS and MR Images. *IEEE Trans Med Imaging*. 2014;33(4):947-960. doi:10.1109/TMI.2014.2300694

94. Qiu W, Rajchl M, Guo F, et al. 3D prostate TRUS segmentation using globally optimized volume-preserving prior. In: *Lecture Notes in Computer Science (Including Subseries Lecture Notes in Artificial Intelligence and Lecture Notes in Bioinformatics)*. Vol 8673 LNCS. ; 2014:796-803. doi:10.1007/978-3-319-10404-1_99

95. Yuan J, Qiu W, Rajchl M, Ukwatta E, Tai X-C, Fenster A. Efficient 3D Endfiring TRUS Prostate Segmentation with Globally Optimized Rotational Symmetry. In: *2013 IEEE Conference on Computer Vision and Pattern Recognition*. IEEE; 2013:2211-2218. doi:10.1109/CVPR.2013.287

96. Qiu W, Yuan J, Ukwatta E, Fenster A. Rotationally resliced 3D prostate TRUS segmentation using convex optimization with shape priors. *Med Phys*. 2015;42(2):877-891. doi:10.1118/1.4906129

97. Ghavami N, Hu Y, Bonmati E, et al. Integration of spatial information in convolutional neural networks for automatic segmentation of intraoperative transrectal ultrasound images. *J Med Imaging*. 2018;6(01):1. doi:10.1117/1.jmi.6.1.011003

98. Lei Y, Tian S, He X, et al. Ultrasound prostate segmentation based on multidirectional deeply supervised V-Net. *Med Phys*. 2019;46(7):3194-3206. doi:10.1002/mp.13577

99. Passera K, Selvaggi S, Scaramuzza D, Garbagnati F, Vergnaghi D, Mainardi L. Radiofrequency ablation of liver tumors: quantitative assessment of tumor coverage through CT image processing. *BMC Med Imaging*. 2013;13(1):3. doi:10.1186/1471-2342-13-3

100. Krücker J, Xu S, Glossop N, et al. Electromagnetic Tracking for Thermal Ablation and Biopsy Guidance: Clinical Evaluation of Spatial Accuracy. *J Vasc Interv Radiol*. 2007;18(9):1141-1150. doi:10.1016/j.jvir.2007.06.014

101. Zhang D, Liang W, Zhang M, et al. Multiple antenna placement in microwave ablation assisted by a three-dimensional fusion image navigation system for hepatocellular carcinoma. *Int J Hyperth*. 2018;35(1):122-132. doi:10.1080/02656736.2018.1484183

102. Liu F, Liang P, Yu X, et al. A three-dimensional visualisation preoperative treatment planning system in microwave ablation for liver cancer: A preliminary clinical application. *Int J Hyperth*. 2013;29(7):671-677. doi:10.3109/02656736.2013.834383

103. Rose SC, Hassanein TI, Easter DW, et al. Value of Three-dimensional US for Optimizing Guidance for Ablating Focal Liver Tumors. *J Vasc Interv Radiol*. 2001;12(4):507-515. doi:10.1016/S1051-0443(07)61892-2

104. Xu H-X, Yin X-Y, Lu M-D, Xie X-Y, Xu Z-F, Liu G-J. Usefulness of Three-dimensional Sonography in Procedures of Ablation for Liver Cancers. *J Ultrasound Med*. 2003;22(11):1239-1247. doi:10.7863/jum.2003.22.11.1239

105. Neshat H, Cool DW, Barker K, Gardi L, Kakani N, Fenster A. A 3D ultrasound scanning system for image guided liver interventions. *Med Phys*. 2013;40(11):112903. doi:10.1118/1.4824326

106. Arif M, Moelker A, van Walsum T. Needle Tip Visibility in 3D Ultrasound Images. *Cardiovasc Intervent Radiol*. 2018;41(1):145-152. doi:10.1007/s00270-017-1798-7

107. Hrinivich WT, Hoover D a., Surry K, et al. Simultaneous automatic segmentation of multiple needles using 3D ultrasound for high-dose-rate prostate brachytherapy. *Med Phys*. 2017;44(4):1234-1245. doi:10.1002/mp.12148

108. Uherčík M, Kybic J, Liebgott H, Cachard C. Model Fitting Using RANSAC for Surgical Tool Localization in 3-D Ultrasound Images. *IEEE Trans Biomed Eng*. 2010;57(8):1907-1916. doi:10.1109/TBME.2010.2046416

109. Novotny PM, Stoll JA, Vasilyev N V, et al. GPU based real-time instrument tracking with three-dimensional ultrasound. *Med Image Anal*. 2007;11(5):458-464. doi:10.1016/j.media.2007.06.009

110. Mwikirize C, Nosher JL, Hacihaliloglu I. Local Phase-Based Learning for Needle Detection and Localization in 3D Ultrasound. In: Vol 10550. ; 2017:108-115. doi:10.1007/978-3-319-67543-5_10

111. Liang P, Yu X-L, Yu J. *Microwave Ablation Treatment of Solid Tumors*. (Liang P, Yu X, Yu J, eds.). Dordrecht: Springer Netherlands; 2015. doi:10.1007/978-94-017-9315-5

112. Mwikirize C, Nosher JL, Hacihaliloglu I. Convolution neural networks for real-time needle detection and localization in 2D ultrasound. *Int J Comput Assist Radiol Surg*. 2018;13(5):647-657. doi:10.1007/s11548-018-1721-y

113. Lee JY, Islam M, Woh JR, et al. Ultrasound needle segmentation and trajectory prediction using excitation network. *Int J Comput Assist Radiol Surg*. 2020;15(3):437-443. doi:10.1007/s11548-019-02113-x

114. Ronneberger O, Fischer P, Brox T. U-net: Convolutional networks for biomedical image segmentation. *Lect Notes Comput Sci (including Subser Lect Notes Artif Intell Lect Notes Bioinformatics)*. 2015;9351:234-241. doi:10.1007/978-3-319-24574-4_28

Chapter 2

2 Real-time registration of 3D to 2D ultrasound images for image-guided prostate biopsy

Real-time registration has the potential to continuously compensate for prostate motion during 3D TRUS-guided biopsy and may increase the accuracy of targeted biopsy approaches. The purpose of Chapter 2 is to present on the development of an automatic registration algorithm for 2D and 3D TRUS images.

The contents of this chapter have previously been published in *Medical Physics*: Gillies DJ, Gardi L, De Silva T, Zhao S, and Fenster A. Medical Physics 2017; 44(9):4708-4723. Permission to reproduce this article was granted by John Wiley and Sons and is provided in Appendix B – Copyright Releases.

2.1 Introduction

Prostate cancer is a global burden, representing the second highest incidence of noncutaneous cancer found in men.[1] Although prostate biopsy is the current clinical standard for definitive diagnosis of cancer, the efficacy of the conventional procedure lacks sensitivity with false negative rates up to 30%.[2,3] During the past decade, investigators and companies have developed improved prostate biopsy techniques over the conventional transrectal ultrasound (TRUS) based sextant biopsy.[4–7] Fusion biopsy is a notable method that involves an image fusion pipeline, which can register and overlay pre-procedural magnetic resonance (MR) images and biopsy targets onto a live, intra-operative 2D TRUS image. This approach typically employs a multi-step image registration process and has the ability to guide biopsy needles to suspicious localized tissues. With the widespread interest in fusion biopsy, the method is becoming predominant with the availability of commercial fusion prostate biopsy systems (e.g., UroNav, Artemis, BiopSee, Urostation, Virtual Navigator, and HI RVS/Real T time Virtual Sonography). Using these devices and others like them, many clinical investigations and studies are currently underway to verify if there is an improvement in cancer diagnosis over the conventional procedure.[8–12] As a result of increased scrutiny, image guidance during prostate fusion biopsies has been identified as a method to improve the detection rates of cancer and depends on accurate targeting to correctly grade the aggressiveness of prostate cancer.[13,14] To guide biopsy needles to their intended targets, image fusions resulting from accurate registrations of the preoperative 3D

MR and 3D TRUS images to the live 2D TRUS images are critical to reap the benefits of multimodal imaging. Any image misregistration between these planning and intraoperative images can prevent correct localization or display of intended targets, which can lead to missed cancer diagnoses.

Methods to improve image guidance have been focused on refining different algorithms used in the multi-step image fusion pipeline. Previous studies have investigated how to accurately register preoperative 3D MR images to 3D TRUS images for biopsy target planning[15–17] and also for 3D TRUS to 3D TRUS registration for preprocedural initialization and intraoperative correction.[18,19] However, in an ideal situation where these registration techniques reduce the error to a negligible amount, needle guidance error remains hindered by external influences, such as prostate motion. Prostate motion due to TRUS transducer pressure and patient motion due to needle pain unrelieved by local anesthesia will cause misregistration of the intended MR identified targets with their actual locations. In these instances, motion of the prostate can be in the form of sudden, random reflexes or slow, systematic shifts and develops as procedural time increases. It is during the live 2D TRUS image registration step when the current image fusion pipeline can fail.

Since the final stage of the current fusion pipeline aims to link all prior data to the live 2D TRUS image, it is crucial that this registration performs with sufficient accuracy. Misalignment between live 2D TRUS images and preoperative MR or 3D TRUS images has been observed up to 10 mm after initialization.[19] It has also been shown that the number of attempts required to sample a clinically significant tumor increases as needle delivery error of a biopsy system increases.[20] Among other techniques, 3D to 2D registration is invaluable to reduce needle delivery error and has been investigated in a broad spectrum of interventions.[21,22] Therefore, to compensate for misalignment error caused by prostate motion, two correction methods are feasible: 1) performing a single, intermittent user initiated registration correction before firing the biopsy needle, and 2) automatic, continuous correcting for any prostate motion throughout the biopsy procedure. With the first solution, image fusion would be displayed throughout the procedure, but a user would determine when to perform a correction based on observed image dissimilarities. Although a short registration time is acceptable, decreasing the computational time to less than 1 or

2 seconds is not a priority. Since this approach requires user interaction, current registration procedures are performed in an acceptable amount of time while the user focuses on preparation of the biopsy gun and biopsy sample. With a continuous scheme, corrections can be performed in the background without any user interaction, registering preoperative image data, targets, and segmentations automatically. Procedures can be completed more effectively by reducing the number of steps that require user attention, which can reduce procedure times and patient discomfort. These proposed motion correction methods for the prostate should not exceed a registration error of 2.5 mm, which has been previously suggested based on the smallest clinically significant tumors with an approximate 5 mm radius.[19,23] Keeping in mind that clinical translation is the key objective, image corrections performed at a real-time rate are also necessary to improve overall usability since user distraction can result if display lag is present. Thus, in the context of a TRUS-guided biopsy, we define real-time to be at or near the approximate frame rate of a conventional ultrasound system (*i.e.*, greater than 15 Hz or a new frame less than every 67 ms) typically used for a prostate biopsy procedure. However, real-time corrections for prostate motion requires fast and robust live 2D TRUS registration to the 3D TRUS image acquired at the beginning of the procedure, which contains the MR identified targets. Occasional mis-registrations due to lack of robustness may cause large aggregated misalignments in a continuous approach, whereas in a user-initiated, interactive approach, any unsatisfactory registrations could be disregarded and repeated at the user's discretion, possibly acquiring more useful data.[24] Therefore, real-time 2D TRUS to 3D TRUS registration to correct for any prostate motion while using an automatic, continuous strategy remains a challenging problem to solve.

Recent work addressing 3D to 2D registration for prostate interventions has been focused on reducing registration error and improving image guidance by incorporating MR images and deformation estimation. With the use of a preprocedural 3D TRUS image to manually initialize the approximate location of a preoperative MRI, Zhang *et al.*[25] proposed an automatic rigid registration method to fuse preoperative MR images directly to live 2D TRUS images during brachytherapy. Promising registration results were shown with target registration errors (TREs) of 1.37 mm and 2.52 mm for phantom and patient studies, respectively, corresponding to registration times of approximately 1 and 3 seconds

following their 3D TRUS manual initialization step. Although these registration times were shorter than previous attempts,[7] this is still too slow for continuous real-time performance. As a solution for deformation occurring during prostate biopsy, Baumann *et al.*[26] presented a 3D ultrasound based tracking system that performed a two-step registration procedure. First, rigid registration was performed on patient data with a TRE of 1.4 ± 0.8 mm and an execution time of approximately 2 seconds. Using deformation estimation to perform a deformable registration, they showed a reduction in registration error to a TRE of 0.8 ± 0.5 mm with an increased total registration time of approximately 7 seconds. The authors also provided an excellent discussion on the tracking errors present during targeted biopsy. With importance focused on accuracy, intra-operative usability is lacking in these techniques due to computation time restrictions from increased complexity of the algorithms. Although patient anatomy is deformable, the majority of prostate motion is rigid.[27] While registration error can be decreased with a deformable registration, a recent study compared deformable and rigid registration methods intra-operatively, concluding no significant differences were found when detecting clinically significant prostate cancers.[28] Considering the feasibility of a rigid registration approach and the current limitation of computational speed, real-time registration and improved intra-operative usability seems to be readily achievable through rigid registration methods since they perform at a reduced computational cost.

Our group has previously shown[29] a fully automated intensity-based rigid registration algorithm to align 3D TRUS images acquired directly before performing a biopsy procedure to live 2D TRUS images acquired immediately before tissue sampling. Our algorithm had a TRE of 1.87 ± 0.81 mm when tested on retrospective clinical images with total registration times of approximately 1.1 s. The algorithm was also tested when performed every second and was shown to have a reduced TRE of 1.63 ± 0.51 mm. By reducing the computation time further, it is anticipated a real-time motion compensation scheme would help improve targeting accuracy and smooth clinical translation when compared to an intermittent approach to motion compensation. With our previous results and clinical motivation, an objective of this work was to perform 2D TRUS to 3D TRUS registration in real-time, defined to be at or near the approximate frame rate of an ultrasound system (*i.e.*, greater than 15 Hz). Real-time computations approaching the frame

rate of an ultrasound system are necessary to provide a responsive feedback system, capable of correcting motion without user interaction to improve image guidance intra-operatively. In this paper, we present image registration and optimization techniques to reduce registration times and provide a direct comparison to our previous implementation with patient TRUS biopsy images. After implementing the optimized registration algorithm on our previously developed biopsy system,[4] phantom tests were performed to evaluate the feasibility and potential real-time motion correction capability of the algorithm.

2.2 Materials and methods

2.2.1 2D-3D image-based registration

The workflow for our motion compensation technique is shown in Figure 2.1 and is based on the assumption that preoperative MRI to 3D TRUS registration (with segmentations and/or annotations) has been accurately completed. Both 2D and 3D TRUS images acquired during the procedure are loaded into a graphics processing unit (GPU) and a mechanical tracker transformation[30] is used to place the images in a common coordinate system, referred to as the world coordinate system. The origin of the world coordinate system is initialized at the tip of the TRUS transducer, establishing the biopsy system that is based on a remote center-of-motion guidance approach.[30] This allows any motion of the 3D TRUS image, 2D TRUS image, and biopsy system to be applied around the initial TRUS transducer tip location during registration. With the mechanical encoder readings on the joints of the biopsy system, the 2D image is transformed to the world coordinate system to initialize its pose as a plane in the 3D image prior to registration.

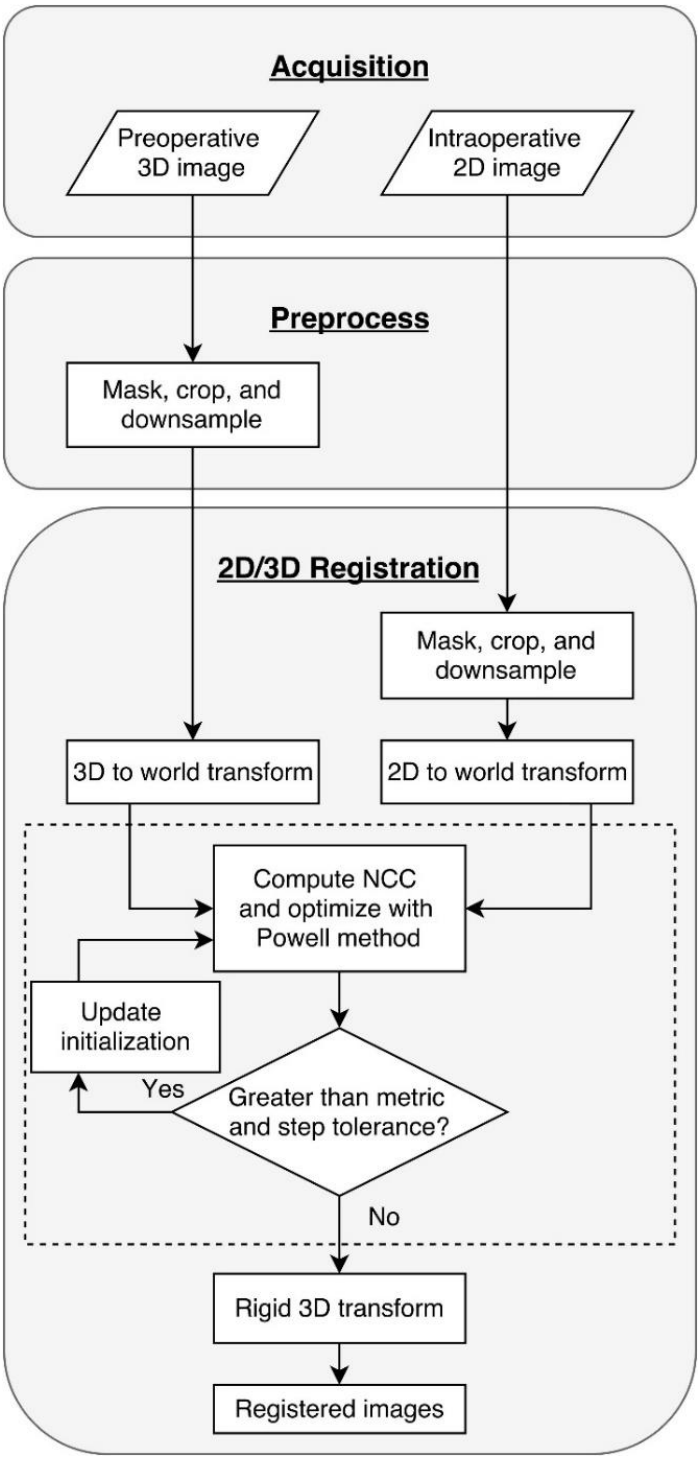

Figure 2.1 Proposed automatic image-based registration workflow. All steps in the "2D/3D registration" box would contribute to the total computation time of the algorithm; image pre-processing of the 2D image was included in "2D/3D registration" since this step would need to be completed as the images are being acquired during the procedure. The normalized cross-correlation is computed between the moving 3D image and the fixed 2D image for each iteration until termination criteria is reached. When the algorithm converges, a final rigid transform is generated and applied to the 3D image.

To compute 3D to 2D registration, a variation of the algorithm previously proposed by De Silva et al[29] was developed to achieve fast and robust performance. A normalized cross-correlation (NCC)[31] similarity metric was optimized with Powell's method,[32] using the Insight Segmentation and Registration Toolkit (ITK)[33] framework, in a rigid search space comprising of three rotations and three translations. Since rotations and translations constitute disproportionate units, the scaling between different directions in the search space was an important parameter during registration optimization. The scaling parameters were selected based on maximum observed rotational and translational displacements in our previous study[29] such that 6° rotation and 10 mm translation attribute to the same amount of displacement in the 6 DoF search space. This created a common *parameter space* with uniform and unitless spacing, permitting the use of simplified and unitless termination criteria during optimization.

Since Powell's method requires multiple iterations to converge, with each iteration consisting of multiple line optimizations in each DoF, a one-dimensional optimization sub-algorithm was necessary. The golden section search (GSS)[32] technique was chosen since it does not require derivative calculations, resulting in a low computational cost. Also, the GSS is more computationally efficient than a conventional bisection approach since it recycles previous points when varying the bracketed interval in which the optimum is predicted to exist in a single line direction. When employing the GSS technique and minimizing the search space, a parameter *step* tolerance and an NCC *metric* tolerance were defined as termination criteria for optimization. These tolerances were compared to the change at each DoF (*i.e.*, step taken during optimization) and the change in NCC metric values at each iteration to terminate when near or at the local optimum. Based on preliminary tests, parameter step tolerances were set at one-thousandth of the expected image displacement ranges (*i.e.*, 0.01 mm and 0.006°) and the NCC metric tolerance was set to 0.0001. In certain circumstances, if the current DoF being searched is initialized at its optimum, the algorithm will terminate prematurely even with image dissimilarity present due to misalignment in the remaining DoFs. To avoid this scenario where these tolerances are reached prematurely due to the lack of progress along a single DoF, the algorithm was forced to search each DoF at least once to always complete a full cycle when searching the parameter space. After successful optimization, a 3D rigid transformation

was output and used to estimate the pose of the 3D TRUS image to correct for any prostate motion during the procedure, as displayed in the live 2D TRUS image. This enabled the resulting 2D TRUS plane from the 3D TRUS image to be displayed during the procedure.

To provide continuous motion compensation, the algorithm initialized the 3D pose of the subsequent images according to the previous image's resulting registration transformation. This initialization approach was performed for three reasons: (1) Powell optimization performs well when adjusting for small corrections near local minima since it is typically used on unimodal objective functions, (2) an initialization close to the function minimum increases the speed of convergence, and (3) it is assumed that motion will be minimal between real-time 2D TRUS images (< 1 mm and < 1°) acquired at 15-50 Hz. This procedure will henceforth be referred to as the *continuous* method.

2.2.1.1 Estimating the optimal scale for registration

The optimal amount of image information necessary to accurately perform registration can vary depending on the available anatomical details, while increasing image size burdens computational cost. Thus, the optimal scale of the images being registered is an important parameter considering the tradeoff between accuracy and computational cost. In our methods, we investigated downsampling of 2D and 3D TRUS images by factors of 2, 4, and 6 without any averaging (binning). The 2D images were additionally cropped, centred on the image, to remove information outside an area of interest (AOI) containing the prostate. The AOI boundaries were chosen outside the approximate prostate anatomical boundary for the largest prostate sizes. Computation times and registration errors were computed for each downsample factor to determine the optimal sampling factor that would decrease the registration time without increasing registration error.

2.2.1.2 Estimating the optimal area of interest

Since the AOI within 2D TRUS images determines the amount of anatomical detail included in the registration, we investigated the AOI size as a variable in the study by performing repeated registrations for different AOI sizes and measuring the resulting registration accuracy and time. After masking the template 2D TRUS images to exclude

embedded text/annotations, the largest AOI containing ultrasound intensity information was found to be 570×466 pixels. Using this size as a template and an upper AOI limit, a constant width to height aspect ratio (1.22:1) was maintained when cropping the 2D image. Beginning with the smallest AOI at 100×82 pixels, the width was iteratively increased by 12 pixels (with the complementary height) until a final AOI was reached at 568×466 pixels. Computation times and errors were determined when completing the registration at each AOI, which included the process of masking and cropping the 2D image, as shown in Figure 2.1. The registration time encompassed this process to resemble a scenario when the 2D TRUS image would be acquired from the frame grabber directly from the ultrasound system during a continuous registration method.

2.2.1.3 Direction search order of optimization

Finding an acceptable registration between images is dependent on how an algorithm searches through 3D space. Conventionally in Powell's method, search directions are updated after each iteration to increase the speed of convergence by predicting the direction containing the largest improvement of the cost function. Search direction is predicted by replacing the vector containing the largest improvement with the most similar direction from the previous iteration in an attempt to avoid linear dependence between search directions. With this strategy, the method can be used to optimize a continuous function with an unknown underlying mathematical definition.[32] With subsequent iterations determining search directions empirically, it is generally thought that the method is insensitive to initial search direction order. Even though the direction search vectors are updated when the optimization is continued beyond the first iteration, the initial search vector order of optimization is an important factor that prioritizes certain directions during search space traversal. Increased initialization misalignments from the target alignment can make the algorithm more susceptible to converge at a local optima of the NCC metric.[29,34] In these instances, it is helpful to avoid these local optima by estimating the line direction that achieves the target extrema quickly and correctly. To study the effect of initial search direction order on registration accuracy, two search orders were explored: rotation vectors initially optimized before translation vectors (referred to as the *rotations first* scheme) and

translation vector optimization followed by rotations (henceforth called the *translations first* scheme).

2.2.2 Experiments

2.2.2.1 Clinical image acquisition

The image acquisition details have been described in De Silva *et al.*[29] and are summarized here. Preoperative 3D TRUS images were acquired using our mechanically assisted 3D TRUS-guided biopsy system. Utilizing encoders, a commercially available end-firing 5–9 MHz TRUS transducer probe (Philips Medical Systems, Seattle, WA) was mechanically tracked to reconstruct a 3D TRUS image from a series of 2D views. These 2D views were masked to remove extraneous system information (e.g., patient information, image scale, etc.) by changing the image intensity data outside the TRUS image field to 0, shown in Figure 2.2a. After reconstruction, the 3D image was then cropped to a rectangular bounding box, reducing the image size to 448×448×350 voxels with dimensions of 0.18×0.18×0.19 mm^3, shown in Figure 2.2b. The coordinate system initialization and 3D image reconstruction occurred only once and at the beginning of the procedure, requiring approximately 3 seconds. After acquiring the 3D TRUS image, 2D TRUS images were saved before firing the biopsy gun at predefined biopsy target locations. Similar to the 3D TRUS image, these 2D images were masked to remove extraneous information, resulting in a total image size of 640×480 pixels and pixel dimensions of 0.18×0.18 mm^2. These images were inputs for the registration algorithm running on an i7-4770 central processing unit (CPU) at 3.40 GHz (Intel Corporation, Santa Clara, CA) with Compute Unified Device Architecture (CUDA) C++ to accelerate the NCC calculation on a GeForce GTX TITAN GPU (NVIDIA Corporation, Santa Clara, CA). Implementation and computation speed of the NCC calculation was improved by parallelizing the computations by dividing the total image matrix into 19,200 blocks with 16 threads per block.

2.2.2.2 Accuracy evaluation

The target registration error (TRE)[35] was assessed by calculating the RMS error between manually annotated corresponding fiducial pairs in the 2D and 3D TRUS images (white arrows shown in Figure 2.2). A total of 45 intrinsic fiducial pairs were identified from 7

patients (14 biopsy needles) to calculate TRE with an average of 3 fiducials per image pair. Since registration is performed using image intensities, the 45 fiducial pairs were chosen once in the original images (i.e., no downsampling) and provided the same pre-registration point clouds to be used for post-registration comparisons. Variability (*i.e.*, fiducial localization error (FLE)) associated with manual localization of the fiducials,[35] has been previously reported to be 0.11 mm in the 2D TRUS images[30] and 0.21 mm in the 3D TRUS images.[18,19]

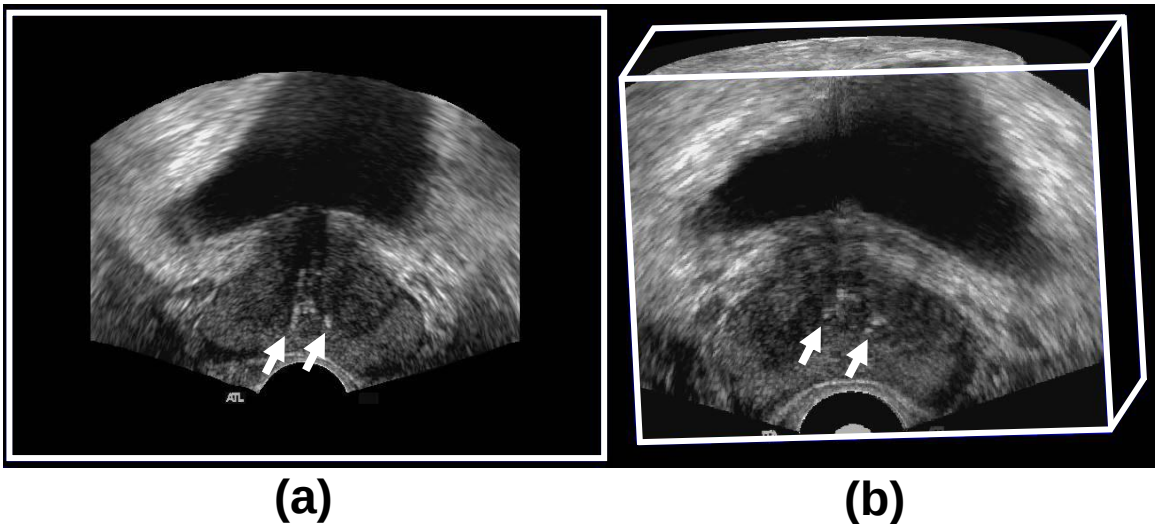

Figure 2.2 Example (a) 2D and (b) 3D TRUS images after masking and cropping before registration computations. The hypoechoic bladder can be seen in the superior portion of the images with the prostate below containing microcalcifications indicated by the white arrows.

2.2.2.3 Phantom image acquisition

Registration method validation using clinical images was limited to the presence of calcifications in the 2D TRUS images to define ground truth motion. Since a subset of the frames in a real-time live 2D TRUS video sequence may not contain such anatomical landmarks, we performed a phantom study to comprehensively analyze the performance of the algorithm in compensating for prostate motion in real-time. An agar-based tissue-mimicking phantom of a prostate model[4] was fabricated that contained beads embedded in a surrounding agar background to provide texture.[6,36] The prostate model, beads, and background were constructed by adding 7% by mass of glycerol solution with agar powder to produce a speed of sound similar to that of human tissue (1540 m/s).[37] The prostate mold

model was generated from a segmented 3D TRUS image of a human prostate and enlarged anisotropically in anterior/posterior, superior/inferior, and left/right dimensions (77:50:36)[38] to a volume of 60 cm^3. The agar beads and background material contained cellulose (15% by weight) and were used to create acoustic backscattering, providing hyperechoic regions in the TRUS images. The agar beads were created with diameters of 3.18 mm and 4.76 mm from standard spherical molds, cooled, and placed in the prostate mold before the model was filled with non-cellulose agar. The prostate model was then suspended in a polycarbonate box using fishing line so the surrounding background agar could be added in a single pour and allowed to cool for 24 hours. This was performed to avoid layering interfaces in the background agar typically observed when a suspension technique is not used.

The primary forms of motion that were encountered during a prostate biopsy included in-plane and out-of-plane translations relative to the 2D TRUS image, as well as rotations around the long axis of the ultrasound probe. The user initiated and continuous registration methods as described below were investigated using this phantom to assess registration performance when compensating for translation and rotation motions in real time.

2.2.2.3.1 Translation range testing

Patients are not anesthetized during a prostate biopsy and we have observed some motion in the form of a translational offset. To simulate these motions, the fabricated prostate phantom was mounted on an independent and movable stage, as shown in Figure 2.3. This stage was used to validate the registration accuracy of our algorithm for known in- and out-of-plane translations since it was capable of generating 1 micrometer increments in translation. After positioning the TRUS probe at the centroid of the prostate phantom and acquiring a 3D image, 3D to 2D registration was performed incrementally (after locking the tracking system) by translating the phantom and registering the resulting live 2D images. In a first approach, the registrations were performed manually at each translation increment, independently of previously performed registrations; this procedure will be referred to as the *user initiated* method. The registrations were repeated at 1 mm translation increments until reaching a maximum measured displacement of 12 mm, which captures a

range comparable to translation motions observed clinically.[19] This process was repeated over ten trials to assess variability and robustness of the user initiated motion compensation algorithm. To validate continuous motion correction and provide comparison to the user initiated method, a similar procedure was performed that added incremental initializations from previous registrations. At each increment, micrometer translation was paused to obtain 2D images, transformation matrices, and computation times before continuing to the subsequent translation. This process was repeated over five trials (due to length of experimental setup and image acquisition) to assess variability and robustness of the continuous motion compensation algorithm. After completing data acquisition for one direction (*e.g.*, in-plane translation), the TRUS probe was rotated by 90°, a new initialization matrix was generated, and the entire experiment was repeated for both methods to perform the registration for an additional translation motion.

As an approach to evaluate the error of the registration algorithm, the offset difference from the initialization matrix to the output registration result was calculated since the translation distance was known and thus provided a ground truth. This error metric was chosen since it was less labour intensive and avoided any errors due to manual fiducial selection used to compute a TRE calculation. Although the translation was intended for a single translation direction, the RMS displacement was determined from the 3-vector offset difference to account for any minor setup errors that would cause 3D errors in overall motion. The offset difference was calculated for each increment to obtain mean differences paired with corresponding mean computation times. Since we intended to compare the continuous method directly to the user initiated method, the first corrected transformation matrix acquired for each increment was used to compute the offset difference from the initialization matrix. This corrected transformation matrix was determined for each increment by searching for the first TRUS frame output with no observed motion, representing the frame when micrometer translation was paused.

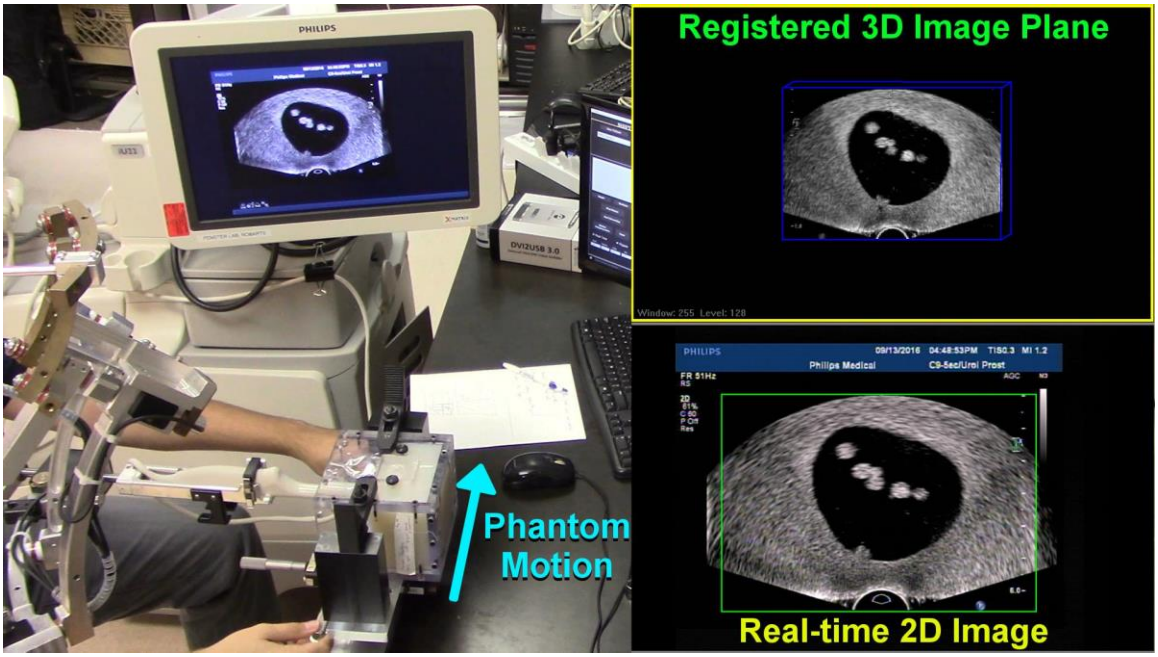

Figure 2.3 Phantom set up during testing of in-plane translation range when using the continuous motion compensation method (Multimedia view online). The live experimental setup can be seen on the left where the live 2D TRUS image is taken from the US machine and shown in the bottom right. After completing 3D to 2D registration, the resulting registered image plane in the 3D TRUS image is displayed, seen in the upper right.

2.2.2.3.2 Roll rotational range testing

Rotation around the long axis of the TRUS transducer was another type of motion we observed during prostate biopsy and was another type of motion we simulated to test our registration algorithm. Since there are no suggested rotational tolerances present in the literature, a rotational tolerance was justified based on the previous[19,23] target TRE of 2.5 mm to determine a target rotational error. Using our image width of 448 pixels with voxel dimensions of 0.18 mm, if a rotation about the center of the 3D image space is assumed, then the region most susceptible from a rotational error will be present near the edges of the image. An error of 2.5 mm located at the edge of the image (*i.e.*, 224 pixels or 40.32 mm from the center) corresponds to a rotational tolerance of 3.55°.

Keeping this target in mind, we performed displacement tests to determine the rotational motion compensation range of the algorithm. To test rotational motion, the TRUS probe was positioned at the center of the base of the prostate phantom to acquire a 3D image. The

initialization transformation matrix was recorded and the mechanical tracking encoders were disabled to ensure the registration algorithm was performed without updated initializations. Although tracking was not performed, mechanical encoder values were still displayed and used to track the rotation of the TRUS probe around its long axis to determine rotations. This probe rotation was performed instead of a phantom rotation purely for the ease of operability. Similar to the translation procedure in the previous section, 3D to 2D user initiated image registration was performed by registering the live 2D image after incrementally rotating the TRUS probe. After each step, the algorithm was reinitialized using the original mechanical encoder transformation, without using previous registration outputs. This reinitialization ensured that the user initiated registration started from the same position for each subsequent rotational increment. Similar to the translational range testing, we repeated this registration procedure in approximately 1° increments until reaching a maximum measured rotation of 15°. Although our expected clinical rotation was 6°, this limit was chosen to potentially reveal the point of unreliable motion compensation. Motion compensation was repeated over ten trials to obtain a mean difference error and computation time for each increment. For comparison with the continuous motion correction, initialization and corrections were not reset between registrations, consistent with the translation testing procedure. Rotational motion was paused at each increment to obtain 2D TRUS images, transformation matrices, and computation times before continuing to the subsequent increment. This protocol for continuous motion compensation was repeated over four trials to obtain a mean rotation difference paired with a mean computation time for each increment.

Since the rotation angle was known, the difference 3 × 3 rotation matrix ($\boldsymbol{T}_{difference}$) between the corrected registration ($\boldsymbol{T}_{corrected}$) and initialization ($\boldsymbol{T}_{initial}$) rotation matrices was calculated by

$$\boldsymbol{T}_{difference} = (\boldsymbol{T}_{initial})^{-1} \times \boldsymbol{T}_{corrected}. \tag{2.1}$$

The corresponding rotation can be calculated from

$$\psi = \tan^{-1}\left(\frac{t_{2,1}}{t_{1,1}}\right), \tag{2.2}$$

where $t_{1,1}$ and $t_{2,1}$ are the $\boldsymbol{T}_{difference}$ matrix elements in the first and second rows of the first column.[39]

Similar to the translation experiment, we compared the continuous method to the user initiated method by using the first corrected transformation matrix acquired at each motion increment to compute the rotation difference from the initialization matrix. This corrected transformation matrix was determined for each increment by searching for the first TRUS frame output with no observed motion, representing the frame when probe rotation was paused.

2.2.2.4 Statistical methods

Statistics calculations were performed using SPSS Statistics v.24.0.0.0 (IBM Corp., Armonk, NY, USA). To check if our image data followed a normal distribution, normality was evaluated using a Shapiro-Wilk test. Nonparametric statistical tests were used where appropriate and are presented in parentheses for the remainder of this section. Results were considered significant when the probability of making a type I error was less than 5% ($p < 0.05$).

Since our previously acquired patient images were tested for every downsample factor, a one-way repeated measures ANOVA (Friedman) test was used as an omnibus test prior to any post-hoc analysis. If significance was found, a Bonferroni correction was used, resulting in a significance level set at $p < 0.017$ for our post-hoc analyses conducted using Tukey's honestly significant difference (Wilcoxon signed-rank) tests. To determine if there is an initialization distance correlation with the accuracy of registration, linear regressions were plotted using Prism 7.00 (Graphpad Software, Inc., La Jolla, CA, USA) to show the TRE trends. The user initiated and continuous correction methods were compared using t-tests (Welch t-tests) after in-plane, out-of-plane, and roll motion corrections for error and computation time distributions.

2.3 Results

2.3.1 3D to 2D registration optimization on clinical images

Interaction effects during optimization of the three tested algorithm settings were investigated and a brief overview of the results are shown in Figure 2.4. Linear regressions were added to provide an estimate of the trends observed for the TRE distributions as initialization offset was increased. Although more AOI comparisons were completed, the smallest error was observed when downsampling by a factor of 4, cropping to an AOI of 356×292, and optimizing the search space by translations first. In the three subsequent sections, each parameter was investigated independently while holding the other settings constant. As a reminder and disclaimer for the reader, all presented TRE results in Sections 2.3.1 and 2.3.2 are susceptible to a small bias introduced when manually selecting fiducials. This should be considered when comparing changes in TRE.

2.3.1.1 Estimating the optimal scale for registration

Estimating the optimal scale for motion compensation was performed with an input AOI of 356×292, while optimizing the search space by translations first. Normality was tested using the Shapiro-Wilk test with significance found for factors 2 and 6, for both TRE and time, suggesting non-normal distributions were present. Nonparametric measures are shown in Table 2.1 for TRE and computation times after downsampling the 2D and 3D clinical ultrasound images by factors of 2, 4, and 6. A repeated measures Friedman test was performed for both TRE and time, which failed to show a statistically significant difference between the distributions of downsample factors, but showed statistical significance when comparing computation times ($p < 0.001$). Post-hoc analysis with the nonparametric dependent-samples Wilcoxon signed-rank test was conducted between the computation times for the three downsampling factors. Significant differences ($p < 0.01$) between all downsample factor combinations was found. A downsampling factor of 4 was determined to be the optimum rate for our application since the median and third quartile were below the 2.5 mm target TRE in addition to a decrease in computation time. The corresponding median computation time of 55 ms was observed, which is a factor of 20 times smaller than previously achieved.[29] This computation time from registering patient images converts to

a rate of 18.2 Hz, which is greater than our real-time definition of 15 Hz. Thus, this reduction in computational time enables motion compensation to be performed as a background software process to continuously register live, real-time streams of 2D TRUS images.

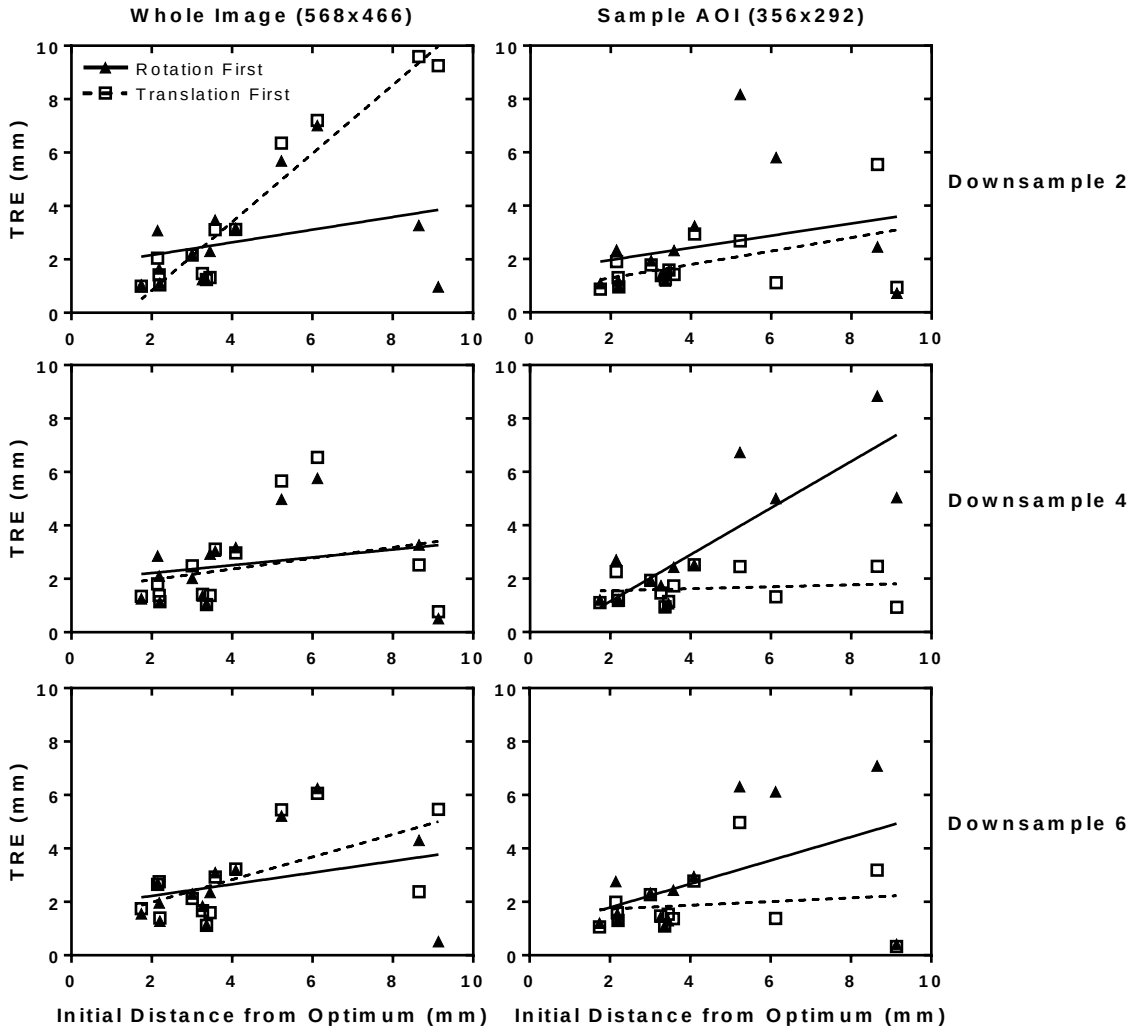

Figure 2.4 An overview of the main interactions observed when optimizing downsampling factor, cropping AOI, and search order.

Table 2.1 Effect of downsampling 2D and 3D images on TRE and computation time for 14 patient images.

Image Downsample Factor	Median TRE [Q1, Q3] (mm)	Median Computation Time [Q1, Q3] (ms)
2	1.37 [1.08, 2.24]	97 [92, 137]
4	1.40 [1.14, 2.31]	55 [41, 64]
6	1.71 [1.17, 2.71]	30 [24, 34]

2.3.1.2 Estimating the optimal area of interest

The optimal AOI was determined with an optimal downsampling factor of 4, while searching translations first. The AOI in the 2D images was iteratively increased from 100×82 pixels with results for computation time and TRE shown in Figure 2.5. A slight increasing trend in computation times (Figure 2.5a) was observed over the range of AOIs. When analyzing TRE to find the ideal AOI (Figure 2.5b), a decreasing trend was initially observed until reaching a minimum at approximately 356×292 pixels, followed by a slight increase and plateau. The observed minimum of the TRE, reduced variability, and the minimal change in computation time led to the selection of a 356×292 AOI for the biopsy application. However, due to the bias in the TRE when manually selecting fiducials, an AOI in the range of 316×259 to 364×298 would equally be justified.

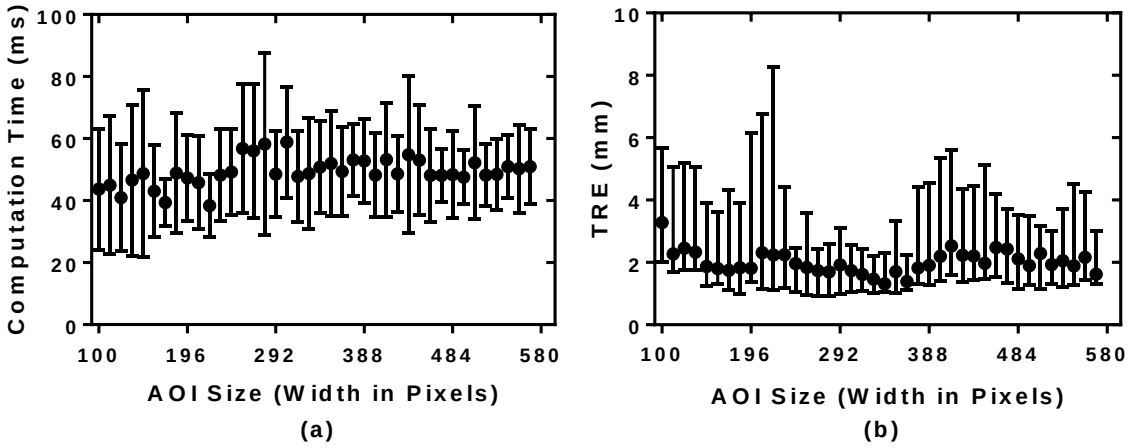

Figure 2.5 Scatter plots of the mean ± standard deviation registration computation time (a) and median [Q1, Q3] TRE (b) as the AOI size in the 2D image was increased. The asymmetric area of the AOI was scaled in a width:height ratio of 1.22:1, corresponding to the aspect ratio of the largest AOI achievable.

2.3.2 Direction search order of optimization

The main direction search order results are shown in Figure 2.4. When using the whole image as an input, similar TRE distributions were observed between all downsample factors when comparing the rotations first strategy. The translation first method was unable to register large initial offsets when using a downsample factor of 2, but was similar to the rotation method when comparing the other downsample factors. When using the cropped AOI input, all translation first TRE results were reduced relative to the whole image input for each downsample factor. However, cropping had minimal influence when optimizing rotations first, with an exception at a downsample factor of 4 since it was unable to register the largest initial offset images effectively.

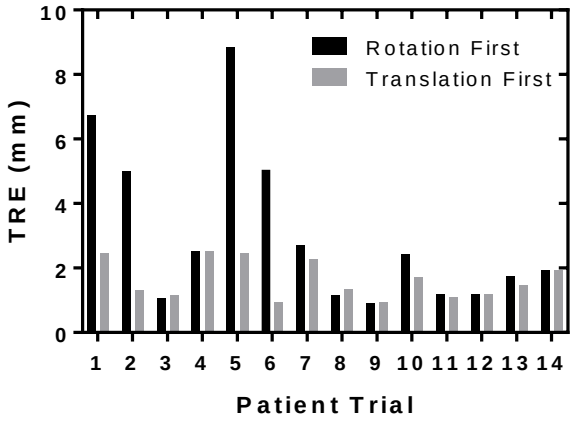

Figure 2.6 The TRE between translation first and rotation first direction search order schemes on 14 patient image sets. Images used for registration were downsampled by a factor of 4 with the 2D images cropped to an image size of 356×292.

When comparing direction search order TREs for downsampling by a factor of 4 and cropping to an AOI of 356×292 (Figure 2.6), normality was tested using the Shapiro-Wilk test with statistical significance found for the rotations first scheme ($p < 0.05$). The median ± interquartile range (IQR) for TRE computed for the rotations first search was 2.18 ± 3.82 mm compared to the translations first median TRE of 1.40 ± 1.17 mm (previously stated in Section 2.3.1.1). Since we know that the algorithm is susceptible to converge prematurely when the initialization is further from the target alignment, both search order schemes were compared to identify any trends using a Spearman's rank-order correlation. The initialization distances between the 2D and 3D images before registration and the

corresponding post-registration errors had a strong, positive correlation (0.644) using the rotations first scheme, which was statistically significant ($p < 0.05$).

The TREs calculated from fiducials before registration (*i.e.*, following encoder pose initialization) and after registration for the translations first search scheme was compared as it yielded better registration performance. Using a Shapiro-Wilk test of normality, the distribution of image distances before registration was shown to be not normally distributed ($p < 0.05$). The TRE frequency distributions before and after registration is shown in Figure 2.7 with a median RMS error before registration of 3.41 ± 3.26 mm with the corresponding median TRE of 1.40 ± 1.18 mm after registration. Analyzing the post-registration group further, 10/14 image pairs (71%) were less than a real-time computation time of 67 ms and 13/14 image pairs (93%) were less than a TRE of 2.5 mm. Since there could be some variability from manual point selection, we investigated a margin around 2.5 mm equal to the FLE measurement for the 3D TRUS and 2D TRUS images combined in quadrature (*i.e.*, 0.237 mm). This resulted in a range from 10/14 (71%) of image pairs below a 2.263 mm error to 14/14 (100%) of image pairs below a 2.737 mm error. We used the Wilcoxon signed-rank test to compare medians of distances to the desired target plane before and after registration, which showed a statistically significant difference when correcting for position ($p < 0.01$).

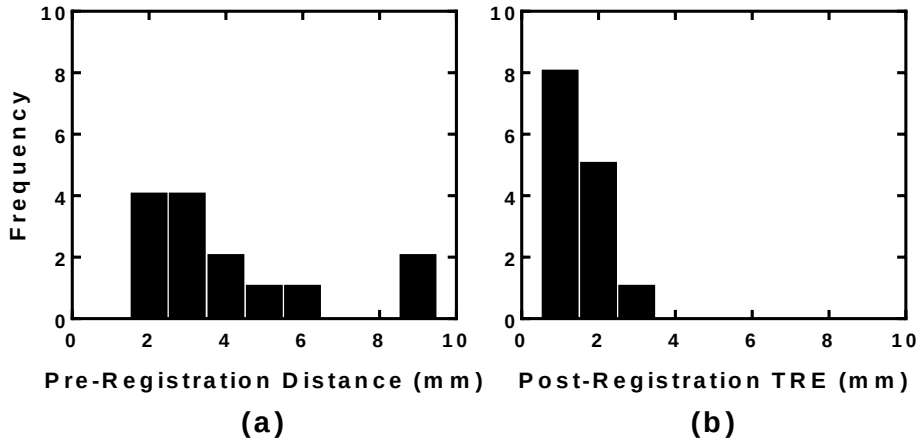

Figure 2.7 Histograms of the distance calculated between 2D and 3D image pairs from the manually chosen intrinsic fiducial markers before (a) and after (b) registration using a translation first search order after pose initialization.

2.3.3 Validation: phantom experiment

A summary of the total mean difference from measured displacement and the mean computation time for both registration methods and the three types of motion is summarized in Table 2.2.

Table 2.2 Mean differences and computation times of the user initiated and continuous registration methods for translation (in-plane and out-of-plane) and rotational motion.

Method	Motion	Mean Difference	Mean Computation Time (ms)
Before registration	Trans	6.0 ± 3.7 mm	
	Rot	8.0 ± 5.2°	
User initiated	In	0.4 ± 0.3 mm	108 ± 38
	Out	0.2 ± 0.4 mm	60 ± 23
	Rot	0.8 ± 0.5°	89 ± 27
Continuous	In	0.2 ± 0.3 mm	35 ± 8
	Out	0.7 ± 0.4 mm	43 ± 16
	Rot	1.2 ± 1.0°	27 ± 5

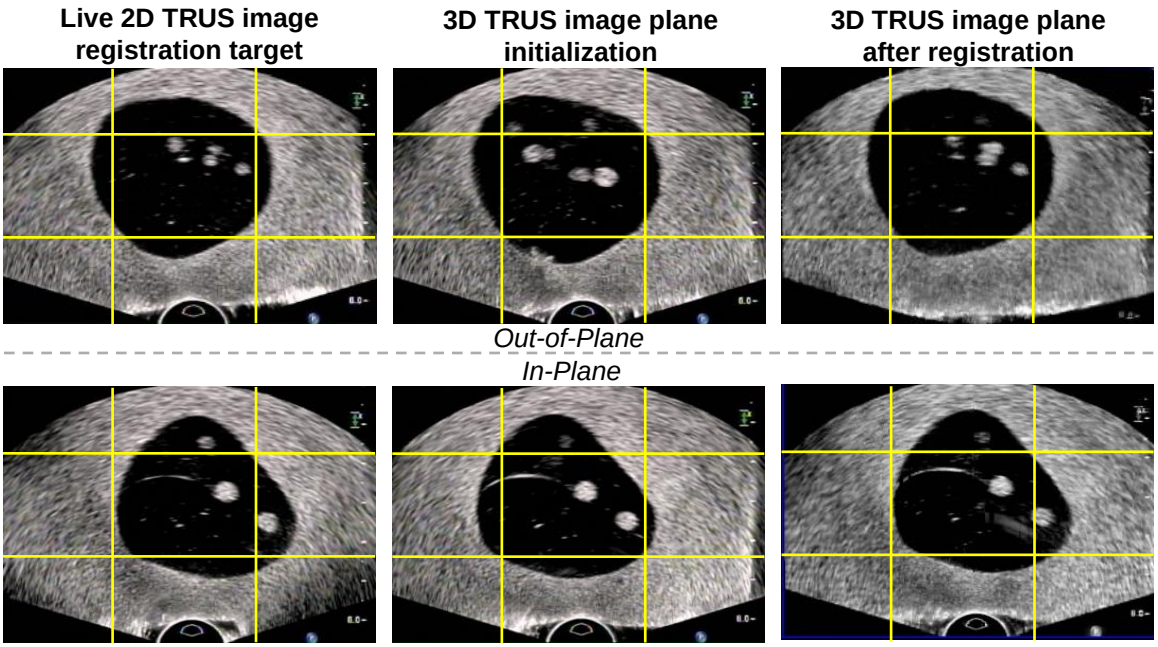

Figure 2.8 Sample prostate phantom images before and after registration for out-of-plane and in-plane translational motion. Images from real-time 2D TRUS are shown in the left column. In the middle column, the initialization 3D TRUS image planes obtained before registration display image misalignment when compared to the 2D TRUS view. 3D TRUS image planes in the right column demonstrate motion compensation capabilities after registration. Grid lines were superimposed following registration to provide spatial reference between image frames.

2.3.3.1 Translation range testing

Sample prostate phantom images of the 2D TRUS live view, the 3D TRUS initialization plane, and the calculated 3D TRUS plane after registration are shown in Figure 2.8. Example setup and image registration results from the continuous motion compensation method are also presented in Figure 2.3 (Multimedia view). An error and computation time comparison between the user initiated method with the continuous method is shown in Figure 2.9 after testing the in-plane and out-of-plane translational range. The average difference between the corrected registration translation offset and the measured micrometer translation is shown for the user initiated method (Figure 2.9a) and the continuous method (Figure 2.9b). When observing the mean difference errors for both correction methods, the mean difference error metric never exceeded 1.25 mm over the entire translation range, falling below half of the 2.5 mm target error. When performing a user initiated correction, out-of-plane motion displacements were observed to be corrected with a smaller mean error when compared to in-plane motion. Conversely, the continuous registration achieved a reduced mean error when correcting in-plane motion. Comparing the two methods with respect to error for each motion, out-of-plane motion was corrected significantly better with the user initiated method ($p < 0.001$) and no difference was found for in-plane motion. In the same figure, the corresponding computation times are shown for the user initiated method (Figure 2.9c) and the continuous method (Figure 2.9d). For the user initiated method, the out-of-plane motion correction computation time had a lower overall variance and consistently fluctuated around 60 ms. Computation times showed an increasing trend when correcting for in-plane motion as the translational displacement was increased, plateauing around 4 mm. From the user initiated method results, all trials for both motions were below an error of 2.5 mm, but only 20/130 (15%) of in-plane and 97/130 (75%) of out-of-plane trials were less than a real-time computation time of 67 ms. When performing a continuous registration, all trials for both motions were below an error of 2.5 mm and computation times were significantly lower than the user initiated correction for in-plane ($p < 0.001$) and out-of-plane ($p < 0.01$) motions. In addition, the continuous method showed 65/65 (100%) of in-plane and 57/65 (88%) of out-of-plane trials less than a real-time computation time of 67 ms.

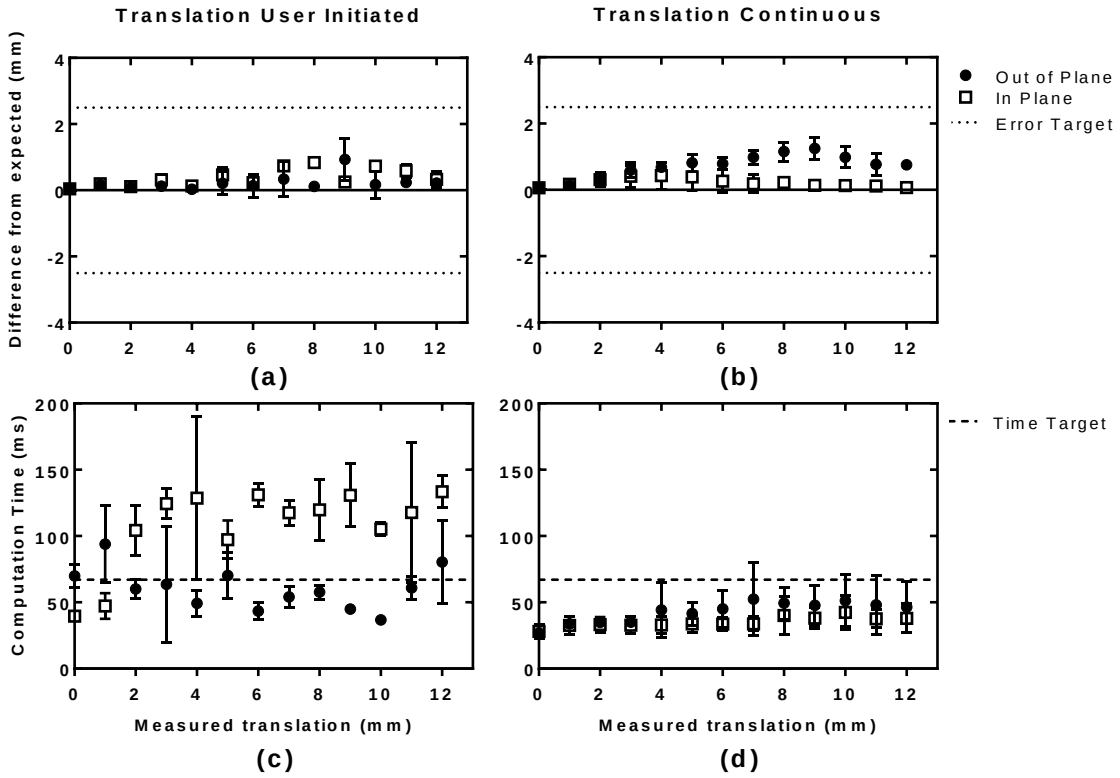

Figure 2.9 Comparison between registration procedures when testing the in-plane and out-of-plane translation compensation range. In the top row, Euclidean translational differences between measured and expected values are shown for the user initiated procedure (a) and the continuous procedure (b). Dotted lines represent a target tolerance of 2.5 mm. The corresponding computation time results for the user initiated procedure (c) and the continuous procedure (d) are shown in the bottom row. Standard deviation error bars are not shown when shorter than the height of the symbol. The dashed line represents the target computation time of 15 Hz or 67 ms.

2.3.3.2 Roll rotational range testing

The comparison between the user initiated method and the continuous method is shown in Figure 2.10 for rotational motion compensation. The average rotation difference between the corrected registration and the measured encoder angles is shown for the user initiated method (Figure 2.10a) and the continuous method (Figure 2.10b). In both methods, all differences were smaller than our rotational tolerance of 3.55° with a maximum mean difference of 2.3 ± 0.8° observed in the continuous method at a 12° displacement. Although the continuous method was observed to have an increasing error near the end of the tested rotations, no overall significant difference was found when compared to the user initiated

method. This increasing trend also occurs beyond the expected rotations of 6°, making this finding less of a concern for clinical translation. The computation times for the user initiated method is shown in Figure 2.10c, and the continuous method in Figure 2.10d. The user initiated method had an overall computation time of 89 ± 27 ms with a much larger variance compared to the continuous method with 15/90 (17%) of trials less than an error of 3.55° and a real-time computation time of 67 ms. Similar to Sec.2.3.3.1, the computation time for the continuous method was observed to be significantly reduced ($p < 0.001$) and nearly constant with a mean computation time of 27 ± 5 ms. The continuous method also had 36/36 (100%) of trials less than an error of 3.55° and a real-time computation time of 67 ms.

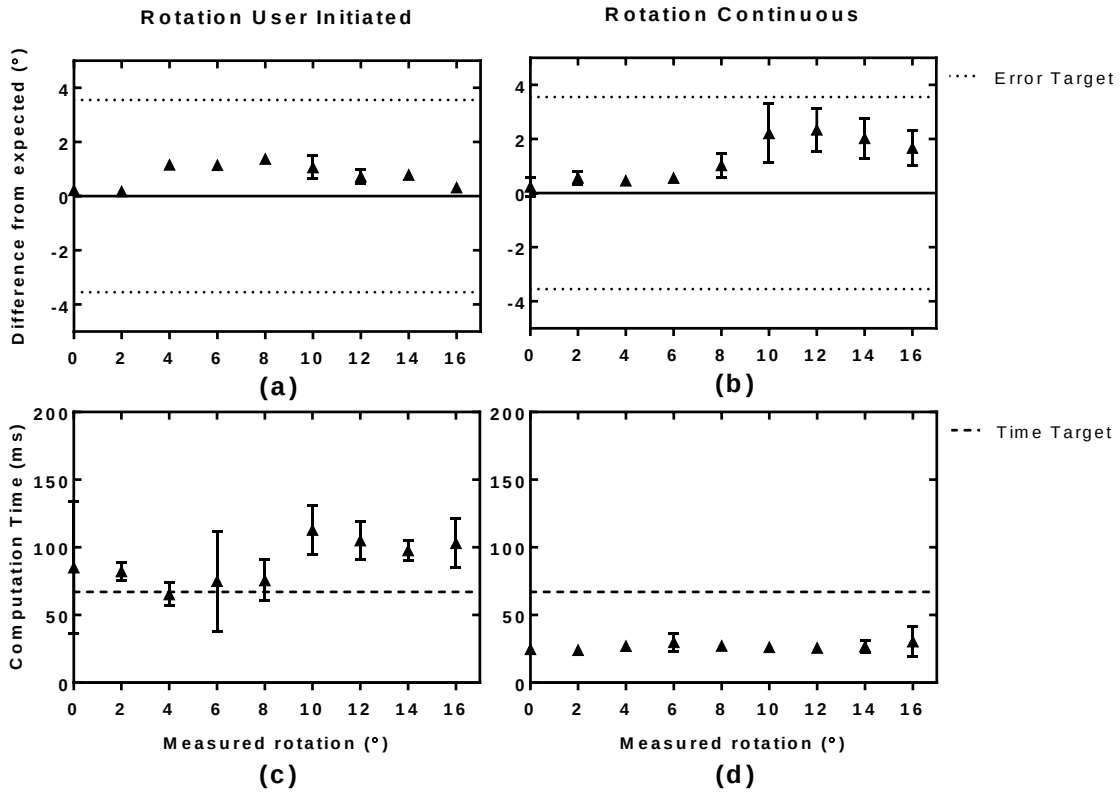

Figure 2.10 Comparison between registration procedures when testing the roll rotation compensation around a clinically expected value of 6°. In the top row, rotational difference results between measured and expected values are shown for the user initiated procedure (a) and the continuous procedure (b). Dotted lines represent a target tolerance of 3.55°. The corresponding computation time results for the user initiated procedure (c) and the continuous procedure (d) are shown in the bottom row. Standard deviation error bars are not shown when shorter than the height of the symbol. The dashed line represents the target computation time of 15 Hz or 67 ms.

2.4 Discussion

In current TRUS-guided prostate biopsies, tracking systems generate transformation matrices and are used to display corresponding MRI image data, as well as preoperatively delineated segmentations and annotations that exist in a separate volume. With the use of a motion compensation module, computational resources will still need to be used for the existing guidance system. Therefore, motion compensation registration times reported in this study was shown as the additional time needed for an existing a TRUS-guided procedure.

2.4.1 Optimal amount of image information for registration

With an optimal downsampling factor, the registration computation time decreased with statistical significance for our clinical prostate images, without an increase in error compared to results reported by De Silva *et al*.[29] For our 3D image size of 448×448×350 pixels, a downsample factor of 4 was chosen, which provided a median and third quartile below a 2.5 mm target TRE (1.40 [1.14, 2.31] mm) and helped to reduce the registration time from approximately 1.1 s to 55 [41, 64] ms. Since the comparison of TREs failed to show statistical significant differences, we performed an equivalence test[40,41] using an approximate 90% confidence interval (CI) on the median of differences using GraphPad Prism 7.00. An equivalence interval of ±0.24 mm was determined by combining the FLE measurements in quadrature for the 3D TRUS (0.21 mm) and 2D TRUS (0.11 mm) images. The results in Table 2.3 failed to show statistical equivalence between all downsample factors and support the decision to determine the optimum downsample factor as 4.

Table 2.3 Equivalence test results of TRE for downsampling factors.

Downsample Factor Comparison	94.26% Median CI	
	Lower	Upper
2 – 4	-0.1665	0.2815[a]
2 – 6	-0.4793[a]	0.0550
4 – 6	-0.3855[a]	-0.0742

[a]Groups are not equivalent with interval = ±0.24 mm

Although having a downsample factor reduced the number of NCC computations, it also reduced the amount of information that needed to be transferred through system memory from the CPU to the GPU. Therefore, by reducing the amount of image data, a reduction in computation times arised from a reduction in data transfer from the CPU to the GPU as well as a reduction in the number of computations. As a reminder for the reader, only TRUS image data is needed to compute a transformation matrix on the GPU. Once the algorithm determines the correction matrix, the transformation can be applied on the CPU to any additional data (*i.e.*, MRI or segmentation data) in a short amount of time that is comparable to what is currently performed using a tracking system.

Although downsampling may introduce aliasing,[42] this was not believed to be a consequential issue for our registration application since we maintained a median TRE below 2.5 mm as the downsampling factor was varied. However, even though our TRE was below an acceptable tolerance of 2.5 mm, reducing the image size used for registration could be removing fine detail structures and prematurely ending the registration iteration loop. With these features removed, the observed 1.5 mm registration error could be the result of emphasized local minima in the NCC cost function. Despite the fact that smaller downsample factors were not observed to be more accurate, a coarse-to-fine downsampling technique could be required to decrease the TRE since these methods are usually more robust to local optima.[43]

Interestingly, reducing the 2D template image size used for registration to a 356×292 pixels AOI (64.08×52.56 mm^2) showed a decrease in TRE. This AOI is larger than an average healthy prostate[44] length and height of approximately 40×30 mm^2 with a volume of 30 cm^3; however, many prostate glands with cancer are often enlarged and can fill this region with anatomical information. Since there is some variability when manually selecting fiducials, the chosen AOI would be influenced by an unknown bias in the TRE measurement given that the TRE was used for AOI selection. Although more image information might intuitively seem necessary for a more accurate registration, having image data outside of the prostate seemed to hinder registration performance. This could be due to the low contrast edges of the bladder or perhaps a lack of acoustic coupling found on the left and right sides of some images. Bladder is also more prone to deformation that may challenge

our rigid registration approach. It should be noted that limiting the area to slightly beyond the average prostate size did not improve registration for every image pair. Despite the presence of the bladder when imaging smaller prostate volumes, the AOI reduction noticeably decreased the overall average error observed.

2.4.2 Direction search order of optimization

To increase the speed of convergence, direction search vectors are typically updated in an efficient manner after the first iteration of optimization in conventional Powell's method. When used in our clinically acquired prostate images, a statistically significant difference was observed when the search order was changed in the first iteration. Searching translation directions first before rotational optimization was shown to be superior in terms of registration accuracy with an overall TRE median ± IQR of 1.40 ± 1.18 mm. A strong correlation (0.644) between initial misalignment and TRE was observed in the rotations first scheme, suggesting the registration algorithm was converging at a local optimum of the NCC function. A primary source of motion we witnessed during prostate biopsy procedures arose from patients moving away from the biopsy gun once the needle was inserted into the tissue. This could result in a translational offset that dominated the overall motion that required compensation. Moreover, if the objective function has quadratic, convex properties, Powell's method should converge at the global optimum irrespective of the initial search direction order. The observed performance dependency on the initial search order, thus, implies non-convexity of the search space challenging the underlying assumptions of Powell's direction set method. The non-convexity of the objective function could be more severe in the rotational directions and therefore these motions could be more susceptible to local optima driving the optimizer away from the desired solution during first steps in the optimization process. A translation first scheme managed to drive the optimizer close to the global optimum and demonstrated robust performance in our experiments when downsampling by a factor of 4 and cropping to an AOI of 356×292. However, there seems to be some interaction effects with downsampling factor, cropped AOI, and optimization order that are currently unpredictable in addition to the small TRE variability due to manual selection of fiducials. It should be noted, the manual selection bias introduced in the TRE can be reduced by having observers select each fiducial multiple

times. Since we selected each fiducial only once, we used the measured FLE as the bias when interpreting Figure 2.4 and Figure 2.5b.

2.4.3 Phantom scanning

In the user-initiated method, motion compensation is performed intermittently and the physician may opt to selectively disregard registration output if it is not satisfactory and repeat the registration. The continuous method, on other hand, provides a more streamlined and automatic mode of clinical implementation of the algorithm with less dependence on manual intervention. However, when implemented on a TRUS-guided biopsy system and tested on a tissue-mimicking phantom, the registration algorithm performed robustly with an overall sub-millimeter and sub-degree error when performing both the user initiated and continuous registration methods. After testing out-of-plane translation, in-plane translation, and roll rotation compensation, the user initiated correction computation time only achieved real-time performance when correcting for out-of-plane motions. During testing of the real-time continuous implementation on the prostate phantom, registration computation times were significantly lower ($p < 0.01$) with less variance than the phantom user initiated correction, overall performing at approximately 36 ± 4 ms (28 Hz). This is approaching the frame rate of the ultrasound system, which updates images at 51 Hz when using a depth of 6 cm with one focal zone, providing near real-time feedback that is sensitive to sudden changes. Results from the user initiated method also supports that the algorithm can compensate for sudden drastic displacements with a temporary increase in computation time of 108 ± 38 ms as a tradeoff, using in-plane motion correction as a reference. The reason for significant difference when testing out-of-plane motion is unknown, but it is likely due to a lack of image features present at the 9 mm displacement. Both methods experienced an increase in registration error up to approximately 1 mm from expected and after scrutinizing the images further, it revealed a minimal presence of agar beads beyond a 6 mm displacement. From this information, it appears that the user initiated method was more suitable to correct for motion when there were reduced image features, but this will need to be investigated further. Although the registration error was significantly lower when performing a user initiated correction during out-of-plane motion, continuous registration still performed with a mean registration error of 0.7 ± 0.4 mm,

which is still below the target error of 2.5 mm. In this case, the clinical benefits provided from a significantly faster computation would likely outweigh the slight decrease in registration error. Results from other studies[25,29] have shown that an increase in registration error will be expected when performed on patient images and this expectation has been alluded to in this study. Since the methods of the clinical image registrations are comparable to the user initiated procedure on the phantom, it can be observed there are sources of error that are not completely captured in the phantom experiment that will need to be investigated in more detailed patient studies. For example, a lack of agar beads could be the underlying cause for a poor registration when performing the out-of-plane translation tests. With clinical images, different image features distributed throughout the acquired 3D TRUS image could potentially lead to different resulting motion compensation trends. However, these results demonstrate robust and real-time registration performance on a phantom and yield valuable insights, encouraging the use of a continuous method for prostate motion compensation during biopsy.

When testing the continuous motion compensation method, variable speeds were not assessed when moving the phantom. Although this matches our minimal motion assumptions between image frames, this might not be realistic of what is observed clinically and could be a potential limitation. In addition, the phantom we fabricated was a rigid body and was proven to be easily compensated using a rigid registration algorithm. Although prostate deformation may occur and has been previously reported to not be an issue for a rigid registration approach,[28,29] the real-time continuous method will need to be verified in patient studies to confirm these findings.

2.5 Conclusions

Real-time registration during prostate biopsy provides key advances by compensating for arbitrary/intermittent motion that hinder accurate targeting of potentially cancerous tissues, decreasing needle targeting error, and improving clinical workflow. Using image downsampling and image cropping with a GPU accelerated optimization, we showed that a significant decrease in computation time can be achieved when performing 3D to 2D rigid registration on human clinical prostate images without any substantial degradation of

registration error. The challenges due to large initialization errors was mitigated after updating the optimization of the conventional Powell's method by systematically searching the image space to avoid local optima. When continuously performing motion compensation, the error of the registration algorithm was shown to have sub-millimeter and sub-degree accuracy with significantly lower computation times than a user initiated correction. Overall registration times of approximately 36 ms were observed, performing near the frame rate of the ultrasound system. With this utility, preoperative annotations and biopsy target locations can continuously be displayed and corrected on live 2D TRUS images, potentially increasing the prostate cancer detection rate of image guided biopsy procedures.

2.6 References

1. Stewart BW, Wild C. *World Cancer Report 2014*. Lyon; 2014.

2. Leite KRM, Camara-Lopes LHA, Dall'Oglio MF, et al. Upgrading the Gleason Score in Extended Prostate Biopsy: Implications for Treatment Choice. *Int J Radiat Oncol Biol Phys*. 2009;73(2):353-356. doi:10.1016/j.ijrobp.2008.04.039

3. Rabbani F, Stroumbakis N, Kava BR, Cookson MS, Fair WR. Incidence and Clinical Significance of False-Negative Sextant Prostate Biopsies. *J Urol*. 1998;159(4):1247-1250. doi: 10.1016/s0022-5347(01)63574-2.

4. Bax J, Cool D, Gardi L, et al. Mechanically assisted 3D ultrasound guided prostate biopsy system. *Med Phys*. 2008;35(12):5397. doi:10.1118/1.3002415

5. Hadaschik BA, Kuru TH, Tulea C, et al. A Novel Stereotactic Prostate Biopsy System Integrating Pre-Interventional Magnetic Resonance Imaging and Live Ultrasound Fusion. *J Urol*. 2011;186(6):2214-2220. doi:10.1016/j.juro.2011.07.102

6. Cool D, Sherebrin S, Izawa J, Chin J, Fenster A. Design and evaluation of a 3D transrectal ultrasound prostate biopsy system. *Med Phys*. 2008;35(10):4695. doi:10.1118/1.2977542

7. Xu S, Kruecker J, Turkbey B, et al. Real-time MRI-TRUS fusion for guidance of targeted prostate biopsies. *Comput Aided Surg*. 2008;13(5):255-264. doi:10.3109/10929080802364645

8. Rastinehad AR, Turkbey B, Salami SS, et al. Improving detection of clinically significant prostate cancer: Magnetic resonance imaging/transrectal ultrasound fusion guided prostate biopsy. *J Urol*. 2014;191(6):1749-1754. doi:10.1016/j.juro.2013.12.007

9. Moore CM, Robertson NL, Arsanious N, et al. Image-guided prostate biopsy using magnetic resonance imaging-derived targets: A systematic review. *Eur Urol*. 2013;63(1):125-140. doi:10.1016/j.eururo.2012.06.004

10. Valerio M, Donaldson I, Emberton M, et al. Detection of clinically significant prostate cancer using magnetic resonance imaging-ultrasound fusion targeted biopsy: A systematic review. *Eur Urol*. 2015;68(1):8-19. doi:10.1016/j.eururo.2014.10.026

11. Arsov C, Rabenalt R, Blondin D, et al. Prospective Randomized Trial Comparing Magnetic Resonance Imaging (MRI)-guided In-bore Biopsy to MRI-ultrasound Fusion and Transrectal Ultrasound-guided Prostate Biopsy in Patients with Prior Negative Biopsies. *Eur Urol*. 2015;68(4):713-720. doi:10.1016/j.eururo.2015.06.008

12. Natarajan S, Marks LS, Margolis DJA, et al. Clinical application of a 3D ultrasound-guided prostate biopsy system. *Urol Oncol*. 2011;29(3):334-342. doi:10.1016/j.urolonc.2011.02.014

13. Van De Ven WJM, Hulsbergen-Van De Kaa CA, Hambrock T, Barentsz JO, Huisman HJ. Simulated required accuracy of image registration tools for targeting high-grade cancer components with prostate biopsies. *Eur Radiol*. 2013;23(5):1401-1407. doi:10.1007/s00330-012-2701-1

14. Kadoury S, Yan P, Xu S, et al. Realtime TRUS/MRI fusion targeted-biopsy for prostate cancer: A clinical demonstration of increased positive biopsy rates. *Lect Notes Comput Sci (including Subser Lect Notes Artif Intell Lect Notes Bioinformatics)*. 2010;6367 LNCS:52-62. doi:10.1007/978-3-642-15989-3_7

15. Hu Y, Ahmed HU, Taylor Z, et al. MR to ultrasound registration for image-guided prostate interventions. *Med Image Anal*. 2012;16(3):687-703. doi:10.1016/j.media.2010.11.003

16. Ukimura O, Desai MM, Palmer S, et al. 3-Dimensional Elastic Registration System of Prostate Biopsy Location by Real-Time 3-Dimensional Transrectal Ultrasound Guidance With Magnetic Resonance/Transrectal Ultrasound Image Fusion. *J Urol*. 2012;187(3):1080-1086. doi:10.1016/j.juro.2011.10.124

17. Sparks R, Nicolas Bloch B, Feleppa E, et al. Multiattribute probabilistic prostate elastic registration (MAPPER): Application to fusion of ultrasound and magnetic resonance imaging. *Med Phys*. 2015;42(3):1153-1163. doi:10.1118/1.4905104

18. Karnik V V., Fenster A, Bax J, Romagnoli C, Ward AD. Evaluation of intersession 3D-TRUS to 3D-TRUS image registration for repeat prostate biopsies. *Med Phys*. 2011;38(4):1832. doi:10.1118/1.3560883

19. Karnik V V, Fenster A, Bax J, et al. Assessment of image registration accuracy in three-dimensional transrectal ultrasound guided prostate biopsy. *Med Phys*. 2010;37(2010):802-813. doi:10.1118/1.3298010

20. Martin PR, Cool DW, Romagnoli C, Fenster A, Ward AD. Magnetic resonance imaging-targeted, 3D transrectal ultrasound-guided fusion biopsy for prostate cancer: Quantifying the impact of needle delivery error on diagnosis. *Med Phys*. 2014;41(7):073504. doi:10.1118/1.4883838

21. Liao R, Zhang L, Sun Y, Miao S, Chefd'Hotel C. A Review of Recent Advances in Registration Techniques Applied to Minimally Invasive Therapy. *IEEE Trans Multimed*. 2013;15(5):983-1000. doi:10.1109/TMM.2013.2244869

22. Markelj P, Tomaževič D, Likar B, Pernuš F. A review of 3D/2D registration methods for image-guided interventions. *Med Image Anal*. 2012;16(3):642-661. doi:10.1016/j.media.2010.03.005

23. Epstein JI, Sanderson H, Carter HB, Scharfstein DO. Utility of saturation biopsy to predict insignificant cancer at radical prostatectomy. *Urology*. 2005;66(2):356-360. doi:10.1016/j.urology.2005.03.002

24. De Silva T, Cool DW, Romagnoli C, Fenster A, Ward AD. Evaluating the utility of intraprocedural 3D TRUS image information in guiding registration for displacement compensation during prostate biopsy. *Med Phys*. 2014;41(8):082901. doi:10.1118/1.4885959

25. Zhang S, Jiang S, Yang Z, Liu R. 2D Ultrasound and 3D MR Image Registration of the Prostate for Brachytherapy Surgical Navigation. *Medicine (Baltimore)*. 2015;94(40):e1643. doi:10.1097/MD.0000000000001643

26. Baumann M, Mozer P, Daanen V, Troccaz J. Prostate biopsy tracking with deformation estimation. *Med Image Anal*. 2012;16(3):562-576. doi:10.1016/j.media.2011.01.008

27. Xu H, Lasso A, Guion P, et al. Accuracy analysis in MRI-guided robotic prostate biopsy. *Int J Comput Assist Radiol Surg*. 2013;8(6):937-944. doi:10.1007/s11548-013-0831-9

28. Venderink W, de Rooij M, Sedelaar J. M, Huisman HJ, Fütterer JJ. Elastic Versus Rigid Image Registration in Magnetic Resonance Imaging–transrectal Ultrasound Fusion Prostate Biopsy: A Systematic Review and Meta-analysis. *Eur Urol Focus*. July 2016. doi:10.1016/j.euf.2016.07.003

29. De Silva T, Fenster A, Cool DW, et al. 2D-3D rigid registration to compensate for prostate motion during 3D TRUS-guided biopsy. *Med Phys*. 2013;40(2):022904. doi:10.1118/1.4773873

30. De Silva T, Fenster A, Bax J, et al. Quantification of prostate deformation due to needle insertion during TRUS-guided biopsy: Comparison of hand-held and mechanically stabilized systems. *Med Phys*. 2011;38(3):1718-1731. doi:10.1118/1.3557883

31. Hajnal J, Hawkes DJ, Hill D. *Medical Image Registration*. Florida: CRC; 2001.

32. Press W, Teukolsky S, Vetterling W, Flannery B. *Numerical Recipes: The Art of Scientific Computing*. 3rd ed. New York: Cambridge University Press; 2007. doi:10.2307/1269484

33. Yoo TS, Ackerman MJ, Lorensen WE, et al. Engineering and Algorithm Design for an Image Processing API: A Technical Report on ITK - The Insight Toolkit. In: Westwood J, ed. *Medicine Meets Virtual Reality*. IOS Press Amsterdam; 2002:586-592.

34. De Silva T, Cool DW, Yuan J, Romognoli C, Fenster A, Ward AD. Improving 2D-3D Registration Optimization Using Learned Prostate Motion Data. In: *Lecture*

Notes in Computer Science (Including Subseries Lecture Notes in Artificial Intelligence and Lecture Notes in Bioinformatics). Vol 8150 LNCS. ; 2013:124-131. doi:10.1007/978-3-642-40763-5_16

35. Fitzpatrick JM, Hill DLG, Maurer CR. Image Registration. In: *Handbook of Medical Image Processing and Analysis, Volume 2:*. Bellingham, WA: SPIE Press; 2000:447-514.

36. Rickey DW, Picot PA, Christopher DA, Fenster A. A wall-less vessel phantom for Doppler ultrasound studies. *Ultrasound Med Biol*. 1995;21(9):1163-1176. doi:10.1016/0301-5629(95)00044-5

37. Fenster A, Downey DB. Three-dimensional ultrasound imaging. *Annu Rev Biomed Eng*. 2000;2:457-475.

38. Ryu B, Bax J, Edirisinge C, et al. Prostate brachytherapy with oblique needles to treat large glands and overcome pubic arch interference. *Int J Radiat Oncol Biol Phys*. 2012;83(5):1463-1472. doi:10.1016/j.ijrobp.2011.10.012

39. Slabaugh GG. *Computing Euler Angles from a Rotation Matrix*. Vol 6.; 1999. http://gregslabaugh.name/publications/euler.pdf.

40. Rogers JL, Howard KI, Vessey JT. Using significance tests to evaluate equivalence between two experimental groups. *Psychol Bull*. 1993;113(3):553-565.

41. Rusticus S a, Lovato CY. Applying Tests of Equivalence for Multiple Group Comparisons : Demonstration of the Confidence Interval Approach. *Pract Assessment, Res Eval*. 2011;16(7):1-6.

42. Bellanger M. Multirate digital signal processing. *IEEE Trans Acoust*. 1984;32(4):941-941. doi:10.1109/TASSP.1984.1164376

43. Oliveira FPM, Tavares JMRS. Medical image registration: a review. *Comput Methods Biomech Biomed Engin*. 2014;17(2):73-93. doi:10.1080/10255842.2012.670855

44. Zhang SJ, Qian HN, Zhao Y, et al. Relationship between age and prostate size. *Asian J Androl*. 2013;15(1):116-20. doi: 10.1038/aja.2012.127. Epub 2012 Dec 1. doi:10.1038/aja.2012.127

Chapter 3

3 Automatic prostate segmentation using deep-learning on clinically diverse 3D transrectal ultrasound images

Minimizing procedure time with an automatic 3D TRUS prostate segmentation method could allow for a more accurate and efficient workflow with improved patient throughput to enable faster patient access to care. The purpose of Chapter 3 is to present on the development of a general automatic prostate segmentation algorithm for image-guided interventions that use 3D TRUS images.

The contents of this chapter have been accepted for publication in *Medical Physics*: Orlando N and Gillies DJ, Gyacskov I, Romagnoli C, D'Souza D, and Fenster A. Medical Physics 2020; 47(6):2413-2426. Permission to reproduce this article was granted by John Wiley and Sons and is provided in Appendix B – Copyright Releases.

3.1 Introduction

Diagnosing and treating prostate cancer continues to burden global populations as it is the second most common noncutaneous cancer among men worldwide.[1] Investigation into methods to diagnose and treat prostate cancer has shifted towards improved needle-based approaches that utilize three-dimensional (3D) information intraoperatively. Magnetic resonance imaging (MRI)-3D transrectal ultrasound (TRUS) guided biopsy is one diagnostic method that fuses the superior soft-tissue contrast of MRI to accurately localize, target, and sample suspicious tissue regions for prostate cancer with the real-time, low-cost, and portable capabilities of ultrasound. In the treatment of prostate cancer, high- and low-dose-rate (H/LDR) brachytherapy (BT) procedures offer therapeutic benefits for patients by exploiting radiobiological effects and offering shorter treatment times, while minimizing adverse side effects. By adding 3D ultrasound intraoperatively, improved spatial context and targeting can be achieved to further improve the conventional clinical workflow of biopsy and brachytherapy procedures; however, both procedures rely on accurate segmentation of the prostate in 3D TRUS images to perform necessary clinical tasks. This includes surface-based registration approaches with MRI[2] and subsequent 3D TRUS images,[3] glandular volume measurements,[4,5] and dose-volume calculations,[6] especially when using a commercial guidance system. These segmentations are predominantly performed manually during the

procedure, which is time-consuming, variable, and often difficult, which can lead to increased patient risk due to increased anesthesia exposure.[7]

Minimizing procedure time through fully or semi-automatic 3D TRUS prostate segmentation has been previously investigated.[8–11] Many methods have been shown to be promising, but have lacked clinical translation due to computational complexity, computation time, and robustness to diverse clinical datasets. Convolutional neural networks (CNNs) have received widespread attention in many image processing applications with much work investigating their accuracy and speed in medical imaging tasks. Prostate segmentation in 3D TRUS is an image processing task that could be an ideal candidate for the data-driven predictions provided by CNNs, although most existing work has investigated their application in MRI,[12,13] as ultrasound is considered more challenging due to noise and image artifacts.

Recent work has investigated and provided promising results for the use of CNNs in 2D TRUS[14] and 3D TRUS[15,16] prostate segmentation. Ghavami *et al*.,[15] evaluated the performance of an adapted U-Net on 109 side-fire sagittally-reconstructed (SR) 3D TRUS images. Predictions were performed on acquired 2D images and varying adjacent neighboring slices were also investigated to evaluate accuracy due to increasing spatial 3D context. The best results reported for the 2D Dice similarity coefficient (DSC), 3D DSC, and boundary distance were 89 ± 12 %, 89 ± 5 %, and 1.68 ± 1.57 mm, respectively. Lei *et al*.,[16] investigated a multidirectional deeply supervised 3D V-Net with contour refinement on 44 patient 3D TRUS images. Their method was shown to improve performance when segmenting the apex and base of the prostate, which is often difficult due to low image contrast, and reported overall segmentation results for a 3D DSC, Hausdorff distance (HD), mean surface distance (MSD), and residual mean surface distance (RMSD) of 92 ± 3 %, 3.94 ± 1.55 mm, 0.60 ± 0.23 mm, and 0.90 ± 0.38 mm, respectively. However, these methods were tested using cross-validation approaches on 3D TRUS images from a single ultrasound machine with matched voxel dimensions and sizes, so further testing is still required on an unseen and variable dataset to provide a complete understanding of performance while avoiding potential limitations due to information bleeding.[17,18] Furthermore, investigations into generalizability across procedures and

acquisition geometries have been limited, to our knowledge, which could restrict usability when applying these techniques across applications.

Our work aims to demonstrate that a diverse image dataset can train a supervised CNN to provide an accurate, fast, automated, and generalizable 3D prostate segmentation prediction. We used 206 3D TRUS patient images from two different procedures and acquisition geometries, two facilities, and four transducers used with three different ultrasound machine models to modify and train a deep learning-based 2D segmentation method followed by reconstruction into a 3D surface. Since deep learning approaches often improve in performance when using large datasets (*i.e.*, >1000 images), we chose to reslice each 3D image to increase the amount of usable data for prostate segmentation training and prediction. Testing was performed on 40 unseen 3D TRUS patient images and segmentation performance was compared to state-of-the-art fully 3D approach's for assessing the impact of reducing spatial context. Various metrics are reported in the literature, and typically vary in choice and quantity between studies, but many metrics are required to obtain a complete understanding of segmentation performance and to allow for comparison with previous studies. By using a clinically diverse dataset with variable image representation and image quality of the prostate, we intend to provide a thorough analysis of performance for a broader scope of comparison. Once this method is evaluated, completion of required intraoperative image-guidance tasks can be facilitated for different needle-based prostate cancer procedures and potentially decrease overall clinical procedure times and anesthesia risks to patients.

3.2 Materials and methods

3.2.1 Clinical dataset

3D images of the prostate were acquired using end-fire (as used in prostate biopsy) and side-fire SR (as used in some HDR-BT) mechanical scanning approaches (Figure 3.1).[19] Both methods rotate a TRUS transducer around the long-axis to create geometrically different reconstructed 3D images that are influenced by the transducer array configuration. The images used in this study were acquired with the C9-5 transducer with the iU22 (Philips, Amsterdam, the Netherlands), the C9-5 and BPTRT9-5 transducers with the ATL

HDI-5000 (Philips, Amsterdam, the Netherlands), and the 8848 transducer with the Profocus 2202 (BK Medical, Peabody, MA, United States) ultrasound machine models. The total dataset of 246 3D TRUS images consisted of 104 end-fire and 142 side-fire 3D TRUS images and was split into training, validation, and testing datasets as shown in Table 3.1. Manual 3D prostate segmentations (excluding the seminal vesicles) were performed by an observer (IG) with approximately 15 years of TRUS prostate image analysis experience. 3D image sizes ranged from [300×400×784] to [408×441×870] voxels with dimensions of [0.094×0.154×0.154] to [0.183×0.186×0.186] mm^3/voxel for side-fire images and from [448×350×448] to [692×520×692] voxels with dimensions of [0.115×0.115×0.115] to [0.190×0.195×0.190] mm^3/voxel for end-fire images.

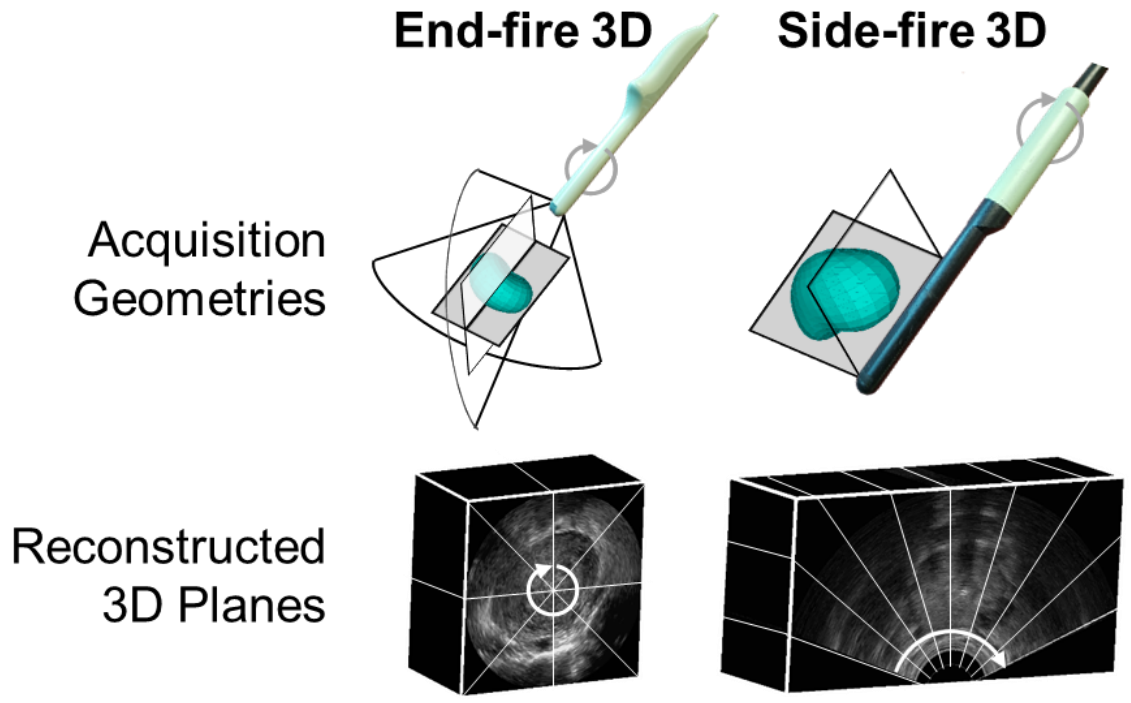

Figure 3.1 Mechanical scanning approaches for acquiring 3D TRUS prostate images using end-fire (left) and side-fire (right) TRUS transducers. 2D images are acquired by rotating around the long axis of the transducer at known sample spacings to create 3D TRUS images. Example 3D TRUS images are shown in the bottom row, with the front face demonstrating the reconstructed image plane and the white lines showing representative acquisition planes.

Table 3.1 Clinical 3D TRUS dataset split based on end-fire and side-fire scan geometries and resulting training, validation, and testing datasets used for deep learning.

Image	Training	Validation	Testing	Total
End-fire	67	17	20	104
Side-fire	98	24	20	142
Total	165	41	40	246

3.2.2 3D segmentation algorithm

A workflow diagram of our proposed method is shown in Figure 3.2. This includes 3D TRUS prostate image input, radial sampling, prediction using a trained modified U-Net, 3D reconstruction, and 3D prostate surface output.

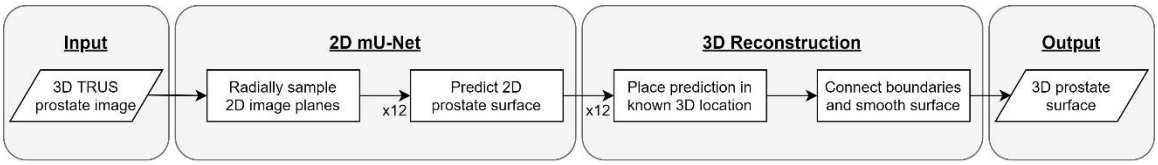

Figure 3.2 Proposed 3D prostate segmentation workflow. A 3D TRUS prostate image is used as input, followed by radial sampling to generate 12 2D image planes. Each image plane was used to predict a prostate boundary with a trained modified U-Net prior to reconstruction into the 3D prostate surface.

3.2.2.1 Training dataset for modified U-Net

Images from the training and validation split were used to obtain resliced 2D images of the prostate. These 2D images were obtained at randomized axial, sagittal, coronal, radial, and oblique image planes with varying rotations and zooms. This resulted in a dataset of 6,773 2D TRUS images with matched manual contours. All 2D images were resized to 256×256 pixels with no preprocessing (*i.e.*, despeckling or bias correction) and were separated into an 80/20 training/validation split for deep learning, resulting in 5418 training and 1355 validation 2D TRUS images.

3.2.2.2 Modified U-Net

The previously published U-Net[20] was implemented using Keras[21] with TensorFlow[22] and modified by adding 50% dropouts at every block on the expansion section of the network to increase regularization and prevent overfitting. In addition, transpose convolutions were

used at each step in the expansion section instead of the standard upsampling followed by convolution, as this allowed for improved performance in preliminary experiments. Data augmentation from random combinations of horizontal flips, 2D shifts (up to 20%), rotations (up to 20°), and zooms (up to 20%) were employed to double the training dataset to 10,836 2D TRUS images. Preliminary experiments led to the selection of an Adam optimizer, 0.0001 learning rate, Dice-coefficient loss function, 200 epochs, and 200 steps per epoch. This network was trained and used for predicting unseen data on a personal computer with two Xeon E5645 central processing units at 2.40 GHz (Intel Corporation, Santa Clara, CA, USA), 24.0 GB of memory, and a 6 GB Ge-Force GTX TITAN (NVIDIA Corporation, Santa Clara, CA, USA) graphics processing unit (GPU).

3.2.2.3 3D reconstruction

Predicted 3D prostate segmentations were obtained by segmenting multiple 2D radial frames generated by rotation around a central axis, followed by reconstruction to a 3D surface following a reconstruction method similar to Qiu *et al*.[11] Previous observations have noted that segmenting the prostate on slices near the apex and base of the prostate can be challenging due to boundary incompleteness,[15] so we chose to radially slice the 3D prostate image as opposed to transverse slicing in an attempt to improve segmentations at all boundaries. This choice was motivated by the experience of segmenting the prostate when the center of the gland is in-plane, which typically presents as an easier image to accurately define and segment the boundaries on the left and right sides of the 2D image. In contrast to this, a transverse slicing approach would result in 2D images with the prostate appearing as a different size and shape, with this difference more pronounced at the prostate apex and base, and when comparing end-fire and side-fire image geometries. Difficulty arises, predominantly in side-fire geometries, when segmenting the ends of the prostate along the axis of acquisition (when using a 2D approach) due to the changes in prostate appearance and size. Thus, radially slicing and segmenting the prostate in these views allows for a method that can train and predict on images containing similar structural shapes, across different acquisition geometries.

Reconstructing a 3D contour was accomplished by radially slicing a 3D image in equal 15° spacings around the approximate central axis of the prostate (Figure 3.3) to produce 12 2D

images for prediction. These 12 images were predicted using the trained modified U-Net to produce 2D prostate segmentations, and 204 equally spaced points were sampled around the boundary of each 2D image. Since the original spatial location of the input 2D image in the 3D volume was known, each predicted 2D segmentation was placed appropriately back into the 3D volume and the boundary points on each segmentation were connected to the adjacent slices. The intermediate surface was smoothed by a windowed *sinc* filter, resulting in a final reconstructed 3D contour.

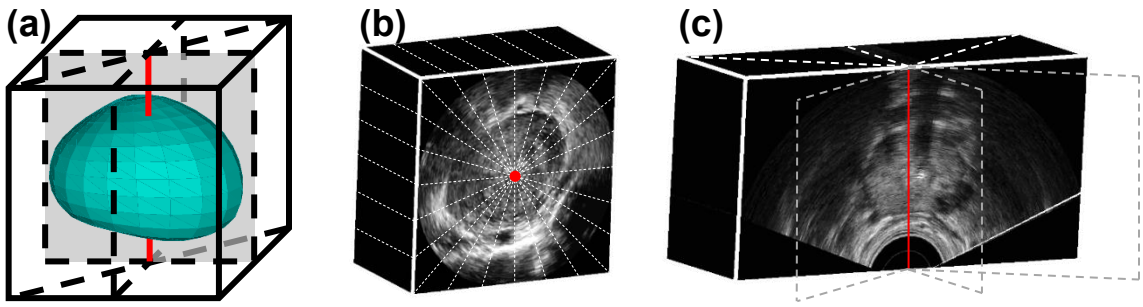

Figure 3.3 (a) Method for acquiring radially sliced 2D TRUS image planes (dotted lines) from previously acquired 3D TRUS images. The axis of rotation (red) is approximately at the central axis of the prostate and in the anterior-posterior direction. (b) 12 image slices were obtained to perform prostate segmentation. For an end-fire 3D TRUS image, 2D images are about the axis of image acquisition. (c) The majority of image slices obtained from side-fire 3D TRUS images are across many acquisition slices and are subject to increased interpolation, except for one slice, which matched the original acquired 2D TRUS image.

3.2.3 Evaluation and comparison

Our algorithm was evaluated on a test data set of 20 unseen end-fire and 20 unseen side-fire 3D TRUS images of the prostate. Standard pixel map comparisons (DSC, recall, precision) were computed for both 2D radial slice segmentations and the reconstructed 3D segmentation for each prostate to obtain an understanding of the prediction quality and reconstruction accuracy. We also computed absolute area/volume percent differences (A/VPD), absolute mean surface distances (MSD), and absolute Hausdorff distances (HD), as well as signed A/VPD (sA/VPD), signed MSD (sMSD), and signed HD (sHD) for all 2D predictions and reconstructed 3D segmentations. The signed metrics, while not commonly reported, are important as they provide information on the segmentation bias

and whether the prostate boundary is over or underpredicted. The inclusion of these metrics will provide a more complete understanding of the performance of our proposed method. All pixel map comparisons and 2D MSD/sMSD and HD/sHD distance metrics were computed using MATLAB R2019a (MathWorks, Natick, MA, United States). The 3D MSD/sMSD and HD/sHD metrics were computed by measuring the distances between all points of the automatically predicted segmentation to the closest point on the manual gold-standard segmentation (CloudCompare v2.10.2).[23] For comparison purposes, the MSD reported here is similar to the boundary distance[15] and mean surface distance[16] presented previously. Computation times were recorded for 2D slice segmentation, 3D reconstruction, and overall 3D segmentation time.

The performance of our algorithm was compared against three state-of-the-art fully 3D predicting CNNs (V-Net,[24] Dense V-Net,[25] and High-resolution 3D-Net[26]) using an open-source implementation on the NiftyNet platform.[27] It is often assumed that performing a prediction based on 3D information allows for an improved result due to increased spatial context, so we completed a direct comparison on the same test dataset to investigate this hypothesis. Similar to our proposed method, the same 165/41 3D TRUS images (Table 3.1) were used for training/validation, respectively. The 3D V-Net was chosen to optimize hyperparameters, including loss function, due to its widespread use and performance in preliminary experiments. For simplicity, these hyperparameters were also used for the Dense V-Net and High-resolution 3D-Net. Parameters were chosen to maximize the spatial window size and usable memory on the GPU with optimized hyperparameters shown in Table 3.2. Previous work has shown improved performance with a hybrid loss function,[16] so we compared performance between a Dice loss function and a Dice plus cross-entropy (DiceXEnt) loss function, as provided in NiftyNet, using the 3D V-Net. Although NiftyNet offers a patch-based analysis, preliminary experiments resulted in 3D segmentations with many flat surfaces throughout the prediction corresponding to patch edges. Since we had one structure of interest (*i.e.*, the prostate), we did not perform a patch-based analysis and predictions were performed on a resized image to match the spatial window. Data augmentation was employed to double the training dataset to 330 3D TRUS images. The chosen hyperparameters for the Dense V-Net and High-resolution 3D-Net were the same as shown in Table 3.2 (with the DiceXEnt loss function). These networks were trained and

used for predicting unseen data on a personal computer with an Intel Core i7-4770 central processing unit at 3.40 GHz (Intel Corporation, Santa Clara, CA, USA), 32.0 GB of memory, and a 6 GB Ge-Force GTX TITAN (NVIDIA Corporation, Santa Clara, CA, USA) graphics processing unit (GPU). Training and 3D segmentation computation times were recorded.

Table 3.2 Hyperparameter selection when employing the V-Net in NiftyNet.

Hyperparameter	Value
Optimizer	Adam
Loss function	Dice and Dice + cross-entropy
Activation function	PReLU
Learning rate	0.0001
Spatial window size	[64, 64, 64]
Mini-batch size	2
Weighted L2-decay	0.0001

3.2.4 Statistical analysis

Statistical calculations were performed in GraphPad Prism 8.3 (Graphpad Software, Inc., San Diego, CA, USA). The normality of distributions was evaluated using the Shapiro-Wilk test and led to the use of nonparametric statistical tests when the assumption was violated. The corresponding nonparametric alternative tests are presented in parentheses for the remainder of the section. The significance level for statistical analysis was chosen such that the probability of making a type I error was less than 5% ($p < 0.05$), with statistically significant differences denoted simply as significant for the remainder of this manuscript.

2D radial slice segmentation and 3D reconstructed segmentation accuracy as well as Dice and DiceXEnt 3D V-Net loss functions were compared using two-tailed paired t-tests (Wilcoxon matched-pairs signed-rank tests). Comparisons between our proposed algorithm and three fully 3D CNNs were performed using two-tailed paired t-tests (Wilcoxon matched-pairs signed-rank tests) with a Bonferroni multiple-comparison correction, which adjusted the significance level to $p < 0.0167$. Comparisons between segmentation accuracy for end-fire and side-fire 3D TRUS images on each network were completed using two-tailed unpaired t-tests (Mann-Whitney tests).

3.3 Results

3.3.1 Reconstructed modified U-Net

The results of our modified U-Net for 2D prostate segmentation and the effects of reconstruction on 3D surface generation are shown in Table 3.3 and Table 3.4 for the absolute and signed evaluation metrics, respectively. Overall, our proposed method generated 3D surfaces with a median [first quartile (Q1), third quartile (Q3)] 3D DSC, recall, and precision of 94.1 [92.6, 94.9] %, 96.0 [93.1, 98.5] %, and 93.2 [88.8, 95.4] %, respectively, for the pixel map comparison metrics. Absolute VPD, MSD, and HD metrics resulted in 5.78 [2.49, 11.5] %, 0.89 [0.73, 1.09] mm, and 2.89 [2.37, 4.35] mm with signed metrics of 2.38 [-2.98, 11.0] %, 0.11 [-0.24, 0.58] mm, and 2.02 [-3.34, 2.88] mm, respectively. All metrics, aside from the absolute and signed HD metrics, showed significant differences between the 2D predictions and 3D reconstructed segmentations. Interestingly, recall and MSD metrics were observed to significantly improve in performance after 3D reconstruction, with the HD metric improving as well when evaluating all unseen images. These findings agreed when splitting the results into end-fire and side-fire 3D TRUS images, other than end-fire A/VPD and the signed metrics. For end-fire images, absolute VPD increased after 3D reconstruction, although this was not significant, while the signed metrics significantly improved after 3D reconstruction. For side-fire images, the opposite was true, with signed metrics significantly improved for 2D slice segmentations. When comparing the performance of our proposed method between end-fire and side-fire 3D TRUS images, we found there was no significant difference in any metric for both 2D radial segmentations and 3D reconstructed segmentations. Mean computation times were observed to be 0.029 s for each 2D segmentation (*i.e.*, 12 images) and 0.27 s for reconstruction into a 3D surface, resulting in a total throughput time of 0.62 s from 3D image input to generated 3D surface.

Table 3.3 Absolute median [Q1, Q3] results comparing 2D radial slice segmentation to 3D reconstructed segmentation on an unseen test dataset of 20 end-fire and 20 side-fire 3D TRUS images of the prostate.

Acquisition	Segmentation	DSC (%)	Recall (%)	Precision (%)	A/VPD (%)	MSD (mm)	HD (mm)
End-fire	2D Radial	**95.0 [93.6, 95.6]**	94.5 [92.7, 97.2]	**95.9 [92.2, 97.4]**	**4.71 [1.71, 7.32]**	1.16 [0.95, 1.37]	3.64 [3.11, 4.47]
	3D Reconstruction	94.3 [93.1, 95.2]	**96.0 [93.2, 98.7]**	94.6 [88.8, 95.8]	5.18 [1.62, 11.2]	**0.99 [0.78, 1.18]**	**3.41 [2.49, 4.41]**
	p-value	0.0052*	0.0102*	<0.0001	0.0532	<0.0001*	0.5217
Side-fire	2D Radial	**94.6 [92.7, 95.4]**	95.3 [90.6, 96.9]	**94.9 [92.6, 96.4]**	**4.05 [1.07, 6.23]**	0.95 [0.82, 1.26]	3.15 [2.51, 4.27]
	3D Reconstruction	93.5 [91.1, 94.6]	**96.2 [92.5, 98.4]**	91.6 [87.8, 94.8]	5.89 [3.17, 11.9]	**0.78 [0.67, 0.98]**	**2.61 [2.32, 4.01]**
	p-value	0.0037	0.0215	<0.0001*	0.0441	<0.0001	0.3683
Overall	2D Radial	**94.9 [93.2, 95.5]**	94.9 [91.9, 97.0]	**95.6 [92.6, 96.7]**	**4.34 [1.60, 6.77]**	1.06 [0.85, 1.32]	3.34 [2.61, 4.41]
	3D Reconstruction	94.1 [92.6, 94.9]	**96.0 [93.1, 98.5]**	93.2 [88.8, 95.4]	5.78 [2.49, 11.5]	**0.89 [0.73, 1.09]**	**2.89 [2.37, 4.35]**
	p-value	<0.0001	0.0005	<0.0001	0.0061	<0.0001*	0.2766

DSC, Dice similarity coefficient; A/VPD, area/volume percent diff.; MSD, mean surface dist.; HD, Hausdorff dist.
*Normal distribution = paired t-test; Bolded metrics highlight the method with reduced relative error.

Table 3.4 Signed median [Q1, Q3] results comparing 2D radial slice segmentation to 3D reconstructed segmentation on an unseen test dataset of 20 end-fire and 20 side-fire 3D TRUS images of the prostate.

Acquisition	Segmentation	sA/VPD (%)	sMSD (mm)	sHD (mm)
End-fire	2D Radial	-1.39 [-3.82, 5.82]	-0.13 [-0.50, 0.71]	-0.91 [-2.74, 2.81]
	3D Reconstruction	**-0.05 [-2.98, 11.2]**	**0.06 [-0.38, 0.85]**	**-0.34 [-3.82, 3.28]**
	p-value	0.0011*	<0.0001*	0.9563
Side-fire	2D Radial	**-0.57 [-5.24, 3.27]**	**0.09 [-0.46, 0.31]**	**-0.31 [-1.83, 1.72]**
	3D Reconstruction	3.20 [-2.96, 10.1]	0.20 [-0.22, 0.46]	2.25 [-2.53, 2.81]
	p-value	0.0001*	<0.0001*	0.2305
Overall	2D Radial	**-0.91 [-4.93, 4.20]**	**-0.09 [-0.46, 0.37]**	**-0.91 [-2.15, 2.02]**
	3D Reconstruction	2.38 [-2.98, 11.0]	0.11 [-0.24, 0.58]	2.02 [-3.34, 2.88]
	p-value	<0.0001*	<0.0001*	0.3611

sA/VPD, signed area/volume percent diff.; sMSD, signed mean surface dist.; sHD, signed Hausdorff dist.
*Normal distribution = paired t-test; Bolded metrics highlight the method with reduced relative error.

3.3.2 3D CNNs and V-Net optimization

Table 3.5 Absolute median [Q1, Q3] results comparing a standard 3D V-Net with a Dice similarity coefficient loss function to a Dice similarity plus cross-entropy (DiceXEnt) loss function on an unseen test dataset of 20 end-fire and 20 side-fire 3D TRUS images of the prostate.

Acquisition	Loss function	DSC (%)	Recall (%)	Precision (%)	VPD (%)	MSD (mm)	HD (mm)
End-fire	Dice	89.5 [84.6, 92.0]	**97.8 [94.6, 98.3]**	83.7 [75.1, 88.4]	17.8 [7.57, 30.7]	1.79 [1.43, 2.47]	8.64 [7.53, 10.8]
	DiceXEnt	**91.7 [89.0, 93.2]**	91.7 [86.8, 94.6]	**94.3 [87.1, 95.8]**	**7.94 [2.95, 12.5]**	**1.32 [0.99, 1.77]**	**6.95 [5.06, 9.10]**
	p-value	0.0037	<0.0001	<0.0001	0.0021	0.0009	0.0172
Side-fire	Dice	90.6 [89.1, 93.2]	**94.5 [91.1, 96.0]**	92.8 [89.9, 96.9]	9.08 [4.35, 14.0]	1.16 [0.89, 1.46]	5.81 [3.85, 9.61]
	DiceXEnt	**91.2 [87.4, 92.8]**	89.5 [80.7, 92.9]	**95.0 [90.8, 97.5]**	**7.71 [3.55, 15.9]**	**1.11 [0.84, 1.47]**	**4.92 [4.28, 6.55]**
	p-value	0.2943	<0.0001	0.0001	0.7012	0.7562	0.2305
Overall	Dice	90.3 [86.5, 92.1]	**95.5 [92.5, 97.8]**	87.8 [81.0, 91.7]	11.4 [4.66, 19.3]	1.46 [1.16, 2.07]	7.99 [5.34, 10.4]
	DiceXEnt	**91.3 [88.6, 93.1]**	90.0 [85.6, 93.3]	**94.5 [90.0, 96.5]**	**7.94 [3.55, 13.4]**	**1.27 [0.92, 1.61]**	**6.18 [4.51, 7.82]**
	p-value	0.1538	<0.0001	<0.0001	0.0356	0.0147	0.0067

DSC, Dice similarity coefficient; VPD, volume percent difference; MSD, mean surface dist.; HD, Hausdorff dist.
*Normal distribution = paired t-test; Bolded metrics highlight the loss function with reduced relative error.

Table 3.6 Signed median [Q1, Q3] results comparing a standard 3D V-Net with a Dice loss function to a Dice plus cross-entropy (DiceXEnt) loss function on an unseen test dataset of 20 end-fire and 20 side-fire 3D TRUS images of the prostate.

Acquisition	Loss function	sVPD (%)	sMSD (mm)	sHD (mm)
End-fire	Dice	17.8 [7.57, 30.7]	1.51 [0.85, 2.23]	7.99 [5.37, 10.84]
	DiceXEnt	**-2.16 [-8.47, 6.10]**	**-0.07 [-0.71, 0.68]**	**-0.05 [-7.33, 6.50]**
	p-value	<0.0001*	<0.0001*	0.0009
Side-fire	Dice	**5.02 [0.93, 11.5]**	0.43 [0.16, 0.80]	5.34 [3.18, 9.61]
	DiceXEnt	-5.50 [-15.6, -0.62]	**-0.30 [-0.88, 0.02]**	**-4.52 [-6.27, -3.04]**
	p-value	<0.0001*	<0.0001*	<0.0001
Overall	Dice	9.63 [3.90, 18.9]	0.83 [0.35, 1.78]	6.91 [3.35, 10.31]
	DiceXEnt	**-3.66 [-9.25, 3.34]**	**-0.13 [-0.73, 0.26]**	**-4.16 [-7.04, 4.76]**
	p-value	<0.0001*	<0.0001*	<0.0001*

sVPD, signed volume percent difference; sMSD, signed mean surface dist.; sHD, signed Hausdorff dist.
*Normal distribution = paired t-test; Bolded metrics highlight the loss function with reduced relative error.

Results of the NiftyNet 3D V-Net with a Dice and DiceXEnt loss function on 20 unseen end-fire and 20 unseen side-fire 3D TRUS images are shown in Table 3.5 and Table 3.6 for the absolute and signed evaluation metrics, respectively. When comparing 3D V-Net performance with Dice and DiceXEnt loss functions on the full testing dataset, all metrics, aside from DSC, showed significant differences. Precision, VPD/sVPD, MSD/sMSD, and HD/sHD were significantly improved with the DiceXEnt loss function, while recall was significantly improved with the Dice loss function. Although there was no significant difference in the DSC metric, the DiceXEnt loss function showed an improved median DSC. When considering end-fire and side-fire images individually, identical trends were observed for precision, recall, sMSD, and sHD. For the DSC, VPD, MSD, and HD metrics, we observed a significant and nonsignificant increase in performance with the DiceXEnt loss function for end-fire images and side-fire images, respectively. For end-fire images, the sVPD metric improved significantly with the DiceXEnt loss function, while the sVPD metric improved significantly with the Dice loss function for side-fire images. When comparing the 3D V-Net performance with DiceXEnt between end-fire and side-fire 3D TRUS images, we found no significant differences in any metric except HD, where side-fire images had a significantly reduced median value compared to end-fire images. Overall, the 3D V-Net showed improved performance with the DiceXEnt loss function and produced 3D segmentations with median [Q1, Q3] 3D DSC, recall, and precision results of 91.3 [88.6, 93.1] %, 90.0 [85.6, 93.3] %, and 94.5 [90.0, 96.5] %, respectively, for the pixel map comparison metrics. Absolute VPD, MSD, and HD metrics resulted in 7.94 [3.55, 13.4] %, 1.27 [0.92, 1.61] mm, and 6.18 [4.51, 7.82] mm with signed variants of -3.66 [-9.25, 3.34] %, -0.13 [-0.73, 0.26] mm, and -4.16 [-7.04, 4.76] mm, respectively. Mean computation times were observed to be 3.43 s for a full 3D segmentation.

Results of the Dense V-Net and High-resolution 3D-Net with a DiceXEnt loss function on 20 unseen end-fire and 20 unseen side-fire 3D TRUS images are shown in Table 3.A1 and Table 3.A2 in Supplement A for the absolute and signed evaluation metrics, respectively. Compared to the 3D V-Net, the High-resolution 3D-Net showed a reduction in median performance for all metrics, while the Dense V-Net showed a reduction in performance for all metrics except recall. In contrast with our proposed method and the 3D V-Net, we observed significant differences in segmentation performance for several metrics when

comparing end-fire and side-fire 3D TRUS images using the Dense V-Net and High-resolution 3D-Net. For the Dense V-Net, improved performance was observed on side-fire images for every metric except recall, with significant differences observed for the precision, recall, VPD/sVPD, and sMSD metrics. For the High-resolution 3D-Net, improved performance was observed on end-fire images for every metric except precision and HD, with significant differences observed for the DSC, precision, recall, VPD/sVPD, and sMSD metrics. Mean 3D segmentation times for the Dense V-Net and High-resolution 3D-Net were observed to be 2.98 s and 2.83 s, respectively.

3.3.3 Comparison of reconstructed modified U-Net and 3D CNNs

Sample segmentation results from the 20 unseen end-fire and 20 unseen side-fire 3D TRUS images from our proposed method compared against the 3D V-Net with a DiceXEnt loss function and manual segmentations are shown in Figure 3.4 and Figure 3.5, respectively. A comparison of segmentation performance between our proposed method and a standard 3D V-Net is shown in Table 3.7 and Table 3.8 for the absolute and signed evaluation metrics, respectively. Overall, our proposed method had significantly improved DSC, Recall, sVPD, MSD/sMSD, and HD when compared to the 3D V-Net. Absolute VPD and sHD, while not significantly different, were reduced for our proposed method. The only evaluation metric where the 3D V-Net outperformed our proposed method was precision, where the 3D V-Net showed a nonsignificant increase. Considering segmentation performance for end-fire and side-fire 3D TRUS images separately, similar trends hold. For end-fire images, our proposed method had better performance in all metrics except sHD, with DSC, recall, sVPD, MSD, and HD showing significant differences, and precision, VPD, and sMSD showing nonsignificant improvements. However, for side-fire images our proposed method was superior in all metrics except precision. Significant improvements were shown for DSC, recall, sVPD, MSD/sMSD, and HD/sHD, while the 3D V-Net had significantly improved precision. As was observed in the overall case, our proposed method showed a nonsignificant decrease in VPD compared to the 3D V-Net for both end-fire and side-fire images.

Overall, our proposed method significantly improved performance on all metrics when compared to the Dense V-Net and showed improved performance on all metrics when

compared to the High-resolution 3D-Net, with significant differences observed for all metrics except precision, sMSD, and sHD, where our method showed a nonsignificant improvement.

Table 3.7 Absolute median [Q1, Q3] results comparing a standard 3D V-Net to our proposed reconstructed modified (rm) U-Net on an unseen test dataset of 20 end-fire and 20 side-fire 3D TRUS images of the prostate.

Acquisition	Segmentation	DSC (%)	Recall (%)	Precision (%)	VPD (%)	MSD (mm)	HD (mm)
End-fire	V-Net	91.7 [89.0, 93.2]	91.7 [86.8, 94.6]	94.3 [87.1, 95.8]	7.94 [2.95, 12.5]	1.32 [0.99, 1.77]	6.95 [5.06, 9.10]
	rmU-Net	**94.3 [93.1, 95.2]**	**96.0 [93.2, 98.7]**	**94.6 [88.8, 95.8]**	**5.18 [1.62, 11.2]**	**0.99 [0.78, 1.18]**	**3.41 [2.49, 4.41]**
	p-value	0.0003*	<0.0001*	0.5459	0.4980	0.0003*	<0.0001
Side-fire	V-Net	91.2 [87.4, 92.8]	89.5 [80.7, 92.9]	**95.0 [90.8, 97.5]**	7.71 [3.55, 15.9]	1.11 [0.84, 1.47]	4.92 [4.28, 6.55]
	rmU-Net	**93.5 [91.1, 94.6]**	**96.2 [92.5, 98.4]**	91.6 [87.8, 94.8]	**5.89 [3.17, 11.9]**	**0.78 [0.67, 0.98]**	**2.61 [2.32, 4.01]**
	p-value	0.0073	0.0002	0.0153	0.2611	0.0027	0.0001
Overall	V-Net	91.3 [88.6, 93.1]	90.0 [85.6, 93.3]	**94.5 [90.0, 96.5]**	7.94 [3.55, 13.4]	1.27 [0.92, 1.61]	6.18 [4.51, 7.82]
	rmU-Net	**94.1 [92.6 , 94.9]**	**96.0 [93.1, 98.5]**	93.2 [88.8, 95.4]	**5.78 [2.49, 11.5]**	**0.89 [0.73, 1.09]**	**2.89 [2.37, 4.35]**
	p-value	<0.0001	<0.0001	0.1499	0.1701	<0.0001*	<0.0001

DSC, Dice similarity coefficient; VPD, volume percent difference; MSD, mean surface dist.; HD, Hausdorff dist.
*Normal distribution = paired t-test; Bolded metrics highlight the method with reduced relative error.

Table 3.8 Signed median [Q1, Q3] results comparing a standard 3D V-Net to our proposed reconstructed modified (rm) U-Net on an unseen test dataset of 20 end-fire and 20 side-fire 3D TRUS images of the prostate.

Acquisition	Segmentation	sVPD (%)	sMSD (mm)	sHD (mm)
End-fire	V-Net	-2.16 [-8.47, 6.10]	-0.07 [-0.71, 0.68]	**-0.05 [-7.33, 6.50]**
	rmU-Net	**-0.05 [-2.98, 11.2]**	**0.06 [-0.38, 0.85]**	-0.34 [-3.82, 3.28]
	p-value	0.0030*	0.0444*	0.7942*
Side-fire	V-Net	-5.50 [-15.6, -0.62]	-0.30 [-0.88, 0.02]	-4.52 [-6.27, -3.04]
	rmU-Net	**3.20 [-2.96, 10.1]**	**0.20 [-0.22, 0.46]**	**2.25 [-2.53, 2.81]**
	p-value	0.0001*	0.0025*	0.0107
Overall	V-Net	-3.66 [-9.25, 3.34]	-0.13 [-0.73, 0.26]	-4.16 [-7.04, 4.76]
	rmU-Net	**2.38 [-2.98, 11.0]**	**0.11 [-0.24, 0.58]**	**2.02 [-3.34, 2.88]**
	p-value	<0.0001*	0.0003*	0.0408

sVPD, signed volume percent difference; sMSD, signed mean surface dist.; sHD, signed Hausdorff dist.
*Normal distribution = paired t-test; Bolded metrics highlight the method with reduced relative error.

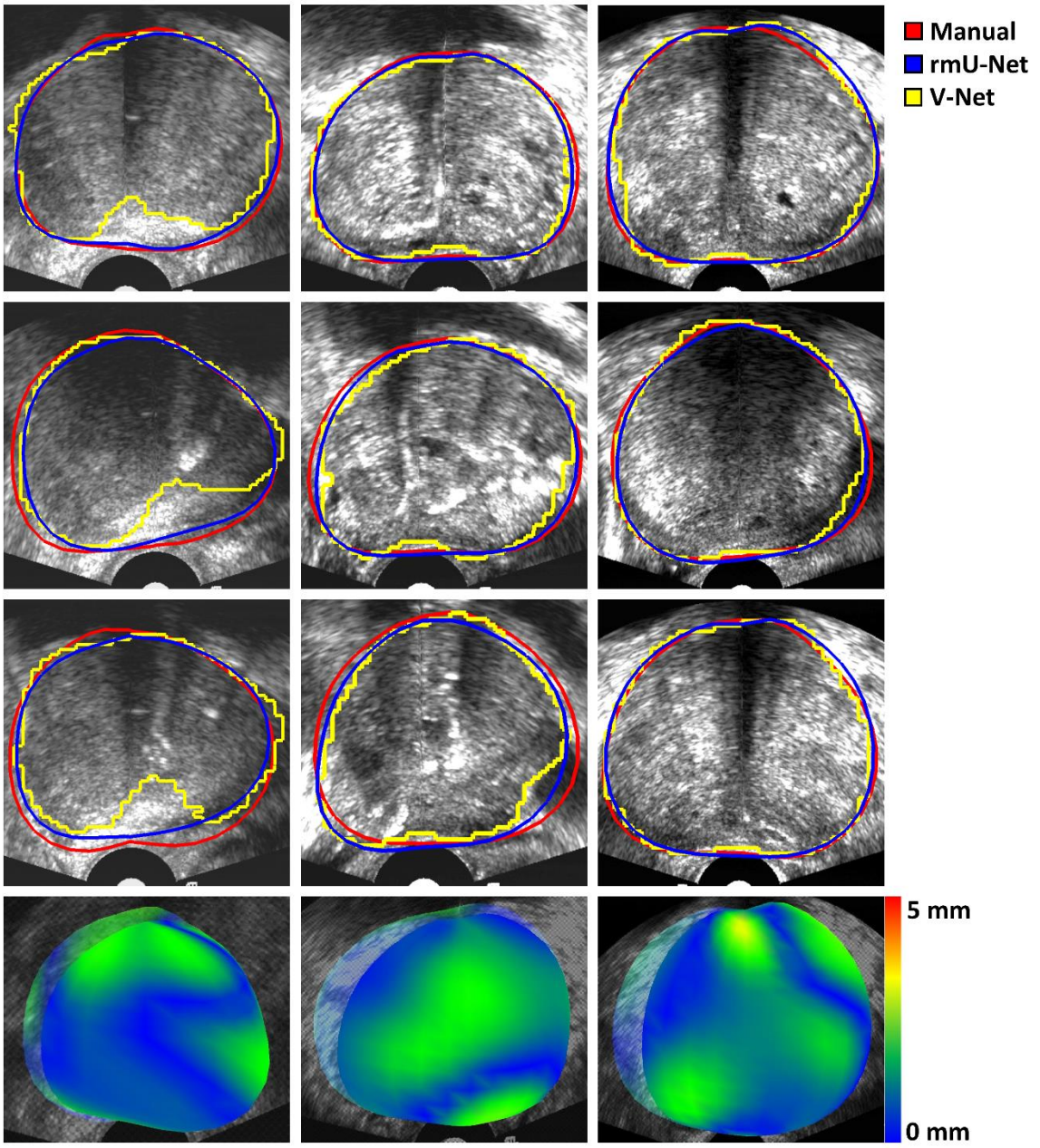

Figure 3.4 End-fire prostate segmentation results comparing manual (red), our proposed reconstructed modified (rm) U-Net (blue), and V-Net (yellow) 3D surfaces. The columns from left to right show the 25th, 50th, and 75th percentile results, respectively, based on DSC metrics. Segmentations in the axial plane, sagittal plane, 45° oblique radial plane, and reconstructed 3D surface error are shown in the respective rows from top to bottom.

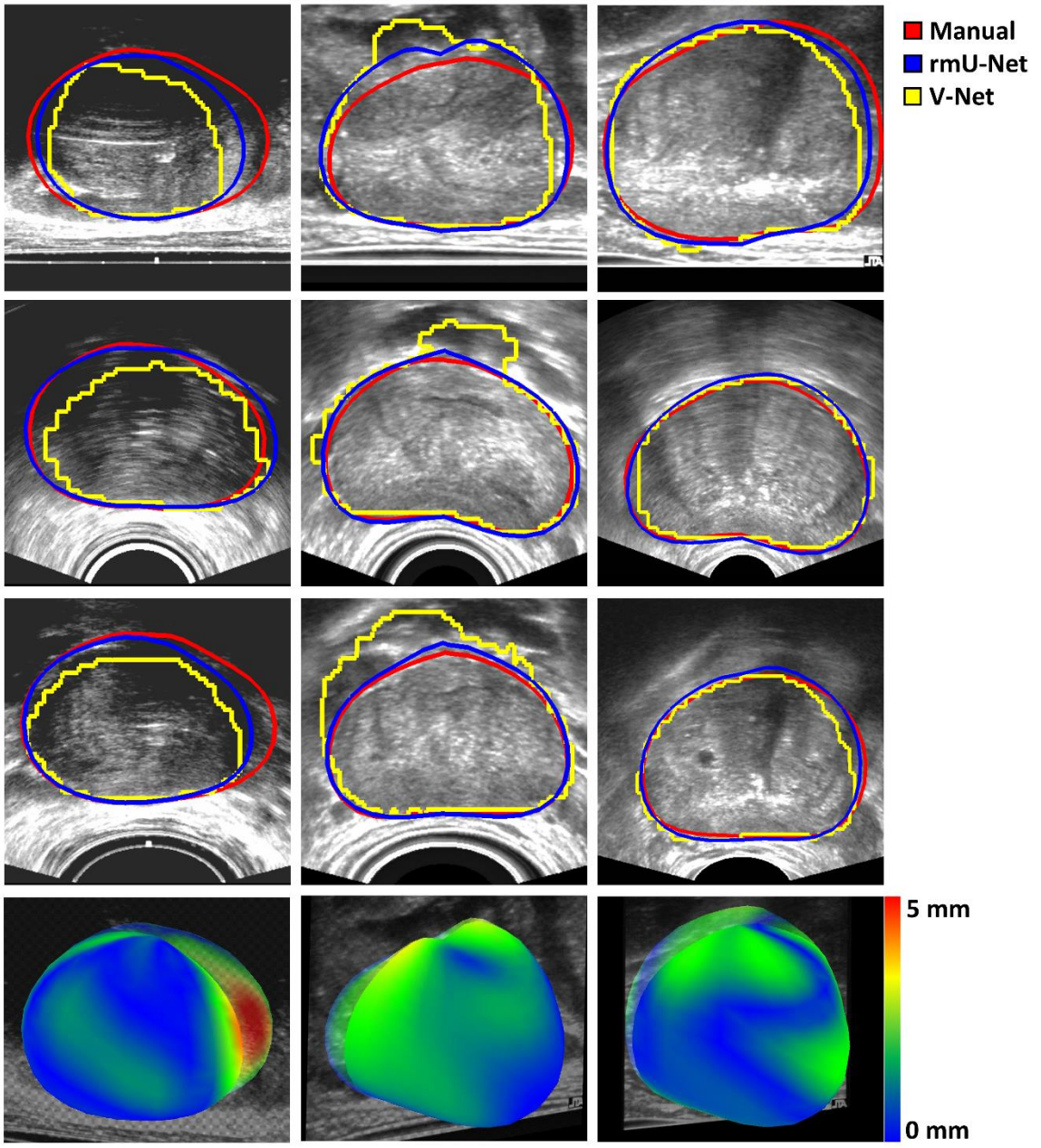

Figure 3.5 Side-fire prostate segmentation results comparing manual (red), our proposed reconstructed modified (rm) U-Net (blue), and V-Net (yellow) 3D surfaces. The columns from left to right show the 25th, 50th, and 75th percentile results, respectively, based on DSC metrics. Segmentations in the axial plane, sagittal plane, 45° oblique radial plane, and reconstructed 3D surface error are shown in the respective rows from top to bottom.

3.4 Discussion

3.4.1 Reconstructed modified U-Net

We proposed a new 3D TRUS prostate segmentation method, which utilizes a modified U-Net to segment 12 2D radial slices, which are then reconstructed into a 3D surface. We first compared segmentation accuracy in these 2D radial slices to segmentation accuracy following 3D reconstruction. In general, the performance was better on the 2D radial slice segmentations compared to the reconstructed 3D surface, but interestingly, our reconstruction method improved recall, MSD, and HD metrics when compared to 2D slice segmentation. When considered in combination, the reduced MSD and HD metrics showed better mean and irregular boundary accuracy, with the improved recall metric implying a reduction in underprediction (since decreasing underpredicted pixels, *i.e.*, false negatives, will increase recall). The reduction in underprediction is contrasted with our method tending to overpredict, supported by the slight positive bias in the signed metrics and reduced precision. In the metrics where performance was worse for our 3D reconstructed segmentations, such as DSC and VPD, the difference in median values were less than 1% and 1.5% respectively. Thus, we saw that our 3D reconstruction method did not drastically reduce performance of the evaluation metrics when compared to our 2D segmentations, with the 3D reconstruction improving performance on select metrics. Examining the signed metrics shown in Table 3.4, we observed that sVPD, sMSD, and sHD are reduced compared to their absolute metrics, with median sVPD reduced to only 2.38 %, median sMSD reduced to 0.11 mm, and median sHD reduced to 2.02 mm. This demonstrated that our algorithm was not significantly biased to over or underpredict the prostate boundary.

As our proposed network was trained and tested on both end-fire and side-fire 3D TRUS images, we directly compared the performance of our method on each image type observing no significant difference between performance for end-fire and side-fire images on any metric. Both independent image geometries also followed the same trends as the total dataset, aside from a reduced signed bias in the end-fire images following reconstruction. These results demonstrated the effectiveness of radially sampling 3D TRUS prostate images to produce similar 2D images for prediction and the ability to

accurately segment the prostate in different 3D TRUS image geometries without the need for multiple trained networks, which, to our knowledge, is the first time this has been shown.

3.4.2 3D CNNs and V-Net Optimization

The initial publication describing the V-Net architecture by Milletari *et al.*[24] proposed the use of a Dice coefficient-based loss function, but recent leave-one-out validation, described in Lei *et al.*,[16] has advocated for the use of hybrid loss functions that combine standard logistic loss, such as the cross-entropy loss metric,[20] with the Dice loss metric. We implemented a 3D V-Net with both a Dice loss function and a hybrid DiceXEnt loss function in order to compare performance between loss functions, as well as to directly compare performance to previously published V-Net implementations[16] on an unseen dataset. Our results reiterate what has been previously reported, with the hybrid DiceXEnt loss function significantly improving performance on all metrics except DSC and recall, where we observed a nonsignificant increase in performance and a significant decrease in performance, respectively. Similar trends held when examining the results for end-fire and side-fire 3D TRUS images individually. Comparing 3D V-Net performance when using a DiceXEnt loss function between end-fire and side-fire 3D TRUS images showed similar results to our proposed network, as there was no significant difference in any metric except HD.

Similar segmentation performance on end-fire and side-fire 3D TRUS images for all three 3D CNNs and our proposed 3D segmentation method demonstrated that we could potentially train a single network to accurately segment the prostate in geometrically variable 3D TRUS images. This was demonstrated predominantly with our approach and the 3D V-Net as the Dense V-Net and High-resolution 3D-Net were observed to have significant differences between several metrics when comparing end-fire and side-fire segmentation performance. Interestingly, performance differed between the Dense V-Net and High-resolution 3D-Net for different image geometries, with better predictions performed on side-fire and end-fires images, respectively. Although our method performed the best, the 3D V-Net outperformed the other two 3D CNNs investigated in this study. This improved performance on 3D US prostate segmentation could be due to the number

of parameters trained by the network since the 3D V-Net has approximately two orders of magnitude more parameters relative to the Dense V-Net and High-resolution 3D-Net. Although the latter networks are more efficient and required less computation time, we found this did not benefit performance.

Although Lei *et al.*[16] reported on a deep supervision method with contour refinement, they also reported on the use of a standard 3D V-Net with a hybrid DiceXEnt loss function to segment the prostate in side-fire 3D TRUS images, showing a 3D DSC, precision, recall, HD, MSD, and RMSD of 90.5 ± 3.0 %, 88.1 ± 6.0 %, 93.5 ± 3.5 %, 4.643 ± 1.926 mm, 0.657 ± 0.270 mm, and 0.977 ± 0.410 mm, respectively. Comparatively, a standard 3D V-Net with a DiceXEnt loss function trained on our dataset and predicted on side-fire images resulted in a 3D DSC, precision, recall, HD, and MSD of 91.2 [87.4, 92.8] %, 95.0 [90.8, 97.5] %, 89.5 [80.7, 92.9] %, 4.92 [4.28, 6.55] mm, and 1.11 [0.84, 1.47] mm, showing very similar performance. Investigating the differences between mean and median values showed our V-Net implementation demonstrated improved 3D DSC and precision, while Lei *et al.*[16] demonstrated improved recall, HD, and MSD. Although VDP or any signed metrics were not reported, this demonstrated similarity in performance. Thus, we suggest future comparisons should use a standardized V-Net, like the NiftyNet open-source implementation, to provide a baseline for comparing network performance on different datasets.

3.4.3 Comparison with 3D V-Net and previously published methods

For an identical training and testing dataset, our proposed method performed significantly better than the standard 3D V-Net with a hybrid loss function, with DSC, recall, sVPD, MSD/sMSD, and HD/sHD showing significant improvement. Our proposed method also demonstrated a reduced median VPD, although this difference was not significant. Similar differences in performance were observed when considering end-fire and side-fire 3D TRUS images separately. Figure 3.4 and Figure 3.5 show this difference in performance qualitatively for both image geometries, with the 3D V-Net often over or underpredicting the correct prostate boundary. This difference is readily apparent in the side-fire middle 50th percentile column of Figure 3.5. The V-Net is shown to have incorrectly contoured part of the bladder as the prostate, drastically affecting the overall segmentation accuracy.

In contrast, our proposed method was able to correctly avoid the bladder, resulting in a more accurate segmentation. A similar result is shown in the left column of Figure 3.4 as well as in Figure 3.6, where we show that the 3D V-Net mistakenly underpredicted the prostate boundary due to the presence of a hyperechoic calcification artifact in the TRUS image, whereas our proposed method was typically able to avoid artifacts of this nature. We demonstrated a mean 3D segmentation time of 0.62 s with our proposed method, over five times faster than the 3D V-Net, which required an average of 3.43 s per segmentation. All segmentations were completed with the same NVIDIA GeForce GTX TITAN GPU with 6 GB of memory.

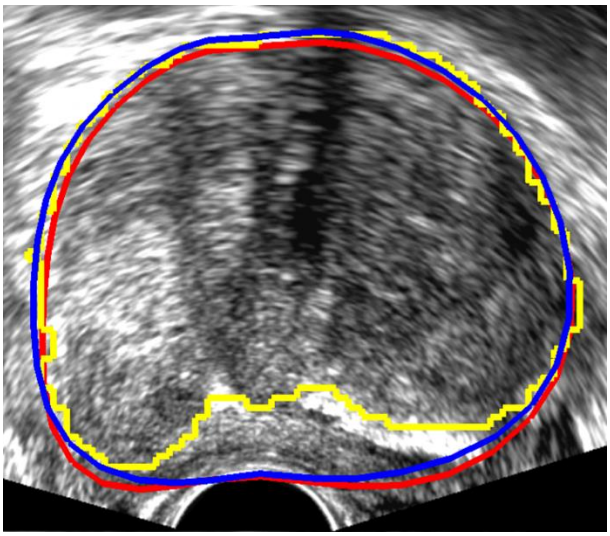

Figure 3.6 A sample end-fire prostate segmentation result comparing manual (red), our proposed algorithm (blue), and V-Net (yellow) 3D surfaces in the presence of a hyperechoic calcification image artifact.

Recent work by Ghavami *et al.*[15] and Lei *et al.*[16] report on automatic prostate segmentation in 3D TRUS images, with Ghavami *et al.*[15] reporting best results for 2D DSC, 3D DSC, and boundary distance of 89 ± 12 %, 89 ± 5 %, and 1.68 ± 1.57 mm, respectively, and Lei *et al.*[16] reporting overall segmentation results for 3D DSC, precision, recall, HD, MSD, and RMSD of 91.9 ± 2.8 %, 90.6 ± 5.5 %, 93.8 ± 4.3 %, 3.938 ± 1.550 mm, 0.599 ± 0.225 mm, and 0.900 ± 0.377 mm, respectively. Our proposed method demonstrated overall segmentation results for 2D DSC, 3D DSC, precision, recall, HD, and MSD of 94.9 [93.2, 95.5] %, 94.1 [92.6, 94.9] %, 93.2 [88.08, 95.4] %, 96.0 [93.1, 98.5] %, 2.89 [2.37, 4.35] mm, and 0.89 [0.73, 1.09] mm, respectively, outperforming the network reported by

Ghavami *et al*.[15] on all reported metrics, and outperforming the network reported by Lei *et al*.[16] on all metrics except MSD. In addition, our paper reports on metrics not used in the studies described here, including VPD, and signed variants of VPD, MSD, and HD, providing additional insight into the performance of our network that is otherwise not present when these metrics are excluded. Lei *et al*.[16] reported segmentation times of approximately 1-2 s for a U-Net, V-Net, and their proposed network, with segmentations completed using an NVIDIA TITAN XP GPU with 12 GB of memory. Comparatively, our V-Net implementation in NiftyNet had a mean segmentation time of 3.43 s, while our proposed method had a mean segmentation time of 0.62 s, with segmentations completed using an NVIDIA GeForce GTX TITAN GPU with 6 GB of memory. Although our V-Net had slower segmentation times, our proposed method was one and a half to three times faster, using a GPU with half the memory, demonstrating the advantage of our proposed method regarding segmentation time.

Studies reported by Ghavami *et al*.[15] and Lei *et al*.[16] are also limited by their use of cross-validation approaches, in addition to their dataset consisting of only one image geometry and a single ultrasound machine with matched voxel dimensions and sizes. In contrast, we used a clinically diverse dataset of 3D TRUS images of different image geometries, generated by several different ultrasound transducers used with different machine models, and used in distinct procedures. This dataset contains images with varying voxel dimensions, size, and image quality, and we have employed no pre-processing before training to reduce process complexity. To our knowledge, the use of a dataset with different image geometries, ultrasound transducers, ultrasound machine models, voxel dimensions, and image sizes for 3D TRUS prostate segmentation is unique and may allow for a more robust and generalizable segmentation method. In addition, we have not used a cross-validation approach, instead testing our algorithm on 3D TRUS images that were completely unseen by the network, which we believe strengthens the significance of our results and may result in improved generalizability.

3.4.4 Limitations and future work

Although we have demonstrated excellent performance with our proposed algorithm, a parameter that may be interesting to explore in future work is the step angle for radial slice

generation. Specifically, it would be interesting to investigate whether a decreased step angle and thus an increased number of radial slices would significantly increase performance, or whether a decreased number of slices could be used while maintaining similar performance. An increased number of radial slices would increase computation time, which motivated our choice of a 15° step angle for the proposed method. When training the 3D CNNs for performance comparison, hyperparameters were optimized on the V-Net and were used for the other two networks. Even though we investigated other combinations and found these hyperparameters to perform the best on the Dense V-Net and High-resolution 3D-Net, a rigorous optimization was not performed and has the potential to increase performance. Another limitation of our study is the use of only one observer for providing ground truth segmentations. This meant we could not directly assess inter-observer variability for our dataset. In addition, we did not directly assess intra-observer variability over several time points. Inter- and intra-observer variability in end-fire 3D TRUS images were previously assessed by our group,[11] and are summarized here. To assess intra-observer variability, one observer segmented 15 3D images five times each, resulting in a 3D DSC of 93.0 ± 2.1 %. To assess inter-observer variability, three untrained observers segmented 15 3D images three times each, resulting in a DSC of 93.5 ± 2.1 %, 92.6 ± 3.1 %, and 92.3 ± 3.2 %, with an ANOVA demonstrating no significant difference. Inter- and intra-observer variability in side-fire 3D TRUS images were also assessed by our group,[28] reporting 5.1 % variability and 99 % reliability in intra-observer prostate volume estimates, and 11.4 % variability and 96 % reliability in inter-observer estimates, for a study of eight observers measuring 15 prostate images twice. This variability is comparable to the reported DSC of our proposed method in this work, showing that our algorithm is performing at the level of intra-observer variability in the ground truth segmentations. Due to the demonstrated variability between different observers when segmenting 3D TRUS images, segmentations from other observers should be incorporated into our testing dataset to further improve the robustness of our proposed method.

3.5 Conclusions

This study investigated the development of a 2D deep learning with 3D reconstruction approach for automatic prostate segmentation in 3D TRUS images. Multiple facilities, ultrasound machine models, and acquisition geometries were investigated to evaluate robustness and generalizability, with comparisons performed against multiple 3D CNNs. A fast, accurate, and generalizable automatic prostate segmentation algorithm could reduce physician burden and procedure time, offering potential workflow benefits for fusion-guided prostate biopsy, tumor-targeted HDR-BT, and TRUS-guided whole-gland BT. Reducing the time a patient is under anesthesia, as in HDR-BT, also promotes a potentially safer procedure with fewer adverse side effects.

3.6 References

1. Stewart BW, Wild C. *World Cancer Report 2014*. Lyon; 2014.

2. Narayanan R, Kurhanewicz J, Shinohara K, Crawford ED, Simoneau A, Suri JS. MRI-ultrasound registration for targeted prostate biopsy. In: *2009 IEEE International Symposium on Biomedical Imaging: From Nano to Macro*. IEEE; 2009:991-994. doi:10.1109/ISBI.2009.5193221

3. Karnik V V, Fenster A, Bax J, et al. Assessment of image registration accuracy in three-dimensional transrectal ultrasound guided prostate biopsy. *Med Phys*. 2010;37(2):802-813. doi:10.1118/1.3298010

4. Choi YJ, Kim JK, Kim HJ, Cho K-S. Interobserver Variability of Transrectal Ultrasound for Prostate Volume Measurement According to Volume and Observer Experience. *Am J Roentgenol*. 2009;192(2):444-449. doi:10.2214/AJR.07.3617

5. Murciano-Goroff YR, Wolfsberger LD, Parekh A, et al. Variability in MRI vs. ultrasound measures of prostate volume and its impact on treatment recommendations for favorable-risk prostate cancer patients: A case series. *Radiat Oncol*. 2014;9(1):200. doi:10.1186/1748-717X-9-200

6. Mahdavi SS, Spadinger I, Chng N, Salcudean SE, Morris WJ. Semiautomatic segmentation for prostate brachytherapy: Dosimetric evaluation. *Brachytherapy*. 2013;12(1):65-76. doi:10.1016/j.brachy.2011.07.007

7. Reich DL, Hossain S, Krol M, et al. Predictors of Hypotension After Induction of General Anesthesia. *Anesth Analg*. 2005;101(3):622-628. doi:10.1213/01.ANE.0000175214.38450.91

8. Qiu W, Yuan J, Ukwatta E, Sun Y, Rajchl M, Fenster A. Prostate Segmentation: An Efficient Convex Optimization Approach With Axial Symmetry Using 3-D TRUS and MR Images. *IEEE Trans Med Imaging*. 2014;33(4):947-960. doi:10.1109/TMI.2014.2300694

9. Qiu W, Rajchl M, Guo F, et al. 3D prostate TRUS segmentation using globally optimized volume-preserving prior. In: *Lecture Notes in Computer Science (Including Subseries Lecture Notes in Artificial Intelligence and Lecture Notes in Bioinformatics)*. Vol 8673 LNCS. ; 2014:796-803. doi:10.1007/978-3-319-10404-1_99

10. Yuan J, Qiu W, Rajchl M, Ukwatta E, Tai X-C, Fenster A. Efficient 3D Endfiring TRUS Prostate Segmentation with Globally Optimized Rotational Symmetry. In: *2013 IEEE Conference on Computer Vision and Pattern Recognition*. IEEE; 2013:2211-2218. doi:10.1109/CVPR.2013.287

11. Qiu W, Yuan J, Ukwatta E, Fenster A. Rotationally resliced 3D prostate TRUS segmentation using convex optimization with shape priors. *Med Phys*. 2015;42(2):877-891. doi:10.1118/1.4906129

12. Ghavami N, Hu Y, Gibson E, et al. Automatic segmentation of prostate MRI using convolutional neural networks: Investigating the impact of network architecture on the accuracy of volume measurement and MRI-ultrasound registration. *Med Image Anal*. 2019;58:101558. doi:10.1016/j.media.2019.101558

13. Litjens G, Toth R, van de Ven W, et al. Evaluation of prostate segmentation algorithms for MRI: the PROMISE12 challenge. *Med Image Anal*. 2014;18(2):359-373. doi:10.1016/j.media.2013.12.002

14. Anas EMA, Mousavi P, Abolmaesumi P. A deep learning approach for real time prostate segmentation in freehand ultrasound guided biopsy. *Med Image Anal*. 2018;48:107-116. doi:10.1016/j.media.2018.05.010

15. Ghavami N, Hu Y, Bonmati E, et al. Integration of spatial information in convolutional neural networks for automatic segmentation of intraoperative transrectal ultrasound images. *J Med Imaging*. 2018;6(01):1. doi:10.1117/1.jmi.6.1.011003

16. Lei Y, Tian S, He X, et al. Ultrasound prostate segmentation based on multidirectional deeply supervised V-Net. *Med Phys*. 2019;46(7):3194-3206. doi:10.1002/mp.13577

17. Dwork C, Feldman V, Hardt M, Pitassi T, Reingold O, Roth A. The reusable holdout: Preserving validity in adaptive data analysis. *Science (80-)*. 2015;349(6248):636-638. doi:10.1126/science.aaa9375

18. Valdes G, Interian Y. Comment on 'Deep convolutional neural network with transfer learning for rectum toxicity prediction in cervical cancer radiotherapy: a feasibility study.' *Phys Med Biol*. 2018;63(6):068001. doi:10.1088/1361-6560/aaae23

19. Fenster A, Parraga G, Bax J. Three-dimensional ultrasound scanning. *Interface Focus*. 2011;1(4):503-519. doi:10.1098/rsfs.2011.0019

20. Ronneberger O, Fischer P, Brox T. U-net: Convolutional networks for biomedical image segmentation. In: *Lecture Notes in Computer Science (Including Subseries Lecture Notes in Artificial Intelligence and Lecture Notes in Bioinformatics)*. Vol 9351. ; 2015:234-241. doi:10.1007/978-3-319-24574-4_28

21. Chollet F and others. Keras. https://keras.io/. Published 2015.

22. Abadi M, Agarwal A, Barham P, et al. *TensorFlow: Large-Scale Machine Learning on Heterogeneous Distributed Systems*. Vol s4-X.; 2016. doi:10.1093/library/s4-X.3.339

23. Girardeau-Montaut D. CloudCompare-open source project. http://www.cloudcompare.org/.

24. Milletari F, Navab N, Ahmadi S-A. V-Net: Fully Convolutional Neural Networks for Volumetric Medical Image Segmentation. June 2016. http://arxiv.org/abs/1606.04797. Accessed December 10, 2018.

25. Gibson E, Giganti F, Hu Y, et al. Automatic Multi-Organ Segmentation on Abdominal CT with Dense V-Networks. *IEEE Trans Med Imaging*. 2018;37(8):1822-1834. doi:10.1109/TMI.2018.2806309

26. Li W, Wang G, Fidon L, Ourselin S, Cardoso MJ, Vercauteren T. On the compactness, efficiency, and representation of 3D convolutional networks: Brain parcellation as a pretext task. In: *Lecture Notes in Computer Science (Including Subseries Lecture Notes in Artificial Intelligence and Lecture Notes in Bioinformatics)*. Vol 10265 LNCS. Springer Verlag; 2017:348-360. doi:10.1007/978-3-319-59050-9_28

27. Gibson E, Li W, Sudre C, et al. NiftyNet: a deep-learning platform for medical imaging. *Comput Methods Programs Biomed*. 2018;158:113-122. doi:10.1016/j.cmpb.2018.01.025

28. Tong S, Cardinal HN, McLoughlin RF, Downey DB, Fenster A. Intra- and inter-observer variability and reliability of prostate volume measurement via two-dimensional and three-dimensional ultrasound imaging. *Ultrasound Med Biol*. 1998;24(5):673-681. doi:10.1016/S0301-5629(98)00039-8

3.7 Supplement A

Table 3.A1 Absolute median [Q1, Q3] results comparing a Dense V-Net (DenseNet) and High-resolution 3D Network (HighRes3dNet) on an unseen test dataset of 20 end-fire and 20 side-fire 3D TRUS images of the prostate.

Acquisition	Segmentation	DSC (%)	Recall (%)	Precision (%)	VPD (%)	MSD (mm)	HD (mm)
End-fire	DenseNet	87.9 [84.9, 90.4]	95.4 [92.9, 97.0]	82.2 [77.4, 86.5]	15.6 [9.42, 20.8]	2.11 [1.55, 2.85]	10.0 [7.82, 12.5]
	HighRes3dNet	90.0 [87.3, 91.4]	91.7 [84.6, 94.9]	89.3 [87.0, 93.7]	6.88 [4.30, 15.7]	1.62 [1.41, 2.08]	8.95 [7.56, 11.2]
Side-fire	DenseNet	88.7 [81.6, 90.7]	89.1 [86.0, 95.1]	89.6 [82.8, 91.9]	6.38 [4.22, 12.6]	1.47 [1.26, 2.56]	8.96 [5.93, 13.8]
	HighRes3dNet	86.2 [84.3, 88.7]	80.5 [76.8, 86.0]	94.9 [90.9, 96.1]	15.3 [9.77, 20.0]	1.64 [1.36, 1.93]	7.82 [6.67, 9.31]
Overall	DenseNet	88.2 [84.3, 90.6]	93.0 [88.9, 96.1]	84.8 [79.2, 90.2]	11.0 [5.96, 19.3]	2.00 [1.36, 2.63]	9.23 [7.00, 13.2]
	HighRes3dNet	87.5 [85.5, 90.3]	85.4 [79.8, 92.1]	92.3 [88.4, 95.8]	11.8 [4.68, 18.0]	1.63 [1.40, 1.97]	8.37 [6.89, 10.9]

DSC, Dice similarity coefficient; VPD, volume percent difference; MSD, mean surface dist.; HD, Hausdorff dist.

Table 3.A2 Signed median [Q1, Q3] results comparing a Dense V-Net (DenseNet) and High-resolution 3D Network (HighRes3dNet) on an unseen test dataset of 20 end-fire and 20 side-fire 3D TRUS images of the prostate.

Acquisition	Segmentation	sVPD (%)	sMSD (mm)	sHD (mm)
End-fire	DenseNet	15.6 [9.42, 20.8]	1.44 [0.92, 2.18]	9.13 [7.19, 12.3]
	HighRes3dNet	2.86 [-6.42, 8.86]	0.37 [-0.46, 0.93]]	6.47 [-8.97, 9.71]
Side-fire	DenseNet	0.36 [-4.91, 7.07]	0.38 [-0.15, 1.03]	8.67 [-2.86, 13.8]
	HighRes3dNet	-13.8 [-20.0, -7.55]	-0.76 [-1.23, -0.08]	-6.69 [-8.40, 4.38]
Overall	DenseNet	8.77 [-2.84, 18.3]	0.95 [0.29, 1.61]	8.87 [5.72, 13.2]
	HighRes3dNet	-6.89 [-16.4, 4.09]	-0.24 [-1.15, 0.58]	-5.84 [-8.46, 8.32]

sVPD, signed volume percent difference; sMSD, signed mean surface dist.; sHD, signed Hausdorff dist.

Chapter 4

4 Geometrically variable three-dimensional ultrasound for mechanically assisted image-guided therapy of focal liver cancer tumors

The use of 3D information during interventional procedures has the potential to improve the accuracy needed for sufficient clinical outcomes. The purpose of Chapter 4 is to present on the development of a novel 3D US system to provide a safe, cost-effective, and accurate intraoperative approach for focal liver tumor therapies.

The contents of this chapter have been accepted for publication on June 28, 2020 in *Medical Physics*: Gillies DJ, Bax J, Barker K, Gardi L, Tessier D, Kakani N, and Fenster A.

4.1 Introduction

Liver cancer is the second and sixth most frequent cause of cancer mortality in men and women, respectively, and its incidence is continuing to increase globally.[1] The high prevalence of this disease is observed in underdeveloped and developing countries due to the increased incidence of Hepatitis B and C, but rates are also increasing globally from factors including exposure to aflatoxins, metabolic syndrome, and alcohol.[1] Without accessible and practical therapy options, the prognosis for the majority of patients diagnosed with liver cancer remains grave. Conventional therapy is often provided in the forms of transplantation and hepatic resection, but patient eligibility is often low due to disease exclusion criteria such as the number of tumors, size, location, and presence of metastases.[2,3] Even in circumstances when a patient is eligible, serious complications can occur in up to 26-33% of procedures.[4]

Image-guided interventions are less invasive alternatives to open surgery that focus on relating preoperative data and images of a patient in an intraoperative setting.[5] Smaller surgical incisions often lead to reduced recovery times and complication rates, which directly benefit a patient's quality-of-life and healthcare costs. Three main techniques for image-guided interventions in the treatment of liver cancer have been investigated: embolization, irreversible electroporation, and ablation, such as cryoablation, ethanol injection, microwave ablation (MWA), and radiofrequency ablation (RFA). In recent years, MWA and RFA have been regarded as the best treatment options for small and

unresectable liver tumors,[6,7] which use needle-like therapy applicators guided to the tumor location to deliver a lethal thermal dose to the tumor.

Image-guidance during ablation procedures varies globally and has been predominantly performed using x-ray computed tomography (CT), magnetic resonance imaging (MRI), and ultrasound (US). In many developed countries, access to CT provides a good depiction of liver tumors and the ablation applicators, but the limited access to the patient in the CT gantry often extends procedure time and can limit complex applicator access angles.[8] Since MR guidance is often limited to institutions with compatible equipment, US is regarded as the most efficient modality for tumors that can be targeted adequately[8] with developing countries often using this approach.[9] Conventional US guidance is a real-time, two-handed approach using a plan based on preoperative CT or MR images where one hand positions and orients a conventional US probe while the other hand performs therapy applicator insertion. However, this approach requires extensive training as the physician must: (1) mentally integrate two-dimensional (2D) imaging to form an appreciation of the complex 3D anatomy of the liver, (2) approximate the tumor volume and spatial extent, (3) align the 2D image plane directly with the applicator to detect and track its placement at the tumor location, and (4) be cognizant of the surrounding anatomy to avoid puncturing unnecessary anatomical structures and organs-at-risk, such as the gallbladder. This time-consuming and challenging task with its compounding forms of mental burden can lead to increased variability in applicator placement and ultimately insufficient tumor ablation. In addition to the high local tumor recurrence that has been observed when ablation margins are less than 5 mm,[10–12] tumors with diameters larger than 5 cm are often avoided as the incidence of local tumor progression is higher due to the accuracy required for placing and repositioning multiple applicators with overlapping ablation volumes.[13] Therefore, there is a clinical need to improve the imaging guidance and placement verification of needle applicators during MWA and RFA procedures.

Investigations into guidance techniques for planning, targeting, monitoring, and controlling ablation therapies and other needle-like procedures have focused on incorporating CT image guidance,[14] MR image guidance,[15] and tracking systems[16,17] into the intraoperative clinical workflow. Incorporating three-dimensional (3D) visualizations can lead to

complete ablations and higher clinical success rates on the first ablation attempt, as well as fewer sessions overall relative to 2D US when subsequent attempts are required.[16,18] CT images can provide 3D multiplanar images to visualize the needle-like applicators, but repeated CT scans are performed at the cost of increased procedure time and radiation dose to the patient. MR imaging has been used as it offers advantages such as improved soft-tissue contrast and the potential for real-time treatment monitoring, but can again increase procedure time and is not readily accessible in many countries due to the sophisticated technology required.[19] Electromagnetic tracking systems have been used to place multiple needle applicators by registering and fusing preoperative CT images with live 2D US images;[20] however, these systems do not often rely on the intraoperative imaging data and are susceptible to environmental limitations that can degrade targeting accuracy.

An alternative approach for real-time image-guided therapy is the use of three-dimensional (3D) US.[21] This approach includes 2D US freehand scanning with optical or electromagnetic position tracking,[22] 2D array probes,[23] or 2D US with mechanical scanners.[24] These images can offer real-time or near real-time multiplanar imaging in an accessible and portable manner, which is an important consideration for widespread dissemination. If combined or fused with preoperative CT images using image registration methods, lesion identification and procedural plans[25] can be incorporated into the intraoperative workflow for an augmented and targeted image-guided procedure. Needle guides can improve placement of applicators over freehand approaches[22] and repeat 3D US images can be obtained safely to inform the physician if the therapy applicator placement is sufficient or repositioning is required with the use of segmentation algorithms,[26] without the need for ionizing radiation exposure and a significant increase in procedure time. When performing guided insertions, 3D US imaging can improve the targeting accuracy of needle applicator placements over freehand 2D US[22,27] and has been observed to detect unacceptable applicator placements in up to 45% of procedures.[28] Additionally, 3D US has been observed to improve operator confidence and visualization of the positional relationship between needle applicators and nearby critical structures.[29] Although therapy monitoring can be difficult on conventional B-mode imaging, intraoperative ultrasound elasticity imaging has the potential to provide real-time monitoring and verification of thermal ablation volumes.[30]

We propose the use of 3D US imaging to provide guidance and localization of ablation applicators in current focal liver tumor ablation therapies. We have previously developed a system capable of providing 3D US images using a mechanical scanning approach for linear, tilt, and hybrid motions of the US probe, which resulted in accurate geometric 3D reconstruction and good agreement with clinical CT patient liver images when assessing tip and trajectory errors.[24] Since the liver is a large internal organ that is partly sheltered by the ribs, flexibility in 3D US acquisition geometries can allow for small physical footprints (*i.e.*, tilt scanning) that are beneficial for intercostal imaging, as well as wide field-of-view (FOV) subcostal imaging (*i.e.*, hybrid scanning) to capture large volumes of the liver. We chose to pursue a mechanical scanning approach as it is cost-effective since any clinically available US system can be used with this approach, the motor assembly can predefine and control probe motion with high accuracy, environmental constraints are minimal, and advances in US imaging probes can be easily integrated into the system without any changes in the scanning mechanism. This work will further expand the design and use of the system by incorporating and evaluating a novel scanning mechanism for increased image size and improved usability, a mechanical tracking system for probe placement reproducibility and freehand needle applicator guidance, and a needle applicator insertion workflow using a custom needle applicator guide for targeted image-guided procedures. Evaluation of the new scanner has been previously discussed briefly,[31,32] but is expanded here to provide context for evaluation of the tracking system and needle applicator insertion workflow performed on 48 phantom 3D US images. A healthy volunteer was also imaged to provide evidence for clinical feasibility. These evaluations aim to give insights on clinical utility for improving applicator placement and reducing local cancer recurrence during interventional procedures treating liver cancer.

4.2 Materials and methods

Our proposed 3D US system (Figure 4.1) consists of four components: (1) a three-motor 3D US scanner, (2) a counterbalanced tracking system, (3) a 3D-printed applicator guide, and (4) software for image acquisition, visualization, and guidance. The stabilizing system also contains electromagnetic brakes, which are disengaged using a foot pedal to improve clinical usability and workflow, for locking the system to limit device motion during 3D

US acquisition and insertion of therapy applicators. The stabilizing system is mounted on a portable cart, which contains a foot-released vertical motion column to accommodate large differences in patient sizes, a power supply, and a personal computer with a monitor to interface with custom visualization and guidance software.

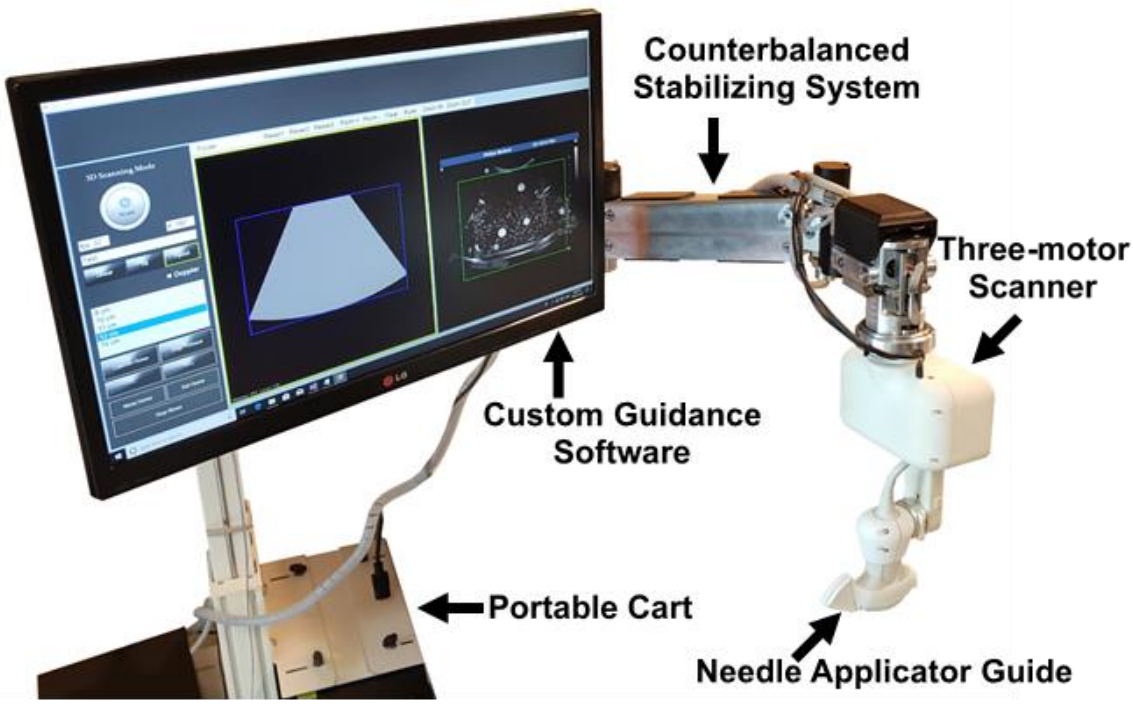

Figure 4.1 Proposed 3D US system consisting of a three-motor 3D US scanner and a counterbalanced stabilizing system mounted on a portable cart. A 3D-printed needle applicator guide and custom visualization and guidance software were developed for this system to perform targeted needle applicator insertions.

4.2.1 3D US scanner design and validation

The proposed 3D US system has been previously discussed and is summarized here.[31] Custom 3D-printed holders were designed to match 2D US probe casings and provide a universal male mating connection for any commercially available US probe. A standard clinical workflow requirement when performing US-guided procedures is the need for patient scout imaging to localize the tumor using freehand US imaging. Once the tumor is localized, a beneficial clinical utility would allow the 2D US probe to maintain its localization position while a 3D enabling scanner is brought to the probe. For this reason, the scanner was created with a female mating spring-loaded quick connection and used

three-motors to manipulate the attached 2D US probe. The configuration of the motors was designed such that the bulk of the scanner was away from the probe face, which maintained the physician's conventional hand position used during freehand US imaging. The connection and scanner design choices allowed for accessibility for any healthcare facility using commercial US systems, easy transition to freehand US (which is often important for patient scout imaging), and a scanner design that provided a more natural feel for the physician as it was able to accommodate their experience and training with regard to hand positioning and the 2D imaging technique. Three-motors were used to manipulate the probe in two linear degrees-of-freedom (DoF) and one rotational DoF to provide a large scanning FOV with consistent image spacing for repeatable 3D US image generation. The large FOV allows for more anatomical landmarks and targets to be captured for reference and potential registration to a planning CT image. These motors controlled horizontal, vertical, and rotational motions up to extents of 98 mm, 19 mm, and 90°, respectively, to form different acquisition geometries, including linear, tilt, and or hybrid. Linear refers to the activation of a single motor for translation of the probe, whereas tilt and hybrid incorporate all three motors to either form a 3D image by rotating a 2D probe about the face of the probe (*i.e.*, tilt) or during translation (*i.e.*, hybrid) to form a wide FOV acquisition, similar to previous methods.[24] 3D image reconstruction was performed by moving the probe in the desired geometry while images were acquired from the US system using a Digital Visual Interface (DVI) to Universal Serial Bus (USB) video frame grabber (Epiphan Systems Inc., Ottawa, Canada). Current implementation focused on clinical simplicity and offers a set of pre-defined 3D scanning directions and ranges, but variable control of each independent motor is possible.

The three-motor scanner used to perform 3D image reconstruction was previously validated for geometric error and volumetric error. Geometric imaging experiments were performed on a grid phantom of known geometry, which resulted in mean geometric errors of ≤0.2%, ≤2.3%, and ≤3.0% for lateral, axial, and elevational image dimensions respectively.[31] Volumetric imaging experiments were performed to further evaluate image reconstruction to assess the combined error contributions of each image dimension. Tissue-mimicking phantoms with spherical structures were used to compute mean volumetric errors of -5.85 ± 6.18%, -6.12 ± 4.82%, and -6.82 ± 3.56% for linear (range: 65 mm to 98

mm scans), tilt (60° scans), and hybrid (range: 40 mm + 40° to 80 mm 60°) image geometries respectively.[33]

4.2.2 Mechanical tracking system and evaluation

The scanner was mounted on a spring-loaded counterbalanced stabilizing system that included a "wrist" with three rotational DoF via a gimbal design and an "arm" with two links for 29.3 cm vertical motion and 115º horizontal rotational range (arc length of 27.2 cm), improving the overall range of motion and working space. The arm incorporated a four-bar parallelogram linkage to avoid an arcing path and provide parallel vertical motion, which limits the propagation of error to downstream joint axes as motion is limited to one Cartesian axis. These components provide a total of five DoF, which are tracked using five electromagnetic encoders, which allow tracking of the US probe in space by detecting joint angles necessary to compute forward kinematics. To compute the orientation of the tracking system end-effector (*i.e.*, 2D US probe), a known position with corresponding joint encoder values was required to initialize the coordinate system of the tracking system. This position was achieved by forcing the joints into a known reference position using a mechanical jig (Figure 4.2A) to obtain the initialization encoder readings on the tracked joints (Figure 4.2B). Forward kinematics of the mechanical stabilizing system are given in Table 4.1 using the Denavit-Hartenberg convention.

Table 4.1 Denavit-Hartenberg parameters of the mechanical stabilizing system using electromagnetic encoders (θ_i).

Link	a_i (mm)	α_i (º)	θ_i (º)	d_i (mm)
Parallelogram (Adjacent)	254	0	θ_0	0
Parallelogram (Vertical)	0	-π/2	θ_0	0
Sway	135.7	-π/2	θ_1	0
Wrist Roll	0	-π/2	θ_2	0
Wrist Pitch	0	-π/2	θ_3	0
Wrist Yaw	0	0	θ_4	366.4

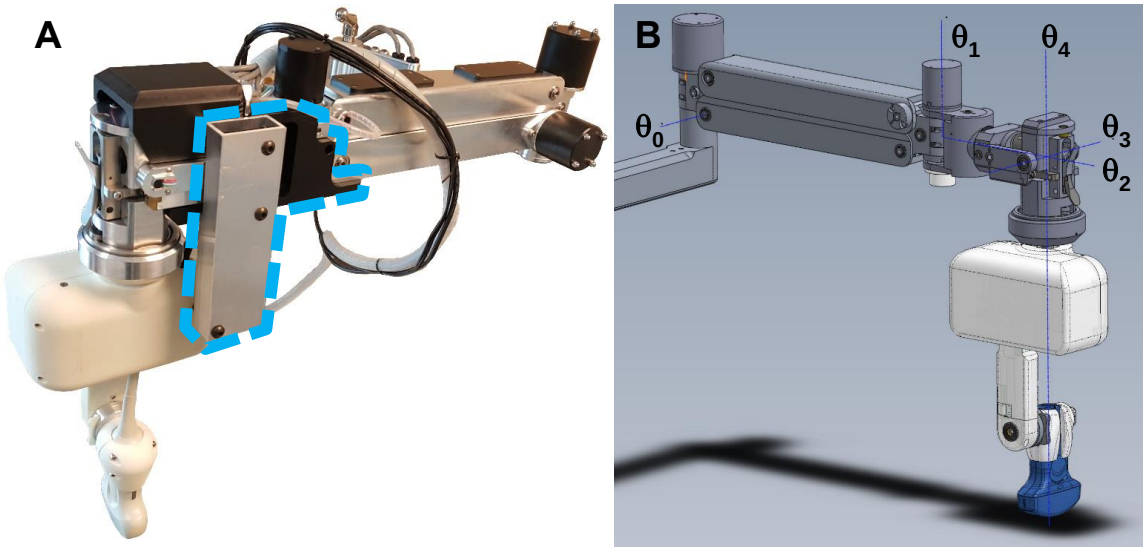

Figure 4.2 (A) A jig (dashed box) was used to place the stabilizing system into a reference position to produce the initialization encoder positions. (B) Axes of rotations that are tracked using the electromagnetic encoders (θ_i) and used to compute forward kinematics using the Denavit-Hartenberg parameters.

Assessing the accuracy of the tracking system was completed by comparing displacements computed by the system to displacements observed by an independent external Polaris Vicra optical tracking system (NDI, Waterloo, Canada). An optical tracking system was chosen as an external method for comparison due to its high accuracy, ease of use with a setup that avoided line-of-sight limitations, and it avoided the need to disassemble the system, which is typically necessary for conventional joint analysis. Since forward kinematics were computed by choosing the 2D US probe tip as the termination point of the tracking system, comparisons were achieved by replacing the 2D US probe with a commercial stylus via a 3D printed attachment that maintained the 2D US probe tip termination point using the tip of the stylus. The position of the stylus was set using a height gauge and was confirmed by optically tracking the probe while only the gimbal wrist was manipulated. This generated a spherical cloud of points that could be fit[34] and used to compare the radius and the expected stylus height.

The five electromagnetically tracked joints were evaluated independently prior to a compound joint motion assessment. After determining an initial position in space near the center of the system's range of motion, a single joint was advanced and stopped to allow

for matched data collection between the mechanical and optical tracking systems. Since the initialization position of each joint was in the center of its range of motion, measurements were acquired on either side of the initialization position to assess the entire range of the joint (Table 4.2). The vertical and horizontal joints on the arm were able to be manipulated without engaging other joints, but the gimbal wrist always incorporated and released all three rotation axes due to the manual locking mechanism used. The benefit of using optical tracking as an evaluation tool was that the 3D displacements could be easily and readily measured, allowing for a direct method of comparison to our system without the need for disassembly or additional manufactured tools for restricting the gimbal wrist axes. Although this method was valuable for evaluation, the manual locking mechanism prevented perfect suppression of the other gimbal joints during investigations of the independent wrist motions. However, due to the range of motions and displacements investigated (Table 4.2), error assessments for each wrist axes were assumed to be independent with minimal contributions from other axes. Since liver diameters are typically less than 15 cm but can range up to approximately 21 cm,[35] we evaluated our system with motion up to 25 cm when testing the compound joint kinematics to ensure the typical working volume of the tracking system was tested.

Quantification of the tracking system error was performed by computing the difference in displacements determined by our mechanical system and the optical tracking system. The center of the system's range of motion was used to create a reference position for computing displacements during subsequent manipulations. Simultaneous transformation matrices were computed by our mechanical system and optical tracking, which determined the moving tip location in their respective coordinate systems as our system was manipulated. Euclidean distances between the new tip location and the initialization position were computed in each tracking system's coordinate system and the difference was used for error quantification.

4.2.3 Mock applicator insertion

The expected clinical accuracy of our 3D US guidance system was evaluated using an end-to-end workflow from 3D US image acquisition for target planning to targeted placement of a needle-like object with errors validated from CT imaging external to our system. A

tissue-mimicking phantom was made using a mixture of agar and glycerol diluted in deionized water (35 g/L_{H2O} and 80 mL/L_{H2O}, respectively) to create a speed-of-sound of approximately 1540 m/s.[36] This mixture was heated to approximately 65°C and provided an approximately hypoechoic background under US imaging once cooled. Agar spheres were fabricated using molds with diameters of 3.18 mm, 4.76 mm, and 9.53 mm to provide visible fiducials for image-based registration. The spheres contained 10 g/L_{H2O} of SigmaCell cellulose to provide acoustic backscatter for US imaging and 10 g/L_{H2O} of Tungsten (monocrystalline powder, 0.6-1 micron, 99.9+%) to create CT contrast. These spheres provided a unique spatial distribution for image registration without any shadowing artifacts or speed-of-sound distortions. A 3D-printed needle guide was made to provide our guidance software with a known geometry that could be used in a targeting workflow (Figure 4.3). This guide was fabricated to match the casing of a C5-1 US probe (Philips, Eindhoven, The Netherlands) and provided known trajectories in a range from 15-60° from the long-axis of the probe and in the plane of the image.

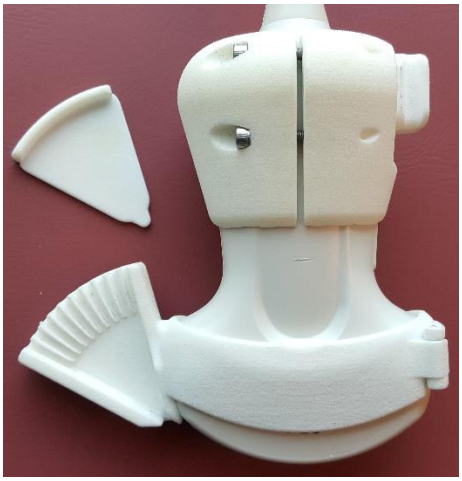

Figure 4.3 A custom 3D-printed needle guide provided known insertion trajectories over a 15-60° range relative to the US probe axis. A detachable face (top-left) allows for the removal of the guide after insertion of a needle into a volume, enabling 3D US imaging without affecting the inserted needle.

Needle targeting was achieved by acquiring a pre-insertion 3D US image, selecting a target in the image, navigating to the target using our system, and inserting a needle. A commercially available iU22 US system with a C5-1 US probe (Philips, Eindhoven, The Netherlands) was attached to the system to acquire a 60° tilt scan or a 60 mm + 60° hybrid

scan. The fabricated phantom allowed for relevant imaging up to a depth of 14 cm, which resulted in image and voxel sizes of $692 \times 542 \times 542$ voxels and $0.25 \times 0.25 \times 0.25\ mm^3$, respectively, for the tilt geometry and $692 \times 542 \times 584$ voxels and $0.25 \times 0.25 \times 0.34\ mm^3$ for the hybrid geometry.

Three different modes of navigation were investigated that required varying levels of user interaction: (1) relying predominantly on the system by using only the motors on the scanner for US probe navigation, (2) a freehand approach that only used the mechanical tracking system for navigation, and (3) a mixed navigation approach that used the scanner motors for image plane navigation and the tracking system for in-plane correction. The targeting accuracy of the system was evaluated using eight independent stainless steel needle insertions per 3D US acquisition geometry (i.e., tilt or hybrid) paired with a target navigation technique (i.e., motors only, tracking system only, or a mixed motor plus in-plane tracking system correction) for a total of 48 needle insertions using the 3D US system.

Figure 4.4 Experimental set-up for a 3D US image-guided needle insertion with an O-arm providing external imaging comparison for targeted needle placements.

3D US needle image-guidance was evaluated using a post-insertion 3D US scan and an external cone-beam computed tomography (CBCT) O-arm imaging system (Medtronic, Dublin, Ireland). The portable CBCT scanner (Figure 4.4) was used to acquire images using imaging parameters of 100 kV, 20 mA, and 150 mAs using a high definition preset. Higher resolution images of $1024 \times 1024 \times 384$ voxels with voxel dimension of $0.22 \times 0.22 \times 0.43\ \text{mm}^3$ were generated by post-processing the raw images.[37]

Analyzing the needle targeting accuracy was completed by registering all images to the same coordinate system and comparing the needle identified in the 3D US and CT images to the intended target location giving 3D US tip error and CT tip error, respectively. 3D fiducial registration was performed by manually selecting five agar sphere centroids in the pre-insertion 3D US image (*i.e.*, containing the target coordinates) and transforming the post-insertion 3D US image and post-insertion CT image using the matched unique fiducials. This enabled computation of the fiducial registration error (FRE). Needle tips were manually identified in the post-insertion images prior to fiducial registration to reduce any user bias on targeting error. Euclidean distances between the target location and transformed needle tip locations were computed to assess targeting tip errors when using the system, but the distance between needle tips identified in 3D US and CT were also compared to verify image modality agreement (i.e., tip agreement).

4.2.4 Clinical feasibility

Our system was used to acquire images of a volunteer under a study approved by the Institutional Review Board of Western University to qualitatively assess expected clinical image quality and usability. This was performed using a breath-hold technique to reduce respiratory motion artifacts during image acquisition and improve liver visibility while reducing the amount of shadowing artifacts produced from the volunteer's ribs. A 2D US image depth of 14 cm was chosen to visualize the liver from the surface of the skin to the subject's diaphragm and compared against 3D images generated using a commercial X6-1 3D US probe (Philips, Eindhoven, The Netherlands).

4.2.5 Statistical analysis

Statistical calculations were performed in GraphPad Prism 8.4.0 (Graphpad Software, Inc., CA, USA). The normality of distributions were evaluated using the Shapiro-Wilk test and were followed by unpaired t-tests or Mann-Whitney tests, depending on the normality of the error distributions. Linear regressions were performed to determine any spatial dependencies on targeting errors using the 3D US and CBCT images. The three navigation approaches were also compared using a one-way analysis of variance (ANOVA) with multiple comparisons performed using a Tukey's test if a significant difference was computed. The significance level for statistical analysis was chosen such that the probability of making a type I error was less than 5% ($p < 0.05$).

4.3 Results

4.3.1 Tracking system accuracy

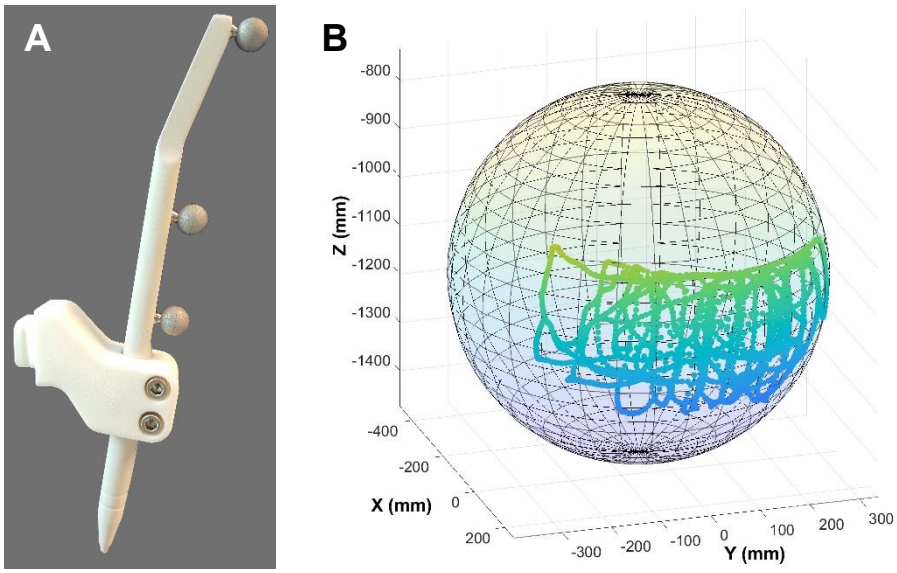

Figure 4.5 Optical tracking stylus height assessment. (A) An optical tracking stylus was mounted to our system using a 3D-printed holder with a slight tilt to avoid collision with the three-motor scanner. (B) A sphere was fit to the point cloud generated during manipulation of the mechanical system gimbal joint to confirm the stylus' height and tip location.

The height of the stylus (Figure 4.5A) was confirmed by fitting a sphere to the point cloud generated during manipulation of the three DoF gimbal joint on the mechanical tracking

system (Figure 4.5B). The radius of the sphere was computed to be 366.0 mm, resulting in a difference of 0.4 mm (0.1 %) from the expected 366.4 mm. Following confirmation of the stylus tip location, each joint on the tracking system was manipulated independently and in compound joint motions with errors shown in Table 4.2.

Table 4.2 Mean ± standard deviation of Euclidean distance differences between our mechanical tracking system and an optical tracking system. The five tracking system joints were evaluated using independent ranges prior to compound joint motions in a 25 cm range of evaluation.

Joint	Joint Range (º)	Displacement Range (mm)	Mean Error (mm)
Vertical	±30º	6.9, 128.1	0.81 ± 0.55
Sway	±30º	9.9, 119.1	0.22 ± 0.18
Wrist Pitch	-45º, 60º	42.2, 172.5	2.06 ± 2.63
Wrist Roll	±30º	20.3, 33.0	2.40 ± 1.16
Wrist Yaw	±90º	137.4, 421.3	2.69 ± 1.62
Compound	—	52.4, 346.0	1.85 ± 1.33

4.3.2 Applicator insertion into phantoms

4.3.2.1 Motor navigation

An example phantom needle insertion with registered 3D US and CBCT images resliced to display the entire needle trajectory is shown in Figure 4.6. When using the three-motor scanner for needle targeting, mean ± standard deviation (SD) tip errors based on the US and CT images were 4.44 ± 3.08 mm and 4.04 ± 2.79 mm, respectively (Table 4.3). Due to the consistency of the motorized approach returning to the image origin, manual registrations were not necessary between the pre-insertion and post-insertion 3D US images. Although navigation when using a hybrid geometry appeared to result in larger tip errors, no statistically significant differences ($p > 0.05$) were observed between the tilt and hybrid scan geometries for FRE, 3D US/CT tip agreement, 3D US tip error, and CT tip error. However, there was a significant, moderate correlation between image depth and error based on tip identification in both the 3D US (Figure 4.7A) and CT images (Figure 4.7D). Each image geometry was investigated separately for the CT tip errors and after removal of a low tip error outlier for the tilt geometry, strong correlations were observed for the hybrid geometry ($p = 0.0079$, $r^2 = 0.72$) and tilt geometry ($p = 0.0196$, $r^2 = 0.78$).

Table 4.3 Needle tip targeting errors when using a motor, tracking system, and mixed motor with in-plane correction navigation approaches. Mean ± SD are reported for fiducial registration error (FRE) between the pre-insertion 3D US and post-insertion 3D US image, FRE between the pre-insertion 3D US and CT image, post-insertion 3D US to CT manual tip location distance (agreement), needle tip to pre-insertion target distance error based on the US image, and needle tip to pre-insertion target distance error based on the CT image as the gold standard.

Navigation Approach	Acquisition Geometry	US/US FRE (mm)	US/CT FRE (mm)	Tip Agreement (mm)	3D US Tip Error (mm)	CT Tip Error (mm)
Motor	Tilt	—	1.12 ± 0.29	1.37 ± 0.49	3.36 ± 1.93	2.73 ± 1.74
	Hybrid	—	0.93 ± 0.36	1.27 ± 0.86	5.01 ± 3.77	5.19 ± 3.13
	Total	—	1.02 ± 0.33	1.32 ± 0.69	4.44 ± 3.08	4.04 ± 2.79
Tracking System	Tilt	0.52 ± 0.16	0.62 ± 0.15	2.76 ± 1.45	5.71 ± 1.86	7.00 ± 1.49
	Hybrid	0.71 ± 0.26	0.76 ± 0.21	1.78 ± 0.61	8.46 ± 2.94	8.68 ± 2.87
	Total	0.61 ± 0.23	0.69 ± 0.19	2.27 ± 1.19	7.08 ± 2.86	7.84 ± 2.37
Mixed	Tilt	0.34 ± 0.09	0.65 ± 0.16	1.73 ± 0.42	3.40 ± 1.94	4.28 ± 2.02
	Hybrid	0.33 ± 0.10	0.50 ± 0.14	1.74 ± 0.34	4.14 ± 2.64	4.25 ± 3.00
	Total	0.33 ± 0.09	0.58 ± 0.17	1.73 ± 0.37	3.77 ± 2.27	4.27 ± 2.47

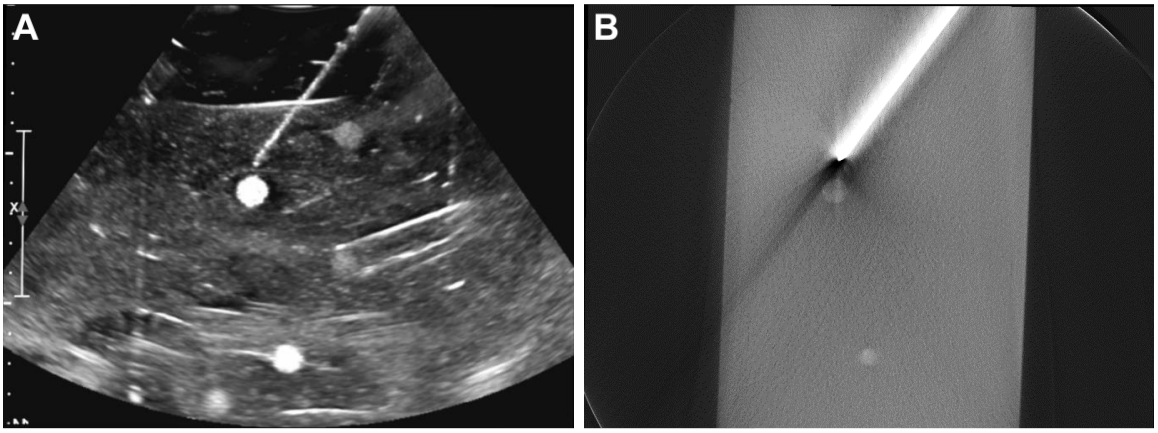

Figure 4.6 Manually registered 3D US (A) and CBCT (B) images of needles inserted into an agar-based tissue-mimicking phantom. The agar spheres contained cellulose and tungsten to provide targets for fiducial registration.

4.3.2.2 Tracking system navigation

Errors associated with needle targeting using the tracking system navigation are shown in Table 4.3. The total mean ± SD tip targeting errors using the 3D US and CT images were 7.08 ± 2.86 mm and 7.84 ± 2.37 mm, respectively. Aside from a statistically significant difference ($p < 0.05$) observed for the 3D US tip error, no statistically significant

differences were observed between tilt and hybrid geometries. However, a statistically significant larger error was observed for the 3D US ($p < 0.05$) and CT ($p < 0.001$) tip errors using the tracking approach compared to the motorized navigation approach (Sec. 4.3.2.1). No significant correlations were observed between tip errors and image depth (Figure 4.7B&E).

4.3.2.3 Mixed navigation

Table 4.3 also shows the needle targeting errors for the combined motor and tracking system navigation approach. Total mean ± SD tip targeting errors using the 3D US and CT images were 3.77 ± 2.27 mm and 4.27 ± 2.47 mm, respectively. No statistically significant differences ($p > 0.05$) were observed between tilt and hybrid geometries for any of the recorded metrics. ANOVA of the tip errors for the motorized navigation approach (Sec. 4.3.2.1), the tracking system approach (Sec. 4.3.2.2), and the mixed navigation method showed a statistically significant difference calculated using 3D US ($p < 0.01$) and CT images ($p < 0.0001$). Tukey's multiple comparisons test showed a significantly larger error when using the tracking system compared to the motor approach ($p < 0.001$) and the mixed navigation approach ($p < 0.001$), but no statistically significant differences were observed between the motorized approach and the mixed navigation method. Unlike the motor only approach, no statistically significant correlation was observed between 3D US (Figure 4.7C) or CT (Figure 4.7F) tip error and image depth. However, strong correlations were observed for the hybrid geometry when 3D US ($p = 0.0316$, $r^2 = 0.56$) and CT ($p = 0.0122$, $r^2 = 0.68$) tip errors were separated by acquisition geometry.

4.3.3 Clinical feasibility

Example 3D US images of a healthy volunteer are shown in Figure 4.8. Important anatomical structures, including the portal vein, diaphragm, gallbladder, and right kidney, were clearly reconstructed with few artifacts due to uncorrected scanner or tissue motion. The full inspiration breath-hold was a successful approach for this volunteer as shadowing artifacts from the rib cage were avoided in the reconstructed 3D US images, generating clinically useful images as assessed by an interventional radiologist (N.K). Hybrid (60 mm + 60º) and tilt (60º) images were acquired in 12 s.

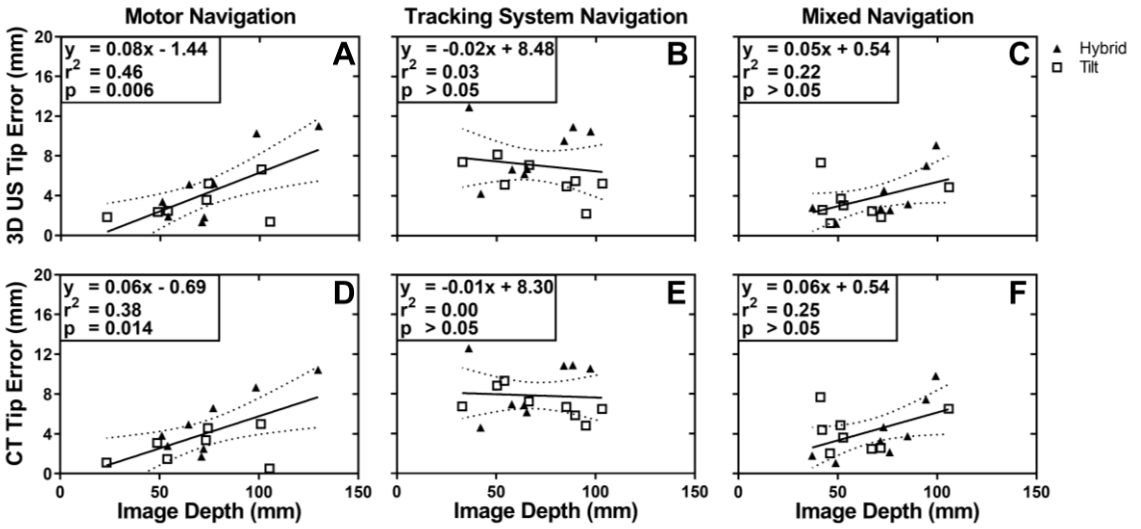

Figure 4.7 Scatter plots showing the 3D US (A-C) and CT (D-F) needle tip targeting error as image depth increases for motor (A, D), tracking system (B, E), and mixed motor with in-plane correction navigation approaches (C, F). Hybrid and tilt image acquisition geometries were used for targeting experiments and linear regressions (solid) are shown with 95% confidence bands (dotted).

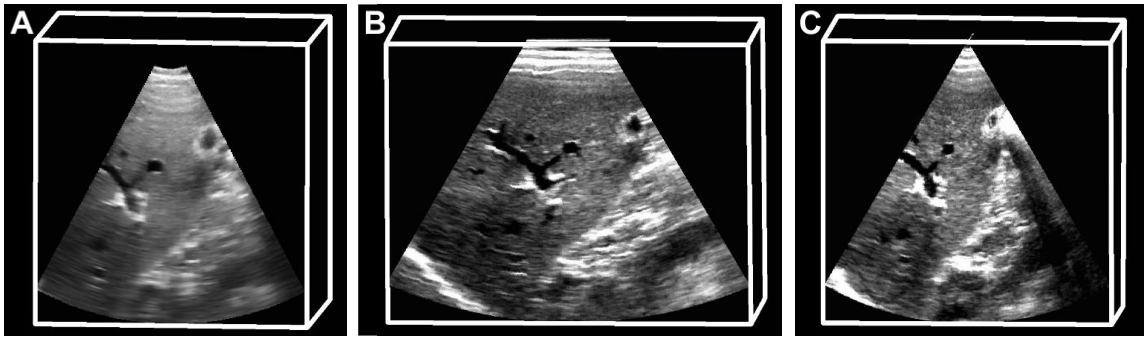

Figure 4.8 3D US images of a volunteer's liver using (A) a commercial X6-1 probe, (B) a hybrid scan geometry using our proposed system, and (C) a tilt scan geometry using our proposed system.

4.4 Discussion

4.4.1 Tracking system accuracy

The mechanical tracking system was assessed using optical tracking to evaluate the error associated with determining a US probe orientation relative to our proposed system. After evaluating the error of each joint independently, a mean positioning error of 1.85 ± 1.33

mm was observed when performing compound joint manipulations in motions expected during interventional focal ablation of liver tumors. Since this error encompasses the tracking system error from the system cart to the 2D US probe, this has the potential to provide sufficient accuracy for initializing position dependent algorithms, such as a 3D US image stitching algorithm to generate a larger view of the liver. This also motivated targeted needle insertions, so a 95% confidence interval was computed to assess the maximum tumor diameter that could reliably be targeted using

$$d_{max} = 2\left(\bar{x} + \frac{1.96\sigma}{\sqrt{N}}\right)\ [mm], \tag{4.1}$$

where $\bar{x}$ is the mean positioning error, σ is the standard deviation, and N is the number of measurements. This resulted in a tumor diameter of 5.54 mm with 95% confidence if no other errors were present. Thus, we believe this diameter to be sufficient for clinical use as most treated liver tumors are between 20 mm and 50 mm. However, since we chose to use magnetic encoders in the tracking system that detect the perpendicular component of the magnetic field of the rotary shaft in the radial-transverse cylindrical plane (for a reduced size advantage), any manufacturing error in the magnetic field alignment with the rotary encoder shafts would increase the measured joint errors due to the nonlinear nature of the detected magnetic field. Although we believe the accuracy we achieved to be sufficient, calibration of each encoded joint could be completed during assembly of the system[38] to reduce this error as the off-axis magnetic field is still extremely consistent and repeatable.

4.4.2 Mock applicator insertion

The motor-only navigation method approach resulted in a needle tip guidance error of 4.04 ± 2.79 mm when evaluated with a registered CT image and was observed to have the lowest mean error of the three approaches, although not statistically significant. Tip targeting errors when using the three-motor scanner approach are likely acceptable for targets located at a depth <75 mm, but the main source of error was likely due to the custom needle guide. Moderate correlations were observed with image depth and tip error, with a strong correlation specifically for the hybrid imaging geometry. Since angular sampling will result in larger distances between available needle guide trajectories proportional to depth, this observation possibly suggested that the needle guide increments of 5° were too large for

deeper targets without an in-plane correction. Since no adjustment was performed to align the target with one of the nearest projected needle guide tracks, an error of 2.5° (i.e., directly in between needle guide trajectories) was assumed to be the maximum error contribution from the needle guide. Taking into account the 10.69 mm template height offset from the US probe tip, a maximum error contribution from the needle guide alone (shown in Figure 4.9) for an image depth of x mm was determined (Eq. 4.2).

$$MaxTemplateError = 0.0436x + 0.466 \quad (4.2)$$

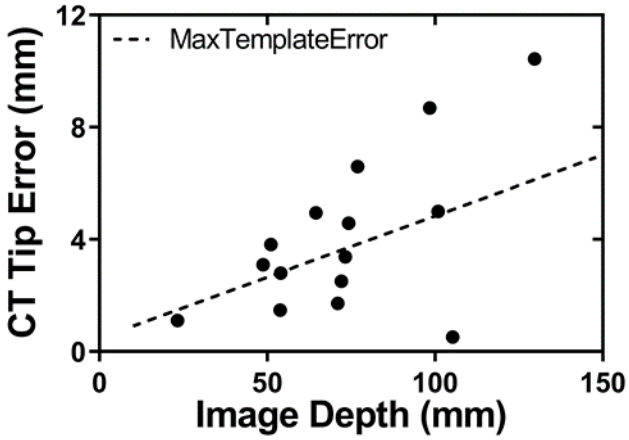

Figure 4.9 Scatter plot showing the needle targeting error using the three-motor approach. The maximum possible error due to the needle template geometry is shown as a dashed line.

Performing guided needle insertion with the tracking system was the worst approach with a statistically significantly higher tip error of 7.84 ± 2.37 mm when compared against the other two methods. Although the mean positioning error reported using optical tracking was less than 3 mm, the increased error observed with needle insertion suggests that there is a small angular miscalibration in the tracking system as the needle tip point of measurement is much further from the US probe tip. In addition, some error from the three-motor scanner could contribute to tracking system error since the scanner must return to the assumed final axis of the tracking system after image acquisition, but this additional source of misalignment is likely minimal. Since no correlations were observed with depth, the needle guide appears to perform as expected as the user could place the target directly on a projected needle trajectory.

A combined approach for navigation that incorporated the motorized movement for out-of-plane motion and the tracking system for in-plane correction resulted in a mean tip error of 4.27 ± 2.47 mm. This approach was not statistically significantly different from a motor only approach and the in-plane correction did not appear to account for the observed correlation between image depth and tip error when using a hybrid image geometry. This mean error and SD suggests a target with a diameter of 10.96 mm can be hit with a 95% confidence, which is on the order of the recommended 5-10 mm margins for image-guided interventions in the liver.[39–41] One caveat of the navigation errors reported in this study is the ideal nature of the needle insertion experiments, which did not contain expected clinical issues such as liver motion. Image registration methods have been investigated for other 3D US-guided procedures[42,43] and could be incorporated into our proposed system to perform coordinate system corrections required to maintain targeting accuracy. Nevertheless, the combined US-based navigation approach could provide an accessible method to motivate further development of stereotactic interventional radiology approaches that use multiple applicator insertions for treating tumor diameters larger than 50 mm.

4.4.3 Clinical feasibility

The healthy volunteer images provided good feedback about anatomical structures relevant for focal liver tumor therapies. The increasing need and potential for accurate image guidance during minimally invasive therapy is also supported by the need for accurate tissue sampling during biopsy procedures. Since cancer is complex and often comprises of multiple genotypic pathologies, more accurate diagnostic biopsy procedures in the abdominal area could likely improve the information given to the clinician and provide more specific pathology data for better informed therapeutic decision trees. Therefore, our system has the potential to improve a wide range of minimally invasive procedures.

One downside of using US imaging for guiding needle applicator insertions in the abdominal area is the low image contrast of some tumors. This can be challenging using conventional clinical workflows using 2D US as insertions must be performed using other anatomical landmarks for approximating tumor locations. A beneficial approach would be to perform an image registration between pre-operative CT images containing tumor

locations with real-time intra-operative US images for guidance, but the multi-modality and difference between 2D and 3D imaging present as a challenge. In addition, patient positioning may change and US probe pressure could introduce deformations, requiring deformable image corrections. With the incorporation of 3D US and our system, a multi-modal 3D image registration could be facilitated as the additional spatial context is available relative to conventional 2D US imaging. By registering the CT image to the 3D US image domain, the navigation approaches presented could be used to target low contrast tumors in US using CT-derived tumor localization.

Avoiding critical structures and organs-at-risk, like the gallbladder, is also an important clinical constraint for maintaining low complication rates. A registration process between pre-operative CT and intra-operative 3D US could allow for pre-operative planning where tumor locations and critical structures can be identified for optimizing the optimal needle applicator trajectories.25 Model views can be generated intra-operatively using segmentation software available on our system31 and used with our needle guide predicted trajectory for real-time avoidance of critical structures. If a freehand insertion is performed without a needle guide, an alternative solution could include a 2D US real-time needle segmentation method for comparing tip and trajectory information to the identified structures.

4.5 Conclusions

A mechanically tracked system with geometrically variable 3D US during minimally invasive liver cancer diagnostic or therapeutic procedures provides a utility that enables enhanced applicator guidance, placement verification, and improved clinical workflow without the need for additional radiation exposure. With this device, intraoperative assessment and applicator adjustments can be performed to potentially decrease the liver cancer recurrence rates associated with minimally invasive procedures and demonstrate a step towards stereotactic interventional approaches.

4.6 References

1. Stewart BW, Wild C. *World Cancer Report 2014*. Lyon; 2014.

2. El-Serag HB, Marrero JA, Rudolph L, Reddy KR. Diagnosis and Treatment of Hepatocellular Carcinoma. *Gastroenterology*. 2008;134(6):1752-1763. doi:10.1053/j.gastro.2008.02.090

3. Ruers T, Bleichrodt RP. Treatment of liver metastases, an update on the possibilities and results. *Eur J Cancer*. 2002;38(7):1023-1033. doi:10.1016/S0959-8049(02)00059-X

4. Schoenberg MB, Bucher JN, Vater A, et al. Resection or Transplant in Early Hepatocellular Carcinoma: A Systematic Review and Meta-analysis. *Dtsch Aerzteblatt Online*. 2017;114(31-32):519-526. doi:10.3238/arztebl.2017.0519

5. Cleary K, Peters TM. Image-Guided Interventions: Technology Review and Clinical Applications. *Annu Rev Biomed Eng*. 2010;12(1):119-142. doi:10.1146/annurev-bioeng-070909-105249

6. Shady W, Petre EN, Gonen M, et al. Percutaneous Radiofrequency Ablation of Colorectal Cancer Liver Metastases: Factors Affecting Outcomes—A 10-year Experience at a Single Center. *Radiology*. 2016;278(2):601-611. doi:10.1148/radiol.2015142489

7. Poggi G, Tosoratti N, Montagna B, Picchi C. Microwave ablation of hepatocellular carcinoma. *World J Hepatol*. 2015;7(25):2578. doi:10.4254/wjh.v7.i25.2578

8. McCarley J, Soulen M. Percutaneous Ablation of Hepatic Tumors. *Semin Intervent Radiol*. 2010;27(03):255-260. doi:10.1055/s-0030-1261783

9. Liang P, Yu J, Lu M-D, et al. Practice guidelines for ultrasound-guided percutaneous microwave ablation for hepatic malignancy. *World J Gastroenterol*. 2013;19(33):5430-5438. doi:10.3748/wjg.v19.i33.5430

10. Shady W, Petre EN, Do KG, et al. Percutaneous Microwave versus Radiofrequency Ablation of Colorectal Liver Metastases: Ablation with Clear Margins (A0) Provides the Best Local Tumor Control. *J Vasc Interv Radiol*. 2018;29(2):268-275.e1. doi:10.1016/j.jvir.2017.08.021

11. Sparchez Z, Mocan T, Hajjar NA, et al. Percutaneous ultrasound guided radiofrequency and microwave ablation in the treatment of hepatic metastases. A monocentric initial experience. *Med Ultrason*. 2019;21(3):217. doi:10.11152/mu-1957

12. Tanis E, Nordlinger B, Mauer M, et al. Local recurrence rates after radiofrequency ablation or resection of colorectal liver metastases. Analysis of the European

Organisation for Research and Treatment of Cancer #40004 and #40983. *Eur J Cancer*. 2014;50(5):912-919. doi:10.1016/j.ejca.2013.12.008

13. Georgiades CS, Hong K, Geschwind J-F. Radiofrequency Ablation and Chemoembolization for Hepatocellular Carcinoma. *Cancer J*. 2008;14(2):117-122. doi:10.1097/PPO.0b013e31816a0fac

14. Moche M, Busse H, Futterer JJ, et al. Clinical evaluation of in silico planning and real-time simulation of hepatic radiofrequency ablation (ClinicIMPPACT Trial). *Eur Radiol*. 2020;30(2):934-942. doi:10.1007/s00330-019-06411-5

15. Vogl TJ, Mack MG, Müller PK, Straub R, Engelmann K, Eichler K. Interventional MR: interstitial therapy. *Eur Radiol*. 1999;9(8):1479-1487. doi:10.1007/s003300050874

16. Zhang D, Liang W, Zhang M, et al. Multiple antenna placement in microwave ablation assisted by a three-dimensional fusion image navigation system for hepatocellular carcinoma. *Int J Hyperth*. 2018;35(1):122-132. doi:10.1080/02656736.2018.1484183

17. Jung EM, Friedrich C, Hoffstetter P, et al. Volume Navigation with Contrast Enhanced Ultrasound and Image Fusion for Percutaneous Interventions: First Results. Rubinsky B, ed. *PLoS One*. 2012;7(3):e33956. doi:10.1371/journal.pone.0033956

18. Liu F, Liang P, Yu X, et al. A three-dimensional visualisation preoperative treatment planning system in microwave ablation for liver cancer: A preliminary clinical application. *Int J Hyperth*. 2013;29(7):671-677. doi:10.3109/02656736.2013.834383

19. Clasen S, Pereira PL. Magnetic resonance guidance for radiofrequency ablation of liver tumors. *J Magn Reson Imaging*. 2008;27(2):421-433. doi:10.1002/jmri.21264

20. Krücker J, Xu S, Glossop N, et al. Electromagnetic Tracking for Thermal Ablation and Biopsy Guidance: Clinical Evaluation of Spatial Accuracy. *J Vasc Interv Radiol*. 2007;18(9):1141-1150. doi:10.1016/j.jvir.2007.06.014

21. Kim SH, Choi BI. Three-dimensional and Four-dimensional Ultrasound: Techniques and Abdominal Applications. *J Med Ultrasound*. 2007;15(4):228-242. doi:10.1016/S0929-6441(08)60040-5

22. Sjolie E, Lango T, Ystgaard B, Tangen GA, Nagelhus Hernes TA, Marvik R. 3D ultrasound-based navigation for radiofrequency thermal ablation in the treatment of liver malignancies. *Surg Endosc*. 2003;17(6):933-938. doi:10.1007/s00464-002-9116-z

23. Hotta N, Yamada S, Murase K, Masuko K. Usefulness of Real-Time 4D Ultrasonography during Radiofrequency Ablation in a Case of Hepatocellular

Carcinoma. *Case Rep Gastroenterol*. 2011;5(1):82-87. doi:10.1159/000321721

24. Neshat H, Cool DW, Barker K, Gardi L, Kakani N, Fenster A. A 3D ultrasound scanning system for image guided liver interventions. *Med Phys*. 2013;40(11):112903. doi:10.1118/1.4824326

25. Liang L, Cool D, Kakani N, Wang G, Ding H, Fenster A. Automatic Radiofrequency Ablation Planning for Liver Tumors with Multiple Constraints Based on Set Covering. *IEEE Trans Med Imaging*. 2019;0062. doi:10.1109/TMI.2019.2950947

26. Gillies DJ, Awad J, Rodgers JR, et al. Three-dimensional therapy needle applicator segmentation for ultrasound-guided focal liver ablation. *Med Phys*. 2019;46(6):mp.13548. doi:10.1002/mp.13548

27. Sindram D, Swan RZ, Lau KN, McKillop IH, Iannitti DA, Martinie JB. Real-time three-dimensional guided ultrasound targeting system for microwave ablation of liver tumors: a human pilot study. *HPB*. 2011;13(3):185-191. doi:10.1111/j.1477-2574.2010.00269.x

28. Rose SC, Hassanein TI, Easter DW, et al. Value of Three-dimensional US for Optimizing Guidance for Ablating Focal Liver Tumors. *J Vasc Interv Radiol*. 2001;12(4):507-515. doi:10.1016/S1051-0443(07)61892-2

29. Xu H-X, Yin X-Y, Lu M-D, Xie X-Y, Xu Z-F, Liu G-J. Usefulness of Three-dimensional Sonography in Procedures of Ablation for Liver Cancers. *J Ultrasound Med*. 2003;22(11):1239-1247. doi:10.7863/jum.2003.22.11.1239

30. Van Vledder MG, Boctor EM, Assumpcao LR, et al. Intra-operative ultrasound elasticity imaging for monitoring of hepatic tumor thermal ablation. *HPB*. 2010;12(10):717-723. doi:10.1111/j.1477-2574.2010.00247.x

31. Gillies DJ, Bax J, Barker K, et al. Mechanically assisted 3D ultrasound with geometrically variable imaging for minimally invasive focal liver tumor therapy. In: Fei B, Linte CA, eds. *Medical Imaging 2019: Image-Guided Procedures, Robotic Interventions, and Modeling*. SPIE; 2019:33. doi:10.1117/12.2512875

32. Gillies DJ, Bax J, Barker K, et al. Assessment of therapy applicator targeting with a mechanically assisted 3D ultrasound system for minimally invasive focal liver tumor therapy. In: Fei B, Linte CA, eds. *Medical Imaging 2020: Image-Guided Procedures, Robotic Interventions, and Modeling*. SPIE; 2020:85. doi:10.1117/12.2549841

33. Gillies DJ, Bax J, Barker K, et al. 3D Ultrasound Image Guidance System for Focal Liver Tumor Therapies. 10th International Conference on Information Processing in Computer Assisted Interventions (IPCAI). https://ipcai2019.github.io/pdf/Long_Abstracts/Gillies_etal_IPCAI_2019_Long_Abstract.pdf. Published 2019.

34. YD S. Fast Geometric Fit Algorithm for Sphere Using Exact Solution. 2015;13244(10). http://arxiv.org/abs/1506.02776.

35. Kratzer W, Fritz V, Mason RA, Haenle MM, Kaechele V. Factors Affecting Liver Size. *J Ultrasound Med*. 2003;22(11):1155-1161. doi:10.7863/jum.2003.22.11.1155

36. Rickey DW, Picot PA, Christopher DA, Fenster A. A wall-less vessel phantom for Doppler ultrasound studies. *Ultrasound Med Biol*. 1995;21(9):1163-1176. doi:10.1016/0301-5629(95)00044-5

37. Petrov IE, Nikolov HN, Holdsworth DW, Drangova M. Image performance evaluation of a 3D surgical imaging platform. In: Pelc NJ, Samei E, Nishikawa RM, eds. *Medical Imaging 2011: Physics of Medical Imaging*. Vol 7961. ; 2011:79615O. doi:10.1117/12.878804

38. Michael J, Morton D, Batchelar D, Hilts M, Crook J, Fenster A. Development of a 3D ultrasound guidance system for permanent breast seed implantation. *Med Phys*. 2018;45(8):3481-3495. doi:10.1002/mp.12990

39. Wells SA, Hinshaw JL, Lubner MG, Ziemlewicz TJ, Brace CL, Lee FT. Liver Ablation: Best Practices. *Radiol Clin North Am*. 2015;53(5):933-971. doi:10.1016/j.rcl.2015.05.012

40. Crocetti L, de Baere T, Lencioni R. Quality Improvement Guidelines for Radiofrequency Ablation of Liver Tumors. *Cardiovasc Intervent Radiol*. 2010;33(1):11-17. doi:10.1007/s00270-009-9736-y

41. Lencioni R, de Baere T, Martin RC, Nutting CW, Narayanan G. Image-Guided Ablation of Malignant Liver Tumors: Recommendations for Clinical Validation of Novel Thermal and Non-Thermal Technologies - A Western Perspective. *Liver Cancer*. 2015;4(4):208-214. doi:10.1159/000367747

42. Gillies DJ, Gardi L, De Silva T, Zhao S, Fenster A. Real-time registration of 3D to 2D ultrasound images for image-guided prostate biopsy. *Med Phys*. 2017;44(9):4708-4723. doi:10.1002/mp.12441

43. De Silva T, Fenster A, Cool DW, et al. 2D-3D rigid registration to compensate for prostate motion during 3D TRUS-guided biopsy. *Med Phys*. 2013;40(2):22904. doi:10.1118/1.4773873

Chapter 5

5 Three-dimensional therapy needle applicator segmentation for ultrasound-guided focal liver ablation

The use of 3D information during interventional procedures has the potential to improve the accuracy needed for sufficient clinical outcomes, but increased procedure times, patient radiation dose, and costly interventional suites can limit widespread adoption. The purpose of Chapter 5 is to present on the development of a novel 3D US system to provide a safe, cost-effective, and accurate intraoperative approach for focal liver tumor therapies.

The contents of this chapter have previously been published in *Medical Physics*: Gillies DJ, Awad J, Rodgers JR, Edirisinghe C, Kakani N, and Fenster A. Medical Physics 2019; 46(6):2646-2658. Permission to reproduce this article was granted by John Wiley and Sons and is provided in Appendix B – Copyright Releases.

5.1 Introduction

Minimally invasive percutaneous interventional techniques are increasingly being adopted throughout the body for a wide range of diagnostic and therapeutic procedures, such as aspiration, biopsy, brachytherapy, and ablation. These techniques are often image-guided procedures and offer promising alternatives to open surgical practices as they have shown decreased patient recovery times and complications due to more localized treatments.[1,2] Minimally invasive focal ablation of liver tumors has received significant attention as liver cancer is the second and sixth most frequent cause of cancer mortality worldwide in men and women, respectively, with high prevalence in under developed and developing countries.[3] Although liver transplantation and resection are the gold standard curative therapy options for cancer with a 5-year survival rate of approximately 40%,[4] these open surgical procedures are often followed by long patient recovery times. Occasionally, serious problems can arise, including organ (graft) rejection, infection, bile duct complications, and immunosuppression related issues, leading to a traumatic hospitalization experience for approximately 26% of liver resection patients and 33% of liver transplant patients.[5] In addition, only 10 to 20% of patients are candidates for surgery based on strict inclusion criteria including the number and location of tumors, malignant spread of the disease or lymph node involvement, and a range of patient factors (*e.g.*, size, age, and existing medical conditions such as cirrhosis of the liver).[6,7] Minimally invasive

techniques, such as radiofrequency ablation (RFA), microwave ablation (MWA), and irreversible electroporation (IRE), have become alternative therapies for early-stage liver cancer with the most common treatment performed on hepatocellular carcinoma.[8] Due to availability of commercial ablation systems, *e.g.*, the Evident^{TM} MWA system (Medtronic, Dublin, Ireland), the StarBurst RFA system (AngioDynamics, Inc., NY, USA), and the Nanoknife IRE system (AngioDynamics, Inc., NY, USA), these procedures have become more clinically feasible and are increasingly being regarded as primary treatment options.

Although a minimally invasive technique offers advantages relative to open surgery, some procedural limitations have prevented its adoption as the gold standard. A majority of the operators using these percutaneous techniques use x-ray computed tomography (CT) images for planning, two-dimensional (2D) ultrasound (US) for intraoperative guidance of the ablation needle applicator(s) into the center of the tumor, and either additional CT or 2D US images to perform further modifications and verify needle applicator placements. Depending on the number and size of tumors, which can typically range from 1 cm to 5 cm in diameter,[8] as well as the type of ablation (radiofrequency vs. microwave), one to four needle applicators are typically required to cause the ablation zone to completely cover the borders of the tumor and allow for adequate treatment coverage. Unfortunately, these procedures have higher local recurrence rates than resection due to insufficient or inaccurate local tumor ablation.[9] One cause for poor ablation coverage has been associated with subjective 2D US guidance and verification, which leads to variability in needle applicator targeting accuracy due to high operator dependence when using 2D US images for 3D spatial localization. Important anatomical markers and structures are difficult to visualize in a single frame when using 2D imaging,[10] which increases complexity and requires the physician to track both the ablation needle applicator and surrounding structures to avoid unnecessary damage.[11] Malposition of the needle applicators can not only lead to unwanted complications, but can increase procedure times and patient radiation dose, from the additional US and CT needed to correct the positions. Thus, if needle applicator targeting accuracy is to be increased without increasing procedure time and minimizing excess radiation dose, a non-ionizing radiation intraoperative imaging workflow is needed to improve upon the conventional 2D US spatial localization method.

Intraoperative magnetic resonance (MR) and three-dimensional (3D) US imaging techniques have been investigated to reduce complexity for the physician, increase visualization of surrounding tissues, and enable accurate localization of the ablation needle applicator into the liver.[12–14] Although MR images can provide superior soft-tissue contrast, 3D US techniques have the advantage of providing real-time or near real-time imaging with an imaging system that is portable and affordable, ultimately addressing major concerns for centres in developing countries where liver cancer incidence is high.[3] Since preoperative contrasted CT images provide a sufficient method for lesion identification and planning, image registration can be performed to transfer the locations of the cancerous tissues to the 3D US image.[15] These resulting fusion images can then allow for accurate planning and verification of the needle applicators' location. Unfortunately, current limitations still exist for visualizing and verifying needle applicator positions in 3D US liver images as the visibility can change with needle applicator insertion angle, depth, and size, in addition to the choice of transducer (*i.e.*, curvilinear) and local anatomical acoustic reflections that result in complicated images containing shadows and reverberation artifacts with unclear line-like interfaces.[16,17] Attempts have been made using a variety of needle applicator enhancing techniques to address these localization concerns for the physician by incorporating additional features like echogenic coatings,[18] magnetic or optical tracking systems,[19] robotic needle steering,[20] augmented reality,[21] and US beam steering.[22] Although many options seem promising, all of the above choices add increased cost and complexity relative to the conventional procedure, which can be a limiting factor for widespread dissemination.

Image-based needle applicator segmentation is an alternative option that aims to localize inserted needle applicators to provide an efficient and low-cost method to inform physicians when needle applicator adjustments are required. By employing a segmentation algorithm, the time for intraoperative identification of the needle applicators can be reduced to improve the overall efficiency of the clinical workflow and reduce mental demand of the physician when trying to accurately ablate the cancerous lesions. Segmenting needle-like objects in 3D US has been used in a broad range of interventional procedures with varying requirements influenced by object orientation with respect to the US probe, object flexibility, and US image quality, which in turn is affected by a variety of sources, including

the commercial system, acquisition settings, imaging artifacts from the medical tools,[23] and anatomical imaging challenges (*e.g.* depth of lesion and acoustically visible internal structures contributing to image clutter).

Applications for 3D US needle-like segmentation have been focused on procedures in prostate,[24–28] breast,[29–31] heart[32,33] and anesthetic administration,[34] but these approaches do not readily translate to liver interventions. This is primarily due to deep insertions into the liver that require needle applicators up to 30 cm in length and large angles relative to the transducer face resulting in poor specular reflections back to the transducer. More specific to liver imaging, Zhao *et al*.[35] have investigated a four-dimensional (4D) US micro-tool localization approach by employing a region-of-interest strategy to a random sample consensus (RANSAC) and Kalman filter localization algorithm. When imaging *ex vivo* porcine liver, they reported root-mean-squared tip errors between 0.6 and 2.4 mm with maximum component trajectory errors less than 3.5°. For needle steering approaches, 2D power Doppler has been used with a vibration module[20,36] for 3D segmentation of curved needles. Experiments performed on *ex vivo* bovine liver[20] showed mean tip errors of 0.92 ± 0.93 mm for a centred, orthogonal, straight needle at a 600 Hz vibration frequency. Beigi *et al*.[37] reported on a 3D needle segmentation from multiple images to detect intensity variations while using a moving stylus inside a hollow cannula. Trajectory errors of 1.4 ± 0.7° and tip identification errors of 0.8 ± 1.1 mm were found when imaged on *ex vivo* bovine liver. While general needle-like segmentation algorithms for 3D US have been discussed in the literature and tested on tissue mimicking models, such as agar, chicken breast, bovine, and porcine tissues, evaluation on *in-vivo* clinically acquired 3D US images has not been reported for the unique imaging characteristics of needle applicators used in percutaneous liver tumor ablations.

We propose the use of 3D US imaging paired with an intraoperative image-based needle applicator segmentation algorithm to provide localization of ablation needle applicators in current focal liver tumor ablation therapies. Needle applicators for these procedures typically have a diameter of 1.5 to 2.8 mm (12 to 17 gauge) and range in length from 12 to 30 cm to accommodate for the variety of patient thicknesses and depth of lesions.[38] These procedures are most commonly performed as a two-handed approach where one hand is

used for positioning and orienting the US transducer and the other is used for needle applicator insertion. Due to the free-hand nature of the conventional approach, a wide range of needle applicator insertion angles with respect to the US transducer are observed, ranging from 10 to 80° from the transducer face. In our approach, we assume needle applicators to be rigid and straight, relying on the assumption of minimal bending within the tissue. This assumption was chosen based on a recent clinical CT study where 93% of ablation applicators (inserted in a range from 32 – 182 mm) were observed to have less than 3 mm of deflection with an overall average deflection of 1.3 mm.[39] Since the majority of these deflection measurements are less than the diameter of the ablation applicators (i.e., 1.5 to 2.8 mm), a straight assumption would likely be appropriate to capture the trajectory, and more importantly tip location, for the majority of observed clinical cases. Furthermore, we used a supervised approach to reduce the complexity of the algorithm and provide a method for the physician to control the algorithm. Our algorithm was optimized and evaluated against manual segmentations of an Evident^{TM} MWA antenna (Medtronic, Dublin, Ireland) needle applicator inserted in plain homogeneous agar phantoms to test idealized imaging conditions. This optimization was followed by needle applicator segmentations in 16 retrospective patient 3D US images to evaluate performance on a clinical dataset. Multiple users with a range of US experience performed segmentations with the algorithm to assess robustness and inter-operator variability of the algorithm. These evaluations aim to provide insights on clinical utility and represent an opportunity for improving needle applicator localization for interventional procedures treating liver cancer.

5.2 Materials and methods

5.2.1 3D therapy needle applicator segmentation algorithm

The overall workflow of the 3D needle applicator segmentation algorithm is shown in Figure 5.1, which is primarily based on voxel intensity thresholding and clustering. After acquiring a 3D US image, the user provides the location of a single point to the algorithm, which is assumed to fall along the trajectory of a visible needle applicator in the 3D US image with unknown insertion angle θ (Figure 5.2a). This initial seed point is used to

generate test points in a spherical coordinate system and creates the search space of potential needle applicator trajectories. Since the locations of the generated test points in the search space coordinate system (b) are influenced by the radius of the sphere and the number of points in the longitudinal (polar angle spacing $\Delta\theta$) and latitudinal (azimuthal angle spacing $\Delta\varphi$) axes, investigation of these parameters are discussed in Sec. 5.2.2.

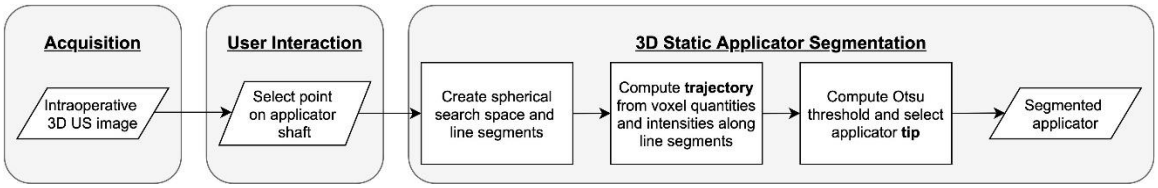

Figure 5.1 Proposed 3D US-based therapy needle applicator segmentation workflow. Line segments are created from a spherical search space to compute the most probable trajectory using a signal-to-background intensity threshold. The Otsu threshold is computed for the most probable trajectory to determine the needle applicator's tip, completing the segmentation.

The second step to find the most probable needle applicator trajectory requires the generation of testable trajectories. Line segments are created for each test point on the sphere and drawn through the initial user seed point to span the diameter of the sphere. Searching diameters of the sphere reduced the testable search space in half as anything beyond the superior hemisphere would result in redundant line segments. Since interventional liver procedures are typically performed with oblique insertion angles on either the left or right side of the US transducer, the range of possible needle applicator slopes was restricted to the sphere's polar angle range θ = 10-80° from the longitudinal axis (*i.e.*, axial axis of the 3D US image). In addition, we also assumed the needle applicators were visualized in the 3D US image approximately in-plane and thus constrained the sphere's azimuthal angle range (*i.e.*, lateral axis of the 3D US image) to φ = 0 ± 60° and 180 ± 60°, as shown in Figure 5.2c.

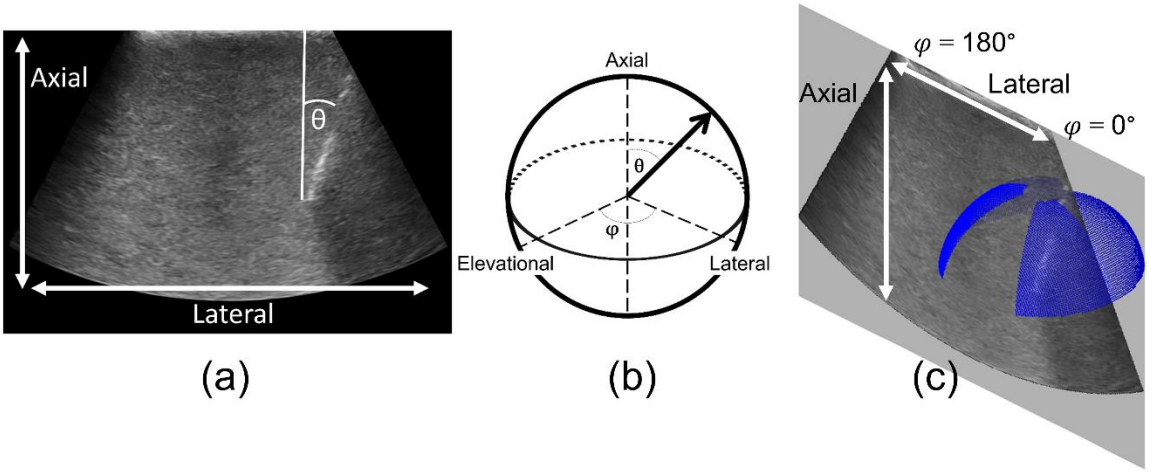

Figure 5.2 (a) Sample 3D US image plane of a needle applicator inserted in a homogeneous phantom with the needle applicator insertion angle (θ) and 2D US axes labelled. (b) Spherical 3D coordinate system to generate test points with 3D US axes labelled for reference. (c) Generated spherical test points used to determine the most probable needle applicator trajectory after incorporating intraoperative assumptions overlaid on the sample 3D US image plane in (a) displayed with a 45° rotation.

The needle applicator's trajectory is determined by maximizing the sum and number of voxels along a line segment that exceeds an intensity threshold. The chosen intensity threshold was selected as the signal-to-background intensity ratio (SBR) that minimized the trajectory error when segmenting needle applicators in phantom images, as described in Sec. 5.2.2. Each potential line segment in the search space is sampled at a spacing equivalent to the average of the lateral and axial in-plane voxel dimensions of the 3D image, which was approximately 0.37 mm. The sum (Sum_i) and total count ($Quantity_i$) of all voxels on a line segment i that are greater than the intensity threshold are saved and used as the metrics to determine the most probable line segment for the needle applicator. The most probable needle applicator trajectory (T) is computed from all possible line segments (n) after normalizing all line segment parameters to the maximum of the computed metric values (*i.e.*, Sum_{max} and $Quantity_{max}$) as:

$$T = \max_{i \in n} \left\{ \left(\frac{Sum_i}{Sum_{max}} \right) + \left(\frac{Quantity_i}{Quantity_{max}} \right) \right\}. \tag{5.1}$$

Once the trajectory is selected, the needle applicator tip is determined by employing a second intensity threshold along the computed one-dimensional vector starting from the manually selected seed point. Under the assumption that a needle applicator (hyper-

intense) and background (hypo-intense) could be represented with a bi-modal histogram of intensities, the Otsu threshold[40] is determined to maximize the interclass variance between the intensity populations. Since the line segment chosen for the needle applicator trajectory would mostly contain voxels corresponding to the needle applicator, the selected line segment is extended by an additional 10 mm to increase the number of background voxels. This aims to approximately equalize the needle applicator and background voxel populations in the intensity distributions, which minimizes uncertainty when determining the Otsu threshold.[41] After determining the Otsu intensity threshold, all voxels along the entire extended needle applicator trajectory with intensity values below the threshold are eliminated. Finally, the last remaining voxel along the trajectory is selected as the tip location.

This complete algorithm was compiled using C++ and ran on an i7-6700K central processing unit (CPU) at 4.0 GHz (Intel Corporation, CA, USA) with the trajectory localization parallelized on 8 threads using OpenMP. This utilized a 3D Slicer[42] user interface to allow for selection of points and passing of voxel coordinates to the segmentation algorithm. Completed segmentations were displayed using the physical dimensions of a 13-gauge ablation needle applicator with a length of 17 cm (Medtronic, Dublin, Ireland).

5.2.2 Phantom images

Since we only had access to 16 patient 3D US images, we used images of needle applicators inserted in phantoms to optimize various parameters required for the algorithm. These optimized parameters were then used to perform segmentations of needle applicators in the patient image dataset. Homogeneous block phantoms were made with distilled water (87.7% by mass), glycerol (8.8% by mass; Sigma-Aldrich, MO, USA), agar (3.1% by mass; Sigma-Aldrich, MO, USA), and cellulose (0.4% by mass; Sigma-Aldrich, MO, USA) for acoustic backscatter.[43] An Evident™ MWA antenna (Medtronic, Dublin, Ireland) was inserted through a custom-made template,[14] which allowed for insertions with one degree of rotational freedom when seated in a compatible box (Figure 5.3). The needle applicators with a length of 17 cm (containing a 3.7 cm radiating tip) and a diameter of 2.1 mm (13 gauge) were inserted through the template into the phantom in a clinically relevant range

of oblique insertion angles with a mounted protractor for approximating visual guidance, but not used for evaluation. 3D US images were captured by employing a freehand approach using the commercially available iU22 US machine with an X6-1 matrix probe (Philips, Amsterdam, NL). The freehand approach was chosen to resemble an interventional procedure where the physician tries to visualize the applicator in the imaging plane while inserting the applicator at various angles depending on the location of the tumor. Since the task of imaging in a single plane is difficult, 3D trajectories were assessed in two degrees of freedom and required the 3D image to be resliced on oblique trajectories to visualize the entire needle. 3D US images containing needle applicators were acquired with a 30% gain, depth of 10 cm, and a 55° angular field of view that resulted in an image size of 512 × 407 × 220 voxels with voxel dimensions of 0.314 × 0.258 × 0.461 mm^3. The needle applicator insertion angles (Figure 5.2a) and insertion depths are provided in Table 5.1. These imaging details were manually determined using the voxel corresponding to the entrance of the needle applicator in the US image and the voxel at the needle applicator's tip location across 10 different insertions.

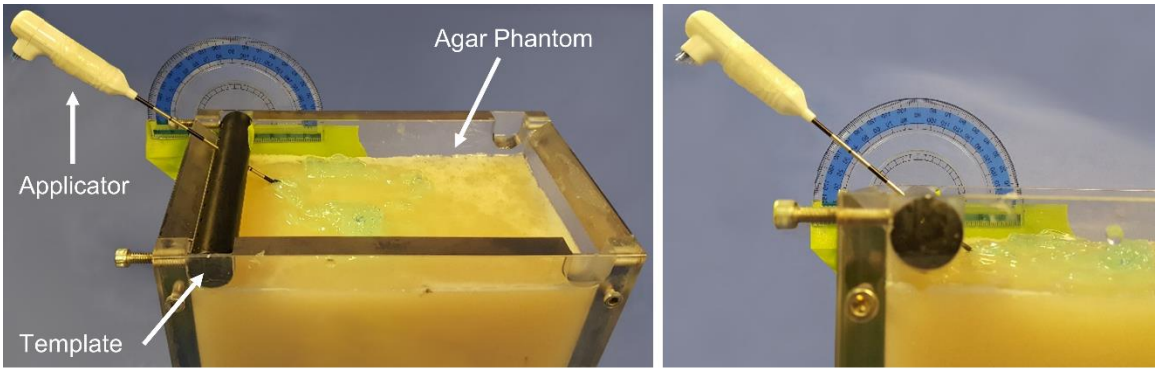

Figure 5.3 (a) Sample MWA needle applicator inserted in a homogeneous phantom through a custom-made template with one degree-of-freedom. (b) Close up perspective on the needle applicator's insertion angle approximated by an attached protractor.

Following 3D image acquisition, manual segmentations of the needle applicators were performed to provide a comparison to the algorithm. The manual segmentations were completed prior to the algorithmic method to ensure an unbiased comparison was provided when quantifying the error of the segmentation algorithm. Manual segmentations were acquired by selecting one point at the visible tip of the needle applicator and a second point

located approximately halfway along the visible shaft. Manual tip locations were repeatedly selected over five different time points, separated by a minimum of 24 hours, to obtain a manual user variability and an average tip location. The second point selected was chosen at the approximate centre of the needle applicator's shaft to ensure the computed trajectory was through the core of the needle applicator. This second point not only provided the necessary information to compute a manual trajectory, but also provided the seed point required to initialize and generate the segmentation from the semi-automated algorithm. Five of these seed points were selected for each phantom 3D US image to investigate if initialization variability affected segmentation performance. With this workflow, a direct comparison between the two methods of segmentation could be achieved to optimize and assess the segmentation algorithm.

Table 5.1 Visualized needle applicators in 3D US images of a homogenous agar phantom.

	Imaged Insertion Angle[a] (°)	Imaged Insertion Depth (mm)
Mean	41.1	68.6
Standard Deviation	16.2	8.4
Minimum	17.4	55.5
Maximum	65.9	81.1

[a]Insertion angle was measured from the axial axis of the US image.

The phantom image dataset was first used to perform optimization of parameters for the trajectory selection component of the segmentation algorithm. The test point spacing, which can be influenced by the spherical radius of the search space, was a major factor to consider when searching for the best trajectory (Figure 5.4). One option could be to choose a large spherical radius to capture all the needle applicator voxels in the image to maximize the trajectory metric in Eq. (5.1). This would also be beneficial since the needle applicator has a non-negligible thickness and capturing points further apart could result in fewer probable trajectories that would maximize the trajectory metric, resulting in a better approximation for the trajectory. However, employing a radius too large could unnecessarily increase computation time and potential for failure on shallow insertions since there would be an increased probability of background voxels that could exceed the static SBR threshold, creating maxima in the trajectory metric. Conversely, choosing a small radius would reduce the number of samples acquired and computation time, but could

result in an increased number of incorrect probable trajectories. Therefore, we optimized for test point spacing by investigating the interaction between coarse, medium, and fine uniformly distributed test point spacings (*i.e.*, $\Delta\theta$ and $\Delta\varphi$) of 2.4°, 1.2°, and 0.6° with small, intermediate, and large spherical search spaces represented by radii of 15, 30, and 45 mm. The choice of these three radii was influenced by the average appearance of needle applicators (*i.e.*, mean insertion depths of approximately 70 mm) in the patient dataset (Table 5.2).

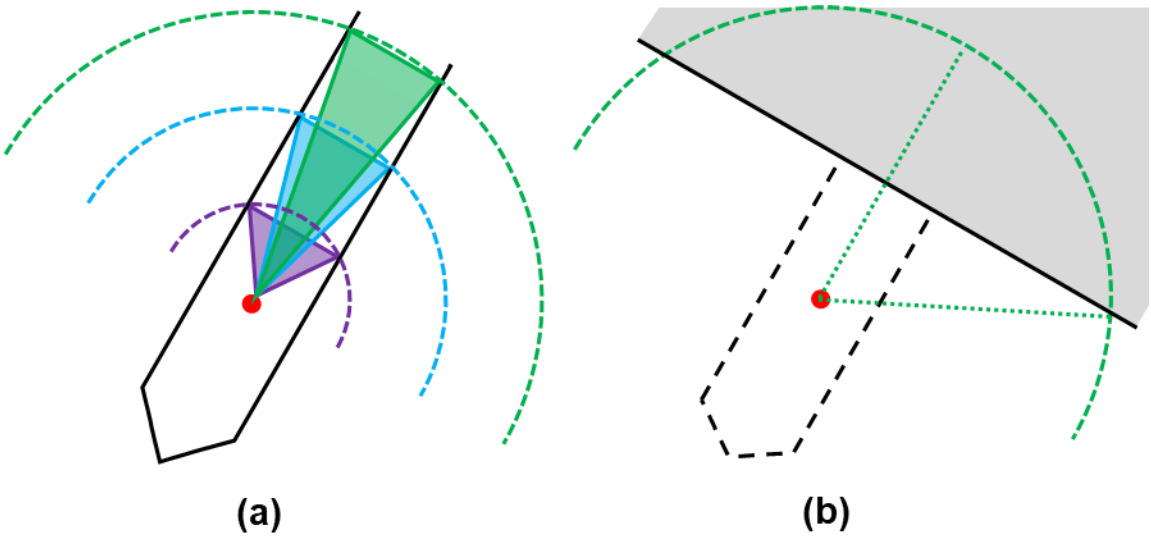

Figure 5.4 Spherical radius influence on most probable trajectory. (a) Since the applicator appearance has a non-negligible thickness, the range and number of potentially acceptable trajectories from the seed point (red) decreases as the spherical search space radius increases from small (purple) to large (green). (b) If a radius search space is too large, an increased probability exists to choose an incorrect trajectory for shallow needle insertions using a larger SBR threshold as the most probably trajectory metric can be increased with larger pixels quantities.

After creating the spherical search space, a background intensity threshold was used as a coarse method to enhance the needle visibility in the 3D US images. Since the user selects a seed point along the shaft of the needle applicator, a single intensity of the needle applicator is known and can be used as an approximation for the entire needle applicator mean intensity level, μ_{app}. Using an SBR ratio defined as:

$$SBR = \frac{\mu_{app}}{\mu_{bg}}, \tag{5.2}$$

the background image intensity, μ_{bg}, can be solved for a chosen SBR, thus, determining the required intensity threshold (μ_{bg}). The SBR was used as an optimization variable to investigate the influence of different background intensity thresholds when determining the needle applicator's most probable trajectory.

After optimizing the trajectory parameters, tip localization error and variability were investigated resulting from the Otsu threshold. As described in Sec. 5.2.1, an extension was added to the selected trajectory to approximately equalize voxel populations of the needle applicator and background. However, since the locations of the manual initialization seed points and the insertion depths of the needle applicators were variable, preliminary observations suggested the distribution of the needle applicator's voxel intensities were overrepresented on average. This overrepresentation led to computation of larger than desired intensity thresholds, which led to shallow predictions of the needle applicator's tip location. Thus, preliminary experiments led to a threshold adjustment that reduced the computed Otsu threshold by 5.

5.2.3 Retrospective patient images

After determining the optimal parameters for the segmentation algorithm from the phantom images, 15 3D US images were acquired on six patients undergoing MWA in the liver. These images were acquired using an iU22 US machine and X6-1 matrix transducer (Philips, Amsterdam, NL) in a study approved by the Human Subjects Research Ethics Board of Western University. All images were acquired post needle applicator insertion, but prior to ablation. Since the physical size of patients was variable, chosen US imaging depths were also variable and resulted in an image size range of 480 × 372 × 218 to 512 × 404 × 222 voxels with a range in voxel dimensions from 0.248 × 0.194 × 0.336 mm^3 to 0.428 × 0.386 × 0.630 mm^3. 14 3D images contained only one needle applicator prior to ablation with 13 images showing a needle applicator approximately in the axial-lateral US plane and one image showing a needle applicator approximately in the axial-elevational US plane. The fifteenth 3D image contained two needle applicators visualized approximately in the axial-lateral US plane, resulting in sixteen needle applicators in total that were visualized and segmented. Needle applicator insertion angle and insertion depth

in the US image are provided in Table 5.2. Similar to the phantom images, these characteristics were manually determined using the voxel corresponding to the entrance of the needle applicator in the US image and the voxel at the needle applicator's tip location.

Table 5.2 Visualized needle applicators in 3D US images of patients undergoing liver tumor MWA.

	Imaged Insertion Angle[a] (°)	Imaged Insertion Depth (mm)
Mean	44.1	71.7
Standard Deviation	14.1	20.9
Minimum	23.3	30.4
Maximum	77.2	99.0

[a]Insertion angle was measured from the axial axis of the US image.

Since our algorithm required initialization, performance is influenced by the location of the user selected seed point. Variability of the algorithm between four trained users of varying US image analysis experience was assessed on these images. The users included: a trained user with four years experience (TU1), a trained user with three years experience (TU2) supervised by the interventional radiologist (N. K.) that acquired the clinical 3D US images, an interventional radiologist 2 years post-fellowship (IR1), and an interventional radiologist 10 years post-fellowship (IR2). All users performed manual identification of the tip prior to generating the algorithm segmentations and determined the mean manual tip locations. Following tip identification from all users, the mean consensus applicator tip location from two or more users was used as the manual annotation for quantifying error, as described in Sec. 5.2.4. All users were instructed to select the shaft seed points near the tip to ensure the location would fall within the spherical search space of the algorithm.

5.2.4 Determination of needle applicator tip and axis errors

The performance of the segmentation algorithm was compared to the manually segmented needle applicator to determine the algorithm segmentation error. The manual trajectory was determined by creating a vector between the user-selected seed point on the shaft and the manually determined mean consensus tip location. Variability in tip localization was calculated by a fiducial localization error (FLE)[44] for all users selected when determining the consensus tip location to characterize inter-subject variability ($\overline{FLE}_{inter}$) and for two

users (*i.e.*, TU1 and TU2) to characterize intra-subject variability ($\overline{FLE}_{intra}$). This was calculated by using the variance (σ^2) for the x, y, and z coordinates of the selected tips (i) in all images (N) over the users in agreement for inter-subject variability and over five trials with 24 hour intervals for the intra-subject variability. Using the definition for FLE of one needle applicator tip as:

$$FLE_i^2 = \sigma^2(x_i) + \sigma^2(y_i) + \sigma^2(z_i), \tag{5.3}$$

the mean FLE for all tips was computed as:

$$\overline{FLE} = \sqrt{\sum_i^N FLE_i^2/N}\ [mm]. \tag{5.4}$$

Variability in the manual identification of the applicator's trajectory was computed across all users after determining the 3D trajectories created between the consensus tip location and the user-specific shaft locations for all patient images.

Three metrics were used to quantify the algorithm's segmentation error when compared to the manual segmentations. The angular difference (ΔT) between the algorithm ($\vec{v}_{alg}$) and manually ($\vec{v}_{man}$) segmented trajectories was quantified as:

$$\Delta T = \cos^{-1}\left(\frac{\vec{v}_{alg} \cdot \vec{v}_{man}}{\|\vec{v}_{alg}\| \cdot \|\vec{v}_{man}\|}\right)[°]. \tag{5.5}$$

The second metric to describe segmentation error has been previously defined by Uherčík *et al.*[29] as the axis localization accuracy (ALA). This metric measures the orthogonal projected distances of the entrance (E) and tip (T) points from the manual to the algorithm segmentation trajectory axes, and reports the maximum of the two distances (*i.e.*, D_E or D_T), as shown in Figure 5.5. The needle applicator tip error (ATE) between manual ($\vec{v}_{man,tip}$) and segmented ($\vec{v}_{alg,tip}$) needle applicator tips was quantified as the Euclidean distance between their coordinates:

$$ATE = \|\vec{v}_{alg,tip} - \vec{v}_{man,tip}\|\ [mm]. \tag{5.6}$$

5.2.5 Statistical analysis

Statistical calculations were performed in GraphPad Prism 7.00 (Graphpad Software, Inc., CA, USA). Normality of distributions were evaluated using the Shapiro-Wilk test and led

to the use of nonparametric statistical tests when the assumption was violated. The corresponding nonparametric alternative tests are presented in parentheses for the remainder of the section. The significance level for statistical analysis was chosen such that the probability of making a type I error was less than 5% ($P < 0.05$). The multi-user error distributions from the patient dataset for trajectory, ALA, and ATE were compared using a one-way repeated measures ANOVA (Friedman) omnibus test, followed by post-hoc analysis using Tukey's honestly significant difference (Dunn's) tests if the omnibus test was significant.

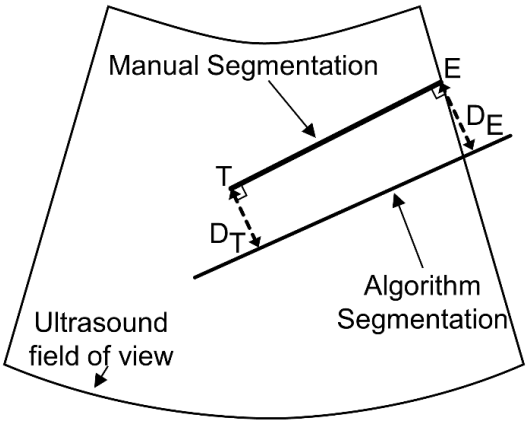

Figure 5.5 Illustration of the axis localization accuracy (ALA) metric simplified to a 2D example for clarity. The entrance and tip locations of the needle applicator from the manual segmentation are used to compute orthogonal distances to the algorithm segmentation axis, which produces the entrance-to-axis distance D_E and the tip-to-axis distance D_T. The maximum of these distances is reported as the axis localization accuracy (ALA).

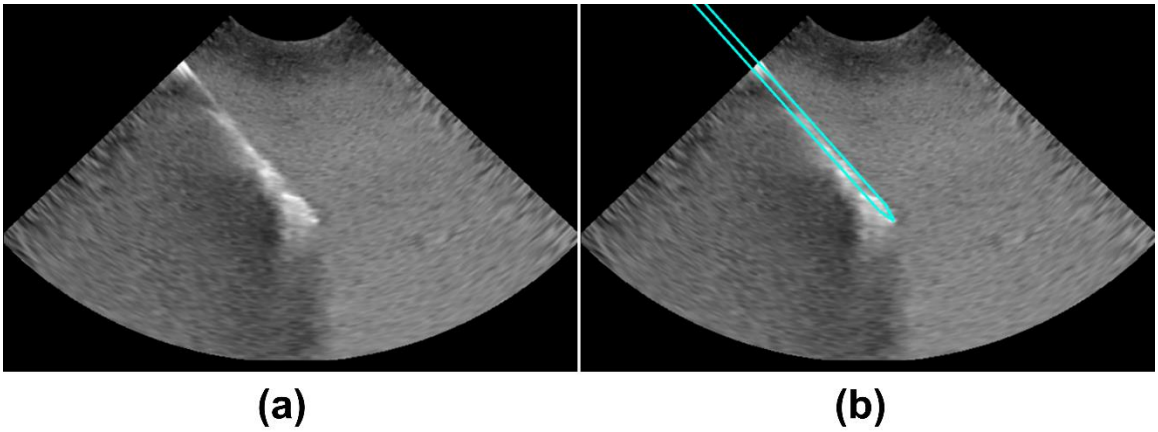

Figure 5.6 Sample oblique plane in a 3D US image of a needle applicator obliquely inserted at 44^0 in a homogeneous tissue mimicking agar phantom before (a) and after (b) segmentation. The 3D US image was resliced to visualize the entire segmentation for clarity.

5.3 Results

5.3.1 Phantom testing

The imaging characteristics of the needle applicators in the phantom images is shown in Table 5.3 with a sample phantom image and segmentation shown in Figure 5.6. Using the five trials of manually localizing the tips in the 3D US images, the mean FLE was found to be 0.43 ± 0.09 mm, which corresponds to approximately one or two voxels.

Table 5.3 Needle applicator imaging characteristics in phantom 3D US images.

Image Characteristic	Mean ± Standard Deviation
Applicator Intensity	178 ± 10
Background Intensity	145 ± 5
SBR	1.22 ± 0.08

The influence of intensity thresholding for three radii sizes and three test point spacings are shown in Figure 5.7. For the largest radius (*i.e.*, 45 mm), ΔT increased as the SBR threshold was increased and resulted in mean errors greater than 5° for SBR thresholds greater than 1.3 for all test point spacings. The trends observed for radii of 15 mm and 30 mm were similar across all spacings. These results led to the choice of a 30 mm radius and an SBR threshold of 1.2 for further experiments as it was the combination that led to one of the lowest trajectory errors while still allowing for some variability in the needle applicator's voxel intensity range. A less restrictive intensity threshold was considered useful and potentially more robust in the patient images as there were more observed artifacts and increased variability in the needle applicator intensities, as shown in Sec. 5.3.2. The mean trajectory computation times for spacings of 2.4°, 1.2°, and 0.6° were 0.233 ± 0.006 s, 0.506 ± 0.043 s, and 1.61 ± 0.04 s, respectively. Since a 30 mm radius and an SBR threshold of 1.2 resulted in similar trajectory errors across all spacing sizes, a 2.4° spacing was chosen since it was associated with the lowest computation time. Using the three selected trajectory parameters, the corresponding ALA failed to pass a normality test (P = 0.0005) and was observed to have a median [first quartile (Q1), third quartile (Q3)] value of 1.3 [0.8, 2.1] mm.

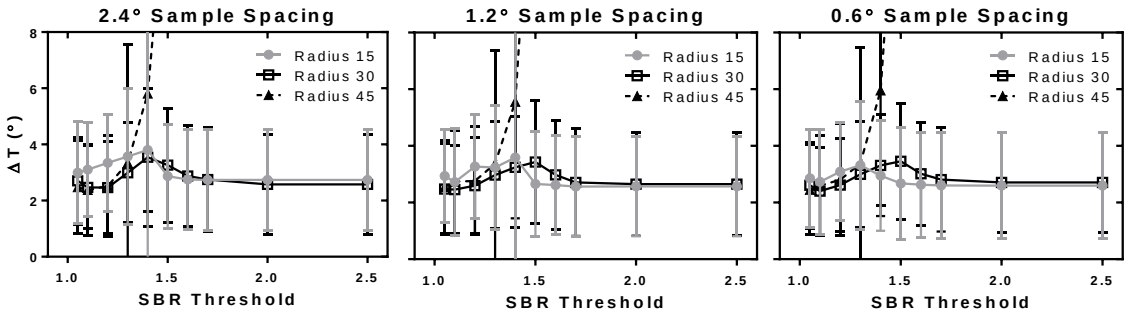

Figure 5.7 The influence of different spherical search space radii and test point spacings on segmentation trajectory error for varying signal-to-background intensity ratio thresholds. Standard deviation error bars are shown for each measurement.

The optimal parameters determined from the phantom images are summarized in Table 5.4. These parameters resulted in an overall mean algorithm segmentation time of 0.246 ± 0.007 s on the phantom images, which encompassed input of the user selected point to the algorithm until display of the segmentation. This sub-second computation time was considered acceptable for intraoperative use and the phantom optimized parameters were used to create segmentations for the clinical dataset as described in Sec. 5.3.2.

Table 5.4 Needle applicator segmentation parameters optimized on phantom images.

Parameter	Value
Test Point Spacing	2.4°
Spherical Radius	30 mm
SBR Threshold	1.2
Tip Threshold	Otsu - 5

5.3.2 Retrospective patient experiments

Table 5.5 Needle applicator imaging characteristics in patient 3D US images.

Image Characteristic	Mean ± Standard Deviation
Applicator Intensity	159 ± 34
Background Intensity	75 ± 21
SBR	2.2 ± 0.5

We first evaluated the imaging characteristics and appearances of the needle applicators in the patient images, shown in Table 5.5. Compared to the phantom images, the standard deviation of mean intensities along the needle applicator was three times greater with an

approximate two-fold increase in the SBR. A sample oblique plane taken from a patient 3D US image with the corresponding segmentation is shown in Figure 5.8. Intensity profiles of a needle applicator taken from a phantom image (Figure 5.9a) and patient image (Figure 5.9b) are shown to further emphasize the appearance differences of the observed needle applicators *in-vivo*.

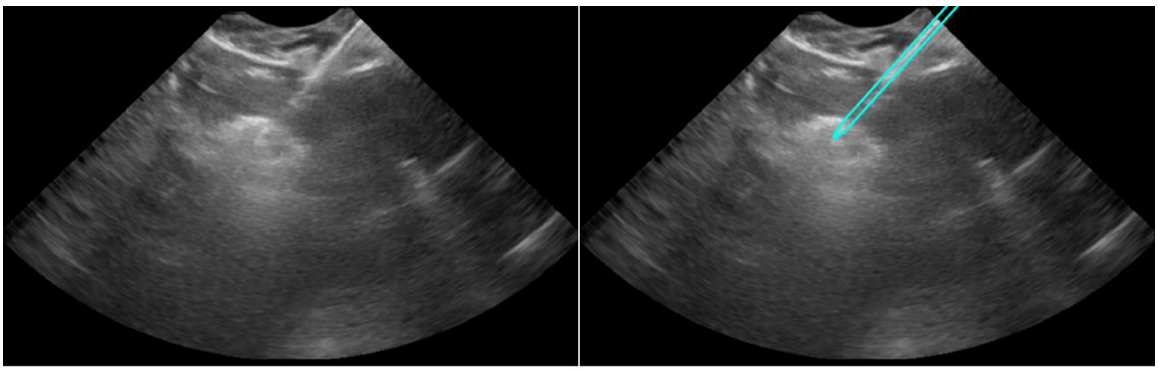

Figure 5.8 Sample oblique plane in a 3D US image of an MWA needle applicator inserted in a patient's liver before (a) and after (b) segmentation. The 3D US image was resliced to visualize the entire segmentation for clarity.

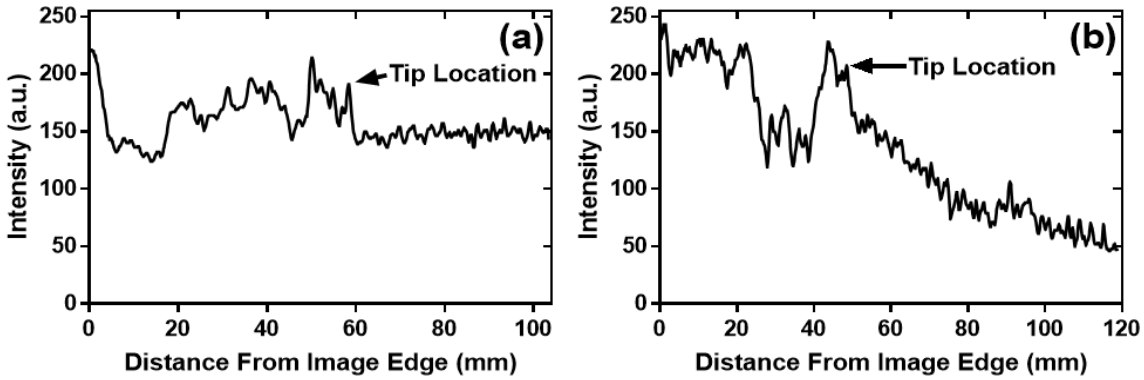

Figure 5.9 Sample intensity profiles of the manually segmented needle applicator trajectory in a phantom image (a) and patient image (b). These line profiles of needle applicators in the phantom and patient images correspond to the images in Figure 5.6 and Figure 5.8, respectively.

Figure 5.10 shows the needle applicator trajectory, axis localization, and tip segmentation errors of the four users and all the patient 3D US images. Error distributions for ΔT for TU1, ALA for TU2, and ATE across all users failed to pass a Shapiro-Wilk normality

test, so non-parametric statistical testing was performed for the remainder of the analysis. A Friedman omnibus test was first performed on the ΔT distributions (Figure 5.10a) and showed a statistically significant difference ($p < 0.0001$) between the users. Investigating multiple comparisons revealed significant differences between TU1-TU2 ($p < 0.05$) and TU2-IR2 ($p < 0.0001$). Median ΔTs of 4.1 °, 1.6 °, 3.9 °, and 4.9 ° were observed for the TU1, TU2, IR1, and IR2 users, respectively. The ALA measurements (Figure 5.10b) also showed a statistically significant difference ($p < 0.01$) between users when performing a Friedman test with multiple comparisons revealing a significant difference between TU2-IR2 ($p < 0.05$). Median ALA measurements of 1.4 mm, 1.2 mm, 2.0 mm, and 2.0 mm were observed. ATE measurements (Figure 5.10c) also showed a statistical significant difference ($p < 0.05$) between users when performing a Friedman omnibus test with multiple comparisons repeating significant differences between TU1-TU2 ($p < 0.05$) and TU2-IR2 ($p < 0.05$). Median ATEs of 3.6 mm, 1.0 mm, 1.8 mm, and 3.7 mm were observed for the TU1, TU2, IR1, and IR2 users, respectively. The mean intra-subject FLE values over five trials for the TU1 and TU2 users and mean inter-subject for all users in consensus agreement are provided in Table 5.6. Finally, the overall segmentation computation time across all users (Table 5.6) was 0.303 ± 0.026 s, which was similar to segmentations performed in the phantom images.

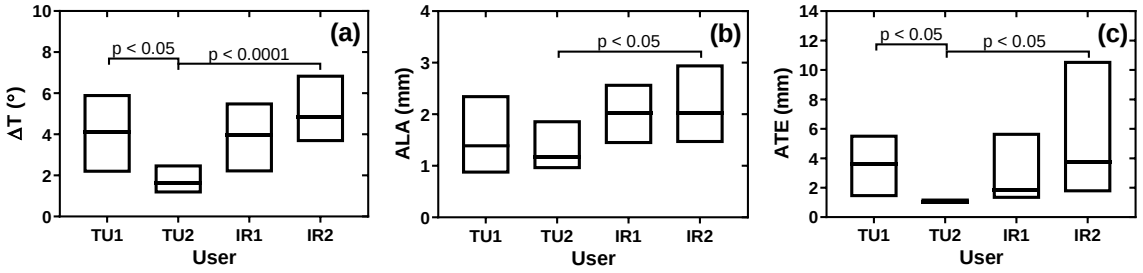

Figure 5.10 Box plots for the resulting trajectory (a), axis localization (c), and tip (b) errors after using the needle applicator segmentation algorithm. These results were performed on 16 patient images for two trained users (TU) and two interventional radiologists (IR). The centre lines represent the distribution median value with the boxes showing the 25% and 75% percentiles.

Table 5.6 Inter- and intra-subject manual applicator tip localization, manual trajectory variability, and algorithm segmentation computation times in 16 patient 3D US images.

User	$\overline{FLE}_{intra}$ ± std (mm)	$\overline{FLE}_{inter}$ ± std (mm)	Manual Trajectory Variability ± std (°)	Segmentation Time ± std (s)
TU1	0.99 ± 1.40	1.37 ± 1.19	1.56 ± 0.75	0.308 ± 0.025
TU2	0.89 ± 0.77			0.296 ± 0.022
IR1	—			0.310 ± 0.028
IR2	—			0.303 ± 0.029

5.4 Discussion

5.4.1 Phantom experiments

Since access to patient 3D US images containing needle applicators was limited, we performed optimization of the proposed segmentation algorithm on phantom images to utilize all available clinical images for evaluation. The selected parameters optimized on the homogenous agar phantom images (Table 5.4) with seed points selected by an expert user resulted in ΔT, ALA, and ATE median [Q1, Q3] measurements of 2.1 [1.1, 3.6] °, 1.3 [0.8, 2.1] mm, and 1.3 [0.7, 2.5] mm, respectively, with an overall algorithmic computation time of 0.246 ± 0.007 s. The manual variability in localizing the needle applicator tip locations in the phantom images (*i.e.*, $\overline{FLE}$) was 0.43 ± 0.09 mm, which was less than two voxels when referenced against the in-plane voxel dimensions of our 3D US images. This could represent a major cause of the observed variability for the three metrics as it is approximately equal to the measured interquartile ranges. However, since we used the average tip location over five trials when performing comparisons to manual segmentations, we believe the impact of FLE on the measured metrics is reduced with minor contributions to the overall errors observed. This belief still falls under the caveat that comparisons are performed to manual segmentations, which assumes that the tip position is visible and can be accurately estimated. Nonetheless, since the phantom images were primarily used for parameter tuning, the visibility of the applicator in ultrasound is adequate for manual segmentation accuracy evaluation.

The investigated test point spacings of 2.4°, 1.2°, and 0.6° did not have a large effect on trajectory error when observing the interaction between different radii and SBR thresholds. Although the fine test point spacing of 0.6° yielded the smallest median observed trajectory

error (*i.e.*, 1.9 [1.2, 3.4]°) with a radius of 30 mm and SBR threshold of 1.1, computation time increased by approximately 6.5 times (*i.e.*, 1.58 ± 0.04 s) and was considered too large for only a minor decrease in observed error. A radius of 45 mm performed the worst across all test point spacings when increasing the SBR thresholds beyond 1.3, which is most likely due to the increasing number of voxels contributing to the most probable trajectory metric in Eq. 5.1. When searching with a radius of 45 mm, line segments along the needle applicator trajectory would be more likely to extend beyond the imaging limits, thus, negatively impacting the $Quantity_i$ measurement in the most probable trajectory metric (Eq. 5.1).

Determining the tip location was performed with the Otsu threshold since we assumed a bimodal intensity distribution when assessing the selected most probable trajectory. Based on the small standard deviation in needle applicator and background intensity values (Table 5.3) and the appearance of the observed line profiles (Figure 5.9a), we believe this was a good approximation for needle applicators in the acquired phantom images. When computing the Otsu threshold without adjustment, thresholds were often determined too high and resulted in needle tip identifications that fell short of the actual position. Shifting the computed threshold by 5 intensity units was chosen as the ideal threshold to determine the tip location as it was observed to have a significantly reduced tip error. Since the Otsu threshold determines a threshold based on the histogram of the intensity distribution to maximize interclass variance, this implied that the maximum interclass variance along the line profile did not encompass enough needle applicator voxel intensities to accurately determine the tip location. Although an extension to the most probable trajectory was added to equalize the intensity population distributions of the needle applicator and background, overlap of the populations may be too great in low SBR imaging conditions to rely on interclass variance alone. Providing an adjustment to the Otsu threshold therefore captured more of the needle applicator's intensity distribution, which appears to be necessary for tip localization. We have shown acceptable results using a fixed adjustment of 5 intensity units, but it is possible the adjustment is influenced by the needle applicator's SBR in the US images and could warrant further investigation.

The visibility and tool SBR in 3D US can greatly influence the success of a segmentation algorithm and typically gets worse as SBR decreases.[45] The effect of background noise has been previously investigated by Barva et al.[31] for an automated parallel integral projection (PIP) algorithm to segment straight electrodes in 3D US. They used a signal-to-noise (SNR) ratio defined as:

$$SNR = 10 \log \frac{\mu_{el}^2 + \sigma_{el}^2}{\mu_{bg}^2 + \sigma_{bg}^2} \; [dB], \tag{5.7}$$

which used the mean μ_{el} and variance σ_{el}^2 of simulated electrode voxels and the mean μ_{bg} and variance σ_{bg}^2 of background voxels. Using this definition with needle applicator voxels in lieu of electrode voxels, the SNR observed for our needle applicators in the phantom images was 1.8 ± 0.5 dB. This was of particular interest since previous work[31] had observed rapid increases in ATE as SNR decreased below 10 dB, which reported an ATE of 2.7 mm at a minimum reported SNR of 7 dB. In comparison to our measured ATE of 1.3 mm at an SNR of 1.8 dB, our algorithm appears to perform well and provide added utility at low SNR levels.

In more recent methods using simulated data,[29] the SBR has been investigated to observe trends in the performance of automated segmentation algorithms. Since an acceptable error has never been strictly defined for algorithms performing segmentation of therapy applications used in liver ablation, previous work considered segmentations a failure if the tip error (*i.e.*, ATE) or axis localization error (*i.e.*, ALA) were greater than or equal to 3 mm. Using these thresholds for failure, segmentations in our phantom images resulted in a failure rate of 26% (13/50). Since the SBR for our phantom images was 1.22 ± 0.08, our method appears to be useful in imaging conditions with low tool SBR since failure rates were observed to be greater than 80% for many recent automated methods.[29]

5.4.2 Retrospective patient experiments

Since adjustments to the US system scanning parameters (*e.g.*, time-gain-compensation, depth, focal zone depth, etc.) when acquiring an US image can be subjective and often depend on external factors, such as experience and environment, a wide range of image qualities are observed in clinical settings. An increase in needle applicator SBR was shown

when imaging needle applicators in patients compared to the phantom images described previously. In addition, the visible needle applicators and background intensities were observed to have increases in variability, resulting from an increased number of anatomical structures causing image clutter and artifacts. Using the definition of SNR in Eq. 5.7, the needle applicator appearance across all patient images was 6.4 ± 1.9 dB, further supporting the increase in SBR relative to the phantom images. When comparing intensity line profiles between the phantom and patient images along the needle applicator trajectories, many line profiles contained a bimodal distribution of intensities and resulted in more consistent and accurate segmentations across users (Figure 5.11a). However, the time-gain compensation adjustment to the US machine appeared to be overlooked during acquisition in some cases, leading to an intensity gradient in the image background and increases in segmentation complexity (Figure 5.11b). More than half of all cases (9/16) violated the bimodal intensity distribution assumption of our segmentation algorithm and could partially explain the increase in resulting ΔT, ALA, and ATE median [Q1, Q3] measurements of 4.5 [2.4, 5.2]°, 1.9 [1.7, 2.1] mm, and 5.1 [2.2, 5.9] mm, respectively, compared to the phantom results. Although there were image quality differences, the overall mean computation time was similar to phantom experiments at 0.303 ± 0.026 s across all users, which is suitable for an intraoperative implementation.

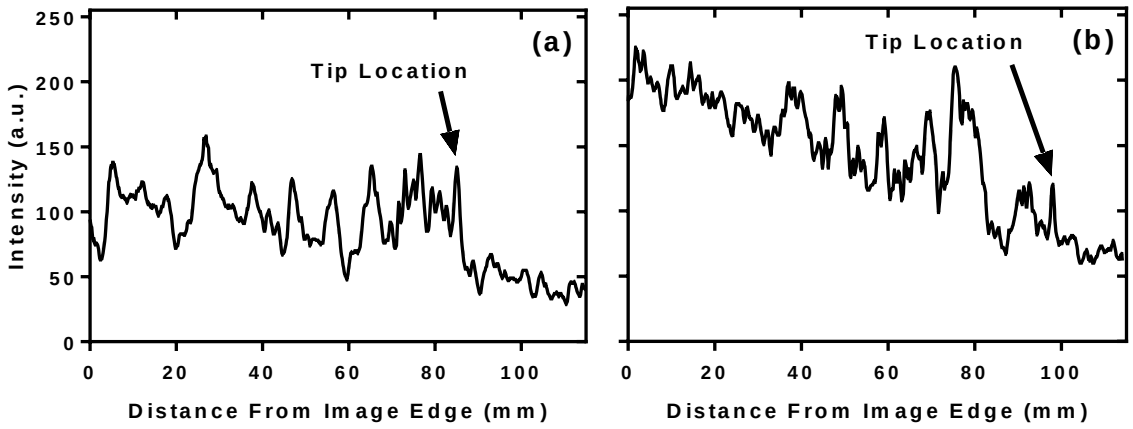

Figure 5.11 Examples of simple (a) and complex (b) intensity profiles of needle applicators for the segmentation algorithm. Line profiles were acquired from two manually segmented trajectories in MWA patient images.

Significant differences between users for all error metrics when using the segmentation algorithm were observed with the most consistent difference between users TU2 and IR2. Currently, the algorithm is not robust to poor initializations, which is a potential source of differences between the different users. Variability in the manual trajectories was observed to be 1.56 ± 0.75 ° and represents a considerable portion of the observed trajectory errors. This implies that localizing the central axis of the needle applicator shaft in 3D US is not trivial and could motivate the need for a central axis localization technique that is able to adjust user selected points to better approximate the applicator's shaft coordinates. Since the algorithm assumes the seed point is along the trajectory of the needle applicator, if the initialization point was not centered correctly, the segmentation would result in an incorrect trajectory and subsequently cause increases in the measured tip localization error. Image features that were observed to cause increased errors across most users were large gaps along the needle applicator shaft (4/16) and the presence of arteries and veins causing similar acoustic reflection intensities (5/16).

The observed user variability in localizing the needle applicator tips and trajectories further emphasizes the increased difficulty of identifying applicators due to image quality variability when performing deep and oblique needle applicator insertions in the clinical setting. An increase in tip localization error was observed when intra-subject variability (*i.e.*, $\overline{FLE}_{intra}$) was compared against phantom experiments, which rose from 0.43 ± 0.09 mm to 0.99 ± 1.40 mm and 0.89 ± 0.59 mm (approximately the size of 4 voxels in-plane) for the TU1 and TU2 users, respectively. When compared across users, the inter-subject tip localization variability (*i.e.*, $\overline{FLE}_{intra}$) was observed to be larger at 1.37 ± 1.19 mm. Unlike the phantom segmentations, these FLE measurements are approaching the magnitude of the measured errors for the four users and is likely contributing a non-negligible amount to the measured errors even though the average position of the identified tip was used. Nevertheless, measured median errors appear to be acceptable for interventional liver procedures where tumors range from 1 cm to 3 cm in diameter.

Interventional procedures in the liver can be performed with slight alterations in workflow, which could offer additional usable information for the segmentation algorithm. Our clinical dataset in this study was obtained from a free-hand insertion approach where no

needle applicator guides were used, increasing the potential search space where needle applicators could be found. One alternative to the current approach to reduce error could utilize a needle applicator guide for insertions, which could increase the *a priori* knowledge that could be taken into account to reduce the potential search space for the trajectory of the needle applicator. By incorporating an initialization for the segmentation, a reduction in the search space would not only reduce computation time further, but it would likely reduce error since a tighter constraint would reduce potential solutions and outliers.

Curved needle applicator segmentations in US images have been previously investigated[36,46–49] for procedures using flexible needles and offers further potential for this algorithm with some investigation into workflow changes. For example, instead of creating a single straight line segment through the user selected point, a spline approach could be performed superior and inferior to the selected point. This could potentially be implemented with multiple, smaller spherical search spaces with searched trajectory solutions reduced after the first few completed line segments by constricting the search space around the locally determined trajectory. With increasing interest in IRE procedures, which use thinner diameter electrodes (16 to 19 gauge)[50] that are more susceptible to deflection during insertion, this possible solution could provide a method for improving needle applicator placements with increased imaging complexity.

5.5 Conclusions

A semi-automated 3D US needle applicator segmentation during minimally invasive liver cancer diagnostic or therapeutic procedures provides a utility that enables enhanced needle applicator guidance, placement verification, and improved clinical workflow without the need for additional radiation exposure. Using *a posteriori* knowledge of the current procedural workflow, we employed constraints on a heuristic intensity-based algorithm to perform 3D needle applicator segmentations in less than 0.31 s. Homogeneous agar phantom images containing needle applicators were used to optimize the trajectory and tip localization parameters of the algorithm prior to investigation on retrospective 3D US images of patients who underwent liver MWA. Median trajectory, axis localization, and tip localization errors across four users were less than or equal to 5°, 2 mm, and 4 mm,

respectively, suggesting this approach could be useful for the clinical environment. With this tool, intraoperative segmentations can be performed to assess and adjust needle applicator placements, potentially decreasing the liver cancer recurrence rates associated with minimally invasive procedures.

5.6 References

1. Okamura AM, Simone C, O'Leary MD. Force Modeling for Needle Insertion Into Soft Tissue. *IEEE Trans Biomed Eng*. 2004;51(10):1707-1716. doi:10.1109/TBME.2004.831542

2. Abolhassani N, Patel R, Moallem M. Needle insertion into soft tissue: A survey. *Med Eng Phys*. 2007;29(4):413-431. doi:10.1016/j.medengphy.2006.07.003

3. Stewart BW, Wild C. *World Cancer Report 2014*. Lyon; 2014.

4. Choti MA, Sitzmann J V, Tiburi MF, et al. Trends in long-term survival following liver resection for hepatic colorectal metastases. *Ann Surg*. 2002;235(6):759-766. doi:10.1097/00000658-200206000-00002

5. Schoenberg MB, Bucher JN, Vater A, et al. Resection or Transplant in Early Hepatocellular Carcinoma: A Systematic Review and Meta-analysis. *Dtsch Aerzteblatt Online*. 2017;114(31-32):519-526. doi:10.3238/arztebl.2017.0519

6. El-Serag HB, Marrero JA, Rudolph L, Reddy KR. Diagnosis and Treatment of Hepatocellular Carcinoma. *Gastroenterology*. 2008;134(6):1752-1763. doi:10.1053/j.gastro.2008.02.090

7. Shady W, Petre EN, Gonen M, et al. Percutaneous Radiofrequency Ablation of Colorectal Cancer Liver Metastases: Factors Affecting Outcomes—A 10-year Experience at a Single Center. *Radiology*. 2016;278(2):601-611. doi:10.1148/radiol.2015142489

8. Poggi G, Tosoratti N, Montagna B, Picchi C. Microwave ablation of hepatocellular carcinoma. *World J Hepatol*. 2015;7(25):2578. doi:10.4254/wjh.v7.i25.2578

9. Tanis E, Nordlinger B, Mauer M, et al. Local recurrence rates after radiofrequency ablation or resection of colorectal liver metastases. Analysis of the European Organisation for Research and Treatment of Cancer #40004 and #40983. *Eur J Cancer*. 2014;50(5):912-919. doi:10.1016/j.ejca.2013.12.008

10. Chapman GA, Johnson D, Bodenham AR. Visualisation of needle position using ultrasonography. *Anaesthesia*. 2006;61(2):148-158. doi:10.1111/j.1365-2044.2005.04475.x

11. Fenster A, Parraga G, Bax J. Three-dimensional ultrasound scanning. *Interface Focus*. 2011;1(4):503-519. doi:10.1098/rsfs.2011.0019

12. Vogl TJ, Mack MG, Müller PK, Straub R, Engelmann K, Eichler K. Interventional MR: interstitial therapy. *Eur Radiol*. 1999;9(8):1479-1487. doi:10.1007/s003300050874

13. Kim SH, Choi BI. Three-dimensional and Four-dimensional Ultrasound: Techniques and Abdominal Applications. *J Med Ultrasound*. 2007;15(4):228-242. doi:10.1016/S0929-6441(08)60040-5

14. Neshat H, Cool DW, Barker K, Gardi L, Kakani N, Fenster A. A 3D ultrasound scanning system for image guided liver interventions. *Med Phys*. 2013;40(11):112903. doi:10.1118/1.4824326

15. Wein W, Brunke S, Khamene A, Callstrom MR, Navab N. Automatic CT-ultrasound registration for diagnostic imaging and image-guided intervention. *Med Image Anal*. 2008;12(5):577-585. doi:10.1016/j.media.2008.06.006

16. Arif M, Moelker A, van Walsum T. Needle Tip Visibility in 3D Ultrasound Images. *Cardiovasc Intervent Radiol*. 2018;41(1):145-152. doi:10.1007/s00270-017-1798-7

17. Beigi P, Rohling R, Salcudean T, Lessoway VA, Ng GC. Detection of an invisible needle in ultrasound using a probabilistic SVM and time-domain features. *Ultrasonics*. 2017;78:18-22. doi:10.1016/j.ultras.2017.02.010

18. Culp WC, McCowan TC, Goertzen TC, et al. Relative Ultrasonographic Echogenicity of Standard, Dimpled, and Polymeric-coated Needles. *J Vasc Interv Radiol*. 2000;11(3):351-358. doi:10.1016/S1051-0443(07)61429-8

19. Krücker J, Xu S, Glossop N, et al. Electromagnetic Tracking for Thermal Ablation and Biopsy Guidance: Clinical Evaluation of Spatial Accuracy. *J Vasc Interv Radiol*. 2007;18(9):1141-1150. doi:10.1016/j.jvir.2007.06.014

20. Adebar TK, Fletcher AE, Okamura AM. 3-D ultrasound-guided robotic needle steering in biological tissue. *IEEE Trans Biomed Eng*. 2014;61(12):2899-2910. doi:10.1109/TBME.2014.2334309

21. Nicolau SA, Pennec X, Soler L, et al. An augmented reality system for liver thermal ablation: Design and evaluation on clinical cases. *Med Image Anal*. 2009;13(3):494-506. doi:10.1016/j.media.2009.02.003

22. Daoud MI, Rohling RN, Salcudean SE, Abolmaesumi P. Needle detection in curvilinear ultrasound images based on the reflection pattern of circular ultrasound waves. *Med Phys*. 2015;42(11):6221-6233. doi:10.1118/1.4932214

23. Huang J, Triedman JK, Vasilyev N V., Suematsu Y, Cleveland RO, Dupont PE. Imaging Artifacts of Medical Instruments in Ultrasound-Guided Interventions. *J Ultrasound Med*. 2007;26(10):1303-1322. doi:10.7863/jum.2007.26.10.1303

24. Hrinivich WT, Hoover D a., Surry K, et al. Simultaneous automatic segmentation of multiple needles using 3D ultrasound for high-dose-rate prostate brachytherapy. *Med Phys*. 2017;44(4):1234-1245. doi:10.1002/mp.12148

25. Waine M, Rossa C, Sloboda R, Usmani N, Tavakoli M. Three-Dimensional Needle Shape Estimation in TRUS-Guided Prostate Brachytherapy Using 2-D Ultrasound Images. *IEEE J Biomed Heal Informatics*. 2016;20(6):1621-1631. doi:10.1109/JBHI.2015.2477829

26. Qiu W, Yuchi M, Ding M, Tessier D, Fenster A. Needle segmentation using 3D Hough transform in 3D TRUS guided prostate transperineal therapy. *Med Phys*. 2013;40(4):042902. doi:10.1118/1.4795337

27. Wei Z, Gardi L, Downey DB, Fenster A. Oblique needle segmentation and tracking for 3D TRUS guided prostate brachytherapy. *Med Phys*. 2005;32(9):2928-2941. doi:10.1118/1.2011108

28. Yan P, Cheeseborough JC, Chao KSC. Automatic Shape-Based Level Set Segmentation for Needle Tracking in 3-D TRUS-Guided Prostate Brachytherapy. *Ultrasound Med Biol*. 2012;38(9):1626-1636. doi:10.1016/j.ultrasmedbio.2012.02.011

29. Uherčík M, Kybic J, Liebgott H, Cachard C. Model Fitting Using RANSAC for Surgical Tool Localization in 3-D Ultrasound Images. *IEEE Trans Biomed Eng*. 2010;57(8):1907-1916. doi:10.1109/TBME.2010.2046416

30. Ding M, Fenster A. Projection-based needle segmentation in 3D ultrasound images‡. *Comput Aided Surg*. 2004;9(5):193-201. doi:10.1080/10929080500079321

31. Barva M, Uhercik M, Mari J-M, et al. Parallel integral projection transform for straight electrode localization in 3-D ultrasound images. *IEEE Trans Ultrason Ferroelectr Freq Control*. 2008;55(7):1559-1569. doi:10.1109/TUFFC.2008.833

32. Novotny PM, Stoll JA, Vasilyev N V, et al. GPU based real-time instrument tracking with three-dimensional ultrasound. *Med Image Anal*. 2007;11(5):458-464. doi:10.1016/j.media.2007.06.009

33. Linguraru MG, Vasilyev N V, Del Nido PJ, Howe RD. Statistical Segmentation of Surgical Instruments in 3-D Ultrasound Images. *Ultrasound Med Biol*. 2007;33(9):1428-1437. doi:10.1016/j.ultrasmedbio.2007.03.003

34. Mwikirize C, Nosher JL, Hacihaliloglu I. Local Phase-Based Learning for Needle Detection and Localization in 3D Ultrasound. In: Vol 10550. ; 2017:108-115. doi:10.1007/978-3-319-67543-5_10

35. Zhao Y, Shen Y, Bernard A, Cachard C, Liebgott H. Evaluation and comparison of current biopsy needle localization and tracking methods using 3D ultrasound. *Ultrasonics*. 2017;73:206-220. doi:10.1016/j.ultras.2016.09.006

36. Greer JD, Adebar TK, Hwang GL, Okamura AM. Real-Time 3D Curved Needle Segmentation Using Combined B-Mode and Power Doppler Ultrasound. In: *Lecture*

Notes in Computer Science (Including Subseries Lecture Notes in Artificial Intelligence and Lecture Notes in Bioinformatics). Vol 8674 LNCS. ; 2014:381-388. doi:10.1007/978-3-319-10470-6_48

37. Beigi P, Rohling R, Salcudean T, Lessoway VA, Ng GC. Needle Trajectory and Tip Localization in Real-Time 3-D Ultrasound Using a Moving Stylus. *Ultrasound Med Biol*. 2015;41(7):2057-2070. doi:10.1016/j.ultrasmedbio.2015.03.013

38. Liang P, Yu X-L, Yu J. *Microwave Ablation Treatment of Solid Tumors*. (Liang P, Yu X, Yu J, eds.). Dordrecht: Springer Netherlands; 2015. doi:10.1007/978-94-017-9315-5

39. de Jong TL, Klink SJC, Moelker A, Dankelman J, van den Dobbelsteen JJ. Needle deflection in thermal ablation procedures of liver tumors: a CT image analysis. In: Webster RJ, Fei B, eds. *Medical Imaging 2018: Image-Guided Procedures, Robotic Interventions, and Modeling*. SPIE; 2018:48. doi:10.1117/12.2292884

40. Otsu N. A Threshold Selection Method from Gray-Level Histograms. *IEEE Trans Syst Man Cybern*. 1979;9(1):62-66. doi:10.1109/TSMC.1979.4310076

41. Petrou M, Petrou C. *Image Processing: The Fundamentals*. 2nd ed. Chichester, UK: John Wiley & Sons, Ltd; 2010. doi:10.1002/9781119994398

42. Fedorov A, Beichel R, Kalpathy-Cramer J, et al. 3D Slicer as an image computing platform for the Quantitative Imaging Network. *Magn Reson Imaging*. 2012;30(9):1323-1341. doi:10.1016/j.mri.2012.05.001

43. Rickey DW, Picot PA, Christopher DA, Fenster A. A wall-less vessel phantom for Doppler ultrasound studies. *Ultrasound Med Biol*. 1995;21(9):1163-1176. doi:10.1016/0301-5629(95)00044-5

44. Fitzpatrick JM, West JB, Maurer CR. Predicting error in rigid-body point-based registration. *IEEE Trans Med Imaging*. 1998;17(5):694-702. doi:10.1109/42.736021

45. Ding M, Cardinal HN, Fenster A. Automatic needle segmentation in three-dimensional ultrasound images using two orthogonal two-dimensional image projections. *Med Phys*. 2003;30(2):222-234. doi:10.1118/1.1538231

46. Okazawa SH, Ebrahimi R, Chuang J, Rohling RN, Salcudean SE. Methods for segmenting curved needles in ultrasound images. *Med Image Anal*. 2006;10(3):330-342. doi:10.1016/j.media.2006.01.002

47. Aboofazeli M, Abolmaesumi P, Mousavi P, Fichtinger G. A new scheme for curved needle segmentation in three-dimensional ultrasound images. In: *2009 IEEE International Symposium on Biomedical Imaging: From Nano to Macro*. IEEE; 2009:1067-1070. doi:10.1109/ISBI.2009.5193240

48. Neshat HRS, Patel R V. Real-time parametric curved needle segmentation in 3D ultrasound images. In: *2008 2nd IEEE RAS & EMBS International Conference on Biomedical Robotics and Biomechatronics*. IEEE; 2008:670-675. doi:10.1109/BIOROB.2008.4762877

49. Adebar TK, Okamura AM. 3D Segmentation of Curved Needles Using Doppler Ultrasound and Vibration. In: *Lecture Notes in Computer Science (Including Subseries Lecture Notes in Artificial Intelligence and Lecture Notes in Bioinformatics)*. Vol 7915 LNCS. ; 2013:61-70. doi:10.1007/978-3-642-38568-1_7

50. Jourabchi N, Beroukhim K, Tafti BA, Kee ST, Lee EW. Irreversible electroporation (NanoKnife) in cancer treatment. *Gastrointest Interv*. 2014;3(1):8-18. doi:10.1016/j.gii.2014.02.002

Chapter 6

6 A deep learning method for general needle and applicator segmentation in two-dimensional ultrasound images from multiple applications and anatomical regions

2D US is widely used for real-time imaging during insertion of interventional tools, but accurate identification is necessary for desired clinical outcomes and is often dependent on subjective physician interpretation. The purpose of Chapter 6 is to present on the development of a general needle-like tool segmentation algorithm for improving intraoperative identification during interventional procedures without the need for additional equipment or operating room set-up.

The contents of this chapter have been submitted for publication in *Medical Physics* and are currently under peer-review: Gillies DJ and Rodgers JR, Gyacskov I, Roy P, Kakani N, Cool DW, and Fenster A.

6.1 Introduction

Ultrasound (US) imaging is often used during interventional procedures to provide portable, accessible, and real-time imaging of anatomy and instruments. This is particularly advantageous for guidance during minimally invasive percutaneous interventional techniques, which offer reduced recovery times and complications relative to open surgery. Despite these benefits, one factor that has limited the guidance accuracy of these techniques is the ability to localize needle-like interventional tools, such as needles and therapy applicators, quickly and accurately in the standard two-dimensional (2D) US images while in the intraoperative environment.[1,2] Diagnostic and therapeutic cancer procedures where accurate localization is essential include brachytherapy, solid organ ablation, and biopsy. High-dose-rate interstitial brachytherapy of prostate or gynecologic malignancies delivers internal radiation via multiple needles (typically about 5–24)[3,4] that are inserted into the tumor and surrounding area, thereby requiring correct needle placement to deliver optimal treatment and reduce risks to nearby structures. In ablation procedures, commonly used in liver and kidney cancers, one to four applicators, such as radiofrequency electrodes or microwave antennae, are inserted into tumors to heat the tissue and destroy malignant cells. Applicators must be accurately placed within the tumor to achieve adequate therapy and minimize local recurrence risk.[5] Similarly, during biopsy procedures, accurate insertion of the biopsy needle into a suspicious mass is essential to ensure proper tissue sampling for

histopathological assessment. In this paper, we use the term “tools” to refer generically to needle-like interventional instruments, including electrodes, antennae, applicators, and needles. Identifying these tools in 2D US images can be challenging, with their precise position difficult to distinguish once placed inside the tissue. Visualization requires the tool to be coplanar with the US probe and localization is often operator-dependent, associated with subjective 2D US guidance.[1] Additionally, anatomical features, such as the body habitus of the patient, fat, and blood vessels in the liver, or artifacts, such as air gaps or needle reverberation in some brachytherapy images, can affect the appearance of the tool and obscure portions of the tool path or confound identification of the tool’s tip position. Implementation of a real-time or near real-time method to automatically identify and segment interventional tools on intraoperative live US images might improve clinicians’ ability to guide, adjust, and verify tool positions, allowing these positions to be refined and misalignments to be corrected without disrupting clinical workflow or extending procedure time.

Image-based approaches for tool guidance, avoiding the requirement for additional equipment, signal processing, and set-up, have been proposed for general tool segmentation in US images, leveraging techniques based on image properties, including projections,[6–9] random sample consensus (RANSAC),[10–12] filtering,[11,13–15] and Hough or Radon transforms,[16–20] or physical properties, such as analyses of motion,[20–24] beam steering,[25] and circular wave generation.[26] Many of these algorithms were developed for three-dimensional (3D) US images;[6–13,18,19,21] however, 2D US is the clinical standard for image-guided minimally invasive interventions at most institutions and therefore is the focus of our work presented in this study. Many of the published approaches were tested only on phantom or *ex vivo* tissue images,[6–22,24–26] *in vivo* on an anesthetized porcine model,[18,23] or, in some cases, US images from one clinical application, such as breast biopsy[8,10,16] or nerve block imaging.[25] Therefore, the generalizability of the algorithms to multiple applications, particularly given the idealized nature of phantom conditions, requires further investigation.

Image-based approaches may suffer from a lack of robustness and longer processing times when used on more complex clinical images.[27] To address these limitations, recent

developments by Pourtaherian et al.[28] and Arif et al.[27] have employed convolutional neural networks (CNNs) for needle detection in 3D US images. The method presented by Pourtaherian et al.[28] used patch classification and semantic segmentation techniques with CNN architectures, testing their approach on chicken breast and porcine leg *ex vivo* datasets with data augmentation. This method achieved tip localization errors of < 0.7 mm. Arif et al.[27] also proposed a CNN-based method using a V-Net model to localize needles in 3D US phantom and liver images, demonstrating a mean tip error of 1 mm and angular error of 2°. Both methods demonstrated the potential of CNNs to accurately localize needles in US images; however, neither were assessed on 2D US images and investigation of their applicability on a range of clinical images has not been performed.

In recent work, Lee et al.[29] proposed segmentation of kidney biopsy needles in 2D US images using a deep learning approach based on a LinkNet architecture with the addition of a concurrent spatial and channel "Squeeze and Excitation" method to independently weight spatial and feature map characteristics. This method used images acquired at three frames per second from eight patient US videos to create a dataset for training and testing, achieving a Dice similarity coefficient (DSC) of 56.65 %, root-mean-square (RMS) distance error of 9.5 pixels, and RMS angular error of 13.3°.[29] Although this approach is susceptible to information leakage since many images were acquired per patient, this study demonstrates many of the challenges associated with localizing needles in kidney images and the extension of this method to applications other than kidney biopsy has not been explored. Mwikirize et al.[30] investigated an algorithm using a fully convolutional network with a fast region-based CNN for interventional applications requiring quick localization of mid-to-steeply inserted needles (40–75°) and deep insertions (up to 9 cm) in 2D US images. This study demonstrated accurate localization with recall and precision rates > 99 %, a mean tip error of 0.23 mm, and a mean angular error of 0.82° with a processing time of 0.58 s.[30] Further investigation of this approach is necessary to assess its generalizability, as the initial study was limited by only using in-plane (or slightly out-of-plane) insertions of a single tool type (17-gauge epidural needle) in *ex vivo* bovine/porcine tissues and phantoms with recall and precision only assessed on images acquired from a single US system and probe, matching the system used for training.

In this study, we have developed and evaluated a deep learning method using a CNN with a U-Net architecture to segment general needle-like interventional tools from 2D US images from multiple anatomical regions and various interventional procedures in near real-time. The proposed algorithm was trained and tested on augmented datasets using 2D US images and manual segmentations from phantom experiments and five different clinical cancer procedures: prostate brachytherapy, gynecologic brachytherapy, liver ablation, and kidney ablation and biopsy.

6.2 Materials and methods

6.2.1 CNN model

The proposed CNN in the U-Net architecture was adapted from Ronneberger et al.[31] and is shown in Figure 6.1. Accommodation of all anticipated image sizes was performed by resizing all images to 256×256 pixels. Convolution kernels were 3×3 pixels with a rectified linear unit (ReLU) activation function and optimization of network weights was performed using an Adam optimizer with a DSC loss function. Regularization was a key consideration to prevent overfitting of the CNN, especially in a small dataset application, so 50 % dropouts were used in the decoder section of the network, as has been previously shown to maximize regularization.[32] Transpose convolutions were used instead of upsampling followed by convolution, based on preliminary experiments to improve performance. Final output masks were produced with a 1×1 convolution kernel and a sigmoid function. All images were used to compute the mean and standard deviation (SD) of intensities for data centering and normalization. Improvements in the network accuracy were investigated by performing experiments on the training dataset (Sec. 6.2.2) for the learning rate and epoch hyper-parameters. Learning rates ranged between 10^{-3} and 10^{-5} with epochs tested from 50 to 200. Training and validation DSCs of approximately 85 % resulted in the selection of a 10^{-4} learning rate with 100 epochs.

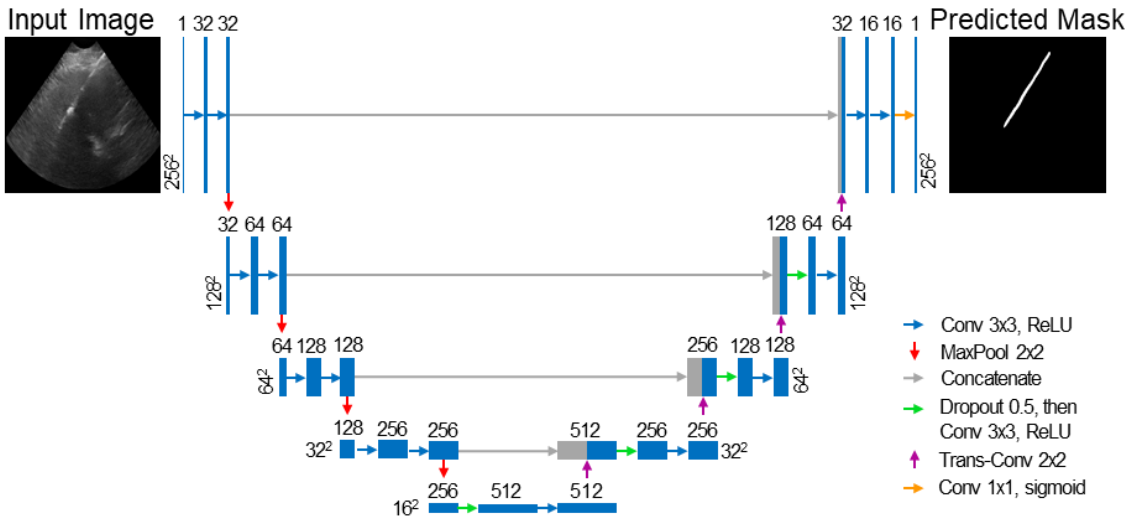

Figure 6.1 A schematic of our CNN in the U-Net architecture with arrows denoting the different operations. The numbers above the rectangles correspond to the output filters in the convolution (i.e., multi-channel feature map) and the numbers along the side correspond to the XY image size in pixels.

6.2.2 Datasets

Images and manual segmentations used for training, validation, and testing of the proposed CNN were acquired from phantoms and five different clinical interventional procedures, including prostate and interstitial gynecologic brachytherapy, liver ablation, and kidney ablation and biopsy, with the assumption that only a single tool was present in each 2D image. A single trained observer generated gold standard manual segmentations by selecting the tool tip and a second point on the tool shaft. An assumption of a 2.1 mm tool diameter with a conical tip was used to create linear, needle-shaped masks (Figure 6.2) along the user-defined axes. In the gynecologic brachytherapy images, the needle tip was not always visible within the image field-of-view and therefore the deepest visible point along the needle path was selected as the tip in these cases and the conical tip assumption was removed from mask generation. This dataset, totaling 1242 images and segmentations, was split into a 74 % training set and a 26 % unseen testing dataset (Table 6.1). Since multiple tools were occasionally visualized per patient, all images for an individual were assigned to either the training or testing dataset to avoid potential redundancies in the anatomical background. This ensured that the testing dataset contained solely unseen data to improve the approximation of future clinical use and robustness. The training dataset

was further split into 80 % training and 20 % validation datasets to train and optimize the network weights.

Table 6.1 Training and testing dataset distributions of 2D US images containing needle-like tools from interventional applications, with the number of unique patients provided for clinical applications and the number of independent tool insertion experiments for the phantom.

Image Background	Images in Training Set (Number of Patients)	Images in Testing Set (Number of Patients)
Phantom	23 (7)	9 (3)
Prostate	18 (4)	8 (1)
Gynecologic	34 (4)	18 (2)
Liver	540 (18)	256 (8)
Kidney	302 (9)	34 (3)
Overall	917	325

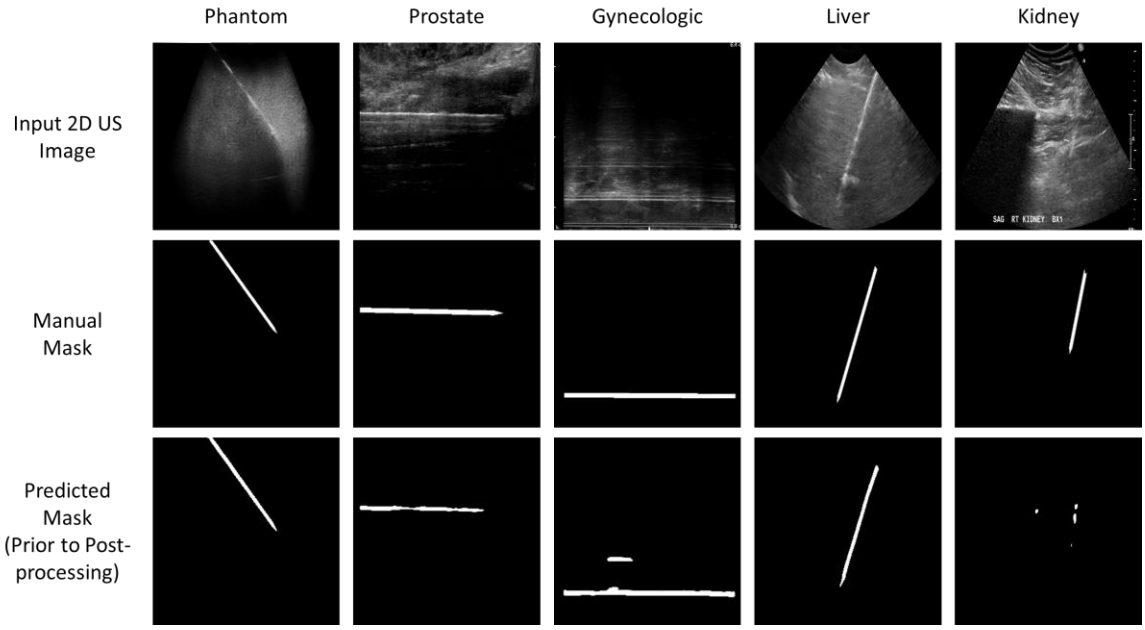

Figure 6.2 Input 2D US images illustrating background and tool appearances (top row), tool masks generated from manual segmentation (middle row), and tool masks predicted by the CNN algorithm prior to post-processing (bottom row) for each of the applications tested, showing examples of various segmentation performance quality.

Data augmentation was investigated to increase the number of images used for training and further reduce overfitting to improve the generalization of the tool segmentation CNN. Combined strategies used to augment our data included horizontal flips, horizontal and vertical shifts up to 20 % of the image size, 20° maximum rotations, and a 20 % zoom range. Augmentation was performed at the time of training in batches of 10, which doubled the dataset for each epoch, but with different augmentations on subsequent epochs. Training and testing of the CNN were performed using a Python implementation of Keras on Windows 10 (Microsoft, WA, USA). This was run on a personal computer with two Xeon E5645 central processing units (CPUs) at 2.40 GHz (Intel Corporation, CA, USA), 24.0 GB of memory, and a GeForce GTX TITAN (NVIDIA Corporation, CA, USA) graphics processing unit (GPU). This hardware allowed for training to be performed in approximately 3.5 hours.

To ensure the generalizability of the algorithm, images from clinical applications with varying tool properties and appearances were used, with examples shown in Figure 6.2. Phantom procedures were performed in a tissue-mimicking agar mixture and microwave ablation applicators with 2.1 mm outer diameters were inserted (depth range: 55.5–81.1 mm) with oblique insertion angles relative to the probe (range: 17.4–65.9°). Phantom images had a pixel size of 0.2×0.2 mm^2 and were acquired with a Philips iU22 US system using a C5-1 curvilinear probe (Philips Healthcare, the Netherlands). Prostate brachytherapy procedures used 2 mm diameter plastic needles, whereas gynecologic brachytherapy procedures used 1.65 mm diameter stainless steel needles. Both prostate and gynecologic brachytherapy images were acquired using a BK ProFocus 2202 US system with an 8848 endocavity probe (BK Medical, MA, USA). Pixel sizes for the brachytherapy images ranged between 0.126×0.126 mm^2 and 0.212×0.212 mm^2. Both brachytherapy procedures had needles inserted nearly parallel to the linear US imaging face, often resulting in reverberation artifacts. Other artifacts also impacted the appearance of these needles, as more anterior needles often appeared partially obstructed due to shadowing in prostate images and air artifacts occasionally created discontinuities in gynecologic images. Ablation and biopsy images with pixel sizes between 0.151×0.151 mm^2 and 0.428×0.386 mm^2 were acquired with a Philips iU22 US system using a C5-1 curvilinear

probe (Philips Healthcare, the Netherlands). For ablation procedures and kidney biopsy, 1.3 mm and 2.1 mm outer diameter applicators were inserted with widely varying depths and angles (depth range: 30.4–99.0 mm; insertion angle range: 23.3–77.2°) resulting from the free-hand nature of applicator insertion. These angles relative to the curvilinear US probe can create discontinuities in the intensity of the applicator with anatomical features creating a large amount of image clutter and making applicator visualization difficult.

6.2.3 Post-processing and evaluation

Smaller disconnected regions were sometimes present in the predicted segmentations. Since we assumed that only a single tool was present in our images, we employed two post-processing methods to filter the predicted masks and fit a single trajectory corresponding to the needle-like tool. Both methods were implemented offline in MATLAB R2019a (MathWorks, MA, USA) using a Windows 10 (Microsoft, WA, USA) personal computer with an i7-5820K CPU at 3.3 GHz (Intel Corporation, CA, USA) following the prediction using the CNN. Neither approach was optimized for speed or for use with a GPU. Processing times reported included only the time for filtering and fit, excluding the time to read or write the predictions and results, as it was assumed that this would be incorporated into the pipeline when implemented as a routine part of the algorithm.

The simpler approach to tool fitting was implemented using a largest island post-processing technique to save only the largest connected region of predicted pixels, as has been previously studied.[29] A linear least-squares fit on this map was then used to predict the tool's tip and trajectory. In an attempt to more robustly establish the tool axis in the presence of disconnected outlier regions, a RANSAC model-fitting approach[10] was also evaluated. The RANSAC method used a linear model with a 14-pixel diameter, as nominal tool widths were between 5 and 14 pixels, depending on the application. The RANSAC fit was initially performed twice with a 90º rotation of the predicted mask between the two fits and the direction that maximized the number of inliers was then selected. To produce a more consistent result and reduce the likelihood of a poor fit resulting from the random nature of the RANSAC fit, the fit was run two more times in the chosen direction. From the three fits in the selected direction, the fit with the largest number of inliers was chosen.

Any pixels that were classified as part of the tool prediction but were not considered inliers were removed from the mask to generate the filtered mask.

Evaluation of the predicted tool segmentations was performed using a combination of traditional metrics for pixel map comparisons and tool segmentation-specific error metrics. Since the number of pixels within the predicted tool region-of-interest (ROI) was expected to be small relative to the total number of pixels within the image, only pixel map comparison metrics that excluded true negative predictions were considered. These criteria included the DSC, recall (i.e., sensitivity), and precision classification statistics. Pixel map comparisons were performed prior to post-processing and following both filtering approaches. Tool segmentation-specific errors included the tip and trajectory errors of the predicted segmentations. Tip errors were computed by determining the Euclidean distance between the manual gold standard tip location and the automated segmentation tip location determined by linear fits for both post-processing approaches. Since two points were used to create the gold standard manual segmentations, vectors for the manual segmentations ($\vec{v}_{man}$) and the computed vector from the algorithm ($\vec{v}_{CNN}$) were used to assess trajectory errors by:

$$\Delta T = \cos^{-1}\left(\frac{\vec{v}_{CNN} \cdot \vec{v}_{man}}{\|\vec{v}_{CNN}\| \cdot \|\vec{v}_{man}\|}\right)[°]. \tag{6.1}$$

6.2.4 User variation

While a single trained user, now denoted U1, generated the gold standard masks used for training and testing, two additional trained users also generated manual segmentations to obtain an insight into the potential variability in the gold standard masks. All users generated two masks per tool on over 200 images with a minimum of 24 hours between segmentations to allow for quantification of the intra-rater repeatability of the masks. Users also generated segmentations on a dataset of 211 images to compare the inter-rater segmentation performance. The intra-rater repeatability was assessed by calculating a tip localization error analogously to a fiducial localization error[33] and the SD of the corresponding trajectories, as well as the DSC, recall, and precision. Agreement metrics for the inter-rater comparison were tip localization error, the SD of corresponding

trajectories, and a three-user DSC,[34] as well as a Fleiss' kappa,[35] which determines the agreement between users while correcting for chance.

6.2.5 Statistical analysis

Statistical calculations were performed in GraphPad Prism 7.00 (GraphPad Software, Inc., CA, USA). The normality of distributions was evaluated using the Shapiro-Wilk test and led to the use of nonparametric statistical tests when the normality assumption was violated. The corresponding nonparametric alternative tests are presented in parentheses for the remainder of the section. For nonparametric distributions, descriptive statistics were reported using medians with interquartile ranges. The significance level for statistical analysis was chosen such that the probability of making a type I error was less than 5 % ($p < 0.05$). The tip and trajectory errors of tools with short visible lengths were compared to the tip and trajectory errors of tools with longer visible lengths using t-tests (Mann-Whitney tests). Intra-rater metrics were compared using a one-way analysis of variance (Kruskal-Wallis) test with multiple comparisons performed using a Tukey (Dunn's) test. The three-user DSC and Fleiss' kappa were implemented in MATLAB R2019a (MathWorks, MA, USA).

6.3 Results

6.3.1 Unfiltered predictions

The CNN algorithm generated predicted segmentations in approximately 50 ms per image. Examples of the predicted masks generated by the algorithm for each application prior to post-processing are shown in Figure 6.2, including the corresponding background images and manual masks used as the gold standard. The small island in the predicted mask of the gynecologic brachytherapy example is a result of a reverberation artifact in the image and was eliminated by both post-processing methods. The algorithm identified tools in 96.9 % of the images in the unseen testing set with three of the ten failures in the kidney images and the remaining seven in the liver images. The pixel map comparison error metrics prior to post-processing for each application are summarized in Table 6.2. It should be noted that due to the large number of liver images available, the overall values reported throughout

this section are strongly influenced by the liver results. The kidney segmentations demonstrated much lower DSC and recall medians relative to the other anatomical backgrounds, reflecting the difficulties in distinguishing needles in kidney US images.[29]

Table 6.2 Resulting medians [first quartile (Q1), third quartile (Q3)] for DSC, recall, and precision metrics on an unseen testing dataset prior to post-processing.

Image Background	DSC (%)	Recall (%)	Precision (%)
Phantom (n = 9)	85.6 [82.1, 89.9]	94.3 [91.0, 99.0]	78.0 [73.0, 84.1]
Prostate (n = 8)	76.2 [71.0, 84.0]	79.3 [62.8, 88.8]	76.3 [71.1, 82.1]
Gynecologic (n = 18)	88.7 [85.8, 92.0]	91.0 [85.7, 95.2]	88.6 [80.8, 91.6]
Liver (n = 249)	71.8 [58.0, 86.2]	72.1 [53.1, 88.5]	83.2 [69.4, 89.5]
Kidney (n = 31)	58.0 [44.7, 70.1]	49.2 [38.6, 59.0]	83.1 [67.2, 98.9]
Overall (n = 315)	71.9 [58.0, 86.3]	72.3 [52.4, 89.3]	83.2 [70.9, 89.8]

6.3.2 Post-processed predictions

The largest island filtering and linear fit were performed with a 2 ms processing time per tool. The median tip, trajectory, and pixel map metrics resulting from this approach are summarized in Table 6.3. Similarly, the error and pixel map metrics using the RANSAC method of fitting and filtering are summarized in Table 6.4 and performed with a processing time of 23 ms per tool. Overall, the RANSAC method produced lower tip and trajectory errors than the largest island approach with median [first quartile (Q1), third quartile (Q3)] tip errors of 3.5 [1.3, 13.5] mm and 4.4 [1.5, 17.8] mm, respectively, and median [Q1, Q3] trajectory errors of 0.8 [0.3, 1.7]° and 1.4 [0.4, 2.5]°, respectively. The RANSAC method also had a slightly higher DSC than the largest island method, as well as improved the precision to a median [Q1, Q3] of 87.5 [76.2, 95.1] % from 84.1 [73.6, 90.4] % obtained with the largest island. Both methods improved the DSC and precision relative to the unfiltered predicted masks. The largest island method yielded a higher recall value with a median [Q1, Q3] of 72.3 [51.5, 89.3] % compared to RANSAC with a median [Q1, Q3] of 67.4 [48.8, 77.6] %, which is also lower than the unfiltered mask recall. Examples of cases from Figure 6.2, showing the performance of the fitting and filtering approaches are shown in Figure 6.3. The gynecologic case demonstrates the feasibility of both approaches to remove the smaller second island generated by the reverberation

artifact. The liver example shows similar performance between the two techniques but with the largest island and linear fit approach producing a more accurate tip position than RANSAC. In the kidney case, the predicted tool appeared fragmented leading to a poor result using the largest island and a much more accurate result using RANSAC. Kidney predictions demonstrated much higher tip errors than the other anatomical backgrounds. Particularly using the largest island approach, removing the kidney from the overall calculations improves the tip error from 4.4 [1.5, 17.8] mm to 3.5 [1.3, 16.6] mm and also improves the overall tip error from 3.5 [1.3, 13.5] mm to 3.1 [1.2, 12.7] mm with RANSAC post-processing. Excluding the kidney results also leads to slight improvements in the overall trajectory error, DSC, and recall with both post-processing methods.

Table 6.3 After largest island filtering and linear fit, resulting medians [Q1, Q3] for tip and trajectory errors and DSC, recall, and precision metrics on an unseen testing dataset.

Image Background	Tip Error (mm)	Trajectory Error (°)	DSC (%)	Recall (%)	Precision (%)
Phantom (n = 9)	2.0 [0.6, 3.6]	0.8 [0.2, 1.9]	85.6 [82.1, 89.9]	94.3 [91.0, 99.0]	78.0 [73.0, 84.1]
Prostate (n = 8)	1.4 [0.9, 8.2]	0.7 [0.2, 1.3]	76.3 [72.6, 84.8]	79.3 [62.7, 88.8]	81.6 [75.5, 93.4]
Gynecologic (n = 18)	0.3 [0.2, 0.4]	0.3 [0.2, 0.6]	89.8 [86.7, 92.9]	89.9 [85.7, 95.2]	89.9 [85.7, 91.7]
Liver (n = 249)	5.0 [1.7, 18.1]	1.4 [0.5, 2.4]	71.8 [58.9, 86.4]	72.1 [52.7, 88.5]	83.9 [72.1, 89.8]
Kidney (n = 31)	10.9 [4.4, 33.4]	3.2 [1.6, 6.0]	58.4 [46.2, 70.5]	44.8 [30.0, 59.0]	87.5 [73.9, 100.0]
Overall (n = 315)	4.4 [1.5, 17.8]	1.4 [0.4, 2.5]	72.2 [59.1, 86.6]	72.3 [51.5, 89.2]	84.1 [73.6, 90.4]

Table 6.4 After RANSAC fitting and filtering, resulting medians [Q1, Q3] for tip and trajectory errors and DSC, recall, and precision metrics on an unseen testing dataset.

Image Background	Tip Error (mm)	Trajectory Error (°)	DSC (%)	Recall (%)	Precision (%)
Phantom (n = 9)	1.0 [0.6, 3.1]	0.5 [0.2, 1.9]	87.3 [83.5, 90.3]	94.2 [89.5, 98.7]	80.8 [78.9, 84.5]
Prostate (n = 8)	1.5 [0.9, 8.3]	0.4 [0.3, 0.7]	78.9 [73.8, 84.7]	73.2 [62.4, 81.9]	87.9 [84.8, 95.8]
Gynecologic (n = 18)	0.3 [0.2, 0.4]	0.4 [0.2, 0.7]	88.7 [84.6, 93.5]	85.2 [80.9, 91.1]	93.2 [89.6, 97.0]
Liver (n = 249)	3.8 [1.6, 14.3]	0.8 [0.3, 1.6]	72.4 [57.0, 81.4]	67.6 [50.2, 75.5]	87.0 [74.0, 95.0]
Kidney (n = 31)	10.1 [3.5, 33.8]	2.9 [1.3, 7.5]	55.8 [36.6, 67.9]	42.2 [33.2, 56.6]	86.1 [65.7, 98.9]
Overall (n = 315)	3.5 [1.3, 13.5]	0.8 [0.3, 1.7]	73.3 [56.2, 82.3]	67.4 [48.8, 77.6]	87.5 [76.2, 95.1]

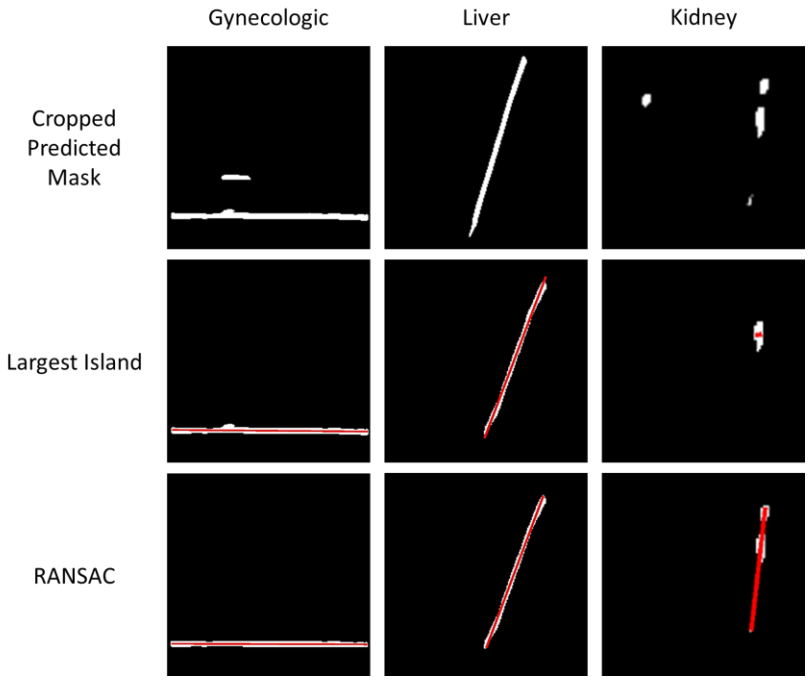

Figure 6.3 Cropped predicted masks of example cases from in Figure 6.2 (top row) and the result after filtering with the largest island approach (middle row) and RANSAC approach (bottom row) with the corresponding fits shown in red. Both methods performed similarly for the gynecologic and liver examples, but the RANSAC approach performed much better than the largest island in the scenario provided by the kidney image.

The visible length of the tool within the image appeared to influence the variability of the tip errors, as shown in Figure 6.4(a), and there also appeared to be a trend, illustrated in Figure 6.4(b), when examining the trajectory errors. This encompassed cases where the tool was captured in an US image when the tool and imaging plane were not coplanar. Based on the trajectory errors, an empirical threshold was established where tools with < 35 mm visible within the image demonstrated larger predicted trajectory errors compared to those tools with ≥ 35 mm visible. Since only liver and kidney images contained tools with short visible lengths (*i.e.*, < 35 mm), only those applications were included in this analysis. The tip and trajectory errors after RANSAC post-processing for tools on either side of this threshold are shown in Table 6.5. As these errors did not pass a normality test, Mann-Whitney tests were used to evaluate the statistical significance between the two groups of tools. While the tests failed to show a significant difference in the tip errors, the liver and kidney tools both showed significant differences between the trajectory errors for the longer and shorter tools; however, there were only a small number of tools meeting the criteria for short visible length (7 in kidney images and 26 in liver images) in this study. Additionally, tip error variability increased for long tools when observing liver and kidney images combined, but this trend was only demonstrated for liver images when investigated independently, as the third quartile for kidney (Table 6.5) decreased for long tools.

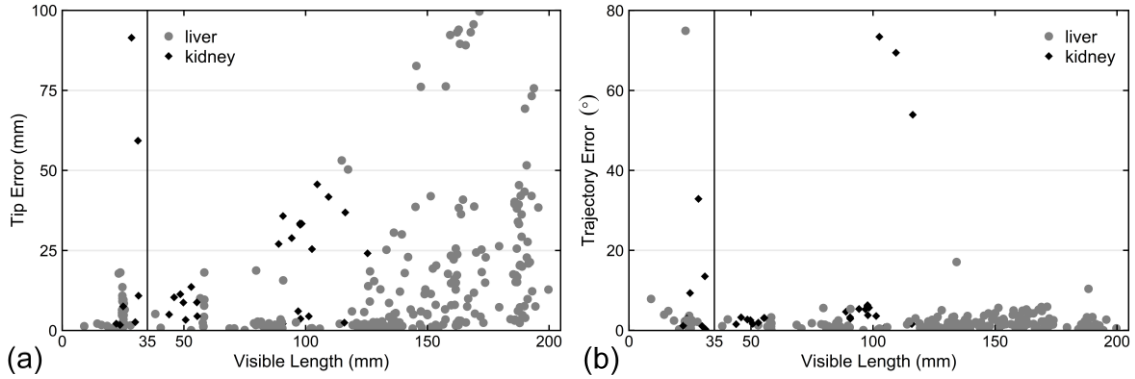

Figure 6.4 Influence of the visible length of the tools in the liver and kidney US images on (a) tip error and (b) trajectory error after RANSAC fitting and filtering. There was a statistically significant difference in the trajectory error between tools with visible lengths longer and shorter than 35 mm, but no significant difference was observed in the tip error. The trajectory difference was only observed in kidney and liver applications as all other applications had all visible lengths longer than 35 mm.

Table 6.5 Median [Q1, Q3] tip and trajectory errors using RANSAC fitting for kidney and liver tools with < 35 mm visible (short) within the 2D image compared those ≥ 35 mm (long) with significance from Mann-Whitney tests shown.

Image Background	Number of Tools		Tip Error (mm)			Trajectory Error (°)		
	Short	Long	Short	Long	p-value	Short	Long	p-value
Liver	26	223	4.6 [1.4, 9.2]	3.7 [1.6, 17.5]	0.4505	1.4 [0.8, 3.0]	0.8 [0.3, 1.5]	0.0007
Kidney	7	24	10.7 [2.6, 71.1]	10.0 [3.7, 31.6]	0.5320	12.6 [2.9, 27.5]	2.0 [0.6, 4.1]	0.0223
Overall	33	247	4.9 [1.8, 10.4]	4.4 [1.7, 18.5]	0.8021	2.1 [1.0, 6.8]	0.8 [0.3, 1.7]	< 0.0001

6.3.3 User variation

A subset of images was used to assess intra-rater repeatability (Table 6.6) for the three trained users that produced manual segmentations. Though the actual differences in user performance were small with all median pixel map metrics differing by < 4 %, a Kruskal-Wallis test found significant intra-rater performance differences ($p < 0.01$) for the DSC and recall metrics. Using Dunn's tests, significant differences ($p < 0.05$) were found between the intra-rater pixel map performance metrics of U1 and U2 and between U2 and U3, but not U1 and U3. This indicated that U2 was significantly more repeatable and sensitive than the other users. U1 and U2 had equivalent tip localization errors of 3.4 mm and median trajectory SDs of 0.3º, whereas U3 had slightly poorer consistency with a tip localization error of 4.3 mm and median trajectory SD of 0.5º.

Table 6.6 Intra-rater repeatability for three trained users producing manual segmentations. Tip localization error and median [Q1, Q3] trajectory SD, DSC, recall, and precision metrics were determined on a repeated image subset (N) with more than 24 hours between segmentations.

User [N]	Tip Localization Error (mm)	Trajectory SD (°)	DSC (%)	Recall (%)	Precision (%)
U1 [215]	3.4	0.3 [0.2, 0.7]	89.7 [84.0, 93.5]	88.9 [82.9, 93.0]	91.3 [86.2, 95.1]
U2 [251]	3.4	0.3 [0.1, 0.6]	91.9 [83.8, 95.7]	92.2 [85.8, 95.8]	92.7 [84.7, 96.3]
U3 [275]	4.3	0.5 [0.2, 0.9]	89.5 [82.1, 94.0]	88.5 [82.3, 93.4]	91.3 [85.7, 95.2]

An identical set of 211 images was used to assess the inter-rater reproducibility (Table 6.7) with the multi-user DSC and Fleiss' kappa both showing very strong agreement between users. The tip localization error, trajectory SD, and DSC had values for the inter-rater agreement on the same order as the intra-rater repeatability.

Table 6.7 Inter-rater reproducibility of the manual segmentations produced by three trained users. Tip localization error and the median [Q1, Q3] values of trajectory SD, DSC, and Fleiss' kappa metrics are reported for a repeated image subset of 211 images.

Tip Localization Error (mm)	Trajectory SD (°)	DSC (%)	Fleiss' Kappa (%)
2.8	0.6 [0.3, 1.1]	90.6 [86.5, 93.8]	87.3 [82.6, 91.7]

6.4 Discussion

In this study, we designed and evaluated a CNN-based method for segmenting needle-like tools in 2D US images in near real-time (approximately 50 ms per tool), demonstrated on unseen data from phantoms and five different interventional applications from four anatomical sites. The widespread use of 2D US makes the algorithm clinically relevant for a large variety of minimally invasive percutaneous interventions that require accurate placement of tools to achieve desired diagnostic and therapeutic results. The near real-time segmentation of the algorithm provides the potential for live localization and better visualization of tools during insertion for interventional procedures. This could enable clinicians to immediately evaluate the tool position and trajectory and adjust accordingly, compensating for misalignments without disrupting the clinical workflow or adding additional segmentation time to the procedure. Future work will involve integrating this segmentation into the live video stream from the US machine to provide intraoperative guidance, which could potentially improve the accuracy of tool placement and clinician confidence in the treatment (e.g., ablation) and sampling (e.g., biopsy) of lesions. One key advantage of our approach over existing general tool segmentation algorithms developed for US is the availability of both phantom and patient images from five different clinical applications and different US machines for development. These images were acquired from

different facilities with different operators and had a variety of characteristics, including variable image and pixel sizes, acquisition with different US systems and probe geometries, and different tool types and diameters. Images from the five clinical interventions, as well as phantom images, were used for evaluation, whereas most current techniques have only been tested in phantom or *ex vivo* environments, occasionally with one clinical application included. The broad testing environment that our study leveraged for assessment of our proposed general algorithm provides evidence that our technique may work across many interventional applications.

Overall pixel map comparisons showed good overlap and agreement between the manual and predicted segmentations, as described by the DSC (71.9 [58.0, 86.3] %), true positive rate (recall) of 72.3 [52.4, 89.3] %, and a positive predictive value (precision) of 83.2 [70.9, 89.8] % prior to post-processing. Following post-processing, there was a minor improvement in the overall DSC, as well as a higher precision. These pixel map comparisons showed DSC > 85 % and recall rates with both post-processing methods > 85 % for phantom and gynecologic images. Using the RANSAC approach, all applications had a precision > 80 % and had higher precision for every image background compared to the largest island approach; however, filtering with the RANSAC approach had the opposite effect on recall, which decreased for every background. Since the largest island approach doesn't modify the predicted pixels and only keeps the largest connected region, these changes in the pixel map metrics indicate that the CNN had a higher chance to over-predict pixel regions relative to the manual mask resulting from lower false-negatives and higher false-positives. Since the RANSAC method only keeps inlier pixels based on the maximum nominal tool diameters, spurious regions, such as the bump on the left side of the gynecologic example shown in Figure 6.3, are removed. As a result, over-predictions or predictions wider than this threshold diameter become slimmer, reducing the number of false positive pixels or increasing the false negative pixels, respectively. Aside from the kidney, a higher DSC also resulted when using a RANSAC approach and produced predictions more representative of the tool's true shape.

The predicted regions were sufficient to estimate the tool's tip and trajectory using both post-processing methods. Overall, the RANSAC approach produced a more accurate tip

and trajectory identification for the tools than the largest island method but performed slower than the largest island approach. While neither approach has been optimized for speed, the chosen method for post-processing could change depending on the application and choice to prioritize speed or accuracy. Although currently slower, there is the potential to implement parallelization of the RANSAC method to improve processing time as the approach executes the fitting step multiple times. Limitations of both approaches are the assumptions that tools are linear and that there is only one tool present in the images; however, the type of fit selected could be modified in the future to include other variations and step-wise predictions with subsequent image filtering could provide a method for multi-tool segmentation, but both will need to be investigated further.

Tool segmentation was not consistent across all images investigated and varied widely by anatomical location. Gynecologic images demonstrated the most accurate tool segmentation-specific metrics when compared to manual masks (median tip: 0.3 mm and median trajectory: 0.4°). This was likely due to the distinct needle appearance attributable to being nearly parallel to the linear US imaging face. However, the tip error in these images may not be a reflection of the true accuracy as they did not always contain the needle tip within the image field-of-view. In some cases, the tip point was selected to be at the edge of the image, which may be easier for the algorithm to detect as it removes the insertion direction component of error. Further investigation into the tip error for this application is necessary, but likely would be similar to that observed in the prostate brachytherapy images. The prostate images also demonstrated low tip and trajectory errors and the overall performance of the algorithm on brachytherapy images demonstrates robustness to large artifacts, such as the reverberation and shadowing observed in these images. Following RANSAC post-processing, phantom, prostate, and gynecologic images all produced median tip errors ≤ 1.5 mm and tools in these images, as well as the liver images, demonstrated median trajectory errors $< 1^{o}$. The trajectory errors associated with kidney and liver ablation tools were shown to improve significantly for tools with more than 35 mm visible in the image field-of-view, but the spread of the tool tip error was also observed to increase proportionally with the tool length. Figure 6.4(a) shows that some liver predictions had very large tip errors, which is also reflected in the high variability in tip error reported in Table 6.3 and Table 6.4. These large errors were typically associated

with deeply inserted tools and, due to the free-hand nature of the procedure, are likely the result of partially visualized tools not entirely in-plane with the US image. In the reported analysis, we did not implement a success/failure threshold; however, in a clinical setting, physicians would be able to keep in mind the insertion depths of tools to interpret the reasonability of the provided segmentation and, in most cases, these large errors likely appear only for a few frames in a video sequence. Therefore, future work will involve investigating a method for segmenting very short visible tool lengths and improving deep tool tip identifications, which may be integrated into the algorithm to improve performance. Despite the variability in performance across anatomical location, the performance on the liver images had a relatively high impact on the overall metrics reported in this study. The negative impact of the poorer performance on kidney predictions also influenced the overall values reported, but this would cause reported values to be more conservative compared to the true performance in other anatomical locations and the relatively larger number of liver images minimizes this influence.

Although the overall median tip error was slightly higher than those reported for other deep learning-based US tool segmentation methods,[27,28] the accuracy achieved is likely sufficient for most clinical applications. As the other methods were developed only in *ex vivo* models[28] or specifically for liver[27] and kidney[29] procedures, they may not reflect the complexity of clinical scenarios, limiting the generalizability of the approaches and diversity of the datasets. We demonstrated a median trajectory error for the liver tools of 0.8°, showing an improvement over the mean error of 2° reported by Arif et al.[27] Since the tool angle of incidence in liver images is steeper relative to the US probe than in other applications, visibility of the tool is reduced[36] and tip identification is more challenging, leading to the observed median tip error of 3.8 mm.

Our algorithm demonstrated much poorer performance in kidney images than the other applications in this study; however, the DSC of 58.0 % prior to post-processing is similar to the value of 56.65 % reported by Lee et al.[29] Additionally, our median trajectory error of 2.9º for the kidney ablation tools may offer a substantial improvement over the trajectory error of 13.3º reported by Lee et al.[29], though a direct comparison is not possible given the use of RMS error in that study. Assuming a similar pixel size, our tip error appears larger

than the distance error from the Lee et al.[29] study; however, their value does not represent the tip error, which is often much higher since the largest segmentation challenge is typically the early truncation of the tool path in the insertion direction. The high errors reported by both studies on the localization of tools in kidney images shows the US visibility challenges associated with steep tool insertion angles and increased number of anatomical interfaces with similar echogenicity, emphasizing the need for further research in this area.

Our precision (83.2 [70.9, 89.8] %) was much higher than that observed by Mwikirize et al.[30] prior to pre-processing, with a similar recall rate; however, Mwikirize et al. emphasized the importance of pre-processing US images to reduce high-intensity artifacts in the image, providing a vast improvement in the recall and precision rates of their algorithm. While pre-processing was avoided in our study to more closely reflect the intraoperative clinical realities, this may be an area of future investigation to further improve the accuracy of our results.

The three users in our study produced high pixel map scores on repeated segmentations of the same tools, all having DSCs > 89 % and recall and precision rates > 88 %, indicating high intra-rater repeatability in these metrics with U2 demonstrating the highest rate of repeatability and sensitivity. Although the median trajectory SDs were all $\leq 0.5^{\circ}$, variability in tip localizations were high with median differences ranging from 3.4 mm to 4.3 mm, demonstrating the difficulty of the task. This variability is also comparable with the tip errors produced by our method, suggesting that a large proportion of our reported algorithm errors are due to manual variability in tip localization. Thus, an alternative to manual segmentation is required to improve ground truth segmentations for further improvement in performance. The inter-rater comparison was consistent with intra-rater metrics and showed that using a single user for earlier comparisons was likely sufficient for assessing our method. The users also showed strong agreement with minimal effects of chance, demonstrated with the median Fleiss' kappa of 89.3 %.

6.5 Conclusions

We have presented a near real-time approach using deep learning techniques for fast and accurate segmentation of general needle-like tools in a variety of clinical cancer applications, demonstrating the potential to improve and ease tool localization in intraoperative environments during minimally invasive percutaneous interventions.

6.6 References

1. Fenster A, Downey DB, Cardinal HN. Three-dimensional ultrasound imaging. *Phys Med Biol*. 2001;46(5):R67-R99. doi:10.1088/0031-9155/46/5/201

2. Chapman GA, Johnson D, Bodenham AR. Visualisation of needle position using ultrasonography. *Anaesthesia*. 2006;61(2):148-158. doi:10.1111/j.1365-2044.2005.04475.x

3. Mendez LC, Weiss Y, D'Souza D, Ravi A, Barbera L, Leung E. Three-dimensional-guided perineal-based interstitial brachytherapy in cervical cancer: A systematic review of technique, local control and toxicities. *Radiother Oncol*. 2017;123(2):312-318. doi:10.1016/j.radonc.2017.03.005

4. Crook J, Marbán M, Batchelar D. HDR Prostate Brachytherapy. *Semin Radiat Oncol*. 2020;30(1):49-60. doi:10.1016/j.semradonc.2019.08.003

5. Liang P, Yu X, Yu J, eds. *Microwave Ablation Treatment of Solid Tumors*. Dordrecht: Springer Netherlands; 2015. doi:10.1007/978-94-017-9315-5

6. Ding M, Cardinal HN, Fenster A. Automatic needle segmentation in three-dimensional ultrasound images using two orthogonal two-dimensional image projections. *Med Phys*. 2003;30(2):222-234. doi:10.1118/1.1538231

7. Ding M, Fenster A. Projection-based needle segmentation in 3D ultrasound images. *Comput Aided Surg*. 2004;9(5):193-201. doi:10.1080/10929080500079321

8. Barva M, Uherčík M, Mari J-M, et al. Parallel Integral Projection Transform for Straight Electrode Localization in 3-D Ultrasound Images. *IEEE Trans Ultrason Ferroelectr Freq Control*. 2008;55(7):1559-1569.

9. Aboofazeli M, Abolmaesumi P, Mousavi P, Fichtinger G. A new scheme for curved needle segmentation in three-dimensional ultrasound images. In: *IEEE International Symposium on Biomedical Imaging: From Nano to Macro*. Vol 27. IEEE; 2009:1067-1070. doi:10.1109/ISBI.2009.5193240

10. Uherčík M, Kybic J, Liebgott H, Cachard C. Model Fitting Using RANSAC for Surgical Tool Localization in 3-D Ultrasound Images. *IEEE Trans Biomed Eng*. 2010;57(8):1907-1916. doi:10.1109/TBME.2010.2046416

11. Zhao Y, Liebgott H, Cachard C. Tracking micro tool in a dynamic 3D ultrasound situation using Kalman filter and RANSAC algorithm. In: *9th IEEE International Symposium on Biomedical Imaging (ISBI)*. IEEE; 2012:1076-1079. doi:10.1109/ISBI.2012.6235745

12. Waine M, Rossa C, Sloboda R, Usmani N, Tavakoli M. 3D Shape Visualization of Curved Needles in Tissue from 2D Ultrasound Images using RANSAC. In: *2015*

IEEE International Conference on Robotics and Automation (ICRA). IEEE; 2015:4723-4728. doi:10.1109/ICRA.2015.7139855

13. Uherčík M, Kybic J, Zhao Y, Cachard C, Liebgott H. Line filtering for surgical tool localization in 3D ultrasound images. *Comput Biol Med*. 2013;43(12):2036-2045. doi:10.1016/j.compbiomed.2013.09.020

14. Kaya M, Bebek O. Needle localization using Gabor filtering in 2D ultrasound images. In: *IEEE International Conference on Robotics and Automation (ICRA)*. IEEE; 2014:4881-4886. doi:10.1109/ICRA.2014.6907574

15. Mathiassen K, Dall'Alba D, Muradore R, Fiorini P, Elle OJ. Robust Real-Time Needle Tracking in 2-D Ultrasound Images Using Statistical Filtering. *IEEE Trans Control Syst Technol*. 2017;25(3):966-978. doi:10.1109/TCST.2016.2587733

16. Ding M, Fenster A. A real-time biopsy needle segmentation technique using Hough Transform. *Med Phys*. 2003;30(8):2222-2233. doi:10.1118/1.1591192

17. Okazawa SH, Ebrahimi R, Chuang J, Rohling RN, Salcudean SE. Methods for segmenting curved needles in ultrasound images. *Med Image Anal*. 2006;10(3):330-342. doi:10.1016/j.media.2006.01.002

18. Novotny PM, Stoll JA, Vasilyev N V, Del Nido PJ, Dupont PE, Howe RD. GPU based real-time instrument tracking with three dimensional ultrasound. *Med Image Anal*. 2007;11(5):458-464. doi:10.1016/j.media.2007.06.009

19. Neshat HRS, Patel R V. Real-Time Parametric Curved Needle Segmentation in 3D Ultrasound Images. In: *2nd IEEE/RAS-EMBS International Conference on Biomedical Robotics and Biomechatronics*. IEEE; 2008:670-675. doi:10.1109/BIOROB.2008.4762877

20. Ayvali E, Desai JP. Optical Flow-Based Tracking of Needles and Needle-Tip Localization Using Circular Hough Transform in Ultrasound Images. *Ann Biomed Eng*. 2015;43(8):1828-1840. doi:10.1007/s10439-014-1208-0

21. Beigi P, Rohling R, Salcudean T, Lessoway VA, Ng GC. Needle Trajectory and Tip Localization in Real-Time 3-D Ultrasound Using a Moving Stylus. *Ultrasound Med Biol*. 2015;41(7):2057-2070. doi:10.1016/j.ultrasmedbio.2015.03.013

22. Beigi P, Rohling R, Salcudean SE, Ng GC. Spectral analysis of the tremor motion for needle detection in curvilinear ultrasound via spatiotemporal linear sampling. *Int J Comput Assist Radiol Surg*. 2016;11(6):1183-1192. doi:10.1007/s11548-016-1402-7

23. Beigi P, Rohling R, Salcudean SE, Ng GC. CASPER: computer-aided segmentation of imperceptible motion—a learning-based tracking of an invisible needle in ultrasound. *Int J Comput Assist Radiol Surg*. 2017;12(11):1857-1866. doi:10.1007/s11548-017-1631-4

24. Beigi P, Rohling R, Salcudean T, Lessoway VA, Ng GC. Detection of an invisible needle in ultrasound using a probabilistic SVM and time-domain features. *Ultrasonics*. 2017;78:18-22. doi:10.1016/j.ultras.2017.02.010

25. Hatt CR, Ng G, Parthasarathy V. Enhanced needle localization in ultrasound using beam steering and learning-based segmentation. *Comput Med Imaging Graph*. 2015;41:46-54. doi:10.1016/j.compmedimag.2014.06.016

26. Daoud MI, Rohling RN, Salcudean SE, Abolmaesumi P. Needle detection in curvilinear ultrasound images based on the reflection pattern of circular ultrasound waves. *Med Phys*. 2015;42(11):6221-6233. doi:10.1118/1.4932214

27. Arif M, Moelker A, van Walsum T. Automatic needle detection and real-time bi-planar needle visualization during 3D ultrasound scanning of the liver. *Med Image Anal*. 2019;53:104-110. doi:10.1016/j.media.2019.02.002

28. Pourtaherian A, Ghazvinian Zanjani F, Zinger S, et al. Robust and semantic needle detection in 3D ultrasound using orthogonal-plane convolutional neural networks. *Int J Comput Assist Radiol Surg*. 2018;13(9):1321-1333. doi:10.1007/s11548-018-1798-3

29. Lee JY, Islam M, Woh JR, et al. Ultrasound needle segmentation and trajectory prediction using excitation network. *Int J Comput Assist Radiol Surg*. 2020;15(3):437-443. doi:10.1007/s11548-019-02113-x

30. Mwikirize C, Nosher JL, Hacihaliloglu I. Convolution neural networks for real-time needle detection and localization in 2D ultrasound. *Int J Comput Assist Radiol Surg*. 2018;13(5):647-657. doi:10.1007/s11548-018-1721-y

31. Ronneberger O, Fischer P, Brox T. U-Net: Convolutional Networks for Biomedical Image Segmentation. *Lect Notes Comput Sci*. 2015:234-241. doi:10.1007/978-3-319-24574-4_28

32. Baldi P, Sadowski PJ. Understanding Dropout. In: Burges CJC, Bottou L, Welling M, Ghahramani Z, Weinberger KQ, eds. *Advances in Neural Information Processing Systems 26*. Curran Associates, Inc.; 2013:2814-2822. http://papers.nips.cc/paper/4878-understanding-dropout.pdf.

33. Fitzpatrick JM, West JB, Maurer, Jr CR. Predicting Error in Rigid-Body Point-Based Registration. *IEEE Trans Med Imaging*. 1998;17(5):694-702. doi:10.1109/42.736021

34. Diserud OH, Ødegaard F. A multiple-site similarity measure. *Biol Lett*. 2007;3:20-22. doi:10.1098/rsbl.2006.0553

35. Fleiss JL. Measuring nominal scale agreement among many raters. *Psychol Bull*. 1971;76(5):378-382. doi:10.1037/h0031619

36. Reusz G, Sarkany P, Gal J, Csomos A. Needle-related ultrasound artifacts and their importance in anaesthetic practice. *Br J Anaesth*. 2014;112(5):794-802. doi:10.1093/bja/aet585

Chapter 7

7 Conclusions and directions for future work

Image-guided medical interventions that use 3D information intraoperatively may provide improvements to the diagnosis and treatment of cancer, but these procedures rely heavily on the accurate targeting, guidance, and verification of needle-like tools for planned outcomes. This thesis focused on the application of 3D US imaging and image processing methods during image-guided interventions in the prostate and liver to provide accessible, fast, and accurate improvements to the clinical workflow. This chapter provides the summary, conclusions, limitations, and future directions from the work in Chapters 2-6.

7.1 Summary and conclusions

In Chapter 2, an automatic 2D-3D registration method approaching the frame rate of a US system was investigated to compensate for prostate motion during 3D TRUS-guided biopsy procedures. Since patient motion can be continuous or intermittent throughout a 3D TRUS-guided biopsy procedure, MR-derived targets can be misaligned during biopsy sampling, which can result in increased needle targeting error and the chance of missing cancer in suspicious regions identified in the MR image. Two registration modes were investigated: motion compensation using a single user-initiated correction that could be performed before biopsy and real-time continuous motion compensation that could be performed automatically as a background process. A previously developed[1] intensity-based algorithm was further optimized on retrospective patient images by implementing the algorithm on a GPU, downsampling the 2D and 3D TRUS images by a factor of four, cropping the 2D TRUS images to 356 × 292 pixels, and optimizing the Powell search space order with translations first to avoid local optima near the registration initialization position. This optimization on patient images resulted in a mean ± SD TRE and computation time of 1.6 ± 0.6 mm and 57 ± 20 ms, respectively. After implementation in a 3D TRUS-guided system, a tissue-mimicking prostate phantom with embedded agar spheres was used to evaluate the user-initiated and continuous registration approaches with known displacements provided by a micrometre-driven stage. The user-initiated mode performed registrations with computation times of 108 ± 38 ms, 60 ± 23 ms, and 89 ± 27 ms for in-plane, out-of-plane, and roll motions, respectively, and corresponding registration errors of 0.4 ± 0.3 mm, 0.2 ± 0.4 mm, and 0.8 ± 0.5°. The continuous method

performed registration significantly faster ($p < 0.05$) than the user-initiated method, with observed computation times of 35 ± 8 ms, 43 ± 16 ms, and 27 ± 5 ms for in-plane, out-of-plane, and roll motions, respectively, and corresponding registration errors of 0.2 ± 0.3 mm, 0.7 ± 0.4 mm, and 0.8 ± 1.0°. The presented method encourages implementation of real-time motion compensation algorithms in a prostate biopsy as registration errors are around the previously determined 1.6 mm requirement for sampling clinically significant prostate cancer with a 95 % confidence.[2] Image registration approaching the frame rate of an ultrasound system offers a key advantage to be smoothly integrated into the clinical workflow and could be used further for a variety of image-guided interventions, like prostate brachytherapy or liver ablation, to treat and diagnose patients by improving targeting accuracy.

Chapter 3 focused on automating the 3D TRUS-guided biopsy workflow further with additional application to 3D TRUS-guided brachytherapy by developing an algorithm using a deep learning-based approach for automatic 3D TRUS prostate segmentation. Using 3D TRUS images effectively typically requires the physician to manually segment the prostate to define the margins and volume used for accurate registration, targeting, and dose calculations. However, manual prostate segmentation is a time-consuming and difficult limitation on clinical workflow, often occurring while the patient is under sedation (biopsy) or anesthetic (brachytherapy).[3] A supervised deep learning-based method was developed to segment the prostate in 3D TRUS images from different facilities, procedures, acquisition methods, and commercial ultrasound machine models to create a generalizable algorithm for needle-based prostate cancer procedures that avoids the development of procedure-specific approaches. The developed modified U-Net with 3D reconstruction performed with a median [Q1, Q3] absolute DSC, recall, precision, VPD, MSD, and HD of 94.1 [92.6, 94.9] %, 96.0 [93.1, 98.5] %, 93.2 [88.8, 95.4] %, 5.78 [2.49, 11.50] %, 0.89 [0.73, 1.09] mm, and 2.89 [2.37, 4.35] mm, respectively, when tested on a dataset of 20 unseen end-fire and 20 side-fire 3D TRUS images. When compared to three fully 3D networks (i.e., V-Net, Dense V-Net, and High-resolution 3D-Net), our proposed method performed with significant improvement across nearly all metrics investigated. Computation time of <0.7 s per prostate was observed, which is a sufficiently short

segmentation time for intraoperative implementation and enables a generalizable intraoperative solution for needle-based prostate cancer procedures.

In Chapter 4, a new geometrically variable 3D US scanner, mechanically assisted system, and 3D-printed therapy applicator guide was developed to provide methods for imaging and guiding focal liver tumor ablations. Image guidance variabilities with 2D US imaging during freehand therapy applicator targeting can limit the sufficiency of ablation volumes and the overall potential of ablation procedures. However, US offers a safe, cheap, accessible, and real-time advantage over other methods of image-guidance. Proposed imaging solutions like CT and MRI can provide useful tools for applicator targeting, but often require longer procedure times, which are more complex and costly, limiting their widespread use. 3D US was proposed as an alternative image-guidance approach and a three-motor scanner was designed to be used with any commercially available US probe to generate accurate, consistent, and geometrically variable 3D US images. The designed scanner was mounted on a counterbalanced stabilizing and mechanical tracking system for determining the US probe position and orientation, which was assessed using optical tracking to have a mean positioning error of 1.85 ± 1.33 mm when performing compound joint manipulations. The utility of the motorized scanner enabled the development of an image-guidance navigation workflow that moved the probe to any identified target within an acquired 3D US image. The complete 3D US guidance system was used to perform mock targeted interventional procedures on a phantom by selecting a target in a 3D US image, navigating to the target, and performing needle insertion using a custom 3D-printed needle applicator guide. Registered post-insertion 3D US images and CBCT images were used to evaluate tip targeting errors when using the motors, tracking system, or mixed navigation approaches. A combined approach for navigation that incorporated the motorized movement and the in-plane tracking system corrections performed best with a mean tip error of 3.77 ± 2.27 mm and 4.27 ± 2.47 mm based on 3D US and CBCT images, respectively. 3D US image geometries used during the needle targeting experiments involved a small-footprint tilt scan and a large field-of-view hybrid scan, which were observed to have no significant differences in needle tip errors over a total of 48 targeted needle insertions. 3D US images were qualitatively evaluated in a healthy volunteer and compared to a commercially available matrix array US probe, which resulted in a clear

reconstruction of clinically relevant anatomy. Overall, this system provides a utility that enables enhanced applicator guidance, placement verification, and improved clinical workflow during focal liver tumor ablation procedures, potentially reducing local cancer recurrence rates and the feasibility of 3D US stereotactic interventional procedures.

Chapter 5 described the development of a semi-automatic 3D US needle-like therapy applicator segmentation algorithm that used a single user input to augment the addition of 3D US, like the system described in Chapter 4, to focal liver tumor ablation workflows. The algorithm was initialized by creating a spherical search space of line segments around a manually chosen seed point that was selected by a user on the needle applicator visualized in a 3D US image. The most probable trajectory was chosen by maximizing the count and intensity of threshold voxels along a line segment and was filtered using the Otsu method to determine the tip location. Homogeneous tissue-mimicking phantom images containing needle applicators with manual segmentations were used to optimize the parameters of the algorithm to median [Q1, Q3] trajectory, axis, and tip errors of 2.1 [1.1, 3.6]°, 1.3 [0.8, 2.1] mm, and 1.3 [0.7, 2.5] mm, respectively, with a mean ± SD segmentation computation time of 0.246 ± 0.007 s. The segmentation method was tested with a four-user study using 16 *in vivo*, retrospective 3D US patient images, which resulted in overall median [Q1, Q3] trajectory, axis, and tip errors of 4.5 [2.4, 5.2]°, 1.9 [1.7, 2.1] mm, and 5.1 [2.2, 5.9] mm. This 3D US semi-automatic tool segmentation offers the ability to quickly assess and adjust needle applicator placements intraoperatively, potentially improving 3D US liver ablation clinical workflow and adoption.

A general needle and applicator tool segmentation algorithm was developed in Chapter 6 for 2D US images from multiple image-guided interventions and anatomical regions. Many interventional procedures, like focal liver ablation, leverage the temporal resolution of 2D US to provide real-time feedback to aid in the accurate placement of interventional tools. Identifying tools in 2D US images during intraoperative insertion is necessary for correctly achieving planned targets for optimal diagnosis or treatment of cancer, but it is often time-consuming with accurate position information difficult to distinguish. A deep learning-based method, similar to Chapter 3, was used to predict tools in 2D US images in approximately 50 ms for multiple anatomical sites, despite the widely varying appearances

across interventional applications. A modified U-Net architecture was trained with real-time data augmentation on 917 images and manual segmentations from prostate/gynecologic brachytherapy, liver ablation, and kidney biopsy/ablation procedures, as well as phantom experiments. Post-processing to identify the tool's tip and trajectory was performed using two different approaches, comparing the largest island with a linear fit to RANSAC fitting. Comparing predictions from 315 unseen test images to manual segmentations, RANSAC post-processing resulted in improved performance with an overall median [Q1, Q3] tip error, trajectory error, and DSC of 3.5 [1.3, 13.5] mm, 0.8 [0.3, 1.7]°, and 73.3 [56.2, 82.3] %, respectively. The predictions with the lowest median tip and trajectory errors were observed in gynecologic images (median tip: 0.3 mm and median trajectory: 0.4°) with the highest errors in kidney images (median tip: 10.1 mm and median trajectory: 2.9°). Although variability was observed across different anatomical applications, the proposed approach could accurately segment tools in 2D US images from multiple anatomical locations and a variety of clinical interventional procedures in near real-time. This avoids the need for application-specific methods and provides the potential to improve image guidance during a broad range of diagnostic and therapeutic cancer interventions.

7.2 Limitations

The significant limitations of this thesis are discussed in this section and provide a summary of the discussions presented in Chapters 2-6.

7.2.1 General limitations

All studies investigating patient data in this thesis were retrospective in nature, which was more practical for developing new methods since relevant images were previously acquired. However, prospective imaging studies including larger unseen patient test data for additional evaluation would provide stronger evidence for the clinical utility of the image processing methods developed. This could include additional evaluations such as the practicality of integration into clinical workflow, physician approval through a Likert scale assessment, and randomized control trials to prove the benefit over conventional, manual techniques. The registration and deep learning methods described in this thesis also

rely on the need for a GPU to perform at the reported computation speeds, which is not traditionally available on systems currently used clinically and could limit translation. However, GPUs are easily incorporated into new systems, such as the liver system described in Chapter 4, and offer the potential for additional software acceleration to processes that could benefit from real-time functionality, such as US colour flow imaging.[4]

Obtaining ground-truth for accuracy assessment is often very complex and difficult, relying on gold standard techniques, such as manual annotations, to perform as a substitute. These gold-standard manual annotations include fiducials for registration, prostate segmentations, and needle applicator tip and shaft locations. All studies investigating patient data did not include external validation from other measurement sources due to the retrospective nature of the studies, which could provide an improved method of accuracy quantification. However, external system evaluation was performed during phantom experiments to address this need, such as a micrometre-driven translation stage, optical tracking, and CBCT images.

7.2.2 Study specific limitations

In Chapter 2, the optimization of the real-time 2D-3D TRUS registration algorithm was performed on a retrospective patient dataset and tested on phantom images in an ideal imaging scenario. Optimization on the patient images enabled an approach to refine the algorithm on expected clinical images, but manually identified fiducials and the TRE metric were used as a surrogate measure of ground truth displacement and were performed by a single user. Despite the variability introduced due to manual selection of corresponding fiducials, an improved method of evaluation would require the knowledge of a patient's true displacement without the uncertainty associated with imaging error, which is an extremely challenging endeavour. This motivated the use of a micrometre-driven phantom as an alternative, feasible, and accurate approach to provide ground truth information for evaluation. However, this approach limits extrapolation to expected clinical use where images might have less contrasting structures and more image artifacts. Three independent motions were testing with the phantom to get an impression of the algorithm's performance, but complex motion combining multiple degrees-of-freedom was not investigated. In addition, obtaining variability in phantom motion speed was

difficult using a hand-driven micrometre stage, but motion speed could influence the performance of a continuous registration approach since inter-frame displacements would be larger than investigated, potentially increasing registration computation time. Although this was not tested, it is assumed the performance would have an upper bound at the level of the user-initiated results since that experiment mimicked large displacements across a single US image frame. Finally, the phantom fabricated was a rigid body and was shown to be easily compensated using a rigid registration algorithm, but the real-time continuous method still needs to be verified in prospective patient studies where additional motion due to prostate deformation may occur.

In Chapter 3, an automatic prostate segmentation method was trained, validated, and tested on a clinically diverse dataset of 3D TRUS images. Although excellent performance was demonstrated with the proposed algorithm, a parameter that may influence computation time and accuracy is the step angle for radial slice generation and 2D predictions. Varying the step angle away from 15° would likely alter computation time since predictions would be performed on different amounts of image information, but the variability in accuracy is unknown. When training the 3D CNNs for performance comparison, hyperparameters were optimized on the V-Net and were used for the other two networks. Although these hyperparameters were found to perform the best during preliminary experiments on the Dense V-Net and High-resolution 3D-Net, a rigorous optimization was not performed and has the potential to increase performance. Another limitation of this study was the use of only one observer for providing gold standard manual segmentations. Although inter- and intra-observer variability was not assessed for the dataset used, variability in end-fire 3D TRUS images[5] and side-fire 3D TRUS images[6] were previously assessed by our group. Previously reported user variabilities were comparable to the reported DSC of the proposed segmentation method in this chapter, showing that the algorithm was performing at the level of variability observed in the gold standard segmentations. Due to the demonstrated variability between different observers when segmenting 3D TRUS images, segmentations from other observers should be investigated and incorporated into the testing dataset to further demonstrate the robustness of the proposed method.

In Chapter 4, a novel mechanically assisted 3D US system with geometrically variable image geometries was evaluated using optical tracking, phantom images, and CBCT images. One caveat of the navigation errors reported in the study was the ideal nature of the needle insertion experiments, which did not contain expected clinical issues such as liver motion. The imaging phantom was also limited in deformation characteristics relative to a patient, which could cause issues like needle deflection during needle insertion. Healthy volunteer images were also acquired under a breath-hold technique to evaluate clinical imaging feasibility. Although the images were reconstructed to visualize clinically relevant anatomy for liver ablation procedures, patients who are unable to hold their breath for 12 s would incorporate motion artifacts during 3D US acquisition. Image acquisition can be performed faster with this system by acquiring fewer images, but alterations to image reconstruction quality were not assessed. Images of healthy volunteers were only shown for one volunteer, so a wider range of body sizes should be investigated in the future.

In Chapter 5, a semi-automatic 3D US needle applicator segmentation algorithm was developed and optimized on phantom images before evaluation on a dataset of patient 3D US images containing needle-like therapy applicators in the liver. This relatively small dataset of patient images limited potential development of the segmentation algorithm as images of phantoms with minimal US echogenecity were relied on for optimizing the approach. Although the dataset was small, this was the largest clinical liver dataset of 3D US images evaluated to-date for needle applicator segmentation. A fixed adjustment to the Otsu threshold was implemented for accurate applicator tip localization, but it is possible that the adjustment is influenced by the needle applicator's SBR in the 3D US images and investigation into a dynamic adjustment was limited. The choice to use an Otsu threshold was also a potential limitation in this study as the assumption of a bimodal intensity distribution that was split between foreground (i.e., applicator) and background was not always maintain when evaluating the clinical images. Image features that were observed to limit the performance of the algorithm were large gaps along the needle applicator shaft and the presence of arteries and veins causing similar acoustic reflection intensities. Needle-like therapy applicators were also assumed to be linear, but this was a sufficient assumption for the clinical images investigated. However, this assumption limits

application to a broader range of procedures that include thinner diameter interventional tools that have a higher probability for deflection and bending.

In Chapter 6, a deep learning-based approach compared two post-processing techniques for segmenting needle-like tools in 2D US images. This method was trained, validated, and tested on unseen data from five different interventional applications from four anatomical sites and phantom experiments. The advantage of this study compared to previously reported methods was the variability in image data used for development; however, the number of patients and images accessible for this study were not balanced across all anatomical sites investigated. Overall values of accuracy were reported, but these results were heavily skewed by the performance using liver images. Tip errors reported for gynecologic images may not be a reflection of the true accuracy for this anatomical region as they did not always contain the needle tip within the image field-of-view. Since the identification of the tip location is typically the most difficult aspect of needle-like tool segmentation, the complete understanding of performance on gynecologic images could be limited. Despite this limitation, performance is expected to be similar to the prostate brachytherapy images since tool trajectories are parallel to the US probe face, which demonstrated low tip and trajectory errors with robustness to large artifacts, such as reverberation and shadowing. The post-processing approaches tested with this method also assumed a single tool was present and that it was linear, which might limit the performance of the algorithm if multiple tools are visible, as in brachytherapy procedures, or if tools deflect within the body. However, the type of fit used in this work could be modified in the future to include other variations and step-wise predictions with subsequent image filtering, which could provide a method for multi-tool segmentation. Lastly, investigation on user variability when producing manual segmentations revealed large median differences for tip identification relative to the reported metrics on the test dataset. This limits a complete understanding of the segmentation performance as errors reported incorporated a non-negligible amount of human error and did not isolate the accuracy solely due to the algorithm, stressing the difficulty of the segmentation problem.

7.3 Future directions

7.3.1 2D-3D prostate motion compensation clinical translation

A 2D-3D TRUS registration method was implemented on a guidance system in Chapter 2 for evaluating the clinical feasibility of a continuous registration approach during prostate biopsy. To expand beyond the phantom experiments and provide additional evidence for clinical feasibility, a proof-of-concept prospective clinical study has been investigated with the implemented method in Chapter 2.[7] Although the patient sample size was small (i.e., three patients), the registration approach was observed to have a median [Q1, Q3] registration error of 3.4 [1.5, 8.2] mm and a mean ± SD computation time of 27 ± 8 ms when evaluating 21 2D-3D image pairs acquired during the conventional biopsy procedure.[7] Larger registration errors were observed during sampling of tissue samples on the lateral edges of the prostate, so a new method of navigation that emphasized US probe rotation was developed during continuous 2D-3D TRUS registration. This new approach resulted in a median [Q1, Q3] registration error of 2.0 [1.3, 2.5] mm and a mean ± SD computation time of 22 ± 3 ms when evaluated on 18 image pairs, providing evidence that clinical implementation of the registration algorithm with a workflow adjustment could improve prostate biopsy targeting. These results support the investigation into a larger clinical trial with prospective patient imaging and may require the need for external imaging after needle insertion to directly verify needle targeting accuracy.

7.3.2 Multi-institutional 3D TRUS prostate segmentation

Chapter 3 described the development and evaluation of an automatic prostate segmentation method on 3D TRUS image acquired using end-fire and side-fire probes. Another common geometry for 3D TRUS image acquisition can be achieved using biplane probes during 3D TRUS-guided prostate brachytherapy, which have transverse elements that can be used to axially-reconstruct 3D images using tracked steppers.[8] A dataset including these images with manual 3D segmentations could easily be evaluated and would enable the proposed approach to have a wider potential impact and further prove the results of the method being image reconstruction geometry independent. Even if significant differences were to be observed when evaluated on this new acquisition geometry, including additional images in

the training set of the deep learning approach may be the only required alteration, which is an easily performed task.

Providing further evidence for prospective clinical utility and impact of the automated segmentation approach could be performed through the use of a multi-user and multi-institutional study. This could either provide evidence that the method is not biased to the single user used for training the approach or stress the need to incorporate alternatives for different users. The clinical impact could also be investigated across multiple users through the evaluation of segmentation accuracy and variability on radiation dose planning. Also, an editing time metric could be investigated to provide supporting evidence for benefits to clinical workflow and patient throughput.[9]

7.3.3 CT-US fusion-guided liver ablation

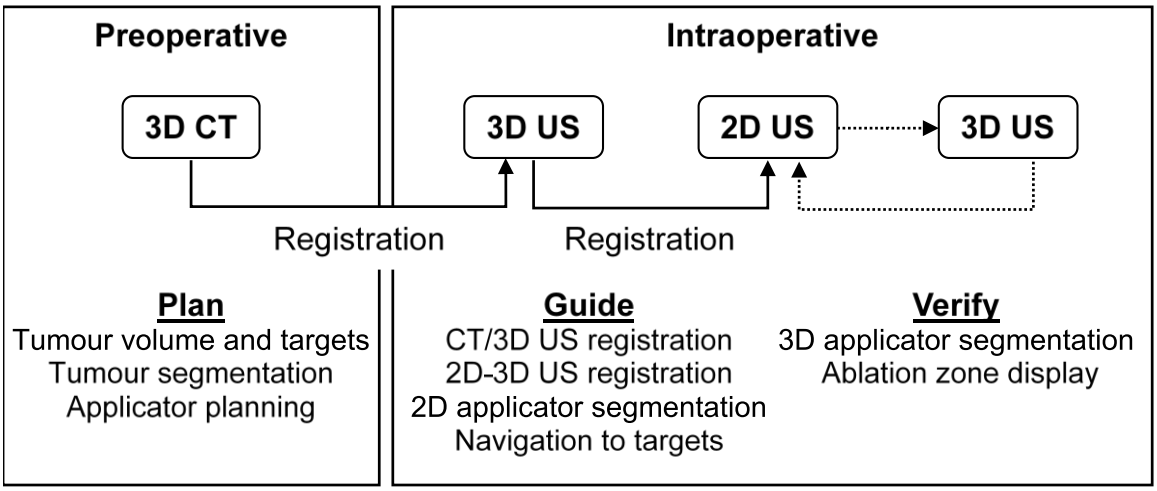

Figure 7.1 Proposed workflow for a CT-3D US-guided focal liver ablation.

3D US has the potential to improve applicator targeting accuracy during focal liver tumor ablation therapies with the opportunity to draw many parallels to MR-TRUS fusion-guided prostate biopsy. Conventional liver ablation procedures are typically only performed on lesions with diameters less than 50 mm due to the accuracy required for placing and repositioning multiple applicators with overlapping ablation volumes,[10] but an accurate image-guidance pipeline and system could provide the tools necessary to expand the number of patients eligible for ablation procedures. As shown in Figure 7.1, many modules can be incorporated into the system to plan, guide, and verify an applicator(s) placement at

the location of a tumor(s). Planning in the preoperative setting based on an initial CT image could allow for the segmentation of the tumor and provide targets for an applicator planning application to determine the optimal configuration, especially for multi-applicator treatments.[11] A CT to 3D US deformable image registration[12] could bring these CT-derived segmentations and targets into the intraoperative setting on the day of the procedure. Image-guidance could be performed using a motion compensation 2D-3D US registration algorithm, like an adaptation from the method described in Chapter 2, to adjust coordinate systems and allow for motorized target navigation, as described in Chapter 4. Using the method described in Chapter 6, 2D applicator segmentation could be performed on the live image sequence to help aid with applicator insertion. Lastly, verification of applicator guidance could be performed with subsequent and repeated 3D US images. These images could be used with the 3D applicator segmentation method developed in Chapter 5, or a fully automated deep-learning approach, for generating applicator locations and planned ablation volumes for therapeutic margin assessment before initiating the therapy session. Technology that enables a stereotactic interventional approach could exploit the low complication rates and recovery times of focal liver ablation procedures, while increasing patient eligibility, decreasing local cancer recurrence rates, and increasing overall patient survival.

7.4 References

1. De Silva T, Fenster A, Cool DW, et al. 2D-3D rigid registration to compensate for prostate motion during 3D TRUS-guided biopsy. *Med Phys*. 2013;40(2):022904. doi:10.1118/1.4773873

2. Martin PR, Cool DW, Romagnoli C, Fenster A, Ward AD. Magnetic resonance imaging-targeted, 3D transrectal ultrasound-guided fusion biopsy for prostate cancer: Quantifying the impact of needle delivery error on diagnosis. *Med Phys*. 2014;41(7):073504. doi:10.1118/1.4883838

3. Reich DL, Hossain S, Krol M, et al. Predictors of Hypotension After Induction of General Anesthesia. *Anesth Analg*. 2005;101(3):622-628. doi:10.1213/01.ANE.0000175214.38450.91

4. Chee AJY, Yiu BYS, Yu ACH. A GPU-Parallelized Eigen-Based Clutter Filter Framework for Ultrasound Color Flow Imaging. *IEEE Trans Ultrason Ferroelectr Freq Control*. 2017;64(1):150-163. doi:10.1109/TUFFC.2016.2606598

5. Qiu W, Yuan J, Ukwatta E, Fenster A. Rotationally resliced 3D prostate TRUS segmentation using convex optimization with shape priors. *Med Phys*. 2015;42(2):877-891. doi:10.1118/1.4906129

6. Tong S, Cardinal HN, McLoughlin RF, Downey DB, Fenster A. Intra- and inter-observer variability and reliability of prostate volume measurement via two-dimensional and three-dimensional ultrasound imaging. *Ultrasound Med Biol*. 1998;24(5):673-681. doi:10.1016/S0301-5629(98)00039-8

7. Gillies DJ, Gardi L, Tessier D, Mercado A, Fenster A. Ring navigation: an ultrasound-guided technique using real-time motion compensation for prostate biopsies. In: Webster RJ, Fei B, eds. *Medical Imaging 2018: Image-Guided Procedures, Robotic Interventions, and Modeling*. SPIE; 2018:105761P. doi:10.1117/12.2292922

8. Batchelar D, Gaztañaga M, Schmid M, Araujo C, Bachand F, Crook J. Validation study of ultrasound-based high-dose-rate prostate brachytherapy planning compared with CT-based planning. *Brachytherapy*. 2014;13(1):75-79. doi:10.1016/j.brachy.2013.08.004

9. Shahedi M, Cool DW, Romagnoli C, et al. Postediting prostate magnetic resonance imaging segmentation consistency and operator time using manual and computer-assisted segmentation: multiobserver study. *J Med Imaging*. 2016;3(4):046002. doi:10.1117/1.JMI.3.4.046002

10. Georgiades CS, Hong K, Geschwind J-F. Radiofrequency Ablation and Chemoembolization for Hepatocellular Carcinoma. *Cancer J*. 2008;14(2):117-122. doi:10.1097/PPO.0b013e31816a0fac

11. Liang L, Cool D, Kakani N, Wang G, Ding H, Fenster A. Automatic Radiofrequency Ablation Planning for Liver Tumors with Multiple Constraints Based on Set Covering. *IEEE Trans Med Imaging*. 2019;0062. doi:10.1109/TMI.2019.2950947

12. Wein W, Kutter O, Aichert A, Zikic D, Kamen A, Navab N. Automatic non-linear mapping of pre-procedure CT volumes to 3D ultrasound. In: *2010 IEEE International Symposium on Biomedical Imaging: From Nano to Macro*. IEEE; 2010:1225-1228. doi:10.1109/ISBI.2010.5490216

Appendix A – Ethics Approvals

Western Research

Research Ethics

Western University Health Science Research Ethics Board
HSREB Amendment Approval Notice

Principal Investigator: Dr. Aaron Fenster
Department & Institution: Schulich School of Medicine and Dentistry\Medical Biophysics,Robarts Research Institute

Review Type: Delegated
HSREB File Number: 106996
Study Title: Using 3-Dimensional Ultrasound Imaging to Track Liver Motion
Sponsor: Ontario Research fund

HSREB Amendment Approval Date: July 21, 2017
HSREB Expiry Date: September 08, 2017

Documents Approved and/or Received for Information:

Document Name	Comments	Version Date
Revised Western University Protocol	Received 2017/07/20	
Revised Letter of Information & Consent		2017/07/20

The Western University Health Science Research Ethics Board (HSREB) has reviewed and approved the amendment to the above named study, as of the HSREB Initial Approval Date noted above.

HSREB approval for this study remains valid until the HSREB Expiry Date noted above, conditional to timely submission and acceptance of HSREB Continuing Ethics Review.

The Western University HSREB operates in compliance with the Tri-Council Policy Statement Ethical Conduct for Research Involving Humans (TCPS2), the International Conference on Harmonization of Technical Requirements for Registration of Pharmaceuticals for Human Use Guideline for Good Clinical Practice Practices (ICH E6 R1), the Ontario Personal Health Information Protection Act (PHIPA, 2004), Part 4 of the Natural Health Product Regulations, Health Canada Medical Device Regulations and Part C, Division 5, of the Food and Drug Regulations of Health Canada.

Members of the HSREB who are named as Investigators in research studies do not participate in discussions related to, nor vote on such studies when they are presented to the REB.

The HSREB is registered with the U.S. Department of Health & Human Services under the IRB registration number IRB 00000940.

Western Research

Date: 31 July 2019

To: Dr. Derek Cool

Project ID: 114000

Study Title: Planning Software Development to Optimize Liver and Kidney Tumour Ablation Treatment

Application Type: HSREB Initial Application

Review Type: Delegated

Meeting Date / Full Board Reporting Date: 06/Aug/2019

Date Approval Issued: 31/Jul/2019

REB Approval Expiry Date: 31/Jul/2020

Dear Dr. Derek Cool

The Western University Health Science Research Ethics Board (HSREB) has reviewed and approved the above mentioned study as described in the WREM application form, as of the HSREB Initial Approval Date noted above. This research study is to be conducted by the investigator noted above. All other required institutional approvals must also be obtained prior to the conduct of the study.

Documents Approved:

Document Name	Document Type	Document Date	Document Version
DCF-Abdominal-DB-July-25_2019-v1.1	Other Data Collection Instruments	25/Jul/2019	1.1
Protocol-25-Jul-2019-1.1	Protocol	25/Jul/2019	1.1

No deviations from, or changes to, the protocol or WREM application should be initiated without prior written approval of an appropriate amendment from Western HSREB , except when necessary to eliminate immediate hazard(s) to study participants or when the change(s) involves only administrative or logistical aspects of the trial.

REB members involved in the research project do not participate in the review, discussion or decision.

The Western University HSREB operates in compliance with, and is constituted in accordance with, the requirements of the TriCouncil Policy Statement: Ethical Conduct for Research Involving Humans (TCPS 2); the International Conference on Harmonisation Good Clinical Practice Consolidated Guideline (ICH GCP); Part C, Division 5 of the Food and Drug Regulations; Part 4 of the Natural Health Products Regulations; Part 3 of the Medical Devices Regulations and the provisions of the Ontario Personal Health Information Protection Act (PHIPA 2004) and its applicable regulations. The HSREB is registered with the U.S. Department of Health & Human Services under the IRB registration number IRB 00000940.

Please do not hesitate to contact us if you have any questions.

Sincerely,

Daniel Wyzynski, Research Ethics Coordinator, on behalf of Dr. Philip Jones, HSREB Vice-Chair

Note: This correspondence includes an electronic signature (validation and approval via an online system that is compliant with all regulations).

Appendix B – Copyright Releases

JOHN WILEY AND SONS LICENSE
TERMS AND CONDITIONS

Apr 20, 2020

This Agreement between Derek J. Gillies ("You") and John Wiley and Sons ("John Wiley and Sons") consists of your license details and the terms and conditions provided by John Wiley and Sons and Copyright Clearance Center.

License Number	4813100896039
License date	Apr 20, 2020
Licensed Content Publisher	John Wiley and Sons
Licensed Content Publication	Medical Physics
Licensed Content Title	Real-time registration of 3D to 2D ultrasound images for image-guided prostate biopsy
Licensed Content Author	Derek J. Gillies, Lori Gardi, Tharindu De Silva, et al
Licensed Content Date	Aug 8, 2017
Licensed Content Volume	44

Licensed Content Issue	9
Licensed Content Pages	16
Type of use	Dissertation/Thesis
Requestor type	Author of this Wiley article
Format	Electronic
Portion	Full article
Will you be translating?	No
Title	A Novel System and Image Processing for Improving 3D Ultrasound-guided Interventional Cancer Procedures
Institution name	Western University
Expected presentation date	Jun 2020
Requestor Location	Derek J. Gillies London, ON N6G3R9 Canada Attn:

JOHN WILEY AND SONS LICENSE
TERMS AND CONDITIONS

Apr 20, 2020

This Agreement between Derek J. Gillies ("You") and John Wiley and Sons ("John Wiley and Sons") consists of your license details and the terms and conditions provided by John Wiley and Sons and Copyright Clearance Center.

License Number	4813110656866
License date	Apr 20, 2020
Licensed Content Publisher	John Wiley and Sons
Licensed Content Publication	Medical Physics
Licensed Content Title	Automatic prostate segmentation using deep learning on clinically diverse 3D transrectal ultrasound images
Licensed Content Author	Nathan Orlando, Derek J. Gillies, Igor Gyacskov, et al
Licensed Content Date	Apr 8, 2020
Licensed Content Volume	0

Licensed Content Issue	0
Licensed Content Pages	14
Type of use	Dissertation/Thesis
Requestor type	Author of this Wiley article
Format	Electronic
Portion	Full article
Will you be translating?	No
Title	A Novel System and Image Processing for Improving 3D Ultrasound-guided Interventional Cancer Procedures
Institution name	Western University
Expected presentation date	Jun 2020
Requestor Location	Derek J. Gillies London, ON N6G3R9 Canada Attn:

JOHN WILEY AND SONS LICENSE
TERMS AND CONDITIONS

Apr 20, 2020

This Agreement between Derek J. Gillies ("You") and John Wiley and Sons ("John Wiley and Sons") consists of your license details and the terms and conditions provided by John Wiley and Sons and Copyright Clearance Center.

License Number	4813101259713
License date	Apr 20, 2020
Licensed Content Publisher	John Wiley and Sons
Licensed Content Publication	Medical Physics
Licensed Content Title	Three-dimensional therapy needle applicator segmentation for ultrasound-guided focal liver ablation
Licensed Content Author	Aaron Fenster, Nirmal Kakani, Derek W. Cool, et al
Licensed Content Date	May 6, 2019
Licensed Content Volume	46

Licensed Content Issue	6
Licensed Content Pages	13
Type of use	Dissertation/Thesis
Requestor type	Author of this Wiley article
Format	Electronic
Portion	Full article
Will you be translating?	No
Title	A Novel System and Image Processing for Improving 3D Ultrasound-guided Interventional Cancer Procedures
Institution name	Western University
Expected presentation date	Jun 2020
Requestor Location	Derek J. Gillies London, ON N6G3R9 Canada Attn:

Publisher Tax ID EU826007151

Total 0.00 CAD

Terms and Conditions

TERMS AND CONDITIONS

This copyrighted material is owned by or exclusively licensed to John Wiley & Sons, Inc. or one of its group companies (each a"Wiley Company") or handled on behalf of a society with which a Wiley Company has exclusive publishing rights in relation to a particular work (collectively "WILEY"). By clicking "accept" in connection with completing this licensing transaction, you agree that the following terms and conditions apply to this transaction (along with the billing and payment terms and conditions established by the Copyright Clearance Center Inc., ("CCC's Billing and Payment terms and conditions"), at the time that you opened your RightsLink account (these are available at any time at http://myaccount.copyright.com).

Terms and Conditions

- The materials you have requested permission to reproduce or reuse (the "Wiley Materials") are protected by copyright.

- You are hereby granted a personal, non-exclusive, non-sub licensable (on a stand-alone basis), non-transferable, worldwide, limited license to reproduce the Wiley Materials for the purpose specified in the licensing process. This license, **and any CONTENT (PDF or image file) purchased as part of your order,** is for a one-time use only and limited to any maximum distribution number specified in the license. The first instance of republication or reuse granted by this license must be completed within two years of the date of the grant of this license (although copies prepared before the end date may be distributed thereafter). The Wiley Materials shall not be used in any other manner or for any other purpose, beyond what is granted in the license. Permission is granted subject to an appropriate acknowledgement given to the author, title of the material/book/journal and the publisher. You shall also duplicate the copyright notice that appears in the Wiley publication in your use of the Wiley Material. Permission is also granted on the understanding that nowhere in the text is a previously published source acknowledged for all or part of this Wiley Material. Any third party content is expressly excluded from this permission.

- With respect to the Wiley Materials, all rights are reserved. Except as expressly granted by the terms of the license, no part of the Wiley Materials may be copied, modified, adapted (except for minor reformatting required by the new Publication), translated, reproduced, transferred or distributed, in any form or by any means, and no derivative works may be made based on the Wiley Materials without the prior permission of the respective copyright owner.**For STM Signatory Publishers clearing permission under the terms of the STM Permissions Guidelines only, the terms of the license are extended to include subsequent editions and for editions in other languages, provided such editions are for the work as a whole in situ and does not involve the separate exploitation of the permitted figures or extracts,** You may not alter, remove or suppress in any manner any copyright, trademark or other notices displayed by the Wiley Materials. You may not license, rent, sell, loan, lease, pledge, offer as security, transfer or assign the Wiley Materials on a stand-alone basis, or any of the rights granted to you hereunder to any other person.

- The Wiley Materials and all of the intellectual property rights therein shall at all times remain the exclusive property of John Wiley & Sons Inc, the Wiley Companies, or their respective licensors, and your interest therein is only that of having possession of and the right to reproduce the Wiley Materials pursuant to Section 2 herein during the continuance of this Agreement. You agree that you own no right, title or interest in or to the Wiley Materials or any of the intellectual property rights therein. You shall have no rights hereunder other than the license as provided for above in Section 2. No right, license or interest to any trademark, trade name, service mark or other branding ("Marks") of WILEY or its licensors is granted hereunder, and you agree that you shall not assert any such right, license or interest with respect thereto

- NEITHER WILEY NOR ITS LICENSORS MAKES ANY WARRANTY OR REPRESENTATION OF ANY KIND TO YOU OR ANY THIRD PARTY, EXPRESS, IMPLIED OR STATUTORY, WITH RESPECT TO THE MATERIALS OR THE ACCURACY OF ANY INFORMATION CONTAINED IN THE MATERIALS, INCLUDING, WITHOUT LIMITATION, ANY IMPLIED WARRANTY OF MERCHANTABILITY, ACCURACY, SATISFACTORY QUALITY, FITNESS FOR A PARTICULAR PURPOSE, USABILITY, INTEGRATION OR NON-INFRINGEMENT AND ALL SUCH WARRANTIES ARE HEREBY EXCLUDED BY WILEY AND ITS LICENSORS AND WAIVED BY YOU.

- WILEY shall have the right to terminate this Agreement immediately upon breach of this Agreement by you.

- You shall indemnify, defend and hold harmless WILEY, its Licensors and their respective directors, officers, agents and employees, from and against any actual or threatened claims, demands, causes of action or proceedings arising from any breach

of this Agreement by you.

- IN NO EVENT SHALL WILEY OR ITS LICENSORS BE LIABLE TO YOU OR ANY OTHER PARTY OR ANY OTHER PERSON OR ENTITY FOR ANY SPECIAL, CONSEQUENTIAL, INCIDENTAL, INDIRECT, EXEMPLARY OR PUNITIVE DAMAGES, HOWEVER CAUSED, ARISING OUT OF OR IN CONNECTION WITH THE DOWNLOADING, PROVISIONING, VIEWING OR USE OF THE MATERIALS REGARDLESS OF THE FORM OF ACTION, WHETHER FOR BREACH OF CONTRACT, BREACH OF WARRANTY, TORT, NEGLIGENCE, INFRINGEMENT OR OTHERWISE (INCLUDING, WITHOUT LIMITATION, DAMAGES BASED ON LOSS OF PROFITS, DATA, FILES, USE, BUSINESS OPPORTUNITY OR CLAIMS OF THIRD PARTIES), AND WHETHER OR NOT THE PARTY HAS BEEN ADVISED OF THE POSSIBILITY OF SUCH DAMAGES. THIS LIMITATION SHALL APPLY NOTWITHSTANDING ANY FAILURE OF ESSENTIAL PURPOSE OF ANY LIMITED REMEDY PROVIDED HEREIN.

- Should any provision of this Agreement be held by a court of competent jurisdiction to be illegal, invalid, or unenforceable, that provision shall be deemed amended to achieve as nearly as possible the same economic effect as the original provision, and the legality, validity and enforceability of the remaining provisions of this Agreement shall not be affected or impaired thereby.

- The failure of either party to enforce any term or condition of this Agreement shall not constitute a waiver of either party's right to enforce each and every term and condition of this Agreement. No breach under this agreement shall be deemed waived or excused by either party unless such waiver or consent is in writing signed by the party granting such waiver or consent. The waiver by or consent of a party to a breach of any provision of this Agreement shall not operate or be construed as a waiver of or consent to any other or subsequent breach by such other party.

- This Agreement may not be assigned (including by operation of law or otherwise) by you without WILEY's prior written consent.

- Any fee required for this permission shall be non-refundable after thirty (30) days from receipt by the CCC.

- These terms and conditions together with CCC's Billing and Payment terms and conditions (which are incorporated herein) form the entire agreement between you and WILEY concerning this licensing transaction and (in the absence of fraud) supersedes all prior agreements and representations of the parties, oral or written. This Agreement may not be amended except in writing signed by both parties. This Agreement shall be binding upon and inure to the benefit of the parties' successors, legal representatives,

and authorized assigns.

- In the event of any conflict between your obligations established by these terms and conditions and those established by CCC's Billing and Payment terms and conditions, these terms and conditions shall prevail.

- WILEY expressly reserves all rights not specifically granted in the combination of (i) the license details provided by you and accepted in the course of this licensing transaction, (ii) these terms and conditions and (iii) CCC's Billing and Payment terms and conditions.

- This Agreement will be void if the Type of Use, Format, Circulation, or Requestor Type was misrepresented during the licensing process.

- This Agreement shall be governed by and construed in accordance with the laws of the State of New York, USA, without regards to such state's conflict of law rules. Any legal action, suit or proceeding arising out of or relating to these Terms and Conditions or the breach thereof shall be instituted in a court of competent jurisdiction in New York County in the State of New York in the United States of America and each party hereby consents and submits to the personal jurisdiction of such court, waives any objection to venue in such court and consents to service of process by registered or certified mail, return receipt requested, at the last known address of such party.

WILEY OPEN ACCESS TERMS AND CONDITIONS

Wiley Publishes Open Access Articles in fully Open Access Journals and in Subscription journals offering Online Open. Although most of the fully Open Access journals publish open access articles under the terms of the Creative Commons Attribution (CC BY) License only, the subscription journals and a few of the Open Access Journals offer a choice of Creative Commons Licenses. The license type is clearly identified on the article.

The Creative Commons Attribution License

The Creative Commons Attribution License (CC-BY) allows users to copy, distribute and transmit an article, adapt the article and make commercial use of the article. The CC-BY license permits commercial and non-

Creative Commons Attribution Non-Commercial License

The Creative Commons Attribution Non-Commercial (CC-BY-NC)License permits use, distribution and reproduction in any medium, provided the original work is properly cited and is not used for commercial purposes.(see below)

Curriculum Vitae

EDUCATION

Doctor of Philosophy 2015-Present
Major: Medical Biophysics
Supervisor: Aaron Fenster, PhD, FCCPM
Thesis: A Novel System and Advanced Image Processing for Interventional Cancer Procedures
Western University, London, ON

Master of Science 2015-2019
Major: Clinical Medical Biophysics (CAMPEP-accredited)
Western University, London, ON

Bachelor of Science (Honours) 2011-2015
With distinction
Major: Physics and High Technology (Medical Physics) with Co-op
Minors: Computer Science and Mathematics
University of Windsor, Windsor, ON

PUBLICATIONS

Peer-reviewed In Press

1. Orlando N and **Gillies DJ,** Gyacskov I, Romagnoli C, D'Souza D, Fenster A, Automatic prostate segmentation in clinically diverse 3D transrectal ultrasound images. *Med Phys.* 2020; doi:10.1002/mp.14134. [Epub ahead of print]

2. **Gillies DJ,** Awad J, Rodgers JR, Edirisinghe C, Kakani N, Fenster A, Three-dimensional Therapy Needle Applicator Segmentation for Ultrasound-guided Focal Liver Ablation. *Med Phys.* 2019; **46**(6):2646-2658. doi: 10.1002/mp.13548.

3. **Gillies DJ,** Gardi L, De Silva T, Zhao S, Fenster A, Real-time Registration of 2D to 3D Ultrasound Images for Image-guided Prostate Biopsy. *Med Phys*. 2017; **44**(9):4708-4723. doi:10.1002/mp.12441.

4. Malenfant DJ, **Gillies DJ**, Rehse S, Bacterial Suspensions Deposited on Microbiological Filter Material for Rapid Laser-Induced Breakdown Spectroscopy Identification. *Appl Spectrosc*. 2016; **70**(3):485-493. doi:10.1177/0003702815626673.

Peer-reviewed Under Review

1. **Gillies DJ,** Bax J, Barker K, Gardi L, Tessier D, Kakani N, Fenster A, Geometrically Variable Three-Dimensional Ultrasound for Mechanically Assisted Image-Guided Therapy of Focal Liver Cancer Tumors. Submitted to *Med Phys*. (Apr. 20, 2020).

2. **Gillies DJ** and Rodgers JR**,** Gyacskov I, Roy P, Kakani N, Cool DW, Fenster A, A Deep Learning Method for General Needle and Applicator Segmentation in Two-dimensional Ultrasound Images from Multiple Applications and Anatomical Regions. Submitted to *Med Phys*. (Apr. 20, 2020).

Conference Proceedings

1. **Gillies DJ,** Bax J, Barker K, Gardi L, Tessier D, Kakani N, Fenster A, Assessment of therapy applicator targeting with a mechanically assisted 3D ultrasound system for minimally invasive focal liver tumor therapy, *Proc. SPIE 11315, Medical Imaging 2020: Image-Guided Procedures, Robotic Interventions, and Modeling*, 113152K (16 March 2020); doi:10.1117/12.2549841.

2. Rodgers JR, **Gillies DJ**, Hrinivich WT, Gyacskov I, Fenster A, Automatic needle localization in intraoperative 3D transvaginal ultrasound images for high-dose-rate interstitial gynecologic brachytherapy, *Proc. SPIE 11315, Medical Imaging 2020: Image-Guided Procedures, Robotic Interventions, and Modeling*, 113150K (16 March 2020); doi: 10.1117/12.2549664.

3. Orlando N and **Gillies DJ**, Gyackov I, Fenster A, Deep learning-based automatic prostate segmentation in 3D transrectal ultrasound images from multiple acquisition geometries and systems, *Proc. SPIE 11315, Medical Imaging 2020: Image-Guided Procedures, Robotic Interventions, and Modeling*, 113152I (16 March 2020); doi: 10.1117/12.2549804.

4. Papernick S, **Gillies DJ**, Appleton T, Fenster A. Three-dimensional ultrasound for monitoring knee inflammation and cartilage damage in osteoarthritis and rheumatoid arthritis, *Proc. SPIE 11315, Medical Imaging 2020: Image-Guided Procedures, Robotic Interventions, and Modeling*, 113150E (16 March 2020); doi: 10.1117/12.2549624.

5. **Gillies DJ,** Bax J, Barker K, Gardi L, Tessier D, Kakani N, Fenster A, Mechanically assisted 3D ultrasound with geometrically variable imaging for minimally invasive focal liver tumor therapy. *Proc. SPIE 10951, Medical Imaging 2019: Image-Guided Procedures, Robotic Interventions, and Modeling*, 109510Y (March 8, 2019); doi: 10.1117/12.2512875.

6. **Gillies DJ,** Gardi L, Tessier D, Mercado A, Fenster A, Ring navigation: an ultrasound-guided technique using real-time motion compensation for prostate biopsies. *Proc. SPIE 10576, Medical Imaging 2018: Image-Guided Procedures, Robotic Interventions, and Modeling*, 105761P (March 13, 2018); doi: 10.1117/12.2292922.

7. **Gillies DJ,** Gardi L, De Silva T, Zhao S, Fenster A, Optimization of real-time rigid registration motion compensation for prostate biopsies using 2D/3D ultrasound. *Proc. SPIE 10135, Medical Imaging 2017: Image-Guided Procedures, Robotic Interventions, and Modeling*, 101351F (March 3, 2017); doi:10.1117/12.2255006.

Book Chapter

1. Fenster A, Rodgers J, Michael J, **Gillies DJ**. *3D Ultrasound Guided Interventions*. In Biomechanics of Soft Tissues: Principles and Applications. Publisher: CRC Press/Taylor & Francis Group, LLC. Al-Mayah A., 2018

AWARDS & RECOGNITIONS

3rd Place Poster Presentation, presenting author ImNO 2020 Symposium	2020
2nd Place Oral Presentation, co-author ImNO 2020 Symposium	2020
1st Place Best Poster, co-author ISCAS Annual Conference	2019
Dr. Alfred Jay Medical Biophysics Award for Translational Research ($2,000)	2019
2nd Place Young Investigator Symposium, presenting author AAPM Spring Meeting ($150)	2019
Western Graduate Research Scholarship (WGRS) ($5,000/yr)	2018-2020
NSERC Alexander Graham Bell Postgraduate Scholarship-Doctoral (PGS D) ($63,000/3yr)	2017-2020
Cancer Research and Technology Transfer (CaRTT) Strategic Training Program Senior Trainee (valued at $16,600)	2017-2018
NSERC Alexander Graham Bell Canada Graduate Scholarship-Master's (CGS M) ($17,500)	2016-2017
Cancer Research and Technology Transfer (CaRTT) Strategic Training Program ($16,600)	2015-2016
Western Graduate Research Scholarship (WGRS) ($7,800/yr)	2015-2018
Schulich Graduate Scholarship ($2,000/yr)	2015-2018
WRCC Harold E. Johns Studentship	2013-2014
Dean's List	2012-2015
President's Honour Roll	2012
Outstanding Scholars Honorarium ($6,000)	2012-2015
Renewable Entrance Scholarship ($6,400)	2011-2015
Outstanding Scholars Award in Physics ($6,000)	2011-2015

RESEARCH PRESENTATIONS & POSTERS

I. Oral Presentations

a. Invited Talks

1. Rodgers JR, Orlando N, **Gillies DJ**, Park C, Fenster A, "2D and 3D Ultrasound Devices for Image-guided Interventions," BC Cancer – Kelowna, Kelowna, BC, September 30, 2019

b. International

1. Rodgers JR, **Gillies DJ**, Hrinivich WT, Gyacskov I, Fenster A, "Automatic needle localization in intraoperative 3D transvaginal ultrasound images for high-dose-rate interstitial gynecologic brachytherapy," SPIE Medical Imaging - Image-Guided Procedures, Robotic Interventions, and Modeling, Marriott Marquis Houston, Houston, TX, USA, February 15-20, 2020

2. Orlando N and **Gillies DJ**, Gyacskov I, Fenster A, "A generalizable deep learning-based method for automatic prostate segmentation in 3D ultrasound," SPIE Medical Imaging – Image Processing, Marriott Marquis Houston, Houston, TX, USA, February 15-20, 2020

3. Papernick S, **Gillies DJ,** Appleton T, Fenster A, "Three-dimensional ultrasound for monitoring knee inflammation and cartilage damage in osteoarthritis and rheumatoid arthritis," SPIE Medical Imaging - Image-Guided Procedures, Robotic Interventions, and Modeling, Marriott Marquis Houston, Houston, TX, USA, February 15-20, 2020

4. **Gillies DJ,** Bax J, Barker K, Gyacskov I, Gardi L, Tessier D, Kakani N, Fenster A, "Towards a 3D ultrasound guidance system for focal liver tumor ablation therapy," AAPM Annual Scientific Meeting, Henry B. Gonzalez Convention Center, San Antonio, TX, USA, July 14-18, 2019

5. **Gillies DJ,** Bax J, Barker K, Gardi L, Tessier D, Kakani N, Fenster A, "A Mechanically Tracked 3D Geometrically Variable Ultrasound Image Guidance System for Focal Liver Tumor Therapies," Artimino Conference on Medical Ultrasound Technology, Nijmegen, The Netherlands, June 23-26, 2019

6. **Gillies DJ,** Bax J, Barker K, Gardi L, Tessier D, Kakani N, Fenster A, "Minimally invasive focal liver tumor therapy using a mechanically assisted 3D ultrasound system for geometrically variable imaging," AAPM Spring Clinical Meeting [2nd Place Young Investigator Symposium], Gaylord Palms Resort and Convention Center, Kissimmee, FL, March 30 – April 2, 2019

7. **Gillies DJ,** Awad J, Rodgers JR, Edirisinghe C, Kakani N, Fenster A, "Mechanically assisted 3D ultrasound with geometrically variable imaging for minimally invasive focal liver tumor therapy," SPIE Medical Imaging - Image-Guided Procedures, Robotic Interventions, and Modeling, Town and Country Resort & Convention Center, San Diego, CA, USA, February 16-21, 2019

8. **Gillies DJ,** Gardi L, Tessier D, Mercado A, Fenster A, "Ring navigation: an ultrasound-guided technique using real-time motion compensation for prostate biopsies," SPIE Medical Imaging - Image-Guided Procedures, Robotic Interventions, and Modeling, Marriott Marquis Houston, Houston, TX, USA, February 10-15, 2018

9. **Gillies DJ,** Gardi L, Zhao R, Fenster A, "Optimization of Real-time Rigid Registration Motion Compensation for Prostate Biopsies Using 2D/3D Ultrasound," SPIE Medical Imaging - Image-Guided Procedures, Robotic Interventions, and Modeling, Renaissance Orlando at SeaWorld, Orlando, FL, USA, February 11-16, 2017

c. National

1. **Gillies DJ**, Gardi L, Zhao R, Fenster A, "Towards Clinical Implementation of a Real-time Ultrasound-based Motion Compensation Algorithm," COMP – Annual Scientific Meeting, The Westin Ottawa, Ottawa, ON, July 12-15, 2017

d. Provincial

1. Orlando N and **Gillies DJ**, Gyacskov I, Romagnoli C, D'Souza D, Fenster A, "A Deep Learning-based Method for Generalized Prostate Segmentation in 3D Ultrasound," Imaging Network Ontario (ImNO), Virtual Meeting, March 26-27, 2020.

2. Rodgers JR, **Gillies DJ**, Hrinivich WT, Gyacskoc I, Surry K, Fenster A, "Localizing high-dose-rate interstitial gynecologic brachytherapy needles intraoperatively using automatic segmentation approaches," Imaging Network Ontario (ImNO) [*2nd Place*], Virtual Meeting, March 26-27, 2020.

3. Papernick S, Dima R, **Gillies DJ**, Appleton T, Fenster A, "Validation of 3D ultrasound for bedside monitoring of osteoarthritis-induced synovium inflammation and cartilage degradation," Imaging Network Ontario (ImNO), Virtual Meeting, March 26-27, 2020.

4. **Gillies DJ,** Bax J, Barker K, Gardi L, Tessier D, Kakani N, Fenster A, "Geometrically Variable 3D Ultrasound with Mechanical Assistance for Interventional Liver Cancer Therapies," Imaging Network Ontario (ImNO), DoubleTree by Hilton, London, ON, March 28-29, 2019

5. **Gillies DJ,** Zhao R, Gardi L, Fenster A, "3D Ultrasound Guided Liver Ablation Therapy: Development Of Real-time Motion Compensation," Imaging Network Ontario (ImNO), The Chestnut Residence, Toronto, ON, March 30-31, 2016

e. Regional

1. **Gillies DJ,** Zhao R, Gardi L, Fenster A, "Double Vision: Real-time 2D/3D Ultrasound Image Registration to Compensate for Liver Motion," London Health Research Day, London Convention Centre, London, ON, March 29, 2016

II. Poster Presentations

a. International

1. **Gillies DJ**, Bax J, Barker K, Gardi L, Tessier D, Kakani N, Fenster A, "Assessment of therapy applicator targeting with a mechanically assisted 3D ultrasound system for minimally invasive focal liver tumor therapy," SPIE Medical Imaging - Image-Guided Procedures, Robotic Interventions, and Modeling, Marriott Marquis Houston, Houston, TX, USA, February 15-20, 2020

2. Orlando N and **Gillies DJ**, Gyacskov I, Fenster A, "Deep learning-based automatic prostate segmentation in 3D transrectal ultrasound images from multiple acquisition geometries and systems," SPIE Medical Imaging - Image-Guided Procedures, Robotic Interventions, and Modeling, Marriott Marquis Houston, Houston, TX, USA, February 15-20, 2020

3. Fenster A, Rodgers J, **Gillies DJ**, Kishimoto J, Papernick S, Kakani N, "Development of Mechanical 3D Ultrasound Scanning Devices for Image-guided Interventions," International Society for Computer Aided Surgery (ISCAS) [*1st Place*], Rennes, France, June 18-19, 2019

4. **Gillies DJ,** Bax J, Barker K, Gardi L, Tessier D, Kakani N, Fenster A, "3D Ultrasound Image Guidance System for Focal Liver Tumor Therapies," International Conference on Information Processing in Computer-Assisted Interventions (IPCAI) [5 min. oral + Poster], Rennes, France, June 18-19, 2019

b. National

1. **Gillies DJ,** Bax J, Barker K, Gyacskov I, Gardi L, Tessier D, Kakani N, Fenster A, "Development of a 3D ultrasound guidance and verification system for focal liver tumour ablation therapy," COMP Annual Scientific Meeting, Delta Hotels By Marriot Grand Okanagan Resort, Kelowna, BC, September 24-27, 2019

2. **Gillies DJ,** Awad J, Rodgers JR, Edirisinghe C, Kakani N, Fenster A, "Segmentation of Applicators in Three-dimensional Ultrasound for Minimally Invasive Liver Therapies," CARO-COMP-CAMRT JSM, Le Centre Sheraton Montreal Hotel, Montreal, QC, September 12-15, 2018

c. Provincial

1. **Gillies DJ,** Bax J, Barker K, Gardi L, Tessier D, Kakani N, Fenster A, "Image-guidance Accuracy of a 3D Ultrasound System for Interventional Liver Cancer Therapies," Imaging Network Ontario (ImNO) [*3rd Place*], Virtual Meeting, March 26-27, 2020

2. Papernick, S, **Gillies DJ,** Barker K, Gardi L, Fenster A, "Validating Three-Dimensional Ultrasound Measurements of the Synovium for Diagnosis of Rheumatoid Arthritis," Imaging Network Ontario (ImNO), DoubleTree by Hilton, London, ON, March 28-29, 2019

3. **Gillies DJ,** Awad J, Rodgers JR, Edirisinghe C, Kakani N, Fenster A, "Mechanically Tracked 3D Geometrically Variable Ultrasound Image Guidance System for Focal Liver Tumor Therapies," Ontario Institute for Cancer Research Translational Research Conference, Kingbridge Conference Centre & Institute, King City, ON, March 21-22, 2019

4. **Gillies DJ,** Awad J, Rodgers JR, Edirisinghe C, Kakani N, Fenster A, "Applicator Segmentation in Three-dimensional Ultrasound for Interventional Liver Therapies," Imaging Network Ontario (ImNO), Chestnut Residence & Conference Centre, Toronto, ON, March 28-29, 2018

5. **Gillies DJ,** Gardi L, De Silva T, Zhao R, Fenster A, "Real-time Motion Compensation for 3D Ultrasound Prostate Biopsy," Ontario Institute for Cancer Research Scientific Meeting, The Westin Harbour Castle Hotel, Toronto, ON, March 23-24, 2017

6. **Gillies DJ,** Gardi L, Zhao R, Fenster A, "A Comparison between User Initiated and Continuous Real-time Motion Compensation Techniques for 3D Ultrasound-guided Prostate Biopsy," Imaging Network Ontario (ImNO), DoubleTree by Hilton, London, ON, March 15-16, 2017

7. **Gillies DJ,** Gardi L, Zhao R, Fenster A, "Real-time Prostate Motion Compensation for 2D/3D Ultrasound-guided Biopsy," Innovations in Radiation Engineered Therapy, The Vaughan Estate of Sunnybrook, Toronto, ON, November 14-15, 2016

d. Regional

1. Papernick S, Dima R, **Gillies DJ**, Appleton T, Fenster A, "Validation of 3D ultrasound for bedside monitoring of osteoarthritis-induced synovium inflammation and cartilage degradation," Western Research Forum, Western University, London, ON, March 19, 2020.

2. **Gillies DJ,** Bax J, Barker K, Gyacskov I, Gardi L, Tessier D, Kakani N, Cool DW, Fenster A, "A 3D ultrasound system to improve image guidance and verification during focal liver cancer therapies," Oncology Research and Education Day, Best Western Lamplighter, London, ON, June 14, 2019

3. **Gillies DJ,** Bax J, Barker K, Gyacskov I, Gardi L, Tessier D, Roy P, Kakani N, Cool DW, Fenster A, "Mechanical and Imaging Methods to Improve Guidance Using a Three-Dimensional Ultrasound System for Liver Cancer Therapy," Robarts Research Retreat, King's College Student Life Centre, London, ON, June 7, 2019

4. **Gillies DJ,** Bax J, Barker K, Gardi L, Tessier D, Kakani N, Fenster A, "The Sound of Guidance: A Novel 3D Ultrasound System for Image-guided Liver Cancer Therapies," London Health Research Day, London Convention Centre, London, ON, April 30, 2019

5. Papernick, S, **Gillies DJ,** Barker K, Gardi L, Fenster A, "Validating 3D ultrasound measurements for the diagnosis of arthritis," MBP Undergraduate Research Day, University Hospital, London, ON, April 8, 2019

6. **Gillies DJ,** Awad J, Rodgers JR, Edirisinghe C, Kakani N, Fenster A, "Development of a Segmentation Algorithm to Increase Localization of Applicators in Three-Dimensional Ultrasound for Liver Cancer Therapies," London Imaging Discovery Day, St. Joseph's Health Care, London, ON, June 14, 2018

7. **Gillies DJ,** Awad J, Rodgers JR, Edirisinghe C, Kakani N, Fenster A, "Localizing Minimally Invasive Applicators in 3D Ultrasound-Guided Liver Cancer Therapies," Oncology Research and Education Day, Best Western Lamplighter Inn, London, ON, June 8, 2018

8. **Gillies DJ,** Awad J, Rodgers JR, Edirisinghe C, Kakani N, Fenster A, "Semi-Automatic Segmentation of Applicators in Three-Dimensional Ultrasound Images," Robarts Research Retreat, King's College, London, ON, June 1, 2018

9. **Gillies DJ,** Awad J, Rodgers JR, Edirisinghe C, Kakani N, Fenster A, "Making It Easier to See: Applicator Segmentation for Interventional Liver Therapies in Three-dimensional Ultrasound," London Health Research Day, London Convention Centre, London, ON, May 10, 2018

10. Harris A, Kishimoto J, Gardi L, **Gillies DJ**, de Ribaupierre S, Fenster A, "Image Registration for Monitoring of Neonatal Intraventricular Hemorrhage Using 3D Ultrasound," London Health Research Day, London Convention Centre, London, ON, May 10, 2018

11. **Gillies DJ,** Gardi L, De Silva T, Zhao R, Fenster A, "Manual or Automatic? Real-time User Initiated and Continuous Motion Compensation Techniques for 3D Ultrasound-guided Prostate Biopsy," London Health Research Day, London Convention Centre, London, ON, March 28, 2017

12. **Gillies DJ,** Gardi L, Zhao R, Fenster A, "Removing the Blindfold: Improved Image Guidance through Real-time 2D/3D Ultrasound Motion Compensation," Imaging Applications in Prostate Cancer [2 min. oral + Poster], Best Western Lamplighter Inn, London, ON, November 25, 2016

13. **Gillies DJ,** Zhao R, Gardi L, Fenster A, "Motion Compensation During Prostate Biopsies Using 2D/3D Ultrasound Rigid Registration," London Imaging Discovery Day, Brescia College, London, ON, June 21, 2016

14. **Gillies DJ,** Zhao R, Gardi L, Fenster A, "Motion Compensation During Prostate Biopsies Using 2D/3D Ultrasound Rigid Registration," Oncology Research and Education Day, Best Western Lamplighter Inn, London, ON, June 17, 2016

15. **Gillies DJ,** Zhao R, Gardi L, Fenster A, "Motion Compensation During Prostate Biopsies Using 2D/3D Ultrasound Rigid Registration," Robarts Research Retreat, Robarts Research Institute, London, ON, June 13, 2016

16. **Gillies DJ**, Fenster A, "2D-3D Real-time Rigid Registration to Compensate for Liver Motion During Interventional Therapy," Co-op Session, University of Windsor, Windsor, ON, August 17, 2015

17. **Gillies DJ**, Rehse SJ, "A New Method of Sample Preparation for Laser-Based Bacterial Identification," Undergraduate Co-op Session, University of Windsor, Windsor, ON, November 14, 2014

18. **Gillies DJ**, Richier J, "Validation of a Monte Carlo Treatment Planning System for Electron Beams," Undergraduate Co-op Session, University of Windsor, Windsor, ON, November 14, 2013

RESEARCH EXPERIENCE

Robarts Research Institute, London, ON 2015
Summer Co-op Student
Supervisor: Dr. Aaron Fenster

University of Windsor, Windsor, ON 2012-2015
Biophysical Research Assistant/Outstanding Scholars Student
Supervisor: Dr. Steven Rehse

Windsor Regional Cancer Centre, Windsor, ON 2013-2014
Medical Physics Co-op Student

TEACHING & WORK EXPERIENCE

University of Western Ontario, London, ON 2019-Current
Graduate Teaching Assistant in Medical Biophysics (3 terms)
BIOPHYS 9672 – Practical Radiotherapy Physics

London Regional Cancer Program, London, ON 2019
Radiotherapy Quality Assurance Internship
University of Western Ontario, London, ON 2018

Graduate Teaching Assistant in Physics
PHYSICS 1301/1401/1501/1028 – Introductory Physics I

London Regional Cancer Program, London, ON 2016-2017
Radiotherapy Quality Assurance Internship (2 terms)

University of Windsor, Windsor, ON 2014-2015
Teaching Assistant in Physics
PHYSICS 64-140 & 64-141 – Introductory Physics I & II

McDonald's Canada, Tecumseh, ON 2008-2013
Crew, Trainer, and Swing Manager

ACADEMIC ACTIVITIES & VOLUNTEER EXPERIENCE

SUPERVISORY EXPERIENCE

Undergraduate Theses

Sam Papernick 2018-2019
Three-Dimensional Ultrasound Use in Diagnosis of Knee Rheumatoid Arthritis and Osteoarthritis

Andrew McCann 2015-2016
Analysis of Needle Segmentation Algorithms in MRI and US Guided Prostate and Breast Procedures

Co-op and Internships

Elina Raščevska	2018
Andy Lam	2017-2018

Summer Students

Melanie Jonnalagadda	2019
Sashini Loku	2019
Imrie Pentz	2016, 2017

ACADEMIC SERVICE

Medical Physics journal reviewer	2019
London Health Research Day Poster Judge	2019
Medical Biophysics Undergraduate Research Day Poster Judge	2019

MEDIA RELEASES

Schulich School of Medicine & Dentistry. (2018, December 11). *SchulichMedDent Live: Exploring 3D-ultrasound technology*. Retrieved from https://www.schulich.uwo.ca/about/news/2018/december/schulichmeddent_live_exploring_the_3dultrasound_technology.html

Western News. (2016, April 7). *PhD candidate looks to focus liver surgery*. Retrieved from https://news .westernu.ca/2016/04/20978/

VOLUNTEER PRESENTATIONS

1. **Gillies DJ,** Rodgers J, Tessier T, "3D Ultrasound Application Demo," Western Engineering Summer Academy [Oral], Robarts Research Institute, London, ON, August 12, 2019

2. **Gillies DJ,** Michael J, Rodgers J, Fenster A, "Ultrasound Beyond Babies," Retiring With Strong Minds [Oral], Kiwanis Senior Community Center, London, ON, January 27, 2017

VOLUNTEER POSITIONS

University of Windsor, Windsor, ON 2014-2015
Physics Club Treasurer

University of Windsor, Windsor, ON 2014-2015
Connecting4Success Mentor

Science Rendezvous, Windsor, ON 2014
Physics Demonstrator

St. Gregory the Great Parish**,** Tecumseh, ON 2007-2009
Youth Leader

CERTIFICATES

Own Your Future - Doctoral Leadership Forum	2018
RSNA Professionalism in Everyday Practice; The Physician Charter	2017
CITI Program Canada Good Clinical Practice Stage 1-BASIC	2017

PROFESSIONAL MEMBERSHIPS

Canadian Organization of Medical Physicists (COMP)	2019-Present
American Association of Physicists in Medicine (AAPM)	2015-Present
SPIE	2017-Present